Postdoctoral Thesis

Lijie Sun

Facility for Rare Isotope Beams, Michigan State University, 640 South Shaw Lane, East Lansing, MI 48824, USA

Abstract

I had the privilege of working with Professor Christopher Wrede as a Visitor for 1 year, from October 2018 to October 2019, and then as a Research Associate for a total of 3.7 years, from October 2019 to October 2021 and again from May 2023 to February 2025. I would like to express my deepest gratitude to my advisor Chris. His ability to identify important scientific problems and develop innovative solutions has profoundly shaped my development as a researcher. I am truly indebted to him for his patience, his willingness to share his extensive knowledge, and his constant encouragement to strive for excellence. Being part of the talented Wrede Group has not only enriched my academic journey but also provided me with lasting friendships that I will treasure throughout my career. I would like to thank our group members, listed in order of age: Moshe Friedman, Tyler Wheeler, Ruchi Mahajan, Brent Glassman, Alexander Adams, Cathleen Fry, Tamas Budner, Jason Surbrook, Joseph Dopfer, and Lexanne Weghorn, and many other collaborators, particularly Barry Davids, for their invaluable support and insightful guidance.

Part I
DSL

1. First application of Markov Chain Monte Carlo-based Bayesian data analysis to the Doppler-Shift Attenuation Method

Motivated primarily by the large uncertainties in the thermonuclear rate of the $^{30}\mathrm{P}(p,\gamma)^{31}\mathrm{S}$ reaction that limit our understanding of classical novae, we carried out lifetime measurements of ^{31}S excited states using the Doppler Shift Lifetimes (DSL) facility at the TRIUMF Isotope Separator and Accelerator (ISAC-II) facility. The ^{31}S excited states were populated by the $^{3}\mathrm{He}(^{32}\mathrm{S},\alpha)^{31}\mathrm{S}$ reaction. The deexcitation γ rays were detected by a clover-type high-purity germanium detector in coincidence with the α particles detected by a silicon detector telescope. We have applied modern Markov chain Monte Carlo-based Bayesian statistical techniques to perform lineshape analyses of Doppler-shift attenuation method γ-ray data for the first time. We have determined the lifetimes of the two lowest-lying ^{31}S excited states. First experimental upper limits on the lifetimes of four higher-lying states have been obtained. The experimental results were compared to shell-model calculations using five universal *sd*-shell Hamiltonians. Evidence for γ rays originating from the astrophysically important $J^{\pi} = 3/2^{+}$, 260-keV $^{30}\mathrm{P}(p,\gamma)^{31}\mathrm{S}$ resonance with an excitation energy of $E_x = 6390.2(7)$ keV in ^{31}S has also been observed, although strong constraints on the lifetime will require better statistics.

2. Introduction

Classical novae are one of the most frequent thermonuclear stellar explosions in the Galaxy. They are powered by thermonuclear runaways occurring in the accreted envelope transferred from a companion star onto a compact white dwarf in a close binary system [404, 400]. In classical novae, the $^{30}\mathrm{P}(p,\gamma)^{31}\mathrm{S}$ reaction acts as a nucleosynthesis bottleneck in the flow of material to heavier masses [3]. The large uncertainty in the $^{30}\mathrm{P}(p,\gamma)^{31}\mathrm{S}$ rate impacts the identification of certain presolar nova grains [4], the calibration of nuclear nova thermometers [5], and the Si/H abundance ratio, which can be used to constrain the degree of mixing between the white dwarf's outer layers and

the accreted envelope [6]. It is not currently possible to measure the ^{30}P$(p,\gamma)^{31}$S reaction directly because intense low energy ^{30}P beams are not available. The thermonuclear rate of the ^{30}P$(p,\gamma)^{31}$S reaction over most of the peak nova temperatures (0.1−0.4 GK) is found to be dominated by proton capture into a 260-keV $3/2^+$ resonance with an excitation energy of E_x = 6390.2(7) keV in ^{31}S [7, 8]. Recent experimental work has unambiguously determined the energy, the spin and parity, and the proton-decay branching ratio of this resonance [8, 9, 443], leaving the lifetime as the final missing piece of the puzzle. So far, the lifetimes of three relatively long-lived ^{31}S states at 1248 [11, 12, 13, 14], 2234 [11], and 4451 keV [14, 15] have been reported. The main scientific goal of this work is to expand lifetime measurements to more excited states in ^{31}S, including the $3/2^+$ state at 6390 keV using the Doppler Shift Attenuation Method (DSAM).

Lifetime measurements using γ-ray spectroscopy provide not only important input for astrophysical models but also a sensitive benchmark for nuclear structure models. DSAM is a widely-used method for measuring lifetimes of excited nuclear states in the fs to ps range [16, 17, 18]. Despite the wide use of this method, a unified statistical treatment of all the uncertainties associated with systematic effects has been a long-standing issue. The classical frequentist approach (χ^2 minimization) does not in itself provide any uncertainty, but it is a common practice to assume a normal distribution and vary each parameter by one standard deviation while fixing other parameters at some plausible values. Uncertainties from different sources are often assessed independently and then added in quadrature to obtain the total uncertainty. The statistical meaning is even less rigorous when combining upper/lower limits instead of finite values. Multiple parameters often have complex interrelationships, and their correlations may be underestimated or overestimated by standard frequentist approaches [19, 20, 21].

Inverse problems are often ill-posed: what are the model parameters that result in a given set of observables [22]? Inferring lifetimes from observed γ-ray spectra is such an inverse problem and represents an ideal case for the application of Bayes's theorem [23, 24]. Bayesian statistics offers a probabilistic framework for parameter estimation and uncertainty quantification [25]. Owing to the distribution complexity and high dimensionality, practical use of Bayesian statistics often requires Markov chain Monte Carlo (MCMC) [26, 27], an efficient sampling method to systematically explore complex high-dimensional parameter spaces [28]. With the advent of modern computational power, there has been a surge of interest in incorporating Bayesian and MCMC techniques in nuclear physics parameter estimation, in particular, the studies of heavy-ion collisions [29, 30, 31, 32, 33, 34, 35, 36, 37, 38, 39], low-energy nuclear reactions [19, 20, 21, 40, 41, 42, 43, 44, 45, 46, 47, 48, 49, 50], nuclear level-density model parameter estimation [51], and spectrum fit [52].

Although Bayesian methods are playing increasingly important roles in many aspects of nuclear physics [53, 54, 55], to the best of our knowledge, no one had performed DSAM lifetime data analysis within a Bayesian framework. Our previous work [56] took the very first step in that direction. In this Letter, we further apply MCMC-based Bayesian parameter estimation methods to DSAM lineshape analyses, providing a statistically meaningful/rigorous/robust/reliable quantification of uncertainties from various sources in Bayesian inference.

3. Experiment

The experiment was done using the Doppler Shift Lifetimes (DSL) chamber [57] specifically designed for DSAM experiments [56, 58, 59, 60, 61] at the ISAC-II facility of TRIUMF. A 128-MeV $^{32}S^{7+}$ beam bombarded a ^{3}He-implanted Au target and the excited states in ^{31}S were populated via the ^{3}He$(^{32}$S$,\alpha)^{31}$S reaction. We employed inverse kinematics to ensure a large Doppler shift in the γ-ray spectra. The α particles were detected using a silicon detector telescope placed downstream of the target. The telescope consisted of two ORTEC B Series Si surface barrier detectors with an active area of 150 mm^2 and thicknesses of 87 μm and 1 mm, respectively [63]. An aperture was placed in front of the telescope, limiting the ejectile acceptance angle to <13°. Deexcitation γ rays were detected in coincidence with α-particles by using a clover-type high-purity germanium detector [64, 65] at a distance of 78 mm from the target, centered at 0° with respect to the beam axis. See the next section for more technical details.

The Si detectors were calibrated using a source containing ^{239}Pu, ^{241}Am, and ^{244}Cm, with strong α lines at 5.155 MeV, 5.486 MeV, and 5.805 MeV. A linear calibration was applied and used to extrapolate to higher energies. The extrapolation was verified by comparing the energy loss of punch-through particles to SRIM calculations [491]. A ^{56}Co source was used initially to calibrate the Ge detector. A line from ^{197}Au Coulomb excitation at 279.01(5) keV [67] and a line from ^{39}K produced in ^{32}S+^{12}C fusion evaporation at 2814.06(20) keV [68] were observed with high statistics. The vast majority of the γ rays constituting these lines were emitted after the recoils

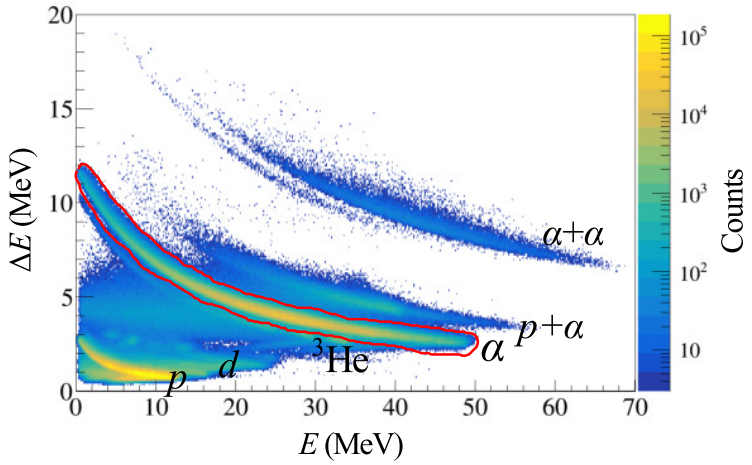

Figure 1: Particle identification plot of the energy loss (ΔE) in the 87-μm Si detector versus the residual energy deposited in the 1-mm Si detector (E). Each locus of points represents a charged particle group or a coincidence summing of two groups. The red contour encloses the α particles of interest.

stopped; hence, they are unshifted and used as run-by-run calibration standards. The accuracy of the calibration at high energies was verified by a 6128.63(4)-keV γ ray originating from the deexcitation of the second excited state in ^{16}O [69]. The energies deposited in all four crystals of the clover detector were summed together to increase the photo-peak efficiency while reducing the Compton scattering background [64]. Lifetimes of ^{31}S states were then determined from a lineshape analysis of this addback spectrum.

The Si detector telescope particle identification plot is shown in Fig. 1. The α-particle group is separated from other charged particle groups. By gating on α particles with specific energies calculated by relativistic reaction kinematics, we suppressed competing reaction channels and indirect feedings from higher-lying levels to ensure a direct population by the transfer reaction, resulting in significantly cleaner γ-ray spectra.

4. Techniques

In this section, we briefly review the basics of the DSAM, the DSL facility, and the data acquisition (DAQ) and sorting used for this study.

4.1. DSAM

The DSAM has been used routinely for measuring the lifetimes of excited nuclear states in the fs to ps range [16, 17, 18]. When an excited nucleus is produced by a nuclear reaction in a target, it carries the initial momentum due to reaction kinematics and starts to travel in a stopping medium. If a γ ray is emitted while the nucleus is still in flight, it will be Doppler shifted in the laboratory frame. A time correlation can be established between the slowdown and deexcitation of the nucleus, and the lifetime of the excited state can be inferred based on the observed Doppler shift of γ rays. The typical slowing down time of the nuclei recoiling from a nuclear reaction is a few hundred fs in solid materials, which implies that DSAM is applicable to lifetimes in the 1 fs to 10 ps range [70, 71, 451, 73].

4.2. DSL facility

Motivated primarily by the unknown or imprecise lifetimes of excited states of astrophysical importance, we built the DSL facility. As shown in Fig. 29, the scattering chamber was designed to provide a clean environment conducive to detecting γ ray emission from excited nuclear states populated in heavy ion-induced transfer reactions in inverse kinematics [57]. Reaction products gain more energy in inverse kinematics and lead to larger Doppler shifts. Since its completion in 2005, the DSL experimental setup has been used to measure the lifetimes of excited states in ^{19}Ne relevant to the ^{15}O$(\alpha,\gamma)^{19}$Ne reaction rate [58, 59], the lifetimes of excited states in ^{15}O relevant to the ^{14}N$(p,\gamma)^{15}$O

reaction rate [56], and the lifetimes of excited states in ^{23}Mg relevant to the ^{22}Na$(p,\gamma)^{23}$Mg reaction rate [60]. The ^{3}He-implanted targets were produced at the Université de Montréal, Canada, by implanting 35-keV ^{3}He ions into a 25 μm-thick Au foil to an areal density of 6×10^{17} cm^{-2}. The Au foil was chosen to be thick enough to stop both the beam and the heavy recoils. In this experiment, two apertures with diameters of 2.5 and 3.0 mm were placed at distances of 73 and 49 mm, respectively, upstream of the target. A 128-MeV $^{32}S^{7+}$ beam passed through the collimator and bombarded the ^{3}He-implanted Au target. The target was kept cool via BeCu fingers in contact with a BN plate attached to a LN_2-cooled Cu shroud. The thermal gradient between the target ladder and the Cu shroud prevents losses of the implanted ^{3}He through heating while mitigating the condensation of contaminants on the surface of the target [62, 61].

4.3. DAQ system

The germanium detector used in this experiment was from the Gamma-Ray Infrastructure For Fundamental Investigations of Nuclei (GRIFFIN) [65]. The GRIFFIN electronics are custom designed and are able to handle data throughput up to 50 kHz per Ge crystal. The signals from the preamplifiers of the germanium and silicon detectors enter the GRIF-16 digitizer modules, which are 16-channel, 14-bit, 100-MHz flash analog-to-digital converters. A series of signal processing algorithms, such as hit detection and pulse-height evaluation, are implemented in the GRIF-16 firmware. After being processed by these algorithms, the signal is collected by GRIF-C Slave modules, concentrated into the GRIF-C Master module, and then packed into events by the DAQ system. The master GRIF-C applies logic to the data received from the slaves and applies experimental filters to the data. These filters are analogous to master triggers used in analog DAQ systems, and reject data not meeting specific criteria - coincidence, for example - in order to reduce the amount of uninteresting data being written to disk. The GRIFFIN DAQ system is a modified version of the Maximum Integrated Data Acquisition System [74]. These data are unpacked by the GRSISort program and turned into more practical data structures for analysis.

A single GRIF-Clk Master clock module houses a Symmetricom Model SA.45s Chip-Sized Atomic Clock (CSAC), which produces a precision 10 MHz reference signal. A 50 MHz master clock signal derived from this reference is then distributed through GRIF-Clk Slave modules to all modules in the system. Each event is timestamped using a hit detection algorithm, which is equivalent to leading-edge timing. Then the timestamp is corrected by a digital constant-fraction discriminator to compensate for the amplitude-dependent time-walk [75]. A key advantage of the digital DAQ is that it behaves essentially as a trigger-less system, with each channel able to record physics events independently of the others.

4.4. Sorting

The sorting part of the package works in three parts. The first step takes raw MIDAS data and converts it to a set of fragments. Fragments are stored in the fragment tree and contain most of the raw information of detector outputs. The fragment information is useful for diagnostic tests, and act as the pre-sorting stage. In principle, as the fragment is essentially the conversion of MIDAS information to ROOT information, this unpacking step is typically only performed once during an analysis. The second part of sorting takes the fragments and builds physics events that are stored in the analysis tree. Finally, scripts can be used to process the analysis tree and build histograms of various dimensions.

Events are typically constructed using the timing of the detection of multiple particles. Events can be constructed by the GRIFFIN DAQ using filters that require certain detector multiplicity conditions to be met before transmitting data to be written to disk. These conditions will often use a static timing window in order to define a coincidence. Filters reduce the amount of data written to disk the same way a master trigger does in a typical analogue system. More precise construction of these events can still occur using the timing of the individual hits within the event constructed by the DAQ filter. In this work, a moving time window of fixed length is used. For example, a moving window of 2 μs is opened whenever a new fragment is found. As new fragments are found within that window, new windows are created and joined to the original event. This process continues, creating a chain of 2 μs windows until the final window does not find a fragment within 2 μs. Once this occurs, all of the fragments associated with the current moving window are 'packaged' into a single analysis tree event.

5. Simulation & Results

The γ-ray lineshape is sensitive to the ^{31}S velocity distribution and all other physical effects, and therefore a lineshape analysis is more rigorous and gives more information than a centroid-shift analysis. Detailed Monte Carlo simulations were written to model Doppler-shifted lineshapes for fs lifetimes [56, 60]. A new Monte Carlo simulation using GEANT4 [522, 523] was developed in this work to model lineshapes for ps lifetimes as well. We began by sampling the position where the transfer reaction happens from a uniform circular transverse profile defined by the beam spot and the ^{3}He implantation depth profile calculated by SRIM [491]. The kinetic energy of the beam was sampled from a Gaussian beam energy distribution with a spread of 0.2% (full width at half maximum) and energy loss in the target based on the reaction location. The emission angle of the α particle was chosen randomly from an isotropic distribution in the laboratory frame. The error introduced by this simplifying assumption was estimated by trying a few different realistic anisotropic distributions and was found to be rather small due to the limited angular acceptance [56, 60]. The energy and momentum of the emitted α particle were calculated using relativistic kinematics from the Q-value of the transfer reaction and the kinetic energy of the beam. The Q-value of the transfer reaction depends on the populated state in ^{31}S as $Q = Q_0 - E_{\rm ex}$ with $Q_0 = 5533.30(23)$ keV corresponding to the ground state and $E_{\rm ex}$ of the excitation energy of the populated state in ^{31}S [428]. We then determine the 4-momentum of the excited ^{31}S recoil. If a γ ray is emitted while the ^{31}S recoil is still moving, it will be Doppler shifted in the laboratory frame. A detector response of the form of an exponentially modified Gaussian (EMG) function [526, 516] was added to the γ-ray energy recorded by the germanium at the end. The decay and width parameters of the EMG function were empirically characterized as a function of energy by fitting unshifted γ-ray peaks originating from long-lived states populated by Coulomb excitation and fusion-evaporation reactions at energies of 279.01(5) and 547.5(3) keV [^{197}Au] [67], 2814.06(20) and 3597.26(25) keV [^{39}K] [68], 3736.5(3) keV [^{40}Ca] [81], and 6128.63(4) keV [^{16}O] [69].

Fitting the simulated γ-ray spectrum to the measured γ-ray spectrum in a given range yields the number of counts and the associated standard deviation (σ). We set a discovery threshold for statistical significance over the background-only hypotheses to be 5σ [82]. The observed ^{31}S γ-ray peaks (Fig. 2) are shown in Figs. 3-9 with the prior and posterior predictive lineshapes superimposed (See Sec. 6). The gate on the energy deposited by the α particles is 2 MeV wide in all cases, corresponding to a 1-MeV window on the excitation energies. We used a fine binning of 2 keV in each lineshape analysis to mitigate the information loss associated with the bin size of the spectrum. The 1248-keV, 2234-keV, 3076-keV, 4971-keV, and 5156-keV ^{31}S states all decay predominantly by a single γ-ray transition to the ground state [9], and their dominant γ rays are clearly observed in the corresponding α-gated γ-ray spectra. Other than these five peaks, a 2186-keV line from the decay of the 3435-keV state is also observed with a statistical significance greater than 5σ. There are two γ rays which are emitted from the 3435-keV ^{31}S state with branching ratios of 54.7(35)% and 45.3(30)% to the ground and first excited states, respectively [9]. The observed significance of the 3435-keV line does not reach the 5σ threshold, so we extract the lifetime based on the lineshape analysis of the 2186-keV line. We estimated the branching ratios to be 38(11)% and 62(12)% using the efficiency-corrected counts in the 3435- and 2186-keV γ-ray peaks with only statistical uncertainties included, consistent with the previous measurement [9]. All six aforementioned ^{31}S states were also observed to be populated in the ^{32}S(^{3}He, α)^{31}S reaction at the same center-of-mass kinetic energy as ours [83].

γ-ray transitions from the $3/2^+$, 6390.2(7)-keV state at 2183, 3106, 3314, 4156, 5141, and 6390 keV were previously identified [9]. Evidence for the 4156 and 5141-keV branches was observed in this data set with significances over 4σ and 3σ, respectively. Consistent with past work [9], the 4156-keV branch is the strongest branch observed. A nearby $5/2^+$, 6392.5(2)-keV state was observed to dominantly populate the $3/2^+$, 1248-keV state with a 5143.1(2)-keV γ-ray branch [84, 85, 86], which could be responsible for the higher intensity we observed for the 5141-keV branch. The absence of the $5/2^+$, 6392 keV $\rightarrow$ $5/2^+$, 2234 keV transition in those experiments [84, 85, 86] is also consistent with our shell model calculations (Sec. 9). Another nearby $11/2^+$, 6394.2(2)-keV state generates 1091.2(4)- and 3042.9(1)-keV branches [84, 85, 87, 88, 89], but neither of these branches was observed in our spectra. A recent study using the ^{32}S$(p,d)^{31}$S single-neutron transfer reaction also indicates that the $(3/2, 5/2)^+$ states near 6390 keV are preferentially populated, but the $11/2^+$ state is not [90]. As the 4156-keV γ ray is likely to be uniquely associated with the $3/2^+$, 6390-keV $\rightarrow$ $5/2^+$, 2234-keV transition, we attempt to extract the lifetime from its lineshape.

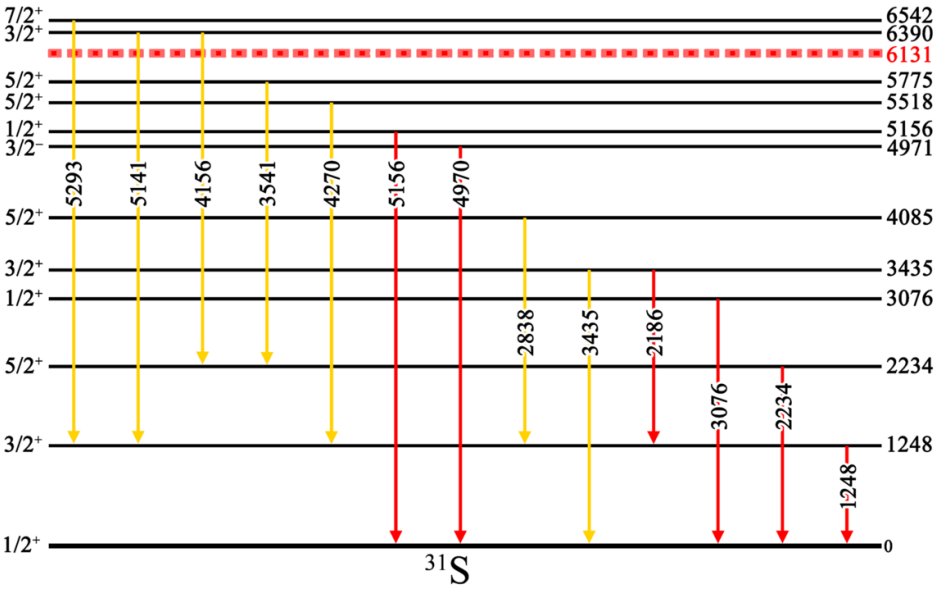

Figure 2: Observed γ-ray transitions in ^{31}S. Red and yellow denote observations with significances over 5σ and below 5σ but above 3σ, respectively.

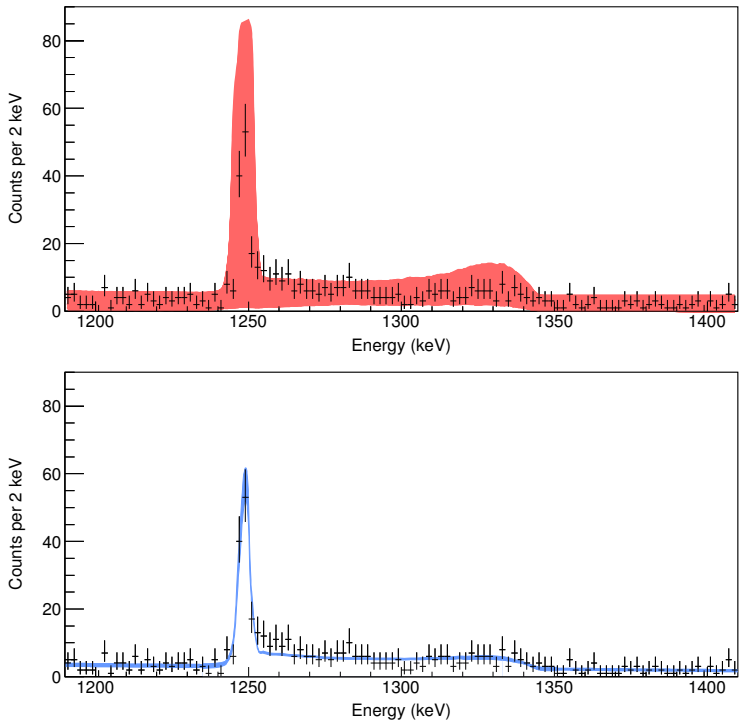

Figure 3: Lineshape analysis of the 49-MeV α-gated γ-ray line from the 1248 keV $\rightarrow$ ground state transition in ^{31}S. The measured lineshape is shown as points with statistical error bars in both panels. Prior lineshape (red, upper panel): hundreds of lineshapes generated by varying each parameter within its prior range in the DSAM simulation. Posterior predictive lineshape (blue, lower panel): 68% credible interval constructed with the number of counts in each bin corresponding to the parameter posterior distributions.

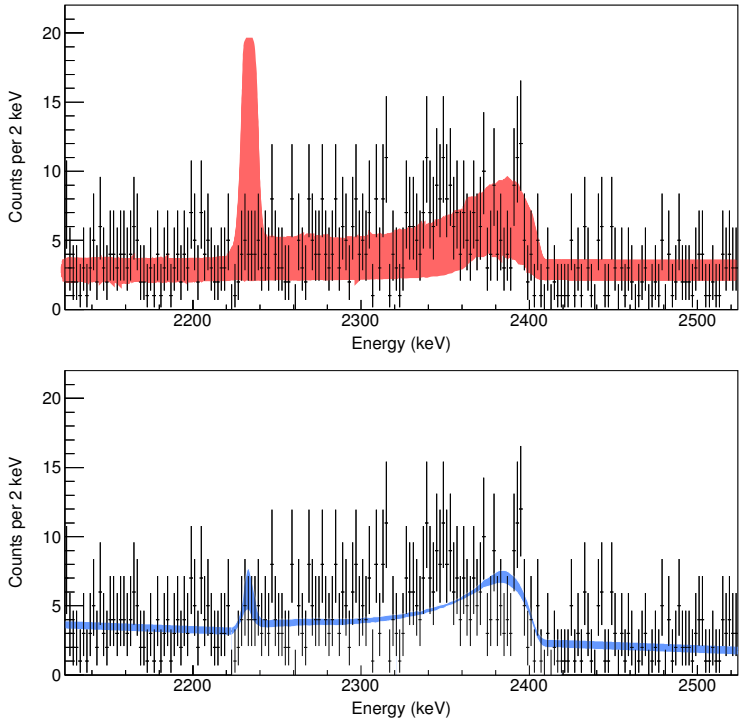

Figure 4: Lineshape analysis of the 47-MeV α-gated γ-ray line from the 2234 keV $\rightarrow$ ground state transition in ^{31}S. The measured lineshape is shown as points with statistical error bars in both panels. Prior lineshape (red, upper panel): hundreds of lineshapes generated by varying each parameter within its prior range in the DSAM simulation. Posterior predictive lineshape (blue, lower panel): 68% credible interval constructed with the number of counts in each bin corresponding to the parameter posterior distributions.

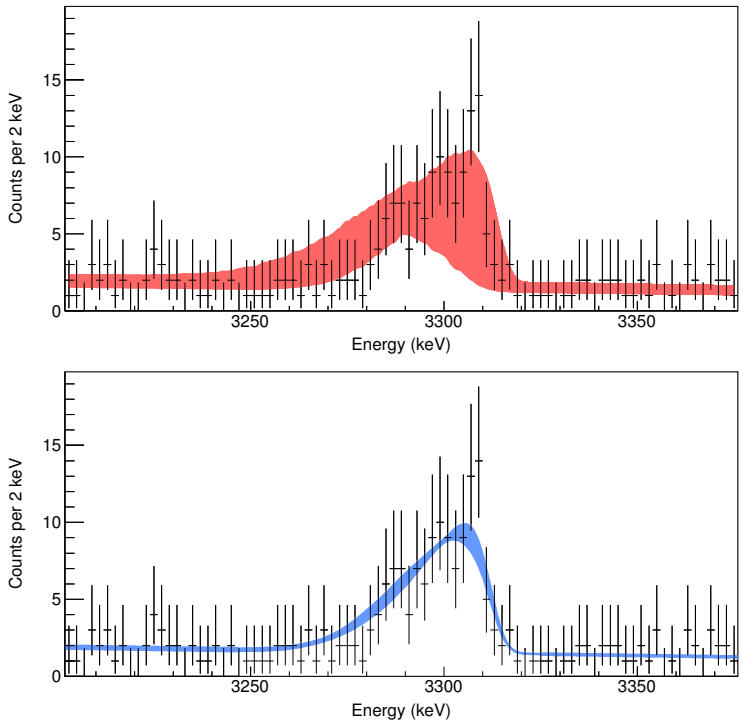

Figure 5: Same as Fig. 4 for the 46-MeV α-gated γ-ray line from the 3076 keV $\rightarrow$ ground state transition in ^{31}S.

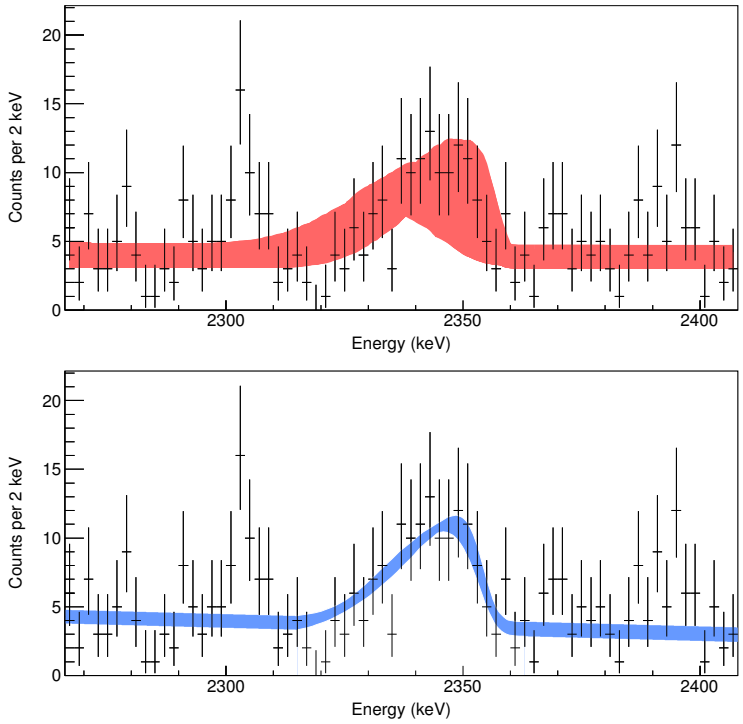

Figure 6: Same as Fig. 4 for the 45-MeV α-gated γ-ray line from the 3435 keV $\rightarrow$ 1248 keV transition in ^{31}S.

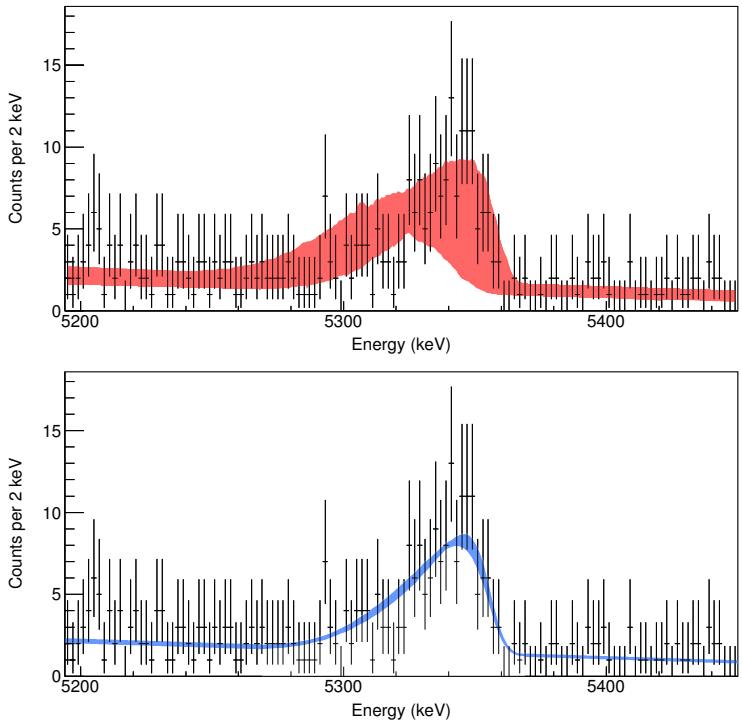

Figure 7: Same as Fig. 4 for the 42-MeV α-gated γ-ray line from the 4971 keV $\rightarrow$ ground state transition in ^{31}S.

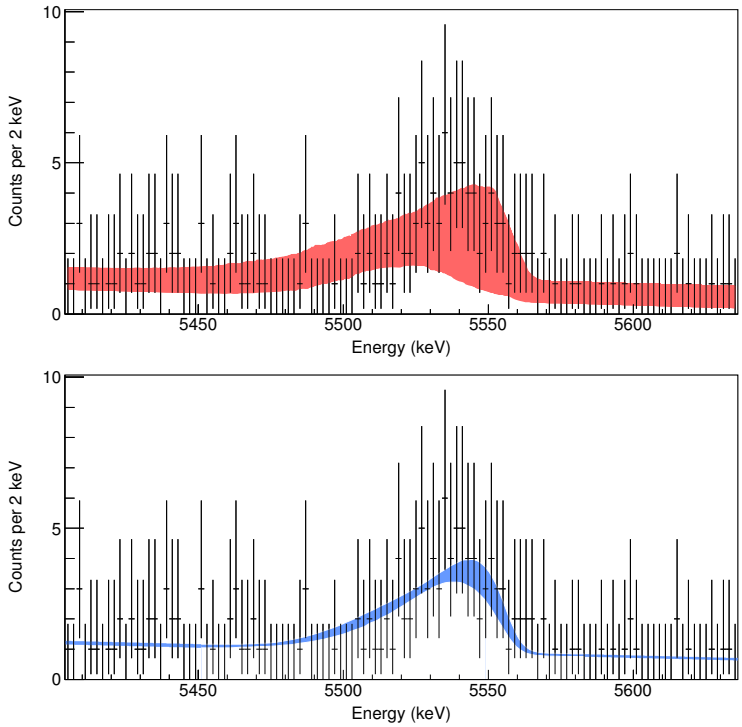

Figure 8: Same as Fig. 4 for the 42-MeV α-gated γ-ray line from the 5156 keV $\rightarrow$ ground state transition in ^{31}S.

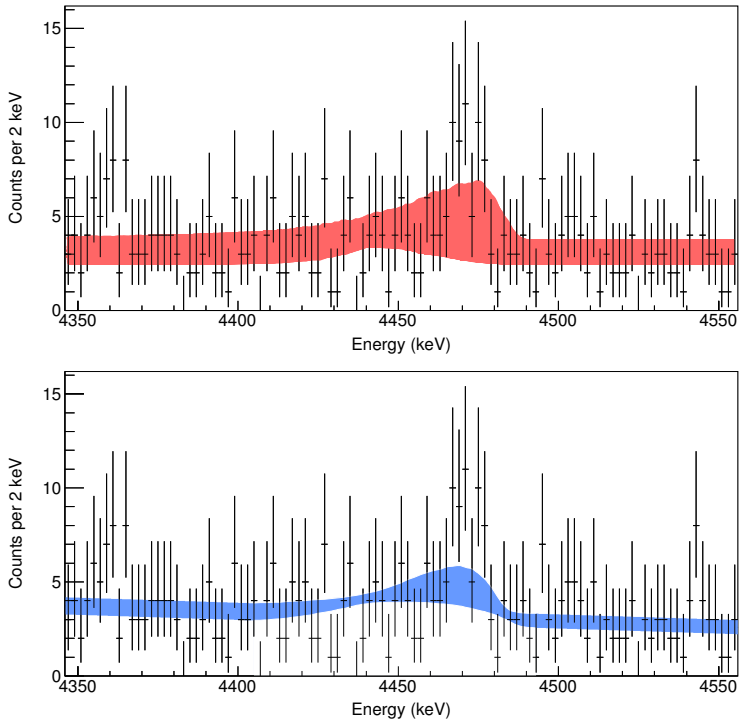

Figure 9: Same as Fig. 4 for the 39-MeV α-gated γ-ray line from the 6390 keV $\rightarrow$ 2234 keV transition in ^{31}S.

6. Bayesian Analyses

Graphical representations of our analysis procedure are shown in Figs. 10 and 11. The analysis framework combined a DSAM model, dimensionality reduction with principal component analysis, emulation with Gaussian processes, and Markov chain Monte Carlo with Metropolis-Hastings algorithms, all of which are necessary in this case. It should also be noted that this framework is scalable and flexible, and other users can tailor each part to their cases. For example, if running their full model is fast, they can omit the emulator and use brute-force MCMC sampling.

6.1. Bayes's theorem

In general, when using Bayes's theorem [23] to set up the problem of calibrating a physics model to data, we have: 1) a deterministic or stochastic physics model $f(x, \theta)$ that nominally explains observable y at controllable inputs x. θ represents parameters that need to be estimated. 2) a set of observations, $y(x)$. 3) a likelihood, $P(y|\theta)$, the probability of the data y being observed given a set of parameters θ, which is determined by running the model with parameters θ and fitting the model output to data. Likelihood quantifies how well the model reproduces the data. 4) a prior probability distribution, $P(\theta)$, encapsulates our initial belief of the parameters. Next, we invoke Bayes's theorem, which states that our updated belief after observing the data, i.e., the posterior probability distribution of the model parameters given the data, $P(\theta|y)$, is proportional to the product of the likelihood and the prior:

$$P(\theta|y) = \frac{P(y|\theta)P(\theta)}{P(y)} \tag{1}$$

The denominator, $P(y)$, is the Bayesian evidence, which is the probability of observing the data without having compared to the model and, given that the data are assumed to be known, serves as a normalization factor. The denominator only becomes relevant in the context of model selection or model averaging problems. Translating for the application here, our model is a DSAM Monte Carlo simulation convoluted with a linear fit function to describe

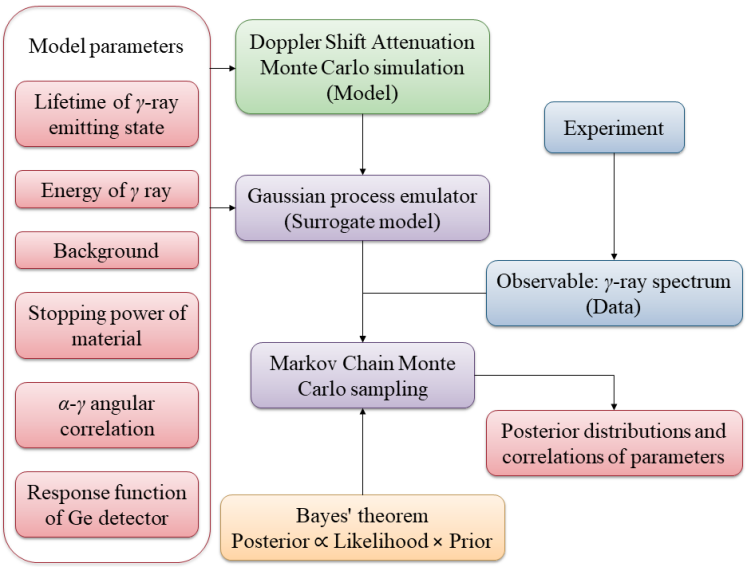

Figure 10: Workflow of the MCMC-based Bayesian DSAM data analysis framework.

the background, which introduces several parameters. The output of the model is a γ-ray spectrum, which is the observable to be compared with data.

6.2. *Prior specification*

Any parameter that might have a meaningful impact on the model calculation should be included in the design. More parameters require more training points, which means more computation time. It is important to vary parameters that could change the behavior of the model. The choice of parameters should be "As many parameters as necessary, as few as possible." [91]. For the choice of priors $P(\theta)$, we specify ranges and distributions for each parameter. A uniform prior is chosen for the lifetime τ. Negative lifetimes are unphysical, so we set the prior to be zero in negative regions:

$$P(\tau) = \begin{cases} \text{constant}, & \tau > 0 \\ 0, & \tau \leqslant 0 \end{cases} \tag{2}$$

We use a Gaussian distribution for the γ-ray energy, E_γ, from the literature values and uncertainties [9]. We construct a Gaussian distribution for the relative background level, bkg, based on the linear fit and its uncertainty in the background region around a γ-ray peak. The stopping power incorporated in GEANT4 is expected to be overall accurate to within 10% [92]. Accuracy is generally higher in the energy range above 10 MeV/nucleon, while the uncertainty increases at energies below 0.1 MeV/nucleon. We use a Gaussian distribution for the relative stopping power, sp, centered at the database values with a 1σ uncertainty of 10% for short-lived states and 20% for long-lived states, respectively. The prior on the coefficient of the Legendre polynomial $P_2(\cos\theta)$ of the α-γ angular-correlation function, A_2, is assumed to be uniform within $[-1, 1]$, and A_4 is fixed to be 0. When a γ ray is emitted from a long-lived state, the emission usually happens after the recoil has undergone a series of collisions with the target atoms. Hence, the γ-ray lineshape is quite insensitive to variations of the angular correlation function. We, therefore, omit the angular correlation parameter for the two long-lived states. Our primary goal is to learn the unknown model parameter τ from observables. τ is the parameter of interest, and the other four, E_γ, bkg, sp, and A_2, are referred to as nuisance parameters, which we do not aim to constrain using this data set.

6.3. *Likelihood formulation*

Choosing a likelihood function for Bayesian inference is not always straightforward. A natural choice of the likelihood function for count data is the Poisson distribution or the normal distribution. We can write the relationship

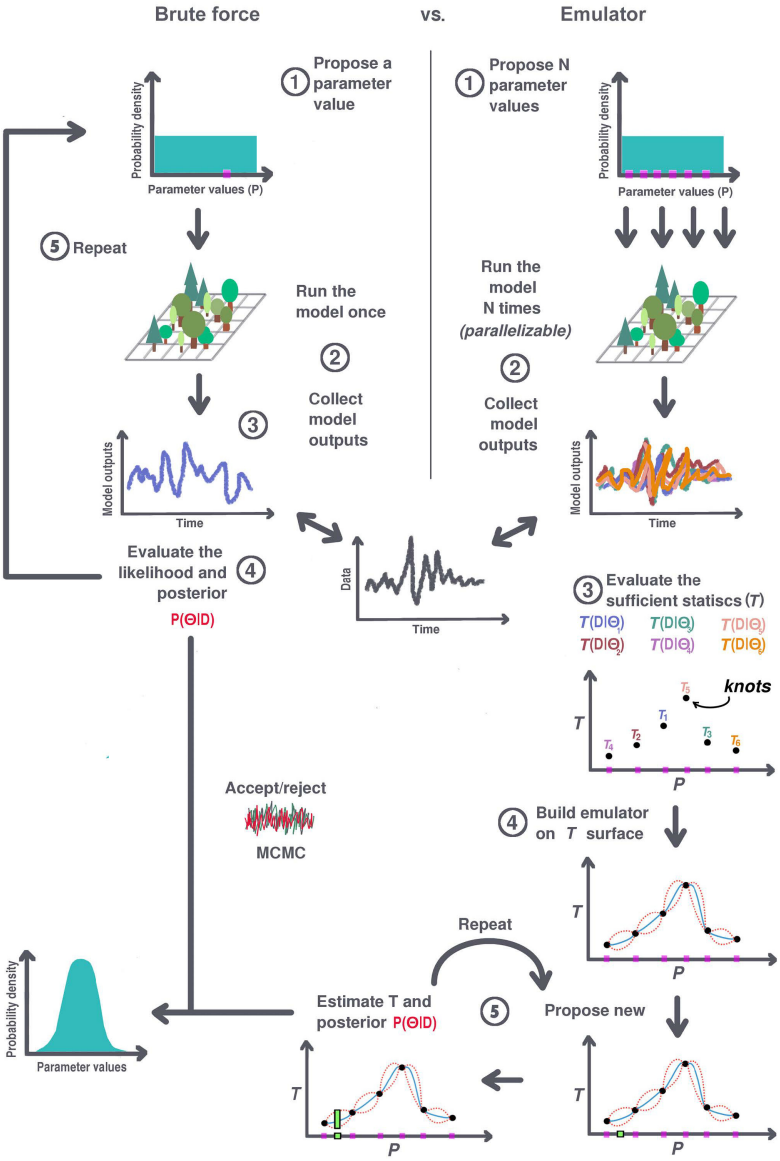

Figure 11: Comparison of brute-force and emulator workflows for a univariate example. These training points, or knots (black dots), are obtained by evaluating the full model. Next, a Gaussian statistical process is fitted (blue solid line) with error estimates for prediction (red dashed lines). Once the emulator is constructed, a new parameter value will be proposed (green box on the x-axis). Finally, values that the response variable can take (green segment) given the newly proposed parameter will be estimated using the emulator. Adapted from Ref. [93].

between the observations and the physics model as $y = f(x, \theta) + \varepsilon$ [91]. This model for the observations then includes both a physics model, $f(x, \theta)$, and a statistical model for the residual error term ε. The statistical model assumes that the error at each measurement point, x_i, is σ_i^2. To perform a bin-by-bin analysis using Bayes's theorem [94], we take the conditional probability of acquiring a measured set of data given the parameters θ to be the likelihood function $P(y \mid \theta, \sigma^2)$:

$$P(y \mid \theta, \sigma^2) \propto \exp\left[-\frac{1}{2}\sum_{i=1}^{n}\frac{[y_i - f(x_i, \theta)]^2}{\sigma_i^2}\right] \tag{3}$$

where n is the number of bins, y_i is the number of counts in the ith bin of the measured spectrum, and $f(x_i, \theta)$ is the number of counts in the ith bin predicted by the model. The error σ_i could come from many sources.

This likelihood Eq. (3) encodes the statement 'this is how likely we think it would be to observe what we see y, under inputs x, based on the model function f that depends on parameters θ, and based on an error σ. It provides a particularly simple example of this kind of statistical model, and it is used very often. Ideally, normalized errors have a standard zero-mean, unit-variance normal distribution:

$$\frac{[y - f(x, \theta)]^2}{\sigma^2} \sim N(0, 1) \tag{4}$$

So, we assume $\sigma \sim \mathrm{MVN}(0, \Sigma)$, which denotes the residual error following a multivariate normal distribution (MVN) with mean 0 and covariance matrix Σ. We obtain a modified likelihood function:

$$p(y \mid \theta) \propto (2\pi)^{-\frac{mn}{2}} |\Sigma|^{-\frac{1}{2}} \exp\left\{-\frac{1}{2}[y - f(\theta)]^\top \Sigma^{-1}[y - f(\theta)]\right\} \tag{5}$$

where m denotes the number of model parameters. The total covariance matrix Σ should subsume both experimental and theoretical uncertainties: $\Sigma = \Sigma_{\mathrm{exp}} + \Sigma_{\mathrm{th}}$, where the statistical component of Σ_{exp} is a diagonal covariance matrix $\Sigma_{\mathrm{exp}}^{\mathrm{stat}}$, and the systematic component of Σ_{exp} is non-diagonal $\Sigma_{\mathrm{exp}}^{\mathrm{sys}}$. Similarly, $\Sigma_{\mathrm{th}} = \Sigma_{\mathrm{th}}^{\mathrm{stat}} + \Sigma_{\mathrm{th}}^{\mathrm{sys}}$. $\Sigma_{\mathrm{th}}^{\mathrm{stat}}$ accounts for statistical fluctuations in the model calculations, which is usually small. $\Sigma_{\mathrm{th}}^{\mathrm{sys}}$ arises from model imperfections. If an emulator is used, $\Sigma_{\mathrm{th}} = \Sigma_{\mathrm{th}}^{\mathrm{stat}} + \Sigma_{\mathrm{th}}^{\mathrm{sys}} + \Sigma_{\mathrm{th}}^{\mathrm{emu}}$. The emulator predictive uncertainty $\Sigma_{\mathrm{th}}^{\mathrm{emu}}$ represents the deviation between the full model calculation and the fast surrogate model calculation. It would be futile to attempt to enumerate every source of uncertainty and compute a covariance matrix for each.

6.4. Model emulation

MCMC algorithms generate a random walk through the parameter space where each step is accepted or rejected according to the product of the prior and the likelihood of reproducing the measured observables [26, 27]. Direct MCMC sampling requires millions of model evaluations. In our case, a single model evaluation requires thousands of individual event simulations and is computationally demanding, so direct MCMC sampling is intractable. As our model space is relatively low-dimensional, we choose a factorial design, in which hundreds of training points uniformly fill the parameter space like a grid.

6.4.1. Principal component analysis

PCA is commonly used for feature extraction and dimensionality reduction.

Let us explain the process using the 4156-keV γ ray demonstrated in the EEC proposal S2373 as an example:

Suppose we have $p = 114$ bins in our measured spectrum, making the data dimension 1×114.

We run the full DSAM simulation with $n = 297$ parameter settings ($n = 297$ training points).

At each of $n = 297$ parameter settings, we generate $p = 114$ simulation output points. So, the dimension of our original simulator output is $n \times p = 297 \times 114$ matrix.

We standardize the simulation outputs $p = 114$ bins, bin-by-bin by subtracting the mean from each value and dividing it by the standard deviation.

We compute the covariance matrix of the standardized simulation outputs.

We perform Singular Value Decomposition (SVD) on the covariance matrix to identify eigenvectors (principal components). The number of PCs should be less or equal than the original number of bins, $q \leq p$. Suppose the first $q = 12$ PCs explain 90% of the variance in the original $p = 114$ data points.

We then project the $n \times p = 297 \times 114$ original simulator outputs onto $q = 12$ principal components (directions/vectors). The coordinates of the $n = 297$ original simulation points per bin when projected onto each principal component are called 'latent outputs'. This projection transforms data from high-dimensional spaces to low-dimensional spaces defined by the principal components.

For each of the $q = 12$ PCs, we project the original $n = 297$ points, resulting in $n = 297$ latent outputs per PC.

Since there are $q = 12$ PCs, we get $q = 12$ sets of $n = 297$ latent outputs. So, the dimension of latent outputs is $n \times q = 297 \times 12$.

We need $q = 12$ Gaussian Process models, one for each PC.

Each GP is trained on the $n = 297$ latent outputs corresponding to that PC.

This way, the high-dimensional model outputs / observable space are transformed into a reduced number of uncorrelated latent outputs using principal component analysis (PCA) [95]. These uncorrelated components are linear combinations of the original features.

The first principal component is aligned with the greatest variance, meaning it captures the most variance of the data. The second principal component captures the next most variance possible while being orthogonal to the first, and so on for subsequent components. For example, if PC1 explains 70% of the variance, this means that by knowing the value of PC1 for each data point, we have a very good idea of where that data point is located in the original high-dimensional space. Explained Variance by each component is an important evaluation metric. Each subsequent component adds to the Cumulative Explained Variance (Fig. 12). You can see that cumulative explained variance increases quickly at first as each additional component explains a large portion of the variance. After a certain point, the gain in explained variance slows down, suggesting that further components contribute less to capturing the structure of the data. Fig. 12 helps us make informed decisions about the number of principal components to use by visualizing the trade-off between dimensionality and variance retained.

Typically, we set the number of principal components to capture 99% of the variance of the original model outputs. This means the simplified low-dimensional dataset after PCA still retains/preserves most of the essential information from the original high-dimensional dataset.

6.4.2. Gaussian process

Gaussian Process (GP) is a machine learning technique, specifically a non-parametric, probabilistic model used for regression and classification tasks. It is not considered deep learning, although it can be combined with deep learning models in certain applications. [96].

It is known that GP's ability to extrapolate beyond the support of its training data is often poor, so we chose a wide range of training points that covers all possible lifetime values so that GPs are not applied outside its training range. That being said, there is no need to include the simulator outputs that drastically differ from the data in the emulator training. It has been shown that filtering out unrealistic simulator outputs would increase the predictive accuracy of the emulator [97]. The calibration input coordinates should cover the range that is plausible for the true value of parameters. This suggests a sequential design approach, beginning with values spanning the prior parameter space and then adding more points over the range giving high posteriors [36, 98, 99, 100].

We estimated the hyperparameters by numerically maximizing the likelihood. In any case, provided a sufficient number of training points, the actual emulator predictions will not depend strongly on the hyperparameters, as long as they are not egregiously over or underfit [91]. In the SURMISE package, hyperparameters are automatically optimized by maximizing the GP marginal likelihood of each PC's score vector with respect to log lengthscales and log nugget using scipy's implementation of the L-BFGS-B algorithm.

We fit a Gaussian Process (GP) model for each latent output, use the fitted GP model to predict the mean, variance, and covariance matrix at the inputs 'x', and reconstruct them in the original high-dimensional space through the inverse PCA transformation. A GP emulator [96] is trained on the input-output behavior of the full model and acts as a fast surrogate to the full model during MCMC sampling. When computing the likelihood during MCMC sampling at another parameter setting, the simulator output is represented by the trained emulator's predictive mean $f^{\mathrm{GP}}(\theta)$ and predictive covariance, $\Sigma^{\mathrm{GP}}(\theta)$, and the prediction uncertainty from the emulator is integrated within the likelihood Eq. (6).

$$p(y \mid \theta) \propto (2\pi)^{-\frac{mn}{2}} |[\Sigma + \Sigma^{\mathrm{GP}}(\theta)]|^{-\frac{1}{2}} \exp\left\{-\frac{1}{2}[y - f^{\mathrm{GP}}(\theta)]^{\top}[\Sigma + \Sigma^{\mathrm{GP}}(\theta)]^{-1}[y - f^{\mathrm{GP}}(\theta)]\right\} \tag{6}$$

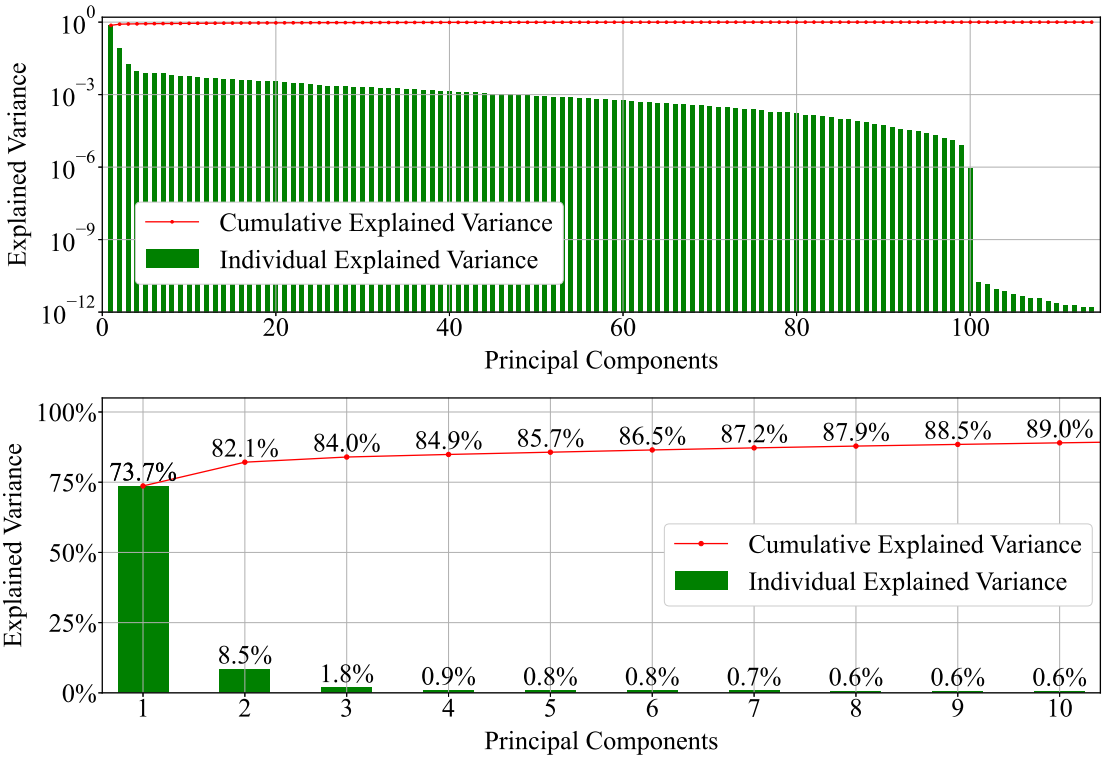

Figure 12: Individual and cumulative explained variance plots in PCA. Upper panel: log scale. Lower panel: linear scale showing the first 10 PCs.

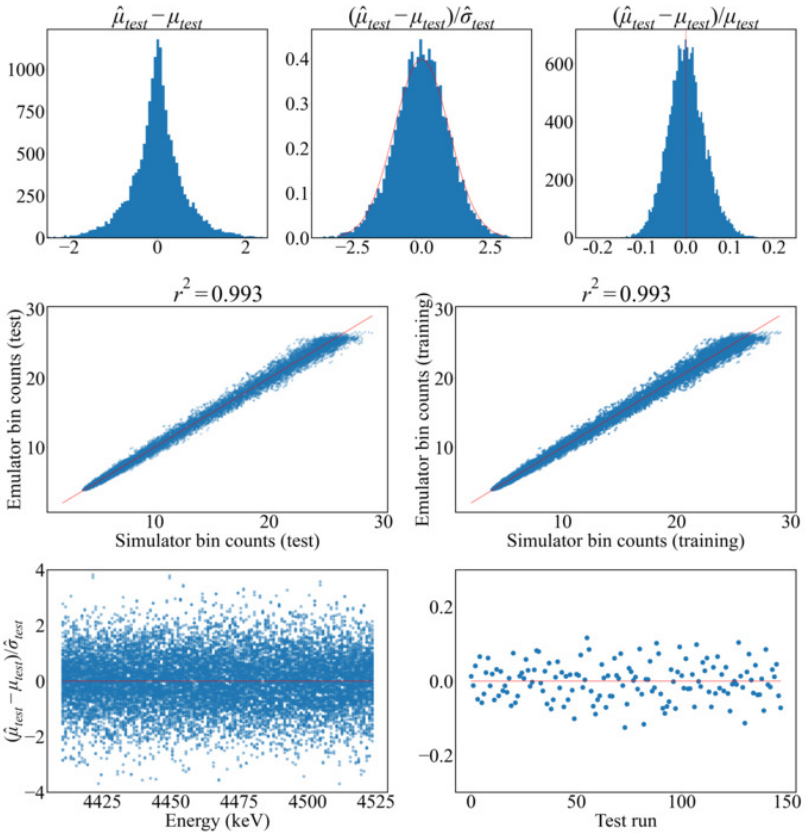

Figure 13: Diagnostics for Gaussian Process Emulators.

After training an emulator, its performance may not always be reliable. To validate the emulator, we split part of the simulations as a training set and a test set. We split the simulations into a training set and a test set. The emulator is fitted using the training set, and its predictive accuracy is evaluated using the test set. As shown in Fig. 13, the typical evaluation metrics to quantify how well a regression model fits the data include the R-squared value and Mean Squared Error (MSE).

In contrast, classification problems typically utilize different evaluation metrics, including:

Accuracy is the ratio of correctly predicted observations to total observations.

Precision is the ratio of correctly predicted positive observations to all expected positive observations.

Recall is the proportion of correctly predicted positive observations to all observations made in the actual class.

F1 Score: An equilibrium between recall and precision.

GP is computationally efficient and accurately accounts for the uncertainty associated with emulation, which is suited for Bayesian parameter estimation purposes [96]. The highest computational cost in the procedure is now associated with obtaining full-model data to train the GP emulator, which can usually be accomplished in a realistic amount of time.

Obviously, when the number of parameters increases, the parameter space to be explored becomes much larger, and the percentage of the parameter space corresponding to a region of high posterior becomes much smaller. In such cases, the training data sets need to be increased considerably to better explore the parameter space. Moreover, the computational cost to fit an accurate emulator and run the MCMC sampler grows when the number of uncertain parameters increases. The one-shot, generate design, simulate, emulate-then-calibrate principle can lead to an ineffective calibration procedure. In such a case, a sequential Bayesian experimental design strategy that incorporates an active learning approach with an acquisition function balancing global exploration and local exploitation can

drastically improve the efficiency of the calibration process for expensive simulation models [47, 100].

6.4.3. Bayesian optimization

Bayesian optimization (BO) is a technique to find the global maximization or minimization of a costly-to-evaluate black-box objective function, such as a beam spot size or beam transmission rate [101, 102] or a χ^2 of a model-to-data fit [47]. A key component of Bayesian optimization is the use of a surrogate model, with the Gaussian Process being one of the most common. This probabilistic model provides a principled way to capture the uncertainty associated with the objective function, allowing for informed decisions about where to sample next. Another key component is the acquisition function. The Expected Improvement (EI) and the Upper Confidence Bound (UCB) are widely used acquisition functions to guide the search process. It quantifies the potential improvement over the current best solution and the exploration-exploitation trade-off, which targets areas with high uncertainty and then focuses on areas with high predicted values. Bayesian optimization has proven highly effective in various applications, including beam-tuning of accelerators and optimizing data acquisition filter parameters. By automating the optimization process, Bayesian optimization can significantly reduce the workload on humans, leading to more efficient and precise instrument operation.

During the last few years, there has been a surge of interest in applying different machine learning and Bayesian methods in nuclear physics. Fast and reliably approximating high-fidelity models creates an ideal environment for applications of machine learning methods. Emulators can be built using various types of machine learning methods, such as Gaussian processes [96], polynomial chaos expansions [103], random forests [104], radial basis functions [105], reduced basis methods [106, 107, 108], eigenvector continuation [109], deep neural networks [110, 111], and many others.

6.5. Model calibration

Calibration is a powerful technique that allows one to combine sparse observables with sparse emulator outputs to perform inference and predictions. The Modeling and Data Analysis Initiative (MADAI) collaboration [112] developed a statistical framework that contains a GP emulator and an MCMC sampler. We have tailored the MADAI infrastructure to our needs. We explored a five-dimensional parameter space by discarding a 50,000-step burn-in phase for the chain to converge and then sampling for another one million MCMC steps. For all but the 4156-keV γ ray, every individual MCMC chain was able to achieve adequate convergence to the posterior distribution with no more than a few thousand iterations. As shown in Fig. 14, the end of the burn-in is signified by likelihood and parameter distributions that oscillate around a mean value and are not consistently increasing or decreasing [21].

The diagonal panels in Figs. 15-21 show the marginal posterior distributions for each parameter with all other parameters integrated out, and the off-diagonal panels show joint distributions between pairs of parameters. The prior distributions for the nuisance parameters, E_γ, bkg, and sp, are restrictive and strongly influence the posteriors. Our experimental data have insufficient constraining power on a nuisance parameter, so we expect the prior and posterior marginal distributions to largely agree. In these cases, the posterior essentially reaffirms the information already contained in the prior. One important merit of Bayesian methods is that a posterior distribution offers more detailed information than a point estimate or an interval from frequentist methods so that propagation of uncertainty can work with richer information than that conveyed by a point estimate [28, 113]. The 2D correlations between parameters allow us to easily capture features, patterns, or anomalies. Strong negative correlations are demonstrated between τ and sp for the two long-lived states, which is physically expected. These two parameters are not correlated for short-lived states as the deexcitations occur before substantial slowing down of the recoils occurs. For the observable itself, the lineshapes based on the prior and posterior distributions of parameters are shown in Figs. 3-9. Values obtained in the model for observables that are not part of the training dataset are referred to as predictions. The close resemblance between the prediction bands and the measured lineshapes indicates the constraining power provided by the experimental data.

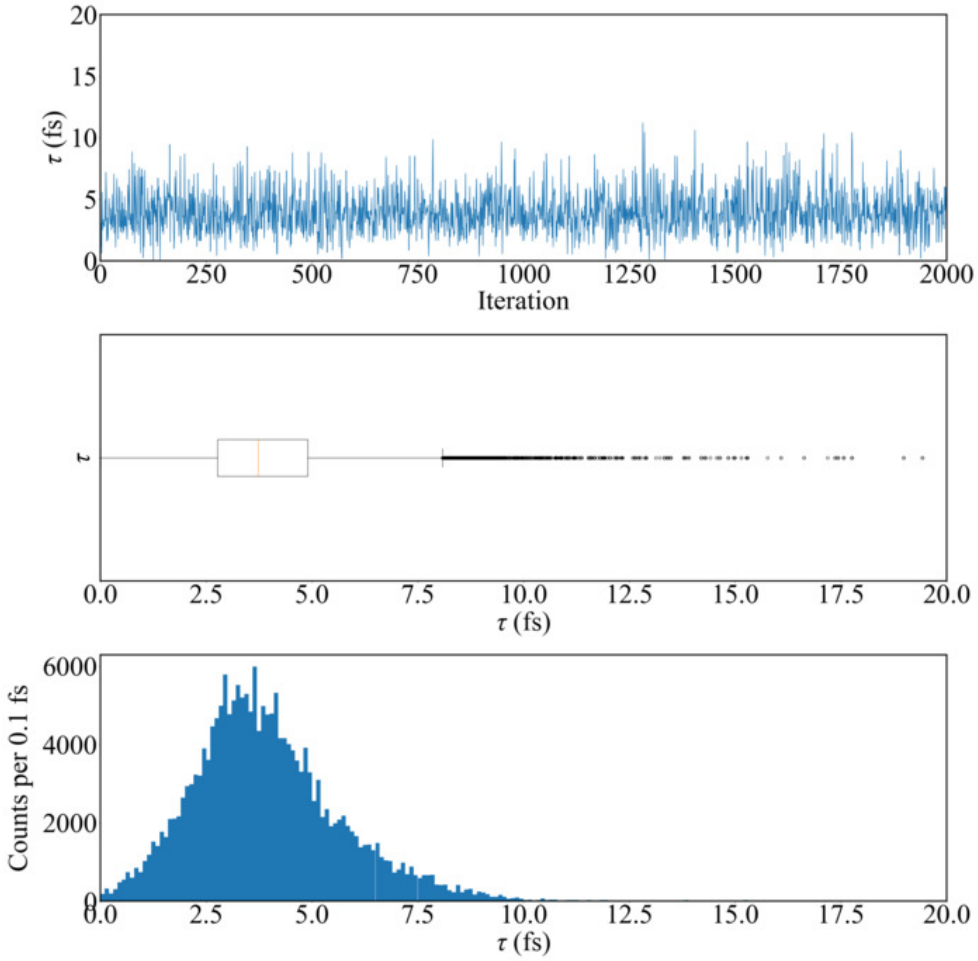

Figure 14: Trace plot of MCMC iterations for the parameter Lifetime.

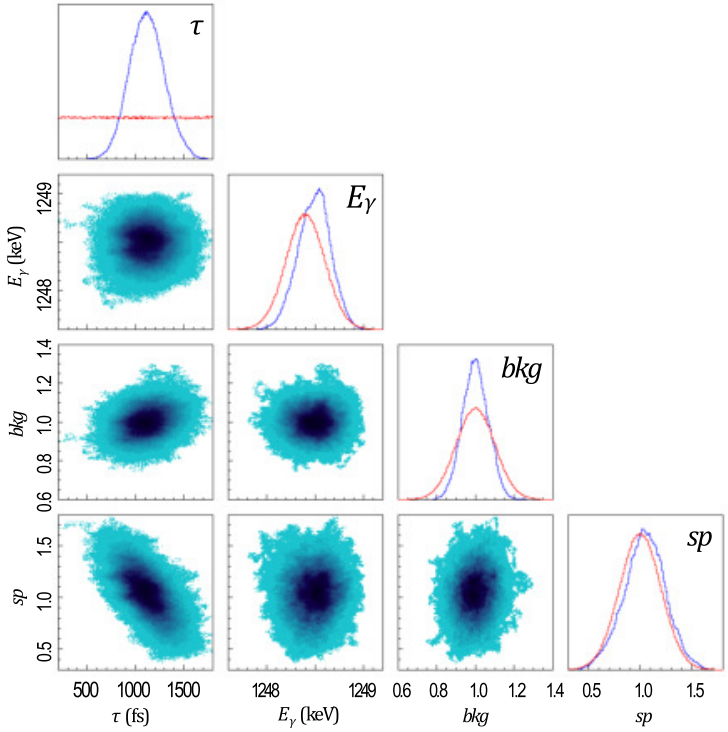

Figure 15: Posterior distributions of the model parameters for the ^{31}S $3/2^+$ state at 1248 keV. Diagonals: prior (red) and posterior (blue) distributions of each parameter. From top left to bottom right: Lifetime τ (fs), γ-ray energy E_γ (keV), relative background bkg, and relative stopping power sp. Off-diagonals: joint distributions showing correlations between pairs of parameters.

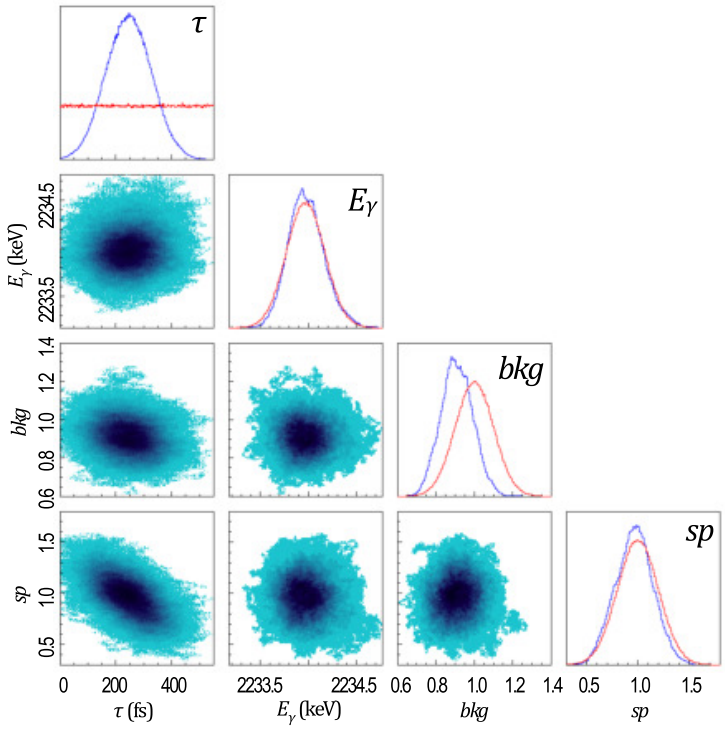

Figure 16: Posterior distributions of the model parameters for the ^{31}S $5/2^+$ state at 2234 keV. Diagonals: prior (red) and posterior (blue) distributions of each parameter. From top left to bottom right: Lifetime τ (fs), γ-ray energy E_γ (keV), relative background *bkg*, and relative stopping power *sp*. Off-diagonals: joint distributions showing correlations between pairs of parameters.

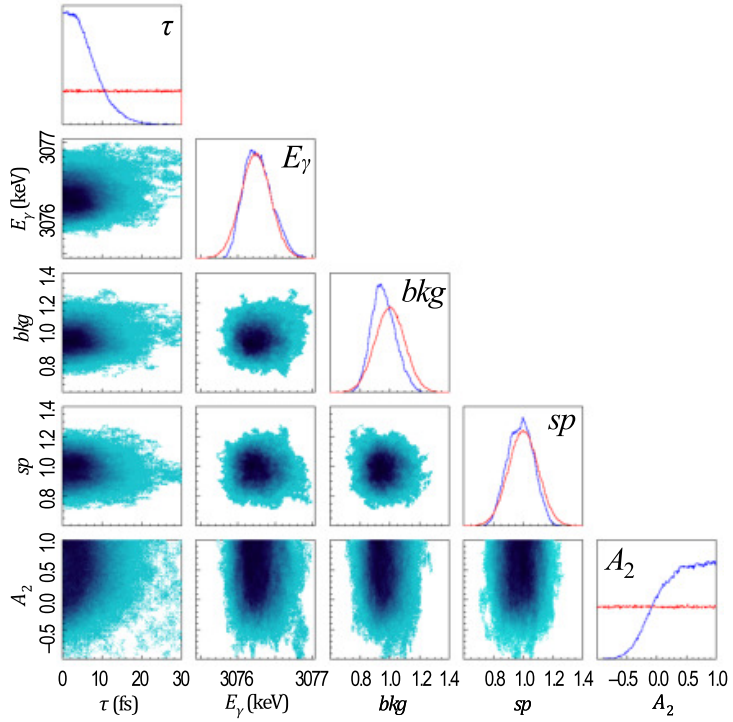

Figure 17: Posterior distributions of the model parameters for the ^{31}S $1/2^+$ state at 3076 keV. Diagonals: prior (red) and posterior (blue) distributions of each parameter. From top left to bottom right: Lifetime τ (fs), γ-ray energy E_γ (keV), relative background *bkg*, relative stopping power *sp*, and the coefficient of the Legendre polynomial $P_2(\cos\theta)$ of the α-γ angular-correlation function, A_2. Off-diagonals: joint distributions showing correlations between pairs of parameters.

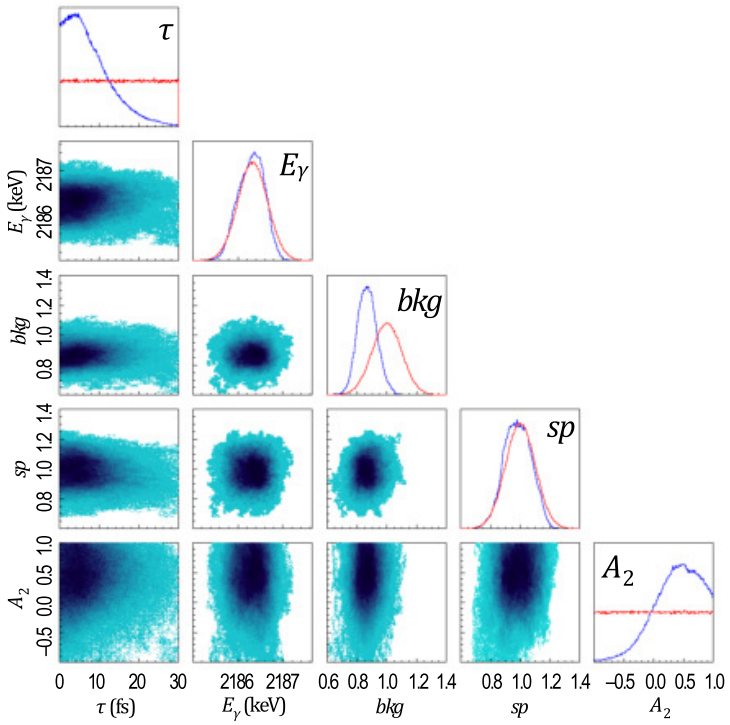

Figure 18: Same as Fig. 17 for the ^{31}S $3/2^+$ state at 3435 keV.

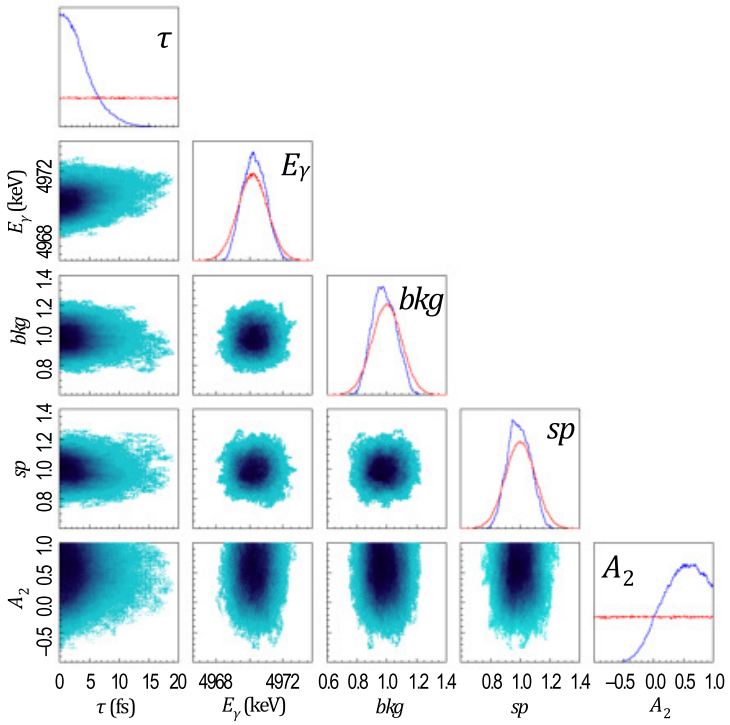

Figure 19: Same as Fig. 17 for the ^{31}S $3/2^-$ state at 4971 keV.

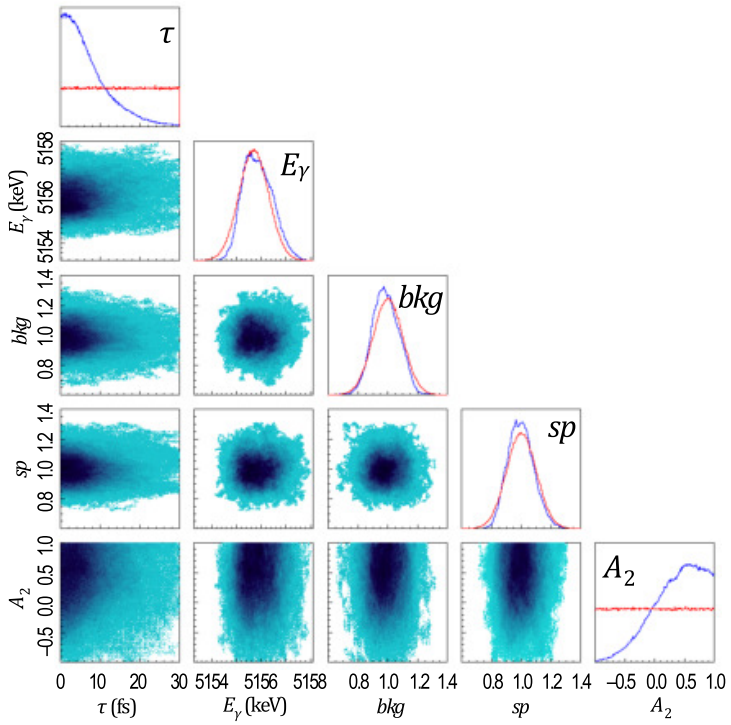

Figure 20: Same as Fig. 17 for the ^{31}S $1/2^+$ state at 5156 keV.

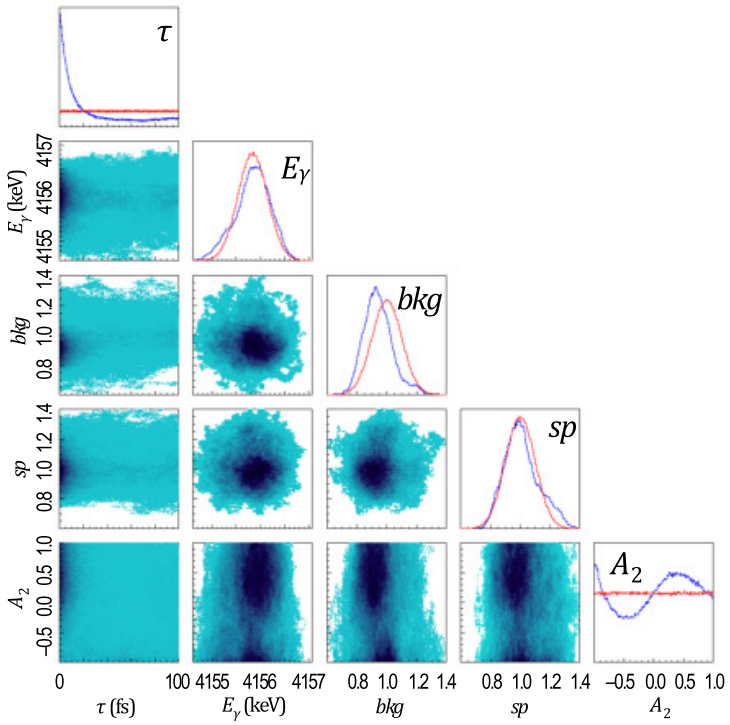

Figure 21: Same as Fig. 17 for the ^{31}S $3/2^+$ state at 6390 keV.

7. Advantages of Bayesian Statistics

What can we achieve with Bayesian methods but not with classical frequentist methods? Will the use of Bayesian statistics add value to our research?

Bayesian inference, guided by Bayes' theorem, is a powerful and versatile data analysis and modeling technique that incorporates prior knowledge and observed data to update beliefs. This method allows for robust estimation and prediction by combining existing knowledge with new observations.

Bayesian statistics offers several advantages:

Comprehensive Uncertainty Analysis. DSAM is a widely-used method for measuring the lifetimes of excited nuclear states in the fs to ps range. Despite the wide use of this method, a unified treatment of all the uncertainties associated with systematic effects has been a long-standing issue. Note that the classical frequentist approach (χ^2 minimization) does not in itself provide any uncertainty, but it is common to assume a normal distribution and vary each parameter by one standard deviation while fixing other parameters at some plausible values. Uncertainties from different sources are often assessed independently and then added in quadrature to obtain the total uncertainty. The statistical meaning is even less rigorous when combining upper/lower limits instead of finite values. Multiple parameters often have complex interrelationships, and their correlations may be underestimated or overestimated by standard frequentist approaches [19, 20, 21]. With these concerns in mind, we turn to another powerful statistical tool: Bayesian inference, which offers a natural parameter estimation method with faithful assessments of uncertainty. Being able to reliably understand and quantify the uncertainties in lineshape analysis is crucial to moving this field forward.

Incorporation of Prior Knowledge. Prior probability distributions are one of the most important ingredients of the Bayesian framework and provide an ability to incorporate our prior knowledge into the analysis. Classical statisticians argue that for this reason, Bayesian methods suffer from a lack of objectivity. Bayesian proponents argue that frequentist methods have built-in subjectivity, and at least in Bayesian approaches, the subjectivity is explained clearly. Priors can play an important role in restricting the posterior, but there is no unique way to choose priors. The consequence is that different people can use different priors for the same experiment and obtain different posteriors and thus make different conclusions. Hence, the choice of priors must be justified explicitly when using Bayesian inference.

To Gain More Information. Estimating a posterior probability distribution of a parameter of interest is at the heart of Bayesian analysis. The posterior distribution represents everything we know about the parameters. One important merit of Bayesian methods is that everything in Bayes is a probability distribution. A complete probabilistic description of uncertainty (Figs. 15-21) offers more detailed information than a point estimate or an interval from frequentist methods so that uncertainty propagation can work with richer information than that conveyed by a point estimate. It also facilitates the updating of knowledge about a parameter as new constraints on other parameters become available, allowing for iterative refinement of knowledge. The 2D correlations between parameters allow us to easily capture features, patterns, or anomalies. There is nothing intrinsically wrong with the idea of reducing it to a single number or an interval, as in frequentist analysis, but we lose useful information. In fact, we lose exactly the information that makes the posterior distribution useful in the first place.

Iterative Refinement of Knowledge. It provides a powerful framework for handling uncertainty and updating beliefs based on evolving evidence. Application of Bayesian inference in machine learning leads to more accurate, reliable, robust, and adaptable models. This method updates models with additional evidence, preventing overfitting and enabling continuous improvement. It supports informed decision-making and efficient model updating, making it ideal for uncertain environments and limited datasets. However, when it comes to applying Bayesian inference in machine learning, one of the key challenges is the scalability issues for large datasets or complex models with increasing dimensionalities.

Another advantage of Bayesian inference is that it can handle missing data in a natural and flexible way. Missing data can be treated as unknown parameters that have a probability distribution, and they can be estimated from the data and the prior beliefs. This means that you do not have to discard or impute the missing data, as you would do in frequentist inference. Instead, you can use Bayesian inference to account for the uncertainty and variability of the missing data, and to generate plausible values for them based on the available information. The Bayesian approach treats missing data as additional parameters, estimating their distribution based on observed data. Through iterative updating, it refines these estimates, producing a comprehensive understanding of both observed and missing values.

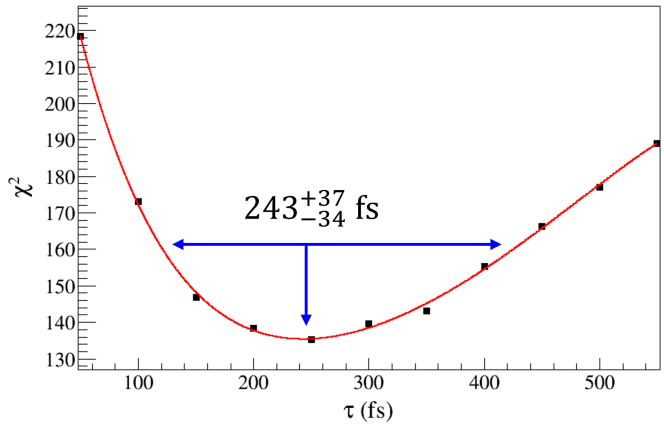

Figure 22: χ^2 distribution as a function of the lifetime of the 2234-keV ^{31}S state. The best-fit lifetime and its statistical uncertainty are obtained from $\chi^2_{\rm min}$ and $(\chi^2_{\rm min}+1)$ values (arrows are for demonstration purposes).

This flexibility provides a more realistic representation of uncertainty and contributes to robust decision-making in the presence of incomplete information.

An interesting phenomenon is that in the Fall Meeting of the American Physical Society Division of Nuclear Physics, the number of Bayesian-related talks has shown a steady upward trend in recent years: 3 in 2016, 8 in 2017, 9 in 2018, 11 in 2019, 13 in 2020, 22 in 2021, 19 in 2022, 23 in 2023, and 18 in 2024. "Bayesian Uncertainty Quantification" has become its own session for the first time in DNP2022. Bayesian thinking has been widely adopted across various research fields. Successful applications of Bayesian analysis have emerged across various research fields.

Why do we pursue MCMC-based Bayesian data analysis? Solving a problem that has been set up using Bayesian theory involves computing multidimensional and complex probability distribution functions that do not have analytical solutions. To numerically evaluate the distribution can be computationally demanding and has acted as a major bottleneck in the past. This is where MCMC methods come to the rescue. MCMC is a class of methods for sampling a probability distribution function using a Markov chain whose equilibrium distribution is the desired distribution. Note that in conventional Monte Carlo integration, the random samples are statistically independent, whereas in MCMC they are correlated. The Metropolis algorithm used in our work has been the main workhorse of MCMC methods, and more efficient MCMC algorithms MCMC methods, such as the Metropolis-Hastings algorithm, Gibbs sampling, or Hamiltonian Monte Carlo that work better for specific problems are continuously being developed [28].

What if we interpret our DSAM data from a frequentist perspective? Frequentist and Bayesian methods answer different questions, provide different kinds of answers, solve different problems, and have their strengths and weaknesses. Although we consider Bayesian statistics a more powerful tool to interpret data, frequentist methods are easier to implement and may remain the mainstream in the nuclear physics community for a while. To get a feel for what we could obtain if we interpret our DSAM data from a frequentist perspective, we have reanalyzed our data. An example analysis of the 2234-keV ^{31}S state is shown in Figs. 22 and 23. The best-fit lifetime and its statistical uncertainty $(\chi^2_{\rm min}+1)$ are taken from a polynomial fit of the χ^2 distribution. The γ-ray energy, background fit, and stopping power are varied up and down by their one standard deviation uncertainty to investigate the systematic uncertainty. Adding the systematic uncertainties with the statistical uncertainty in quadrature yields the total uncertainty for the lifetime. Other states are analyzed following the same procedure, and all the results are summarized in Table 1. The lifetimes of higher-lying states are consistent with zero, and we deduce their 90% confidence level upper limits by multiplying the one standard deviation by a factor of 1.28 [114]. χ^2 minimization can also be performed in a two-dimensional space (Fig. 24), but it is not a viable solution in higher dimensions. Hence Bayesian methods are a better fit for lineshape analysis, which usually involves multiple parameters.

Each parameter enters the Bayesian analysis as a source of uncertainty as well as a constraint on the observable.

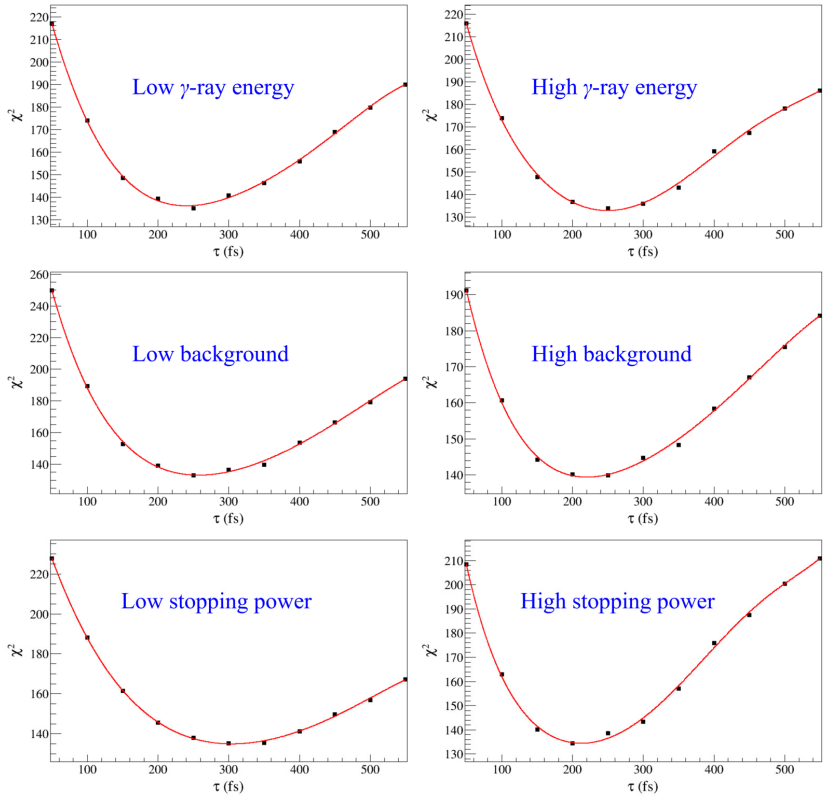

Figure 23: The γ-ray energy, background level, and stopping power are varied up and down by their one standard deviation uncertainty to investigate the systematic uncertainty. Adding the systematic uncertainties with the statistical uncertainty in quadrature yields the total uncertainty for the lifetime. $\tau = 243^{+37}_{-34}(\text{stat})^{+63}_{-38}(\text{syst}) = 243^{+73}_{-51}$ fs.

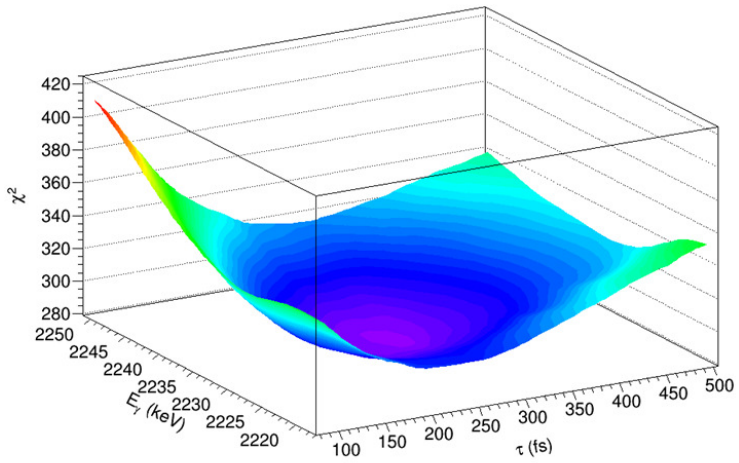

Figure 24: 2D χ^2 distribution as a function of the lifetime and the energy of γ ray from the 2234-keV ^{31}S state.

Table 1: Lifetimes of ^{31}S states obtained using frequentist and Bayesian approaches.

$E_x(^{31}\mathrm{S})$ (keV)	$\tau_{\mathrm{frequentist}}$ (fs)	τ_{Bayesian} (fs)[1]
1248	958^{+274}_{-209}	1116^{+183}_{-177}
2234	243^{+73}_{-51}	247^{+81}_{-82}
3076	<6	<11
3435	<16	<16
4971	<7	<7
5156	<5	<15
6390	<30	<20[2]

[1] More digits are displayed for comparison.
[2] Not a 90% CL limit as its posterior distribution exhibits a long tail over the prior range.

One should not assume that the χ^2 minimum obtained from the frequentist approach matches the results obtained in the Bayesian-MCMC method and that the uncertainties estimated by the two methods are consistent [19]. In this case, we have a reasonable sense of the range of lifetimes, and we do not expect the results from the two methods to diverge from each other by orders of magnitude. It is physically expected that when the stopping power increases, the inferred lifetime decreases, and vice versa. In both Bayesian and frequentist analyses, a negative correlation is indeed observed between the lifetime and the stopping power for the two long-lived states.

Although Bayesian analysis usually provides a posterior probability distribution rather than a point estimate, we could still extract the corresponding χ^2 values and p-values, which are usually used as an indicator of goodness-of-fit in the frequentist analysis. The resultant best-fit γ-ray lineshapes from the Bayesian analysis are a good description of the data points, and we are able to achieve a minimum in the χ^2_ν distribution close to 1 in all cases. It should also be noted that we did obtain similar uncertainties using the Bayesian approach and the frequentist approach in this work. However, that is not always the case. There have been systematic studies using both methods to quantify uncertainties in direct nuclear reactions. The frequentist approach has been found to underestimate uncertainties. It is desirable to extend this comparison to other subfields, such as DSAM. If large discrepancies were found, it might indicate the necessity of an overhaul of past DSAM data using statistically rigorous methods.

We can also extend the Bayesian-MCMC method to the Doppler broadening lineshape analysis [516]. From a Bayesian perspective, the Doppler broadening Monte Carlo simulation could be viewed as the model that introduces parameters such as the stopping power, the lifetime of the γ-ray emitting state, the energy, and the relative intensity of the proton branches populating the γ-ray emitting state. The output of the model is a γ-ray spectrum, which is the observable to be compared with data. The fields of heavy-ion collisions and low-energy nuclear reactions have shifted toward Bayesian statistics for evaluating confidence intervals in recent years. Although much work has been done, there are many exciting opportunities ahead. More advanced Bayesian frameworks to incorporate multiple observables and models are being developed. Additional observables would increase constraining power. Gaussian process emulation is trending toward machine learning techniques such as Bayesian neural networks. Bayesian inference can also help you build and evaluate models for your data. Suppose multiple models are available in DSAM analysis; the question of which model is better suited or even mixing models can be answered via Bayesian model comparisons.

8. BAND for DSL

The Bayesian Analysis for Nuclear Dynamics (BAND) software Framework provides tools and examples that facilitate principled Uncertainty Quantification in Nuclear Physics. They provide tools and examples that demonstrate how emulation of computationally expensive models, model calibration, and Bayesian model mixing can be combined in order to provide a full accounting of the uncertainties in Nuclear Physics models-including model uncertainty [53]. The SURMISE package is categorized into three routines [97]:

Emulation: Carries out Bayesian emulation of computer model output and generates inputs to calibration.

Calibration: Generates estimates of the calibration parameters based on field observations of the real process and output from emulation.

Utilities: Performs different utility tasks such as a sampler (e.g., Metropolis-Hastings) to generate posterior draws of calibration parameters.

Workflow diagrams are shown in Figs. 25 and 26 [115, 116]. It is to be noted that the simulation-data comparison code calculates and outputs all the χ^2 values. Therefore, analysis using the classical χ^2-minimization approach remains an available option if needed.

In SURMISE, all emulator methods inherit from the base class surmise.emulation.emulator. An emulator class calls the user input method, and fits the corresponding emulator. surmise.emulation.emulator.fit() and surmise.emulation.emulator.predict() are the main surmise.emulation.emulator class methods. fit() and predict() are the two obligatory functions for an emulation method. fit() takes the inputs X, parameters θ, and the function evaluations f, where $X \in R^{N\times p}$, $\theta \in R^{M\times d}$, and $f \in R^{N\times M}$. In other words, each column in f should correspond to a row in θ. Each row in f should correspond to a row in X. In addition, the dictionary fitinfo is passed to the fit() function to place the fitting information once complete. This dictionary is used to keep the information that will be used by predict() later.

fit() is the only obligatory function for a calibration method. fit() takes the fitted emulator class object surmise.emulation.emulator, inputs X, and observed values y, where $X \in R^{N\times p}$, $y \in R^{N\times 1}$, and the dictionary fitinfo to place the fitting information once complete.

8.1. Model emulation methods

1) 'indGP': skips the PCA dimensionality reduction step and builds independent emulators directly on the original outputs, hence, no epsilon is needed. However, the subsequent MCMC process incurs significant computational costs (CPU and RAM) associated with large covariance matrices. MCMC results look similar to PCGP.

2) 'PCGP': Principal Component Gaussian Process emulator uses PCA to reduce the dimensionality of the simulation output before fitting a Gaussian Process model to each Principal Component separately. 'PCGP' is the default emulation method. A modified version 'PCGP_numPCs' is recommended for DSL analysis.

3) 'PCGPR': Principal Component Gaussian Process Regression utilizes scikit-learn's GaussianProcessRegressor for GP modeling.

4) 'PCGPRG': Principal Component Gaussian Process Regression with Grouped observables. PCGPR emulation are performed for each subgroup separately.

Ref. [36] found that PCSK>PCGPR>PCGPR in terms of R^2 scores.

5) 'PCGPwM': Principal Component Gaussian Process with Missingness properly handle missing points in the simulation output due to simulation failures through imputation and incorporating additional variance estimates at each point requiring imputation, before performing PCA and fitting Gaussian Process models.

6) 'PCGPwImpute': Principal Component Gaussian Process with Imputation: extends PCGPwM by first externally imputing missing values using iterative imputation techniques (such as K-Nearest Neighbors, Bayesian Ridge Regression, or Random Forest) from scikit-learn, and then applies the PCGPwM method on the completed dataset.

7) 'PCSK': Principal Component Stochastic Kriging.

Both PCGP and PCSK are Gaussian Process-based emulators. Both use PCA to reduce high-dimensional outputs into manageable dimensions for modeling. PCGP is developed to handle deterministic simulation models, where the simulator returns the same output every time given the same input parameters. PCGP considers mean but ignores any variance of simulation data. Our GEANT4 simulation model is stochastic, meaning that for the same input parameters, the simulator can return different outputs when being run multiple times. Instead of only taking into account the mean values of the emulator training data, the PCSK method also considers the standard deviation at the training points ('simsd'). The PCSK emulation incorporates this variation in the accuracy between the resulting data points, known as heteroscedasticity, by using stochastic kriging.

PCSK considers mean but ignores variance of simulation data during hyperparameter optimization, but considers variance in posterior predictive distribution.

PCGP and PCSK with or without the uncertainties of the training data give consistent posterior results and both PCGP and PCSK outperform standard Gaussian Process implementations like Scikit GP in predictive accuracy and uncertainty estimation [98].

8) 'LCGP': Latent Component Gaussian Process handles stochastic multivariate outputs with heterogeneous errors [117]. Unavailable in SURMISE version 0.3.0.

8.2. Model calibration methods

1) 'directbayes': default calibration method. It builds a log-posterior by combining a prior (fitinfo[''thetaprior']) with a likelihood (loglik) comparing emulator-predicted means/covariances to observed data. 'directbayes' uses standard matrix operations. The final posterior samples are stored in fitinfo['thetarnd'].

2) 'directbayeswoodbury': leverages the Woodbury identity to handle Gaussian covariance manipulations, which can be more efficient or numerically stable for large datasets. The final posterior samples are stored in fitinfo['thetarnd']. 'directbayeswoodbury' is recommended for DSL analysis.

3) 'mlbayeswoodbury': clf_method must be a trained classifier (e.g., a scikit-learn model) that implements .predict_proba(...) on each sampled theta to get acceptance probabilities, which it folds into the posterior. If this ML-based weighting is not needed, either pass clf_method=None or use a different calibration method (directbayes or directbayeswoodbury).

8.3. Utilities methods (samplers)

1) 'metropolis_hastings': default sampler that draws from a target posterior distribution; recommended for DSL analysis.

2) 'LMC': Langevin Monte Carlo uses gradient-based proposals to guide samples toward high-posterior regions, often improving acceptance over plain metropoli_hastings. Users do not need to set stepParam explicitly: by default, LMC will estimate an initial scale from the starting samples and adapt from there. Users do not need to set burn-in explicitly. Instead, LMC uses an iterative procedure (e.g., maxiters=10, numsamppc=200) and tries to adapt acceptance rates. It then returns a single final chain (theta) with size numsamp.

3) 'PTLMC': Parallel Tempering Langevin Monte Carlo combines Parallel Tempering (running multiple chains at different temperatures and exchanging states periodically) and Langevin Monte Carlo (using gradient-based proposals). PTLMC has the advantages of faster convergence, especially for complex or multimodal distributions, and reduced risk of trapping in local minima. In the analysis of the S2193 7333-keV γ-ray data, the posterior distribution exhibits numerous nearby local minima compared to that obtained using the Metropolis-Hastings sampler, indicating it is less suitable for DSL lineshape analysis. 'PTLMC' does not perform better than the default 'metropolis_hastings' when it comes to handling multimodal distributions. The overall credible intervals by integrating the posterior distributions are consistent with those from 'metropolis_hastings' sampling. The acceptance rate for PTLMC is approximately 0.004, while Metropolis-Hastings has an acceptance rate of about 0.22.

4) 'PTMC': required positional arguments: 'log_likelihood' and 'log_prior'. PTMC is not supported in the version 0.3.0 of SURMISE.

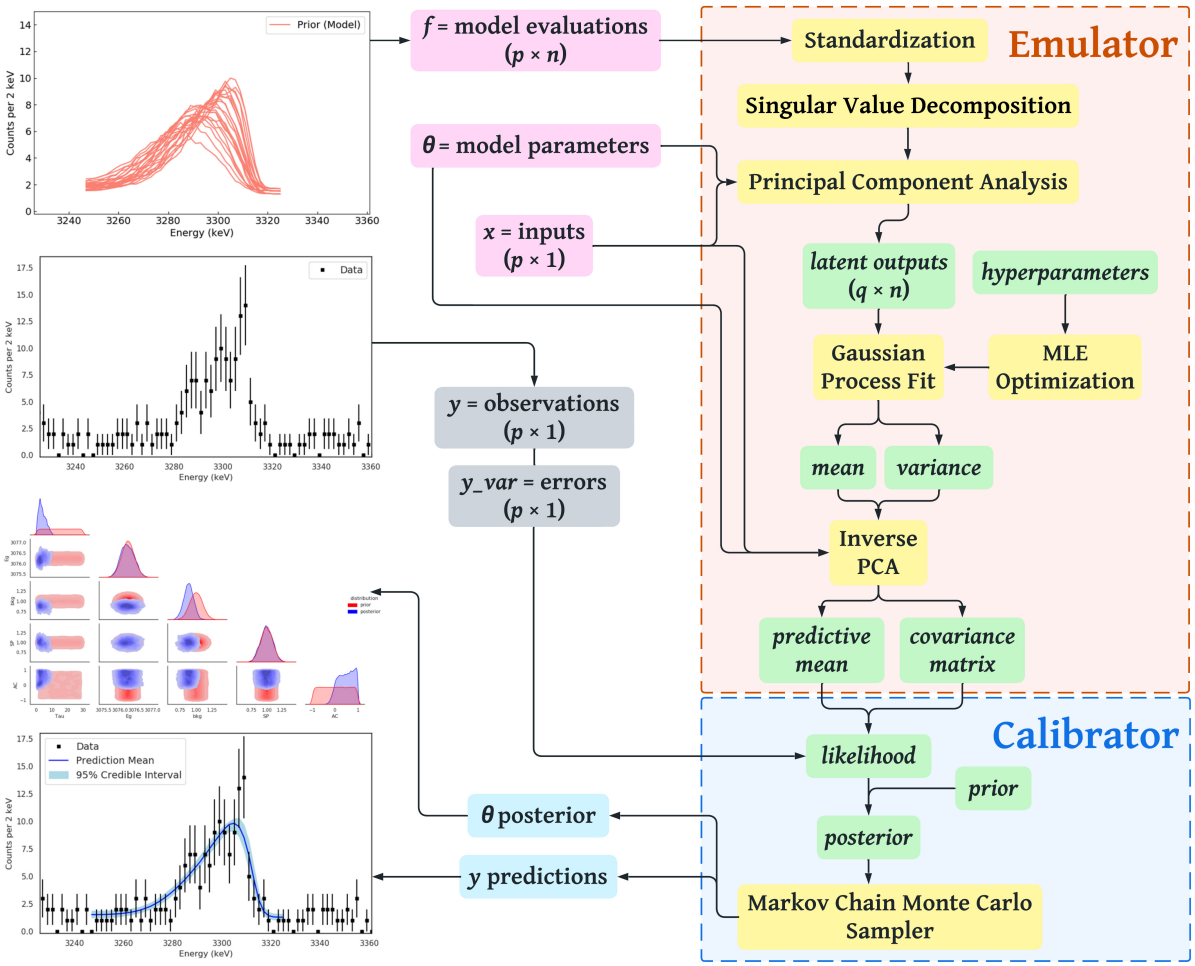

Figure 25: Flowchart of the Bayesian analysis based on the SURMISE package.

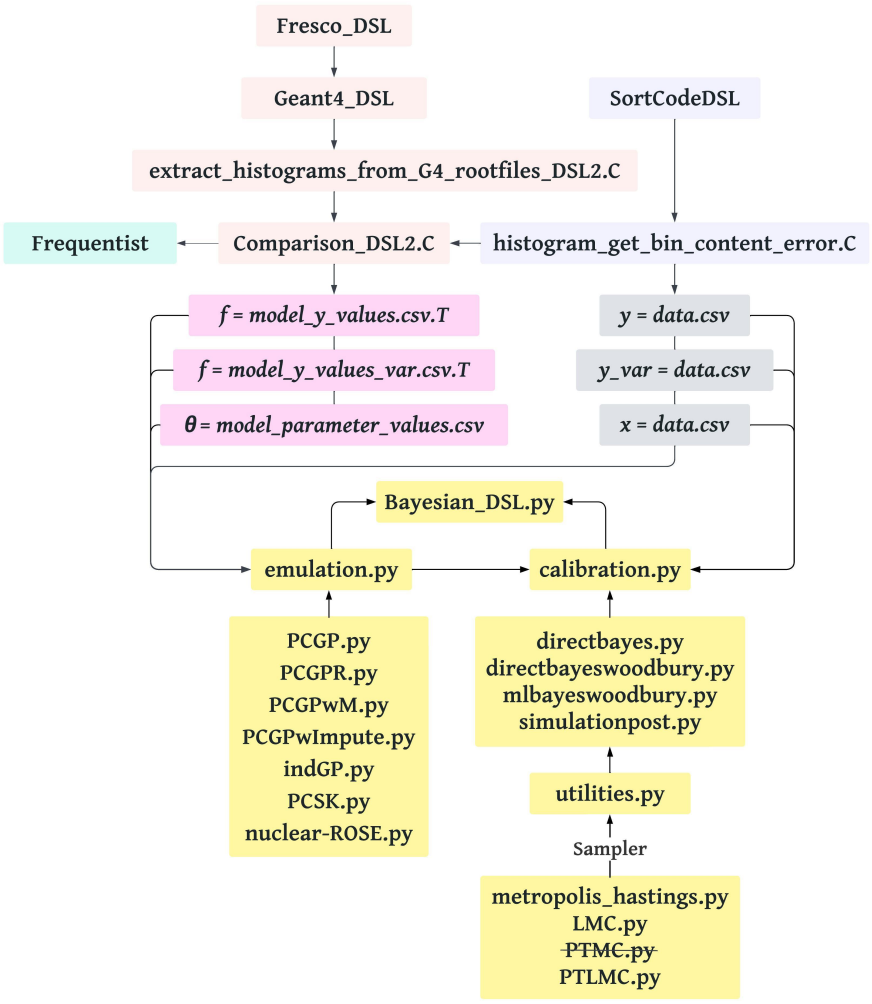

Figure 26: Framework of the DSL-surmise workflow, highlighting the key components and processes involved.

9. Lifetimes of ^{31}S States

For the two lowest-lying states, the central lifetime values and the 1σ uncertainties are constructed by using the 16th, 50th, and 84th percentile values from the lifetime posterior distributions. For the four higher-lying states, the most probable lifetime values are close to zero, and therefore, the 90th percentile values for the lifetime posterior distributions are adopted as the 90% confidence upper limits. For the first excited state at 1248 keV, we obtained a lifetime of 1120 ± 180 fs, which agrees with the literature values of 720 ± 180 fs [11], 1200^{+1500}_{-1100} fs [12], 3200 ± 7000 fs [12], and 964^{+312}_{-91} fs [13]. Tonev *et al.* recently reported a lifetime of 624 ± 32 fs [14] for the 1248-keV state, lower than all the other results. They reported 543 ± 49 fs for the $7/2^-$ state at 4451 keV, which is also much lower than another measurement of 1030 ± 210 fs [15]. For the second excited state at 2234 keV, our result 250 ± 80 fs agrees with the only literature value of 320 ± 80 fs [11]. We obtained consistent lifetime values and limits for all γ-ray lines using the standard frequentist approach.

We performed theoretical calculations using the shell-model code NuShellX [540] in the *sd*-shell-model space involving the $\pi 0d_{5/2}$, $\pi 1s_{1/2}$, $\pi 0d_{3/2}$, $\nu 0d_{5/2}$, $\nu 1s_{1/2}$, and $\nu 0d_{3/2}$ valence orbits. Five universal *sd*-shell type A (USDA) [119], type B (USDB) [119], type C (USDC) [120], type E (USDE), and type I (USDI) [120] Hamiltonians have been used in our calculations. Given that decay widths are very sensitive to energies, we have applied a correction to the theoretical γ-ray partial widths (Γ_γ) based on the experimental energies [9]. Each theoretical Γ_γ is obtained using the effective $M1$ and $E2$ transition operators [121] and then scaled for the E_γ^{2L+1} energy dependence, where L denotes the multipolarity of the radiation.

All the measured and calculated lifetimes of ^{31}S states are summarized in Table 2. The negative-parity 4971-keV state is not matched with any theoretical state as cross-shell excitations were not taken into account in our shell-model predictions. The calculated γ decay of the 1248-keV state is dominated by an $M1$ transition. Correcting for the USDB-calculated partial lifetime for the $E2$ transition of 6.9 ps, the experimental partial lifetime for the $M1$ transition is 1.33(26) ps. This gives an experimental transition probability of $B(M1)_{\rm exp} = 0.022(4)\,\mu_N^2$. With $B(M1) = [M(M1)]^2/(2J_i + 1)$, where $M(M1)$ is the transition matrix element and J_i is the spin of the γ-emitting state, we have $|M(M1)|_{\rm exp} = 0.30(3)\,\mu_N$ to be compared with, for example, $|M(M1)|_{\rm USDA} = 0.22\,\mu_N$ and $|M(M1)|_{\rm USDB} = 0.17\,\mu_N$. The comparison between theory and experiment for other $M(M1)$ values in the *sd* shell is shown in Fig. 4 of Ref. [121]. It is observed that theory and experiment differ by about $\pm 0.3\ \mu_N$ independent of the size of $M(M1)$. The present results are consistent with this observation. The measured lifetimes of all other states are in good agreement with our shell-model calculations. The lifetimes of most states in the mirror nucleus ^{31}P have been well measured [123] and are listed in Table 2 for comparison. The lifetimes for all the mirror states are consistent with isospin being a good symmetry in the ^{31}P-^{31}S system.

Dedicated shell model calculations have been performed to reproduce the strong isospin mixing between the 6390-keV state and the nearby isobaric analog state [8, 443, 122]. We obtained $\tau = 1.3$ fs using a shifted USDC Hamiltonian. Limited mainly by the low statistics collected on the 6390 → 2234 keV transition, we are not able to set a finite constraint on the lifetime of the 6390-keV ^{31}S state. The posterior clearly favors a short lifetime as it exceeds the prior below 20 fs (Fig. 21). An upper limit of the lifetime $\tau < 20$ fs is equivalent to a lower limit on the decay width of $\Gamma > 33$ meV. Combining with the finite proton branching ratio value [443] yields a resonance strength of

Table 2: Lifetimes of the two lowest-lying ^{31}S states and the 90% confidence upper limits on the lifetimes of four higher-lying ^{31}S states measured in the present work are listed in column 4. The only other state with previously measured lifetimes [123] is also included (row 6). The spins and parities (J^π), excitation energies (E_x), and γ-ray energies (E_γ) of the dominant branch for each state are adopted from Ref. [123]. The excitation energies and the lifetimes of ^{31}P mirror states listed in the last two columns are adopted from Ref. [123]. All E_x and E_γ are rounded to the closest integer. A hyphen (−) is placed where the value is unavailable.

J^π	$E_x(^{31}\mathrm{S})$ (keV)	E_γ (keV)	$\tau_{\rm exp}$ (fs)	$\tau_{\rm USDA}$ (fs)	$\tau_{\rm USDB}$ (fs)	$\tau_{\rm USDC}$ (fs)	$\tau_{\rm USDE}$ (fs)	$\tau_{\rm USDI}$ (fs)	$E_x(^{31}\mathrm{P})$ (keV)	$\tau(^{31}\mathrm{P})$ (fs)
$3/2^+$	1248.60(8)	1248.68(10)	1120(180)	1794	2633	2428	2735	2734	1266.08(8)	736(35)
$5/2^+$	2234.33(11)	2234.19(22)	250(80)	285	311	306	325	317	2233.63(8)	369(25)
$1/2^+$	3076.54(14)	3076.24(20)	<11	16	14	13	15	12	3134.3(4)	10.2(6)
$3/2^+$	3434.93(19)	2186.33(33)	<16	19	16	15	15	14	3506.1(6)	$12.7^{+2.3}_{-1.7}$
$7/2^-$	4449.86(23)	1165.7(4)	790(240)	–	–	–	–	–	4430.84(11)	612(45)
$3/2^-$	4970.8(8)	4970.2(9)	<7	–	–	–	–	–	5015.2(8)	11(7)
$1/2^+$	5156.2(3)	5155.7(6)	<15	3.0	3.2	3.3	2.7	4.2	5256.8(15)	<15
$3/2^+$	6390.46(16)	4155.84(31)	goal	4.3	24	2.7	1.8	2.8	6380.8(20)	<10

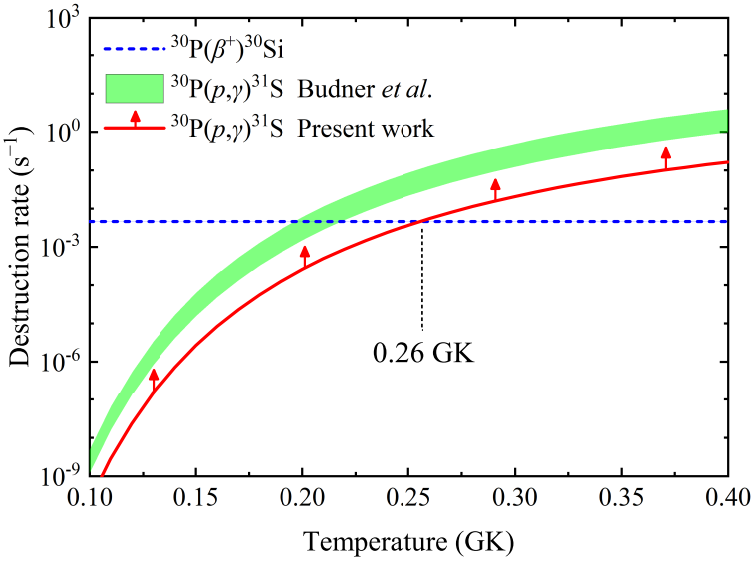

Figure 27: ^{30}P destruction rates for the ^{30}P$(p,\gamma)^{31}$S reaction (lower limit denoted by solid red line with upward arrows) and ^{30}P$(\beta^+)^{30}$Si decay (dashed blue line) as a function of temperature. The rate derived from Ref. [443] (green band) is shown for comparison. Only the resonant-capture contribution from the $3/2^+$ ^{30}P$(p,\gamma)^{31}$S resonance is taken into account.

$\omega\gamma > 5.5$ μeV, consistent with the previous $\omega\gamma = 80(48)$ μeV based on the measured proton branching ratio and a theoretical lifetime [443].

Here we provide a qualitative picture of the astrophysical impact. The ^{30}P$(p,\gamma)^{31}$S reaction and the ^{30}P$(\beta^+)^{30}$Si decay are the two main destruction mechanisms for ^{30}P in ONe novae [404]. Assuming a stellar density of $\rho = 300$ g/cm^3 and a hydrogen mass fraction of $X_{\rm H} = 0.3$ [400], we derive the destruction rates for both processes from the literature ^{30}P half-life of $T_{1/2} = 2.498(5)$ min [124] and the newly-determined lower limit on the strength of the $3/2^+$ resonance, $\omega\gamma = 5.5$ μeV. Figure 27 shows equal destruction rates of the two processes at 0.26 GK, implying that the proton capture becomes more likely than the competing β^+ decay beyond a temperature within the peak nova temperatures of $T_{\rm peak} = 0.1-0.4$ GK. The location of the crossing point would affect interesting nova observables, such as the ^{30}Si/^{28}Si isotopic abundance ratios useful for the identification of pre-solar nova grains [4], the O/S, S/Al, O/P, and P/Al abundance ratios that are good candidates for nova thermometers [5], and the Si/H abundance ratio as a useful nuclear mixing meter in ONe novae [6].

10. Conclusion & Outlook

To summarize, we performed DSAM lifetime measurements of ^{31}S states using the DSL facility. We applied the MCMC-based Bayesian method to rigorously constrain model parameters and quantify uncertainties, demonstrating the usefulness of Bayesian parameter estimation for DSAM lineshape analyses. As more powerful Bayesian tools are continuously being developed [53, 54, 55, 97], we expect to see that the framework established in this work has broad applicability to more lineshape analyses. The methodology can be readily extended to constrain model parameters based on observations in various contexts.

Our newly-determined lifetime upper limits for the four high-lying states contribute to the understanding of the nuclear structure of ^{31}S. The observation of γ rays from the 6390-keV state is very promising for future measurements with higher statistics. This work represents a major step toward an entirely experimentally-determined thermonuclear rate of the ^{30}P$(p,\gamma)^{31}$S reaction. Advancing this work will be the DSL2 facility, consisting of a segmented Si detector telescope with higher solid angle coverage and reduced γ-ray attenuation. The granularity of the new telescope provides the position resolution necessary to maintain the angular/kinematic resolution that

enables gating on excitation energies. The lifetime sensitivity will benefit greatly from the large solid angle and position resolution of the new telescope.

11. Lifetime of the key ^{30}P$(p,\gamma)^{31}$S resonance in novae (EEC S2373)

In classical novae, the ^{30}P$(p,\gamma)^{31}$S reaction acts as a nucleosynthesis bottleneck in the flow of material to heavier masses affecting several observables. The dominant source of uncertainty in the current recommended reaction rate is the γ decay width of the $J^\pi = 3/2^+$, 259.81(29)-keV resonance at $E_x = 6390.46(16)$ keV in ^{31}S. We propose to measure the lifetime of the key ^{31}S resonance using the Doppler Shift Lifetimes 2 (DSL2) facility at TRIUMF. The ^{31}S excited states will be populated by the ^{3}He$(^{32}$S$,\alpha)^{31}$S reaction. The deexcitation γ rays will be detected by a clover-type high-purity germanium detector in coincidence with the α particles detected by a silicon detector telescope. We will employ the Doppler-shift attenuation method and Markov chain Monte Carlo-based Bayesian statistical techniques to perform lineshape analyses of γ-ray data. Our primary objective is to establish the first experimental constraint on the lifetime, with statistically meaningful rigorous uncertainty quantification. Combining the well-known energy, spin and parity, and proton-decay branching ratio of this resonance, we will be able to pin down the ^{30}P$(p,\gamma)^{31}$S reaction rate, enabling more accurate simulations of nova observables.

12. Scientific Value

Classical novae are among the most frequent thermonuclear stellar explosions in the Galaxy. They are powered by thermonuclear runaways occurring in the accreted envelope transferred from a companion star onto a compact white dwarf in a close binary system [404, 400]. The ^{30}P$(p,\gamma)^{31}$S reaction plays an important role in understanding the nucleosynthesis of $A \geq 30$ nuclides in oxygen-neon novae [3]. The uncertainty in the ^{30}P$(p,\gamma)^{31}$S rate impacts the nova observables, such as the ^{30}Si/^{28}Si isotopic abundance ratios useful for the identification of pre-solar nova grains [4], the O/S, S/Al, O/P, and P/Al abundance ratios that are good candidates for nova thermometers [5], and the Si/H abundance ratio, which can be used to constrain the degree of mixing between the white dwarf's outer layers and the accreted envelope [6]. It is not currently possible to measure the ^{30}P$(p,\gamma)^{31}$S reaction directly because intense low energy ^{30}P beams are not available. Through nuclear structure measurements, the thermonuclear rate of the ^{30}P$(p,\gamma)^{31}$S reaction over most of the peak nova temperatures (0.1−0.4 GK) has been found to be dominated by $\ell = 0$ proton capture into a 260-keV resonance [7, 8, 123] (Fig. 28). Recent experimental work has unambiguously determined the energy, the spin and parity, and the decay branching ratios of this resonance [8, 9, 443], leaving the lifetime as the largest remaining source of uncertainty in the resonance strength, as well as the last missing piece of experimental information for this state.

Until Feb 2023, only five relatively long-lived ^{31}S states at 1248 [11, 12, 13, 14], 2234 [11], 4451 keV [14, 15], 6376 keV [15], and 6833 keV [15] had reported lifetime measurements. In our experiment S1582 with the original Doppler Shift Lifetimes (DSL) facility at TRIUMF, we determined the lifetimes of the two long-lived ^{31}S states at 1248 and 2234 keV and obtained strong upper limits on the lifetimes of four short-lived states at 3076, 3435, 4971, and 5156 keV for the first time. We applied Markov chain Monte Carlo (MCMC) based Bayesian inference techniques to analyze γ-ray lineshapes acquired with the Doppler-shift attenuation method (DSAM) for the first time. We also observed evidence for γ rays originating from the astrophysically important $3/2^+$ resonance at 6390 keV, and the probability distribution obtained from Bayesian analysis suggests a lifetime below 20 fs. Shell model calculations using USD Hamiltonians predicted its lifetime to be 4.3 fs (USDA), 24 fs (USDB), 2.7 fs (USDC), 1.8 fs (USDE), 2.8 fs (USDI), and 1.3 fs (USDC-shifted) [62, 125, 126]. The lifetime of its mirror state in ^{31}P at 6380.8(20) keV was measured to be $\tau < 10$ fs [127]. Based on the aforementioned studies, we can estimate that the lifetime falls within the femtosecond range, and therefore, the DSAM remains the most applicable approach. However, in order to establish stronger constraints on the lifetime, it is necessary to conduct a more sensitive measurement [62].

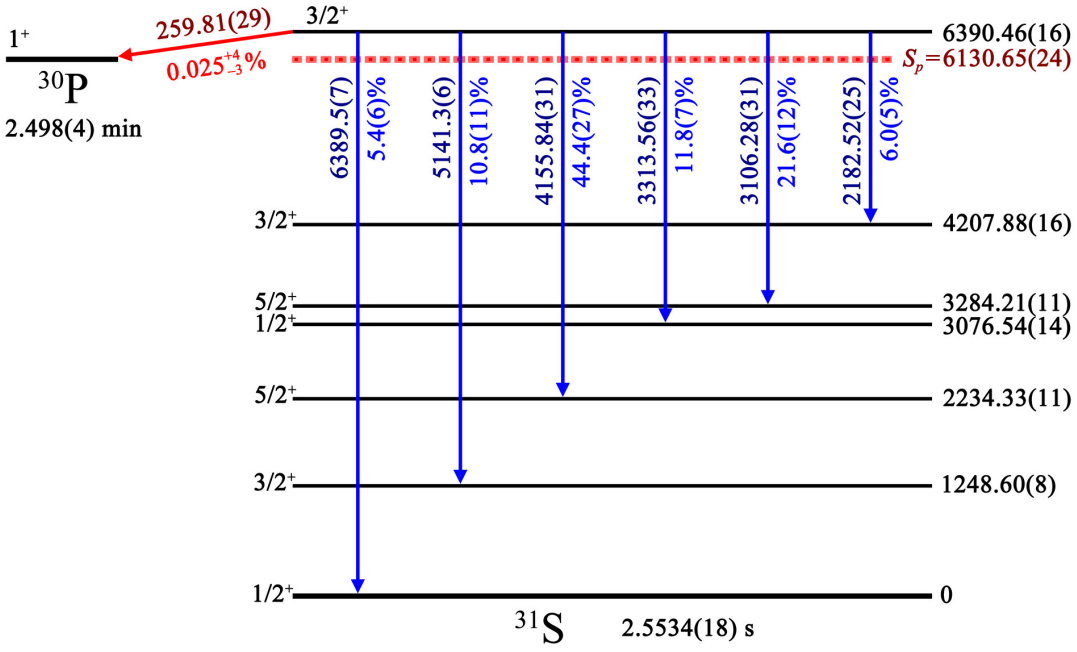

Figure 28: Known decay scheme of the ^{30}P$(p,\gamma)^{31}$S resonance at 6390 keV. The excitation energies and the proton separation energy are in units of keV and adopted from Ref. [123]. The transition energies and decay branching ratios are adopted from Refs. [8, 9, 443, 125].

13. Experimental Equipment

Motivated primarily by the unknown or imprecise lifetimes of excited states of astrophysical importance, we built the DSL facility at TRIUMF. As shown in Fig. 29, a scattering chamber was designed to provide a clean environment conducive to detecting γ ray emission from excited nuclear states populated in heavy ion-induced transfer reactions in inverse kinematics [57]. Reaction products gain more energy in inverse kinematics and lead to larger Doppler shifts in γ ray peaks, thereby improving the lifetime sensitivity of the DSAM.

Since its completion in 2005, the DSL setup has been used with (^{3}He, α) reactions to measure the lifetimes of ^{19}Ne states relevant to the ^{15}O$(\alpha,\gamma)^{19}$Ne reaction rate [58, 59], the lifetimes of ^{15}O states relevant to the ^{14}N$(p,\gamma)^{15}$O reaction rate [56], the lifetimes of ^{23}Mg states relevant to the ^{22}Na$(p,\gamma)^{23}$Mg reaction rate [60], and the lifetimes of ^{31}S states relevant to the ^{30}P$(p,\gamma)^{31}$S reaction [62, 61].

There are several factors that limit the sensitivity of the DSL lifetime measurements. The maximum beam power that can be tolerated without degrading the target by ^{3}He diffusion is 0.37 W, corresponding to a beam intensity of 1.8×10^{10} pps or 2.88 pnA. We cannot significantly increase the ^{32}S beam intensity above what was used in S1582 due to target heating. Also, we cannot increase the amount of ^{3}He implanted due to blistering of the Au substrate. As a result, our focus has been on improving the detection efficiency. In 2021, we upgraded the DSL facility to DSL2 by replacing the two ORTEC B Series silicon surface barrier detectors [63] with a 139 μm thick MICRON W1 double-sided silicon strip detector (DSSD) [128] and a 1011 μm thick MSX25 single-sided silicon detector [129] (Fig. 30). The surface area of the two ORTEC detectors was 150 mm^2. Limited by the aperture in front of them, the telescope only covered 1.0% of the 4π solid angle. In contrast, the new telescope consists of larger detectors with an area of 2500 mm^2 and is able to cover approximately 17% of the 4π solid angle.

We have developed a detailed Monte Carlo simulation using GEANT4 [522, 523] to model the γ-ray lineshapes obtained by both DSL and DSL2 (Fig. 31). Based on our simulation results on the key ^{31}S resonance, the α detection efficiency is increased by a factor 11 primarily due to the much higher solid angle coverage of the new Si telescope. The γ-ray detection efficiency is increased by a factor of 1.3. This improvement is attributed to the elimination of the collimator and detector mount, resulting in less attenuation of γ rays between the target and the Ge detector in DSL2.

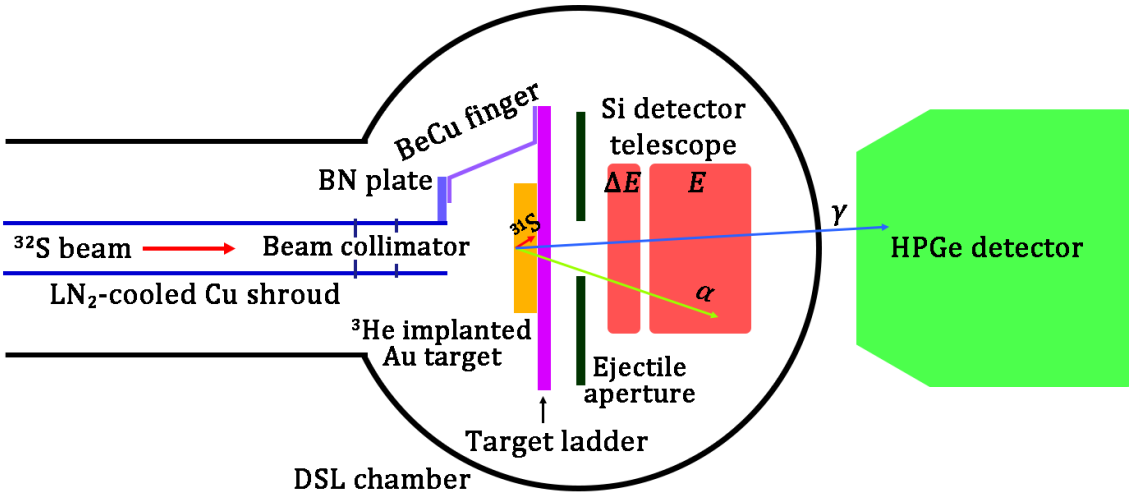

Figure 29: Schematic of the DSL experimental setup. The ejectile aperture has been removed in the DSL2 setup.

With the same amount of beam time, the overall statistics of the γ ray of interest at 4156 keV can be increased by a factor of 14, which will greatly benefit the sensitivity of lifetime measurements. Furthermore, the overall lineshape observed in DSL2 is subject to more kinematic broadening, but we can leverage the segmented feature of the DSSD to investigate lineshapes by selectively gating on α-particles in individual pixels.

The DSL2 setup has been successfully commissioned during the first run of S2193: Lifetime of the key ^{22}Na$(p,\gamma)^{23}$Mg resonance in novae, in December 2022 [130]. The data analysis is currently in progress [131].

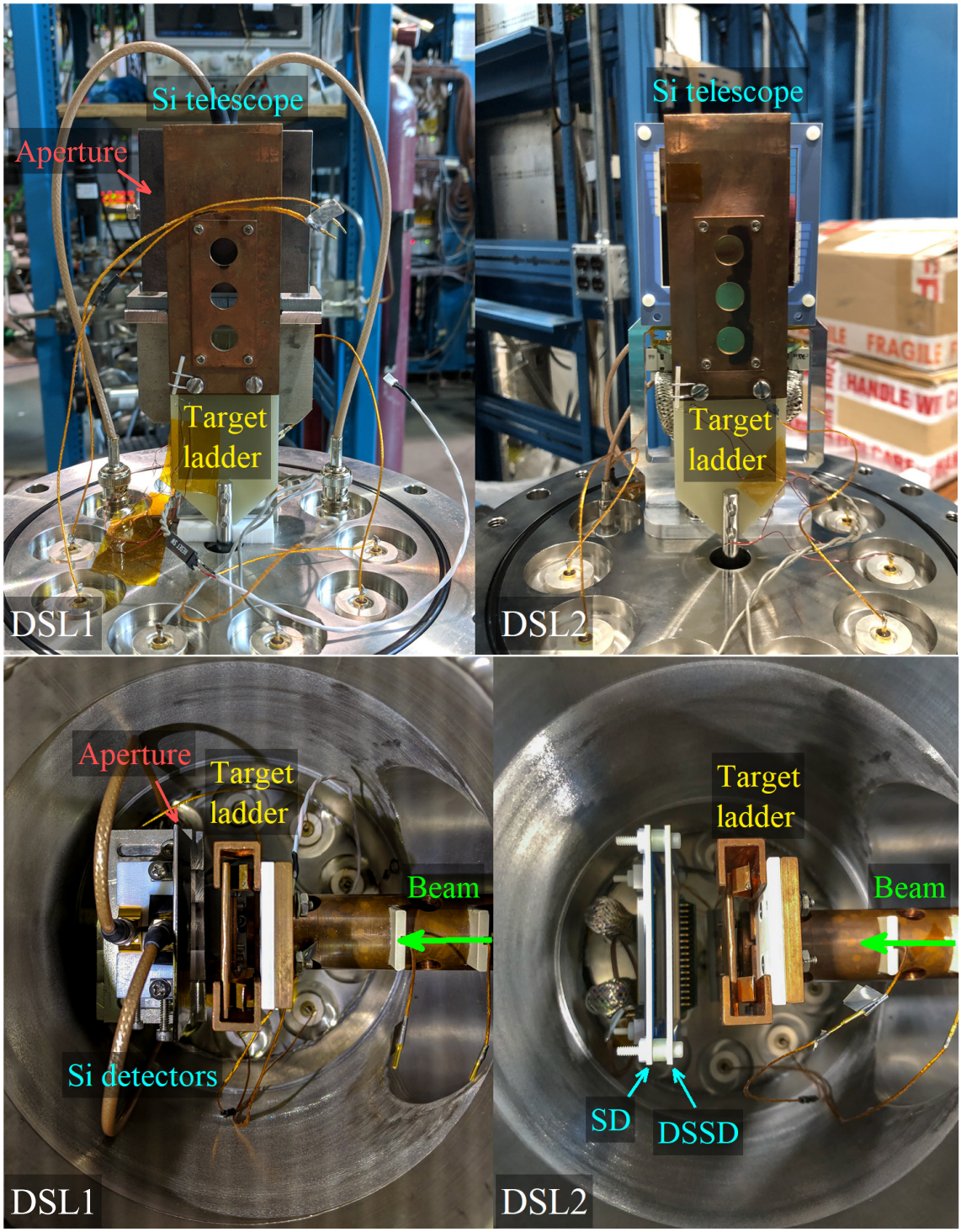

Figure 30: Comparison between the DSL and DSL2 setups.

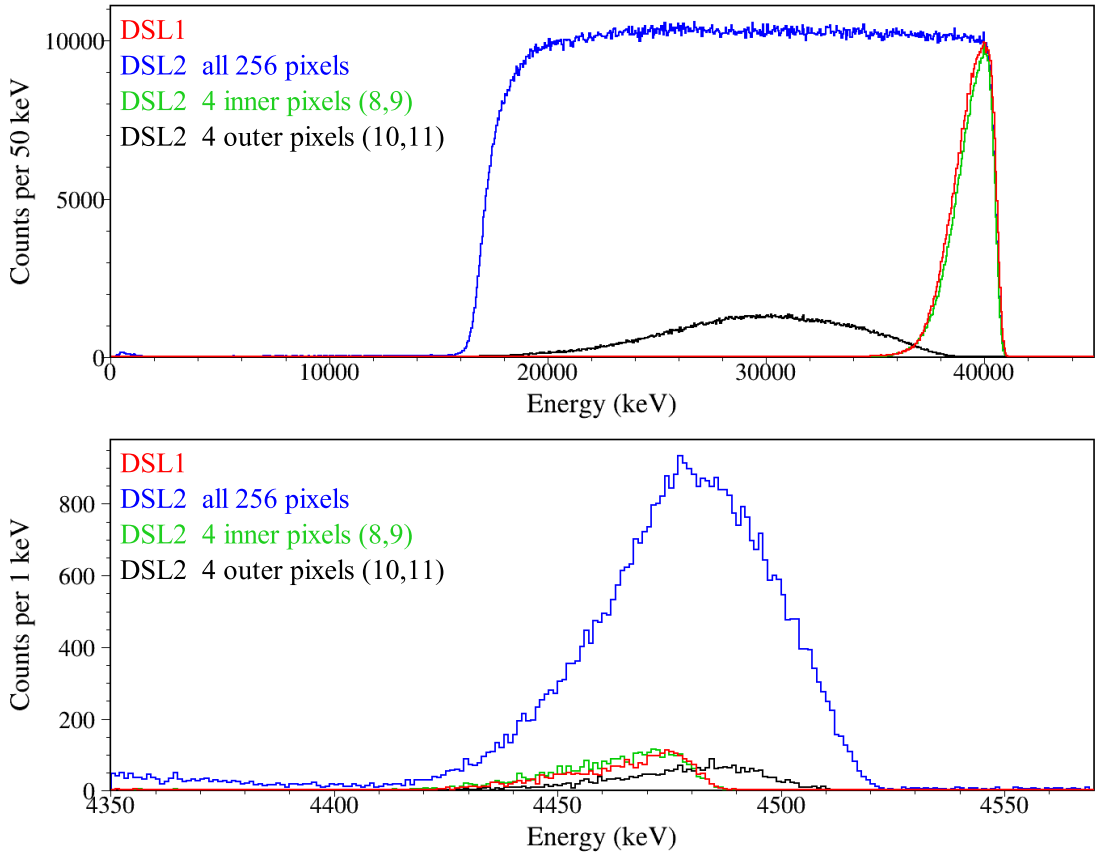

Figure 31: α and γ-ray spectra for the 6390 keV $\rightarrow$ 2234 keV transition in ^{31}S. The simulation is performed using the DSL1 and DSL2 configuration, respectively, while assuming an equal amount of beam time.

14. Description of the Experiment

The experiment will be conducted using the DSL2 facility [57] at TRIUMF-ISAC-II. A 1.8×10^{10} pps, 128-MeV $^{32}S^{7+}$ beam will bombard a ^{3}He-implanted Au target and the excited states in ^{31}S will be populated via the ^{3}He(^{32}S, α)^{31}S reaction. 128-MeV beam energy corresponds to a center of mass kinetic energy of E_{CM} = 11 MeV used by a (^{3}He, α) measurement in regular kinematics [83]. The target will be kept cool via BeCu fingers in contact with a BN plate attached to a LN_2-cooled Cu shroud. The thermal gradient between the target ladder and the Cu shroud prevents losses of the implanted ^{3}He through heating while mitigating the condensation of contaminants on the surface of the target [61]. The α particles will be detected by the Si detector telescope placed 18.4 mm downstream of the target. The beam and the heavy recoils will be fully stopped inside the 25 μm-thick Au foil. Deexcitation γ rays will be detected by a GRIFFIN Ge detector [64, 65] placed at a distance of 78 mm from the target, centered at 0° with respect to the beam axis. The signals from the preamplifiers of the Si and Ge detectors will be collected by the 14-bit, 100-MHz, GRIF-16 digitizers. The data will be processed by the GRIFFIN DAQ [75] and unpacked by the GRSISort program.

The Si detectors will be calibrated using a source containing ^{239}Pu, ^{241}Am, and ^{244}Cm, with strong α lines at 5.155 MeV, 5.486 MeV, and 5.805 MeV. A linear calibration will be applied and used to extrapolate to higher energies. The extrapolation will be verified by comparing the energy loss of punch-through particles to SRIM calculations [491]. The GRIFFIN Ge detector will be calibrated using a ^{56}Co source. A line from ^{197}Au Coulomb excitation at 279.01(5) keV [67] and a line from ^{39}K produced in ^{32}S+^{12}C fusion evaporation at 2814.06(20) keV [68] are usually observed with high statistics. The vast majority of the γ rays constituting these lines were emitted after the recoils stopped; hence, they are unshifted and can used as run-by-run calibration standards. The accuracy of the calibration at high energies will be verified by a 6128.63(4)-keV γ ray originating from the deexcitation of the second excited state in ^{16}O [69]. The energies deposited in all four crystals of the Ge detector will be summed together to increase the photo-peak efficiency while reducing the Compton scattering background [64]. Lifetimes of ^{31}S states will then be determined from a lineshape analysis of this addback spectrum.

After the calibration, we will select α particles with specific energies based on relativistic reaction kinematics, to suppress the competing reaction channels and indirect feedings from higher-lying levels. This approach ensures a direct level population by the transfer reaction, leading to significantly cleaner γ-ray spectra for lineshape analysis. To model the lineshapes in the GEANT4 simulation, the GRIFFIN Ge detector response has to be accurately characterized. We will employ an empirical technique by fitting an exponentially modified Gaussian function [516] to unshifted γ-ray peaks originating from long-lived states populated by Coulomb excitation and fusion-evaporation reactions at 279.01(5) and 547.5(3) keV [^{197}Au] [67], 2814.06(20) and 3597.26(25) keV [^{39}K] [68], 3736.5(3) keV [^{40}Ca] [81], and 6128.63(4) keV [^{16}O] [69].

15. Readiness

We possess all the equipment needed for the experiment at TRIUMF.

16. Beam Time Required

We acquired ~110 hours of data in S1582 using the original DSL setup and observed a total of 51 ± 11 counts in the 4156-keV dominant decay branch of the key ^{31}S resonance at 6390 keV, corresponding to 0.46 counts per hour. Based on the GEANT4 simulation and assuming a beam rate similar to that of S1582, we anticipate 6.6 counts per hour in S2373. This translates to a total of 1020 counts over a period of 152 hours. To investigate the lifetime sensitivity that can be achieved with a factor of 20 increase in statistics, we have generated the same amount of synthetic data for the 4156-keV γ-ray line and incorporated a realistic background level based on our observations in S1582.

The literature energy of the γ ray, the background level beneath the peak, and the stopping power of the target foil have been identified as the most significant factors affecting the lineshapes and, consequently, the inferred lifetime. In the Bayesian framework, the model parameters are viewed as random variables. By varying these parameters within a reasonable range, we first run the GEANT4 simulation with ~300 parameter settings (Fig. 32). We have established the analysis framework based on the SURMISE package [97, 116] developed by the Bayesian Analysis for Nuclear Dynamics (BAND) Collaboration [53]. Briefly, we standardize the simulation outputs, perform Singular

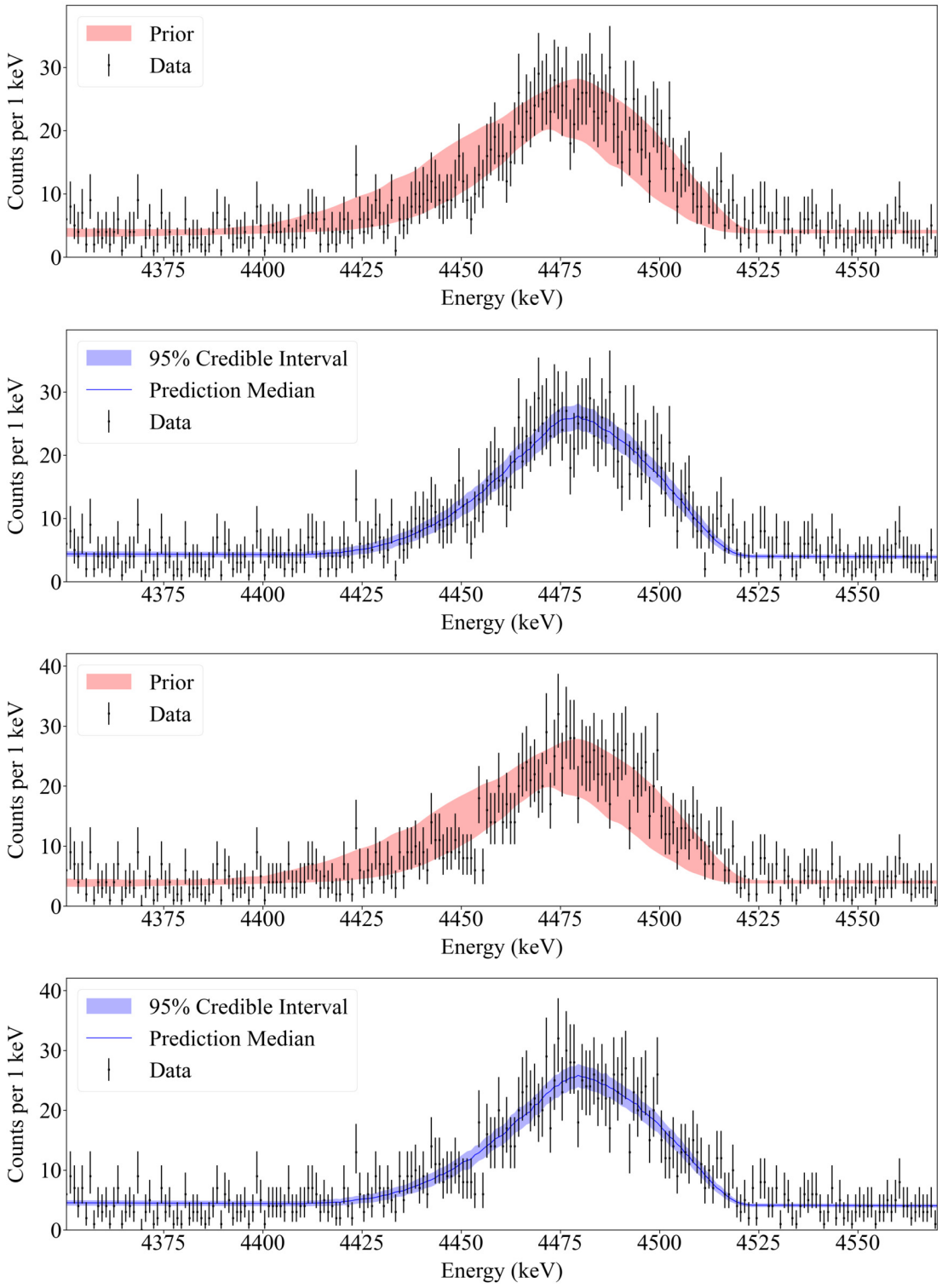

Figure 32: Lineshape analysis of the 4156-keV γ-ray line from the 6390 keV $\rightarrow$ 2234 keV transition in ^{31}S. The lineshapes assuming τ = 3 fs (top two panels) and 0 fs (bottom two panels) are shown as data points with statistical error bars in both panels. Prior lineshape (red, upper panel): hundreds of lineshapes generated by varying each parameter within its prior range in the GEANT4 simulation. Posterior predictive lineshape (blue, lower panel): 95% credible interval constructed with the number of counts in each bin corresponding to the parameter posterior distributions.

Value Decomposition (SVD) on the standardized data matrix to identify principal components, and then project the original simulator outputs onto a lower-dimensional space spanned by an orthogonal basis. This way, the high-dimensional model outputs / observable space are transformed into a reduced number of uncorrelated latent outputs using principal component analysis (PCA) [95]. Typically, we set the number of principal components to capture 99.99% of the variance of the model. This means the reduced data set using PCA still retains most of the important information from the original data set. We fit a Gaussian Process (GP) model for each latent output, use the fitted GP model to predict the mean, variance, and covariance matrix, and reconstruct them in the original high-dimensional space through the inverse PCA transformation. When computing the likelihood during MCMC sampling at another parameter setting, the simulator output is represented by the trained emulator's predictive mean and covariance, and the prediction uncertainty from the emulator is integrated within the likelihood. GP is computationally efficient and accurately accounts for the uncertainty associated with emulation, which is suited for Bayesian parameter estimation purposes [96].

The final results obtained from the MCMC sampling are demonstrated in Fig. 33. The lifetime value and its 1σ uncertainties are typically determined by extracting the 16th, 50th, and 84th percentile values from the posterior distribution. In situations where the lifetime falls beyond our sensitivity and is compatible with zero, we can establish its upper limit at a 90% confidence level by using the 90th percentile value from the posterior distribution. The inferred lifetime values closely align with the true values used to generate the pseudo data, serving as a closure test for validation of our Bayesian parameter inference framework. One important merit of Bayesian methods is that a posterior distribution offers more detailed information than a point estimate or an interval from frequentist methods so that uncertainty propagation can work with richer information than that conveyed by a point estimate [28, 113]. The 2D correlations between parameters allow us to easily capture features, patterns, or anomalies. The lineshapes based on the prior and posterior distributions of parameters are shown in Fig. 32. The close resemblance between the prediction bands and the measured lineshapes indicates the constraining power provided by the experimental data. With the higher statistics offered by DSL2, it may also be possible to extend the lineshape analysis to other weaker transitions from the resonance to achieve even higher sensitivity on the lifetime, thus facilitating a clearer distinction between the shell-model predictions and contributing to the understanding of the nuclear structure of ^{31}S.

Fig. 35 demonstrates how well we can constrain the resonance strength and the reaction rate with the inferred lifetime. Combining $\tau = 3.1^{+1.6}_{-1.3}$ fs and $\tau \leq 2.5$ fs (90% CI), respectively, with our experimentally determined proton branching ratio $B_p = 2.5^{+0.4}_{-0.3} \times 10^{-4}$ [443] yields resonance strengths $\omega\gamma = 35^{+26}_{-13}$ μeV and $\omega\gamma \geq 43$ μeV (90% CI), respectively. Combined with the well-measured resonance energy $E_r = 259.81(29)$ keV [123], the reaction rate and its uncertainties can be determined without relying on any theoretical assumptions for the first time. Combining with the known properties of other resonances making small contributions within the Gamow window [84, 85, 86, 87, 88, 89, 90], the total thermonuclear ^{30}P$(p,\gamma)^{31}$S rate can be determined.

We can apply Monte Carlo reaction rate calculations, in which all of the measured nuclear physics properties entering into the reaction rate calculation are randomly sampled according to their individual probability density functions. Instead of reporting a single value at a given temperature, our result will be statistically meaningful recommended reaction rates and uncertainties that correspond to a desired coverage probability that takes into account the uncertainties of all inputs in a consistent manner [544, 545, 546, 547, 548]. The code RatesMC can also account for correlations between nuclear quantities that enter those calculations and possible interferences between resonant amplitudes [137, 138]. Reaction rates at low temperatures that are dominated by a few isolated resonances have been found not to be substantially affected by correlation effects [137, 138]. Therefore, our ^{30}P$(p,\gamma)^{31}$S Monte Carlo rate is computed assuming no correlations between the physical quantities that enter the rate calculation.

The next potential step is to employ these rates in Monte Carlo nucleosynthesis studies. Notice that we are referring to two different Monte Carlo procedures: the first is used to derive reaction rates by randomly sampling over the experimental nuclear physics input, while the second refers to estimating abundances by randomly sampling over the reaction rates.

To investigate the astrophysical impact, we will perform hydrodynamic simulations of oxygen-neon novae with the spherically symmetric, implicit, Lagrangian, hydrodynamic code SHIVA coupled to a full nuclear reaction network [404, 139]. Briefly, the ^{30}P$(p,\gamma)^{31}$S reaction rate and the ^{30}P$(\beta^+)^{30}$Si decay are the two main destruction mechanisms for ^{30}P in ONe novae [404]. Fig. 35 shows the proton capture becomes more likely than the competing β^+ decay beyond a temperature within the peak nova temperature range of $T_{\rm peak} = 0.1$–0.4 GK. The location of the crossing point influences the predicted Si isotopic ratio for ONe nova ejecta. With the experimentally determined ^{30}P$(p,\gamma)^{31}$S

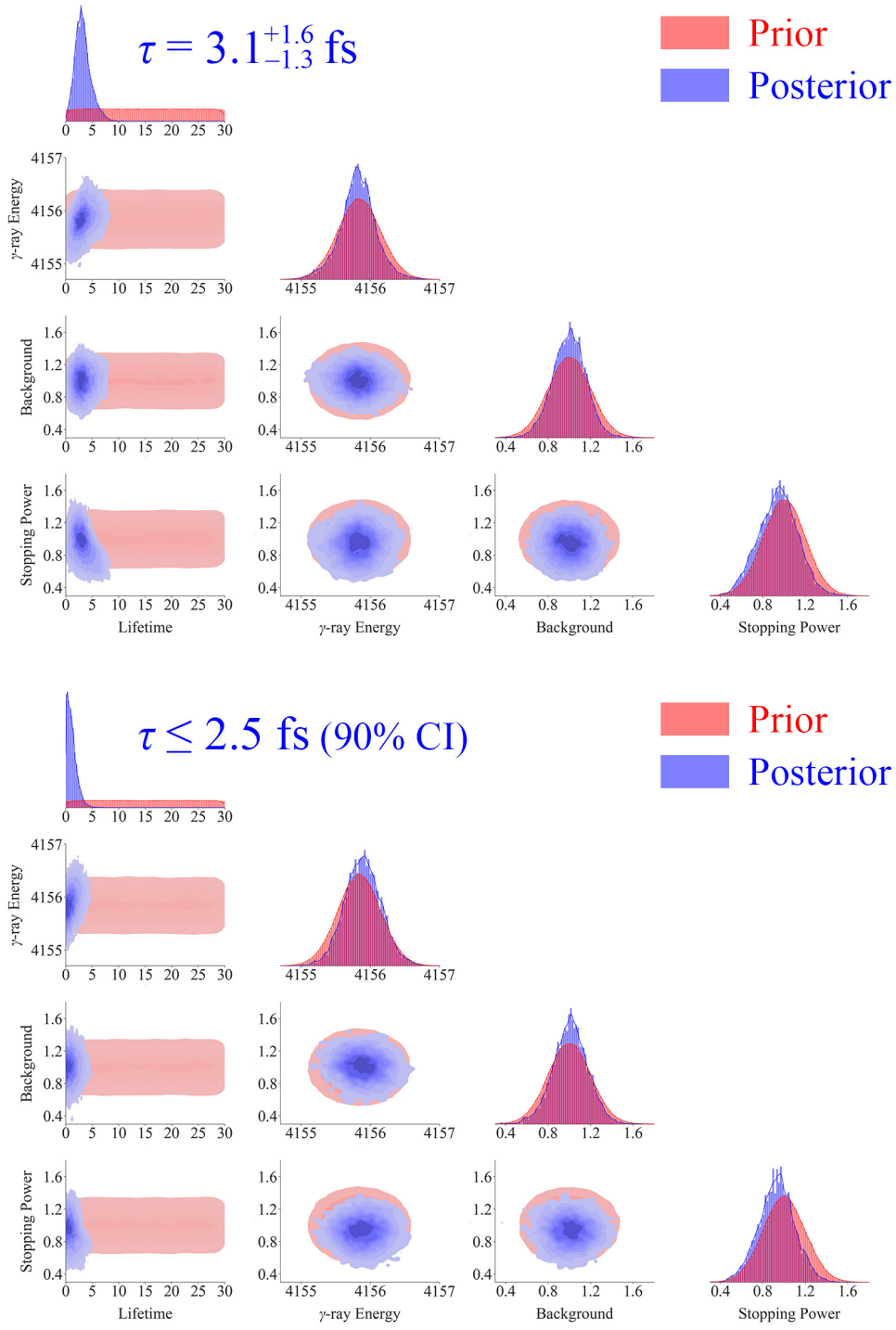

Figure 33: Posterior distributions of the model parameters for the ^{31}S $3/2^+$ resonance at 6390 keV assuming a lifetime τ = 3 fs and 0 fs, respectively. Diagonals: prior (red) and posterior (blue) distributions of each parameter. From top left to bottom right: Lifetime τ (fs), γ-ray energy E_γ (keV) of the dominant branch, relative background *bkg*, and relative stopping power *sp*. Off-diagonals: joint distributions showing correlations between pairs of parameters.

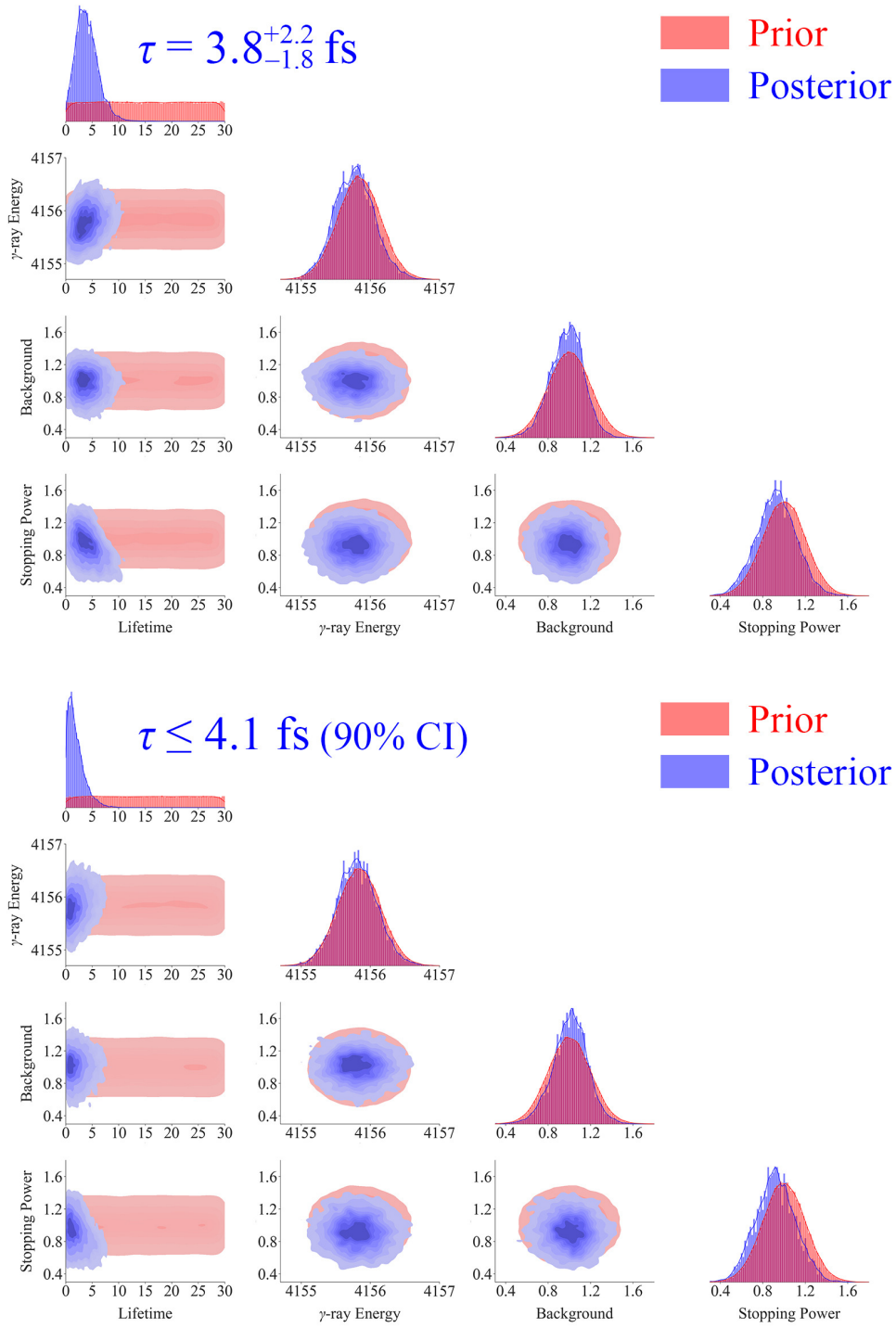

Figure 34: Same as Fig. 33, but with half statistics (510 counts).

rate, we can eliminate the nuclear uncertainties in reaching a concrete prediction regarding a series of isotopic and elemental abundance ratios in nova ejecta. This will provide valuable insights into identifying the origin of several presolar grains with enhancements in the ^{29}Si:^{28}Si and ^{30}Si:^{28}Si ratios. The elemental abundance ratios of O:S, S:Al, O:P, and P:Al exhibit a strong dependence on both nova temperature and the ^{30}P$(p,\gamma)^{31}$S rate. The new rate from this work will allow us to reduce the dominant nuclear uncertainties and make these ratios more robust nova thermometers.

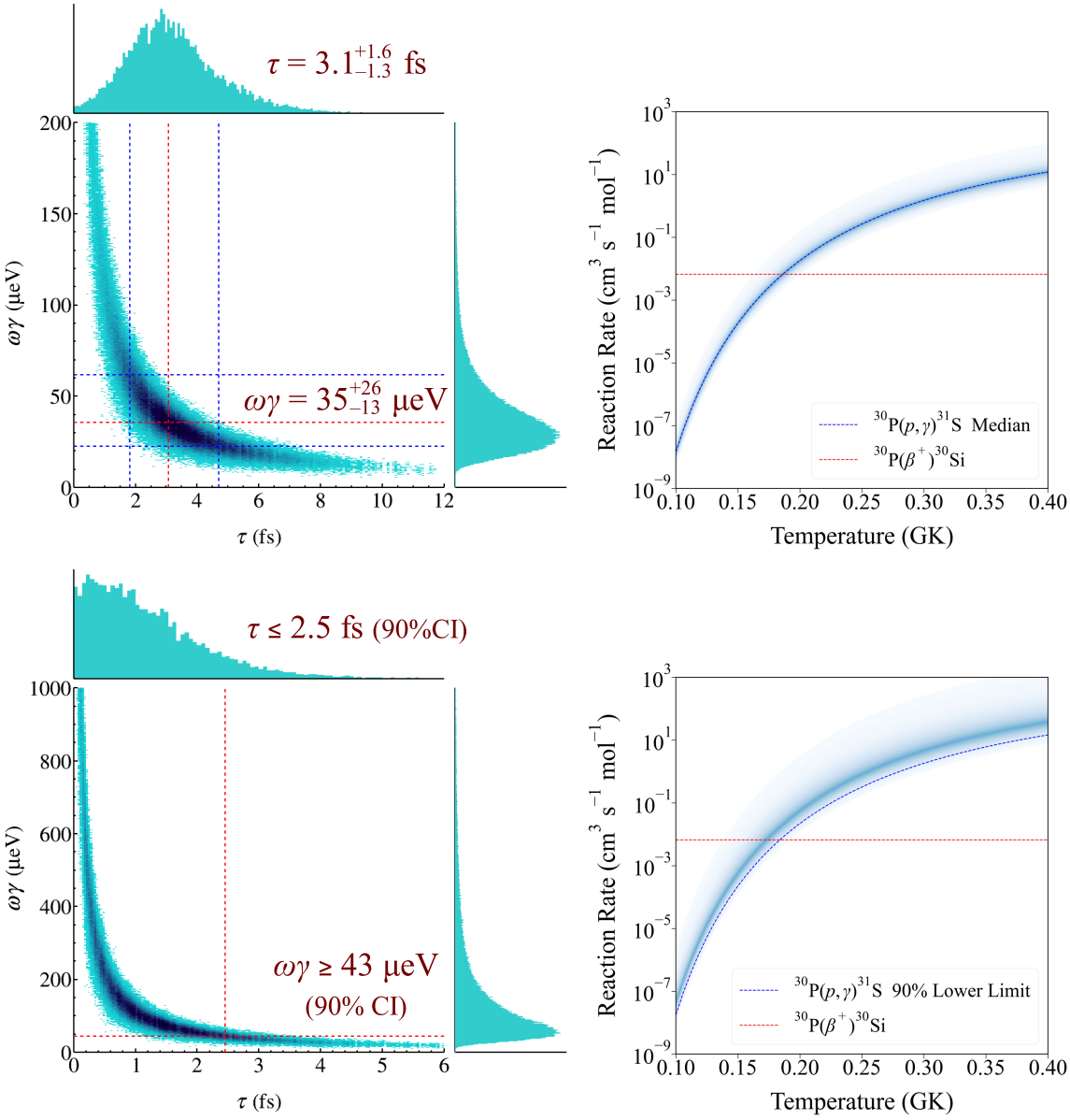

Figure 35: Left: the strengths of the 260-keV $3/2^+$ resonance derived from the inferred lifetime of 3 fs and 0 fs, respectively, and the known proton branching ratio [443]. For τ = 3 fs, the resonance strength and its corresponding uncertainties are determined by using the 16th, 50th, and 84th percentile values, which are indicated by dashed lines. For τ = 0 fs, the lower limit of the resonance strength is determined using the 95th percentile value. Right: the corresponding thermonuclear ^{30}P$(p,\gamma)^{31}$S reaction rates from the dominant $3/2^+$ resonance contribution corresponding to these two scenarios.

To summarize, our analysis has demonstrated that with 19 shifts, we can either obtain a finite value as low as 3 fs

or set a strong upper limit of 2.5 fs on the lifetime of the astrophysically important $J^\pi = 3/2^+$, 260-keV ^{30}P$(p,\gamma)^{31}$S resonance. This level of precision will put the reaction rate on a fully experimental footing for the first time, and will potentially eliminate the largest nuclear uncertainty associated with the aforementioned nova observables. Taking into account an additional 2 shifts of downtime, we request a total of 21 shifts (7 days) to run the experiment.

17. Data analysis

The data analysis will be conducted on the FRIB Lab server located at Michigan State University, USA.

18. Lifetime of the key ^{22}Na$(p,\gamma)^{23}$Mg resonance in novae (EEC S2193)

The radioactive nucleus ^{22}Na ($T_{1/2}$ = 2.6 y) is a long-sought target of γ-ray astronomy that is expected to be produced in thermonuclear explosions on the surfaces of accreting white-dwarf stars (classical novae) [3, 140, 141, 142]. Space-based γ-ray observatories have been on the verge of being able to detect the characteristic 1275-keV β-delayed γ decay radiation predicted from some of the closest novae over the past few decades and future observatories will provide higher sensitivity. A precise determination of the ^{22}Na$(p,\gamma)^{23}$Mg thermonuclear rate is necessary to improve the predicted abundances of nuclei in the mass region $A > 20$ during nova outbursts, including the ^{22}Na abundance in the ejecta that impacts in turn the predicted ^{20}Ne/^{22}Ne ratios in presolar grains of a putative nova origin, as well as, the corresponding γ-ray emission flux. A simultaneous goal of the low-energy nuclear physics community has been to provide the nuclear data necessary to interpret the observations by comparing them to predictions using nova models coupled to full nuclear reaction networks. Much of the necessary nuclear data on thermonuclear reaction rates in the vicinity of ^{22}Na has now been obtained.

However, there are persistent and growing discrepancies in the experimentally determined rate of the ^{22}Na$(p,\gamma)^{23}$Mg reaction (Q = 7580.79 keV), which destroys ^{22}Na while it is being produced during a nova, affecting predictions of the ejected yield substantially. A single resonance with a center-of-mass energy of 204 keV and an excitation energy of 7786 keV in ^{23}Mg dominates the rate of this reaction at peak nova temperatures of 0.1-0.4 GK. The strength of this resonance has been measured directly twice in challenging experiments with radioactive ^{22}Na targets yielding discrepant results of 1.8(7) meV [143, 144] and $5.7^{+1.6}_{-0.9}$ meV [145, 146]. The strength can also be determined by combining the resonance's lifetime and proton-branching ratio. Measurements have yielded values for the proton branching ratio of $10(8) \times 10^{-3}$ [147], $3.7(9) \times 10^{-2}$ [148], $6.5(8) \times 10^{-3}$ [149], and $6.8(17) \times 10^{-3}$ [150, 151], which also span a large range, two finite values the lifetime of 10(3) fs [152] and 11^{+7}_{-5} fs [150, 151], and one upper limit of <12 fs [60]. Depending on the combinations of values adopted, the indirect measurements yield resonance strengths of 0.24(8) meV, 0.4(3) meV, 1.4(5) meV, >0.71 meV, and >0.16 meV, many of which are inconsistent with the direct measurements [149]. The broad range of finite resonance-strength values causes the ^{22}Na yield predicted by nova models to vary by a factor of 3.8 [149]. The relevant nuclear data are summarized in Table 3.

Combining the most sensitive proton branching ratio [149] with the only finite lifetime value [152] leads to the resonance strength of 0.24(8) meV, which is lower than the directly measured values by approximately an order of magnitude. It is difficult to imagine that the direct measurements could both be too high by so much. However, the shell model predicts a lifetime value of 0.6-1.7 fs for the resonance of interest [159], which is an order of magnitude lower than the measured value [152], and corresponds to a resonance strength of 1.4-4.1 meV when combined with the same branching ratio. This range is generally consistent with the direct measurements. Therefore, it would be valuable to produce a second finite lifetime measurement to distinguish between the shell-model prediction and the existing measurement.

An experiment recently took place at GANIL to measure the lifetime, the proton branching ratio and the spin of the 7786 keV excited state, populated by the ^{3}He(^{24}Mg, α)^{23}Mg reaction [150, 151]. We have fabricated ^{3}He-implanted targets at TRIUMF and the Lawrence Livermore National Laboratory, by implanting 30-keV ^{3}He ions into a 25 μm-thick Au foil to an areal density of $\sim 6 \times 10^{17}$ cm^{-2}. We have replaced the ORTEC silicon detector telescope used by the DSL1 facility with a MICRON W1 double-sided silicon strip detector [128] and a MICRON MSX25 single-sided large area silicon detector [129]. We have conducted a more sensitive lifetime measurement using an upgraded version of the DSL setup called DSL2 at TRIUMF-ISAC in December 2022. The data analysis is ongoing.

Table 3: Nuclear data of the key ^{23}Mg resonance. Columns list the reference, experimental method, lifetime τ, spin and parity (J^π), excitation energy (E_x), γ-ray energy (E_γ), relative γ-ray intensity (I_γ), the ratio of the 7.3-MeV γ-ray branch to the 5.7-MeV branch ($R_{7.3/5.7}$), and the proton-decay branching ratio.

Literature	Method	τ (fs)	J^π	E_x (keV)	E_γ (keV)	I_γ (%)	$R_{7.3/5.7}$	Γ_p/Γ
Stegmüller [144]	^{22}Na$(p,\gamma)^{23}$Mg	–	–	7785(3)	7334 –	– –	>3.5	–
Sallaska [145, 146]	^{22}Na$(p,\gamma)^{23}$Mg	–	–	7784.7(12)	7332.7(12) 5732	100 12(6)	8.4(42)	–
Jenkins [152, 153]	^{12}C(^{12}C,$n\gamma$)^{23}Mg	10(3)	$(7/2^+)$ [152] $7/2^{(+)}$ [153]	7784.6(11)[a]	7333.7(11) –	100 –	∞	–
Kirsebom [60]	^{3}He(^{24}Mg,α)^{23}Mg	<12	$(7/2)^+$[b]	7787.2(6)[c]	7335 –	– –	∞	–
Kwag [154]	^{24}Mg$(p,d)^{23}$Mg	–	$3/2^+, 5/2^+$	7788(5)	– –	– –	–	–
Fougères [151]	^{3}He(^{24}Mg,α)^{23}Mg	11^{+7}_{-5}	$7/2^+$	7785.0(7)	7333.0^{+5}_{-2} 5734	100 <3	>32	$6.8(17)\times10^{-3}$
Iacob [155]	^{23}Al$(\beta\gamma)^{23}$Mg	–	$(7/2)^+$	7787.4	7335.1 5736 7786	100 20(5) 3.8(25)	5.0(12)	–
Zhai [156]	^{23}Al$(\beta\gamma)^{23}$Mg	–	$(5/2,7/2)^+$	7787.2(6)	7335.2(6) 5735.4(7)	100 23	4.3(12)	–
Saastamoinen [148]	^{23}Al$(\beta\gamma)^{23}$Mg ^{23}Al$(\beta p)^{22}$Na	–	$(7/2)^+$	7786.9(5)	7335 5736	– –	–	$3.7(9)\times10^{-2}$
Goldberg [157] Friedman [149]	^{23}Al$(\beta\gamma)^{23}$Mg ^{23}Al$(\beta p\gamma)^{22}$Na	–	$(7/2)^+$	7787.2(5)	7335.1(9) 5735.8(6)	100 25	4.0(4)	$6.5(8)\times10^{-3}$
Basunia [158]	Evaluation	10(3)	$3/2^+, 5/2^+$	7784.7(8)	7333.2(11) 5732	100(6) 16(4)	6.2(22)	–

[a] Revised to be 7785.7(11) by Kirsebom [60].
[b] Adoped by Kirsebom [60].
[c] Adoped for Doppler lineshape analysis by Kirsebom [60].

In the case where multiple γ-ray branches deexciting the same level and are observed with high statistics. The individual γ-ray spectra can be concatenated create a wider/longer observable for the DSL- SURMISE analysis framework and would enhance the overall constraining power [98].

19. Machine learning

Artificial intelligence is everywhere. Many people are integrating AI not because they need it but because they have developed a case of FOMO (fear of missing out).

Artificial intelligence (AI) and machine learning (ML) is a rapidly developing field focused on computational technologies that can be trained with data to augment or automate human skills. AI encompasses a broader spectrum of technologies, including rule-based systems, expert systems, and symbolic reasoning. ML focuses specifically on learning from data to make informed decisions. Over the last few decades, AI has become increasingly prominent in all sectors of everyday life. This is largely due to the adoption of statistical and probabilistic methods, the availability of large amounts of data, and increased computer processing power. Machine learning and data science are playing increasingly important roles in many aspects of modern technology, ranging from biotechnology to the engineering of self-driving cars and smart devices.

The ability to harness the power of data for intelligent decision-making positions ML as a cornerstone in the current technological landscape. As we continue to unlock the potential of Machine Learning, its applications in diverse fields promise to redefine our understanding of automation, decision-making, and problem-solving, ushering in an era of unprecedented innovation and efficiency.

Machine learning is a subfield of artificial intelligence with the goal of developing algorithms capable of learning from data automatically. Machine learning represents the science of building models that can perform tasks without explicit instructions. Unlike traditional programming, where explicit programming is required to perform specific tasks, ML empowers machines to learn and improve from experience without being explicitly programmed. Machine Learning systems rely on data-driven algorithms, allowing them to handle a wider range of tasks without the need for constant manual reprogramming.

19.1. Types of machine learning

Machine learning includes three main categories: supervised learning, unsupervised learning, and reinforcement learning (Fig. 36).

Supervised Learning - Guided Intelligence: In supervised learning, algorithms are trained on labeled datasets, where each input is paired with the corresponding desired output. This process enables the model to establish mappings between inputs and outputs, facilitating predictions for new, unseen data. Regression and classification are the two primary types of supervised learning. Regression aims to predict continuous numerical values, whereas classification aims to predict categories or classes for given inputs.

Unsupervised Learning - Discovering Hidden Patterns: Unsupervised learning operates on unlabeled data, allowing algorithms to identify latent patterns and relationships without explicit guidance. Types of unsupervised learning tasks include clustering, dimensionality reduction, and association rule learning. Clustering involves grouping similar data points together into clusters or segments based on their features. An association rule is a rule-based method for finding relationships between variables in a given dataset.

Semi-supervised learning is similar to supervised learning, but instead uses both labelled and unlabelled data. In semi-supervised learning, the algorithm learns from a dataset that contains a small amount of labeled data and a much larger amount of unlabeled data. This approach is particularly useful in scenarios where obtaining labeled data is expensive or time-consuming, but unlabeled data is abundant.

Reinforcement Learning - Learning through Interaction: Reinforcement machine learning trains machines through trial and error to take the best action by establishing a reward system. Reinforcement learning involves an agent interacting with an environment, learning to make decisions through feedback in the form of rewards or penalties. This paradigm finds applications in diverse domains, such as robotics and strategic game-playing.

Ultimately, selecting appropriate techniques depends on task complexity, dataset size, available resources, and desired outcome metrics.

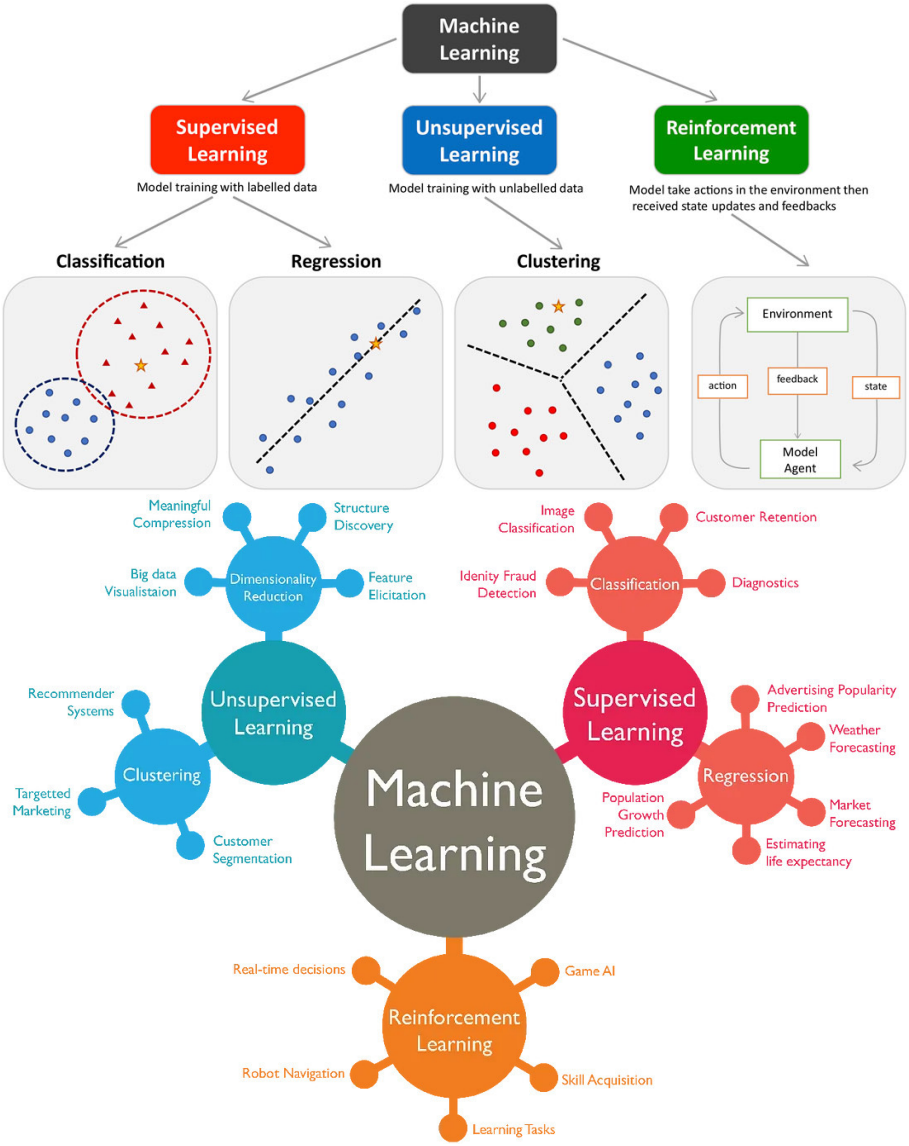

Figure 36: Types of Machine Learning. Adapted from Ref. [160].

19.2. Machine learning models

Key Components of Machine Learning include data, algorithms, and training.

Data serves as the bedrock of Machine Learning. The quality, quantity, and diversity of data are pivotal in shaping the efficacy of ML models.

ML algorithms are the intellectual engines that power the learning process. Ranging from elementary linear regression models to sophisticated neural networks, these algorithms are selected based on the specific nature of the problem at hand, whether it involves classification, regression, clustering, or reinforcement learning.

Decision trees are a type of machine-learning algorithm that can be used for both classification and regression tasks. They are based on the idea of recursively splitting the data into smaller and smaller subsets based on the values of the input features.

Random forest are an ensemble learning algorithm that uses multiple decision trees to make predictions. Random Forests work by training multiple decision trees on different subsets of the data. The predictions of the individual decision trees are then averaged to produce the final prediction.

A Support Vector Machine (SVM) is a supervised machine learning algorithm used for classification and regression tasks. It works by finding the hyperplane that best separates data points of different classes in a high-dimensional space. The optimal hyperplane maximizes the margin between the nearest data points from each class, known as support vectors.

Physics Informed Neural Networks (PINNs) use data-driven supervised neural networks to learn the model, but also use physics equations that are given to the model to encourage consistency with the known physics of the system. They have the advantage of being both data-driven to learn a model, but also able to ensure consistency with the physics, as well as being able to extrapolate accurately beyond the available data. As such, PINNs are able to generate more robust models, with less data.

The training phase embodies the essence of ML, wherein algorithms learn from historical data. Through iterative refinements of parameters, the model refines its understanding of patterns, minimizing the disparity between predicted outcomes and actual results.

Nowadays, many large language models can reason through complex tasks and solve harder problems than previous models in science, coding, and math. These enhanced reasoning capabilities may be particularly useful if you are tackling complex problems in science, coding, math, and similar fields. For example, ChatGPT-o1 can be used by healthcare researchers to annotate cell sequencing data, by physicists to generate complicated mathematical formulas needed for quantum optics, and by developers in all fields to build and execute multi-step workflows.

19.2.1. Neurons

A neuron is a basic building block of a neural network. It's like a tiny computer that can perform simple calculations and make decisions based on inputs. Neurons are connected to each other in a network, and they work together to perform complex tasks, such as image classification or language translation. The inputs to a neuron are numbers that represent the information, and the output of a neuron is a decision about what to do with that information.

One of the most crucial roles in neural network architecture is played by activation functions. Activation functions are simple transformations that are applied to the outputs of individual neurons in the network, introducing non-linearity to it and enabling it to learn more complex patterns.

Part II
GADGET & Doppler Technique

20. β-delayed proton and lifetime measurement using a Doppler broadening technique

Background β-decay spectroscopy provides valuable information on exotic nuclei and a stringent test for nuclear theories beyond the stability line.

Purpose To search for new β-delayed protons and γ rays of ^{25}Si to investigate the properties of ^{25}Al excited states.

Method ^{25}Si β decays were measured by using the Gaseous Detector with Germanium Tagging system at the National Superconducting Cyclotron Laboratory. The protons and γ rays emitted in the decay were detected simultaneously. A Monte Carlo method was used to model the Doppler broadening of ^{24}Mg γ-ray lines caused by nuclear recoil from proton emission. Shell-model calculations using two newly developed universal *sd*-shell Hamiltonians, USDC and USDI, were performed.

Results The most precise ^{25}Si half-life to date has been determined. A new proton branch at 724(4) keV and new proton-γ-ray coincidences have been identified. Three ^{24}Mg γ-ray lines and eight ^{25}Al γ-ray lines are observed for the first time in ^{25}Si decay. The first measurement of the ^{25}Si β-delayed γ ray intensities through the ^{25}Al unbound states is reported. All the bound states of ^{25}Al are observed to be populated in the β decay of ^{25}Si. Several inconsistencies between the previous measurements have been resolved, and new information on the ^{25}Al level scheme is provided. An enhanced decay scheme has been constructed and compared to the mirror decay of ^{25}Na and the shell-model calculations.

Conclusions The measured excitation energies, γ-ray and proton branchings, log ft values, and Gamow-Teller transition strengths for the states of ^{25}Al populated in the β decay of ^{25}Si are in good agreement with the shell-model calculations, offering gratifyingly consistent insights into the fine nuclear structure of ^{25}Al.

21. Introduction

The investigation of exotic nuclei lying far from the stability line has been one of the attractive topics of nuclear physics during the past few decades [161]. β-decay studies have proved to be a powerful tool to obtain a variety of spectroscopic information on nuclei far from stability that are difficult to obtain otherwise [162, 163], which provides an excellent and stringent test of nuclear structure theories and fundamental symmetries [164] and also deepens our understanding of the astrophysical rapid proton capture process [165], rapid neutron capture process [166], and p process [167].

Nuclei near the proton drip line with large Q values for β^+ decay and low proton separation energies often decay by β-delayed proton emission (βp). Since the discovery of the first βp emitter ^{25}Si in 1963, a total of 196 βp emitters (including isomers) have been identified ranging from C (Z = 6) to Lu (Z = 71) [168]. The β decay of ^{25}Si has been one of the most studied cases [169, 170, 171, 172, 173, 174, 175, 176, 177, 178]. All the β-decay measurements of ^{25}Si were focused on the proton spectrum, whereas the γ-ray spectrum has not been measured with high statistics. Construction of the decay scheme based solely on proton spectra could lead to inaccurate assignments. Thomas *et al.* [178] reported the most comprehensive measurement but with very limited γ-ray information. They may have missed some of the low-intensity and high-energy γ rays due to low statistics and low efficiency. The existing information on ^{25}Si decay properties is still incomplete and therefore motivates new experiments to search for new β-delayed particles and γ rays. Detecting protons and γ rays in ^{25}Si β decay and the coincidence between them allows one to reliably construct the decay scheme. ^{25}Si β-decay spectroscopy provides a sensitive and selective means to probe the properties of ^{25}Al excited states as well as a good verification of the information on the structure of ^{25}Al previously collected by other experimental approaches.

It should be noted that most of the information on the β-delayed proton decay of ^{25}Si was obtained with silicon implantation detectors. A major problem for this method is the strong β-summing effect caused by energy deposited by β particles [162]. Robertson *et al.* employed a gas-silicon detector telescope to detect ^{25}Si β-delayed protons for the first time. Despite the small solid angle coverage and the existence of dead layers for incident particles, they were able to identify several new low-energy proton peaks [177]. Hence, the development of complementary experimental tools for the clean detection of low-energy β-delayed proton branches is particularly valuable.

In this paper, the emitted particles and γ rays in the β decay of ^{25}Si were measured simultaneously with high efficiency and high energy resolution. Combining all available experimental information yields an improved decay scheme of ^{25}Si, which is compared to theoretical calculations and to the β^- decay of the mirror nucleus, ^{25}Na. A comparison between the mirror Gamow-Teller decays also provides an opportunity to investigate isospin asymmetry. A nonzero mirror asymmetry parameter implies abnormal nuclear structure, such as halo structure in the initial and/or final state. In view of the asymmetries reported in the nearby *sd*-shell nuclei ^{20}Mg–^{20}O [179, 180, 181, 182], ^{22}Si–^{22}O [183, 184], ^{24}Si–^{24}Al [185, 186, 187] ^{26}P–^{26}Na [188, 189], ^{27}S–^{27}Na [190, 191, 192, 193], it is desirable to extend this test to ^{25}Si and its mirror partner nucleus ^{25}Na [194, 195, 196].

22. Experimental Techniques

The experiment was conducted at the National Superconducting Cyclotron Laboratory (NSCL) in May 2018. The experimental procedure has been detailed in Ref. [197] and is briefly repeated here for completeness. A ^{36}Ar^{18+} primary beam was accelerated by the K500 and K1200 Coupled Cyclotron Facility to 150 MeV/nucleon at a beam current of $\sim$75 *p*nA. The secondary ^{25}Si beam was produced via the projectile fragmentation of the ^{36}Ar beam impinging on a 1363 mg/cm^2 thick ^{9}Be target and purified using the A1900 fragment separator [198]. The Gaseous Detector with Germanium Tagging (GADGET) [197], composed of the Proton Detector and the Segmented Germanium Array (SeGA) [199], has been built and successfully commissioned to measure the decays for the nuclei near the proton-drip line. In the current experiment, a total of 3×10^7 ^{25}Si ions were implanted into the gaseous Proton Detector with an average beam rate of approximately 1800 particles per second. The Proton Detector was filled with P10 gas mixture at a pressure of 780 Torr, which is ideally suited for low-energy proton detection because the background contributed by β particles was mitigated. The charged-particle measurement was carried out under a pulsed-beam mode, i.e., the beam ions were delivered for 500 ms, then the decays were detected during the 500-ms beam-off period. The Proton Detector was mounted at the center of SeGA, which consists of 16 high-purity germanium detectors arranged into two rings surrounding the Proton Detector. These two rings of eight detectors will be referred to as "upstream" and "downstream". The detection for the γ rays emitted from decays was done over both the beam on/off periods. The preamplifier signals from the Proton Detector and SeGA were read into Pixie-16 cards (16-Channel 250-MHz PXI Digital Processor) and processed by the NSCL digital data acquisition system [506].

23. Analysis

23.1. γ-ray energy and efficiency calibration

To create a cumulative γ-ray energy spectrum, the spectrum of each SeGA detector was linearly gain-matched run by run using room background lines at 1460.820 ± 0.005 and 2614.511 ± 0.010 keV from the β decays of ^{40}K [81] and ^{208}Tl [201], respectively. An exponentially modified Gaussian (EMG) function of the form

$$f(x;N,\mu,\sigma,\tau) = \frac{N}{2\tau}\exp\left[\frac{1}{2}\left(\frac{\sigma}{\tau}\right)^2 + \frac{x-\mu}{\tau}\right] \times \mathrm{erfc}\left[\frac{1}{\sqrt{2}}\left(\frac{\sigma}{\tau} + \frac{x-\mu}{\sigma}\right)\right], \tag{7}$$

was used to fit each β-delayed γ-ray line in the spectrum. The EMG is characterized by an exponential decay constant τ, width σ, mean μ, energy x, and area below the curve N. Also, a linear function is added to this formula to model the local background. Four ^{25}Si β-delayed γ-ray lines with known energies and the corresponding absolute intensities shown in brackets–451.7(5) keV [18.4(42)%], 493.3(7) keV [15.3(34)%], 944.9(5) keV [10.4(23)%], and 1612.4(5) keV [14.7(32)%] [178, 202, 203]–were observed with high statistics and used as energy calibration standards. The maximum values from the fits of these γ-ray lines were plotted against the standard energies to provide an internal energy calibration of each SeGA detector. In this paper, all the γ-ray energies are reported in the laboratory frame, and all the excitation energies are reported in the center-of-mass frame with recoil corrections applied. One of the 16 SeGA detectors malfunctioned during the experiment and three of the others displayed relatively poor resolutions, so these four detectors are excluded from the subsequent analysis. A cumulative spectrum

incorporating the other 12 SeGA detectors was generated for analysis. The characteristic resolution for the cumulative SeGA spectrum is 0.19% full width at half maximum at 1612 keV.

To reduce the systematic uncertainty associated with extrapolation, further energy calibration was applied by including four ^{25}Si($\beta p\gamma$)^{24}Mg lines known with very good precision at 1368.626(5), 2754.007(11), 2869.50(6), and 4237.96(6) keV as standards [204]. These γ rays are emitted from the recoiling ^{24}Mg after the β-delayed proton emission of ^{25}Si. Therefore, the γ-ray line shape is Doppler broadened, and the regular EMG function is not suited to fit the peak. To accurately extract information from each peak, we applied the Doppler broadening line shape analysis. The detailed procedure will be described in Sec. 23.4.

23.2. Proton energy and efficiency calibration

As detailed in Ref. [197], the anode plane of the Proton Detector is segmented into 13 readout pads, labeled A−M. The β-delayed proton spectrum is usually produced by event-level summing of the five central pads (A−E) and the eight surrounding pads (F−M) are usually used to veto the high-energy protons that escape the active volume and deposit only part of their energy in the active volume. In the current experiment, four veto pads (F, G, L, M) were not instrumented, so the resulting background caused by the escaping high-energy protons hindered the identification of low-energy protons. Instead, we could obtain the proton spectrum measured by three central pads (A+C+D) and used the other six neighboring pads (B, E, H, I, J, K) as veto triggers. The strong β-delayed proton peaks at 402, 1268, and 1924 keV were used for the energy calibration of the Proton Detector. We took a weighted average of the literature proton energies [173, 176, 177, 178] as calibration standards. The proton information in our paper is incomplete compared with other literature as our Proton Detector is not sensitive to protons above 2.4 MeV. Besides, the proton-detection efficiency simulated for full utilization of all 13 readout pads [197] cannot be used in this case. It is simpler and more accurate to determine the intensities for each proton branch by normalizing the literature relative intensities to the ^{25}Si($\beta p\gamma$)^{24}Mg intensities measured in this paper (Sec. 24.2).

23.3. Normalization

In Ref. [197], we investigated the longitudinal beam distribution via the proton drift time distribution, and the beam in the radial direction was estimated as a Gaussian beam with the transverse distribution determined based on the distribution of proton counts in different pads of the Proton Detector. The investigation showed that the ^{25}Si beam ions were mainly contained in the active volume of the Proton Detector. We modeled the Brownian motion of the ^{25}Si atoms using a Monte Carlo simulation. The diffusion of the ^{25}Si atoms is estimated to be less than 1 cm within four lifetimes, and there was very little drift of ^{25}Si ions to the cathode of the Proton Detector. The β-delayed γ rays and protons from subsequent decays were detected by the SeGA detectors and the Proton Detector, respectively. The geometry of our experimental setup and the beam spatial distribution were used as inputs for a GEANT4 [522, 523] Monte Carlo simulation to determine a γ-ray photopeak efficiency curve for the SeGA detectors. We then verified the simulated efficiency curve by using a ^{152}Eu calibration source [525] between 245 and 1408 keV and ^{23}Al data [156] up to 7801 keV. The source data were taken with the ^{152}Eu source placed at the center of SeGA before the Proton Detector was installed and the ^{23}Al($\beta\gamma$)^{23}Mg was measured using the same detection setup in a subsequent experiment in the same campaign [149]. Although the ^{152}Eu source was absolutely calibrated, our procedure for determining the absolute intensities of the γ rays only requires relative efficiencies. We extracted the γ-ray efficiency from both data and simulation, and the simulated efficiency is matched with the measured efficiency when scaled by a constant factor on the order of unity. The uncertainties associated with the scaling factors are determined to be 0.7% for γ-ray energies <1.4 MeV based on the ^{152}Eu source data and 4.2% for γ-ray energies >1.4 MeV based on the ^{23}Al data, which give a measure of the uncertainty on the relative efficiency. We then add a flat 2% uncertainty in the efficiencies at all energies to account for the $\gamma\gamma$ summing effect [526]. Ultimately, we adopt a conservative 3% uncertainty envelope for γ-ray energies <1.4 MeV and a 5% uncertainty envelope for γ-ray energies >1.4 MeV. The uncertainties associated with the relative efficiencies were propagated through the calculation of each γ-ray intensity.

We adopt an I_{gs} = 21.5(12)% β feeding for the ^{25}Al ground state based on our shell-model calculated I_{gs} = 20.9 and 22.2%. The difference between the two theoretical I_{gs} represents the uncertainty coming from the Hamiltonian (Sec. 24.6). We can perform the normalization by requiring the intensity of all decay paths sum to 100%:

$$I_{\beta p} + I_{\beta\gamma} + I_{\rm gs} = 100\%,$$
$$\frac{I_{\beta p\gamma}}{I_{\beta p}} = 59.0(5)\%, \tag{8}$$

where $I_{\beta p}$ is the total intensity of all ^{25}Si(βp)^{24}Mg transitions, and $I_{\beta\gamma}$ is the total intensity of all ^{25}Si($\beta\gamma$)^{25}Al transitions. The intensity of the ^{25}Si($\beta p\gamma$)^{24}Mg ($I_{\beta p\gamma}$) accounts for 59.0(5)% of the total ^{25}Si(βp)^{24}Mg intensity based on the previous β-delayed proton measurements [176, 177, 178]. The remainder of our normalization procedure is entirely based on the γ-ray intensities. Using the simulated relative efficiency and the number of counts in each peak extracted from the EMG fits yields the intensity for each γ ray. Multiple γ rays in one cascade are treated as one transition. Thus, we determine the total intensities of the β-delayed proton and β-delayed γ decays to be $I_{\beta\gamma}$ = 40.1(14)% and $I_{\beta p}$ = 38.3(15)%, respectively. These values can be converted into the β feedings to all the unbound ^{25}Al states $I_{\rm unb}$ = 39.3(15)% and all the bound ^{25}Al states $I_{\rm bnd}$ = 60.7(18)% when taking into account the weak γ-ray intensities originating from the unbound states (Sec. 24.3). Our values may be compared with the previous literature values of $I_{\rm unb}$ = 40.5(14)% [176], 37.7(15)% [177], and 35.2(12)% [178] and $I_{\rm bnd}$ = 58.7(13)% [176], 61.9(26)% [177], and 66(9)% [178].

23.4. Doppler broadening analysis

When a proton is emitted from a nucleus, the daughter nucleus will recoil with equal and opposite momentum as the ejected proton due to the conservation of momentum. If a γ ray is emitted while the nucleus is still recoiling, it will be Doppler shifted in the laboratory frame. For an ensemble of such events, the resulting γ-ray line shape in the measured energy spectrum will be Doppler broadened. In this experiment, we observed four γ-ray lines emitted from the ^{24}Mg recoiling in the gas after the β-delayed proton emission of ^{25}Si. Detailed Monte Carlo simulations have been developed to model the Doppler broadening. The results are then compared to the actual γ-ray data [526, 206, 207, 208, 209, 210]. The simulation takes into account the energy and relative intensity of each proton branch populating the ^{24}Mg excited state, the energy of the γ ray deexciting the ^{24}Mg excited state, the lifetime of the ^{24}Mg excited state, the stopping power of the implantation material (780-Torr P10 gas), and the response function of each SeGA detector.

Robertson *et al.* [177] and Thomas *et al.* [178] reported the most comprehensive ^{25}Si(βp)^{24}Mg assignments and they are generally in agreement. Hence, we adopted their proton energies and proton feeding intensities in the simulation. The stopping power of the recoiling ^{24}Mg in P10 gas is estimated as a function of energy using the code SRIM, which is expected to be accurate to within 10% [491]. The lifetimes for the three low-lying ^{24}Mg excited states at 1368, 4123, and 4238 keV have been precisely measured to be 1.92(9) ps, 31.7(3) fs, and 59.2(6) fs, respectively [204]. An isotropic distribution of γ rays with respect to the proton distribution is assumed in each simulation. Another input of the simulation is the intrinsic response function for each of the SeGA detectors. By fitting unbroadened β-delayed γ-ray peaks with the EMG function Eq. (1) at energies of 451.7(5), 493.3(7), 944.9(5), and 1612.4(5) keV [^{25}Si($\beta\gamma$)^{25}Al] [202] and 450.70(15), 1599(2), 2908(3), and 7801(2) keV [^{23}Al($\beta\gamma$)^{23}Mg] [211], the parameters τ and σ were characterized as a function of energy for each SeGA detector. Every detector has a different contribution to the total number of counts in the peak depending on its detection efficiency, and the simulation accounts for this by normalizing the number of counts simulated for each detector.

A linear function is adopted to model the local background and added to each simulated peak when compared to the actual data. Then, the simulation-data comparison can be done using the classical χ^2-minimization method. Because of the relatively low statistics collected in the present experiment compared to the ^{20}Mg($\beta p\gamma$)^{19}Ne experiment [526], the construction of a simulated peak shape follows the same method of Ref. [526] with one major change. Although least-squares based χ^2 statistics (e.g., Neyman's χ^2 or Pearson's χ^2) are widely used for this type of analysis, they do not always give reliable results for low-statistics data. An alternative method better suited for low-statistics analysis is to derive a χ^2 statistic from a Poisson maximum likelihood function [212, 213]. The "likelihood χ^2" is defined in the equation

$$\chi^2 = -2\ln\lambda = 2\sum_{i=1}^{N}\left[f(x_i,\theta) - y_i + y_i\ln\frac{y_i}{f(x_i,\theta)}\right] \tag{9}$$

where λ is the likelihood ratio, N is the number of bins, y_i is the number of counts in the ith bin of the measured spectrum, and $f(x_i, \theta)$ is the number of counts in the ith bin (bin center x_i) predicted by the simulation. The minimization of χ^2 is equivalent to the maximization of λ. The binned maximum likelihood method is known to miss the information with feature size smaller than the bin size of the spectrum. It is therefore necessary to use a fine binning for line-shape analysis. We used a 0.1-keV bin size for the γ-ray spectrum. The application of this likelihood ratio χ^2 method to the ^{25}Si$(\beta p\gamma)^{24}$Mg line-shape analysis is discussed in Sec. 24.2.

24. Results and Discussion

24.1. Half-life of ^{25}Si

The ^{25}Si half-life has been previously measured to be 225(6) ms [170], 218(4) ms [172], 232(15) ms [176], and 222.6(59) ms [177]. A weighted average of all previously published values gives $t_{1/2}$ = 221.1(28) ms. In Ref. [197], we have shown the decay curve of ^{25}Si by using the count rate of the 402-keV proton as a function of time during the decay period of the implant-decay cycle. Here, we further investigated the systematics to provide a half-life measurement. The ^{25}Si half-life is extracted by fitting the count rate of all the protons within 350−2400 keV recorded by the five central pads as a function of time elapsed since the beginning of each implant-decay cycle. The decay in the count rate is enhanced by diffusion of ^{25}Si out of the active volume. This effect is modeled by a Monte Carlo simulation of the Brownian motion of the ^{25}Si atoms. The effect of ^{25}Si losses due to diffusion out of the central pads is parametrized by a fourth degree polynomial $P_4(t - t_0)$ where t is the clock time within the cycle and t_0 is the beginning of the decay period of the cycle. The data are fit using the function

$$f(t; N, t_{1/2}, t_0, B) = Ne^{-\frac{\ln(2)(t-t_0)}{t_{1/2}}} P_4(t - t_0) + B, \tag{10}$$

where N is the initial count rate of protons at the beginning of the decay period of the cycle. We measured the background during the interval between each run and estimated the background level B to be 0.82(2) count/s. The systematic effect associated with the uncertainty on t_0 is estimated to be 0.05 ms, and the systematic effect associated with the fit range is estimated to be ±0.9 ms by varying t_0 and the fit range within reasonable values. The diffusion is estimated to decrease the decay lifetime by 1.8 ms. However, this assumes that the ^{25}Si is in the atomic form. In reality, it is plausible that Si atoms bond with hydrogen and carbon atoms that exist in the P10 mixture. As a result, the diffusion is expected to decrease in a nontrivial manner. We then estimate other systematic effects due to the diffusion by varying the initial ^{25}Si beam distribution in the volume and the gas pressure of the simulation. The total uncertainty associated with diffusion is determined to be $^{+0.3}_{-0.9}$ ms. Other effects, such as the trigger threshold, the time window for the trigger, and the contribution of the beam contaminants, are found to be negligible. The effects contributing to the uncertainty are summarized in Table 4. The final result is determined to be $t_{1/2} = 218.9 \pm 0.5(\text{stat})^{+0.9}_{-1.3}(\text{syst})$ ms, where the uncertainties are statistical and systematic, respectively. This value can be written as $t_{1/2} = 218.9^{+1.0}_{-1.4}$ ms with the statistical and systematic uncertainties added in quadrature. As can be seen from Fig. 37, our result is consistent with, and more precise than, all the literature values [170, 172, 176, 177]. We have reevaluated the half-life to be $t_{1/2} = 219.2^{+0.9}_{-1.2}$ ms by taking a weighted average of all published values.

Table 4: Uncertainty budget for the measured half-life of ^{25}Si.

Source of uncertainty	Uncertainty (ms)
Statistics	±0.5
Diffusion of ^{25}Si atoms	$^{+0.3}_{-0.9}$
Starting time of decay period	±0.05
Fit range	±0.9
Trigger threshold	negligible
Event window	negligible
Contaminants	negligible
Total	$^{+1.0}_{-1.4}$

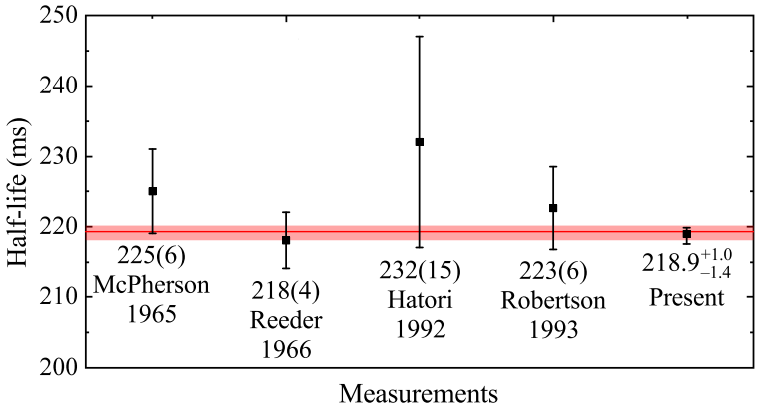

Figure 37: Half-life of ^{25}Si measured in the present paper compared with the values previously measured by McPherson and Hardy [170], Reeder *et al*. [172], Hatori *et al*. [176], and Robertson *et al*. [177]. The weighed average of all published values is indicated by the solid red band.

24.2. $^{25}Si(\beta p\gamma)^{24}Mg$

A 1369-keV γ ray originating from the first excited state of ^{24}Mg was observed in the previous ^{25}Si β-decay measurements [175, 178]. In this paper, we observed three additional ^{24}Mg γ-ray lines following ^{25}Si β-delayed proton emissions. Figure 38 shows four γ-ray lines at 1369, 2754, 2870, and 4238 keV, corresponding to the deexcitations from the three lowest-lying ^{24}Mg excited states populated by ^{25}Si(βp). The placement of γ rays is also verified using $\gamma\gamma$ coincidences. To remove the disturbance from a room background γ-ray line near the 1369-keV peak, the Proton-Detector-gated γ-ray spectrum was generated for the 1369-keV peak. This coincidence gate is set by any signal above 15 keV recorded by the Proton Detector, and all the protons emitted from decays essentially have equal probabilities to trigger a 10-μs backward time window and select the coincident γ-ray signals. Therefore, the Proton-Detector gate only reduces the number of counts in the 1369-keV γ-ray line and does not alter its relative proton feedings and the resulting peak shape. Distributions of χ^2 values from the simulated and experimental spectra were constructed for each peak. An example of the χ^2 distribution of the 1369-keV γ-ray line is shown in Fig. 39, where the γ-ray centroid is considered a free parameter for χ^2 minimization. The best-fit peak centroid and integral as well as their statistical uncertainties ($\chi^2_{\rm min}$ + 1) were taken from a quadratic polynomial fit of the χ^2 distribution. We obtained the reduced χ^2 value (χ^2_ν) by dividing the χ^2 value by the number of degrees of freedom. Each statistical uncertainty is then inflated by the square root of the χ^2_ν value for the corresponding fit. We are able to achieve a minimum in the χ^2_ν distribution close to 1 for all four ^{24}Mg γ-ray lines, using the proton energies and the relative proton feeding intensities measured by Thomas *et al*. [178]. The resultant best fits from the χ^2 minimization are shown in Fig. 38. Replacing the proton energies and the relative proton feeding intensities with the values measured by Robertson *et al*. [177] in our simulation yields very similar χ^2 values. Our Doppler broadening analysis does not have sufficient sensitivity to distinguish discrepancies in the intensities of weak proton branches in this relatively low-statistics case. Nevertheless, their proton inputs both fit the γ-ray data equally well, indicating that both of the previous measurements placed the majority of the proton intensity in the decay scheme correctly.

The γ-ray intensities per ^{25}Si β decay ($I_{\beta p\gamma}$) are derived from the integral of each fit corrected for the SeGA efficiency and normalized to the aforementioned total γ-ray intensity. The lifetime and the fit parameters τ and σ are varied by their one standard deviation uncertainty and the stopping power is varied up and down by 50% to investigate the systematic uncertainty. The uncertainties associated with the aforementioned simulated efficiency, the stopping power of the P10 gas, the lifetime of ^{24}Mg states, the proton feedings, the parameters τ and σ, and the deviation caused by adopting proton energies and intensities from different literature [177, 178] were added in quadrature to obtain the total systematic uncertainty. Adding the systematic uncertainties with the statistical uncertainty in quadrature yields the total uncertainty for each γ-ray intensity.

The ^{24}Al($\beta\gamma$)^{24}Mg decay from the beam contaminant ^{24}Al might yield a small portion of counts in the ^{25}Si($\beta p\gamma$)^{24}Mg peaks as they both produce ^{24}Mg excited states. The ^{24}Al($\beta\gamma$)^{24}Mg lines are unbroadened and should also be included in the Doppler broadening simulation. A 7070-keV γ-ray peak is identified in the spectrum, and it

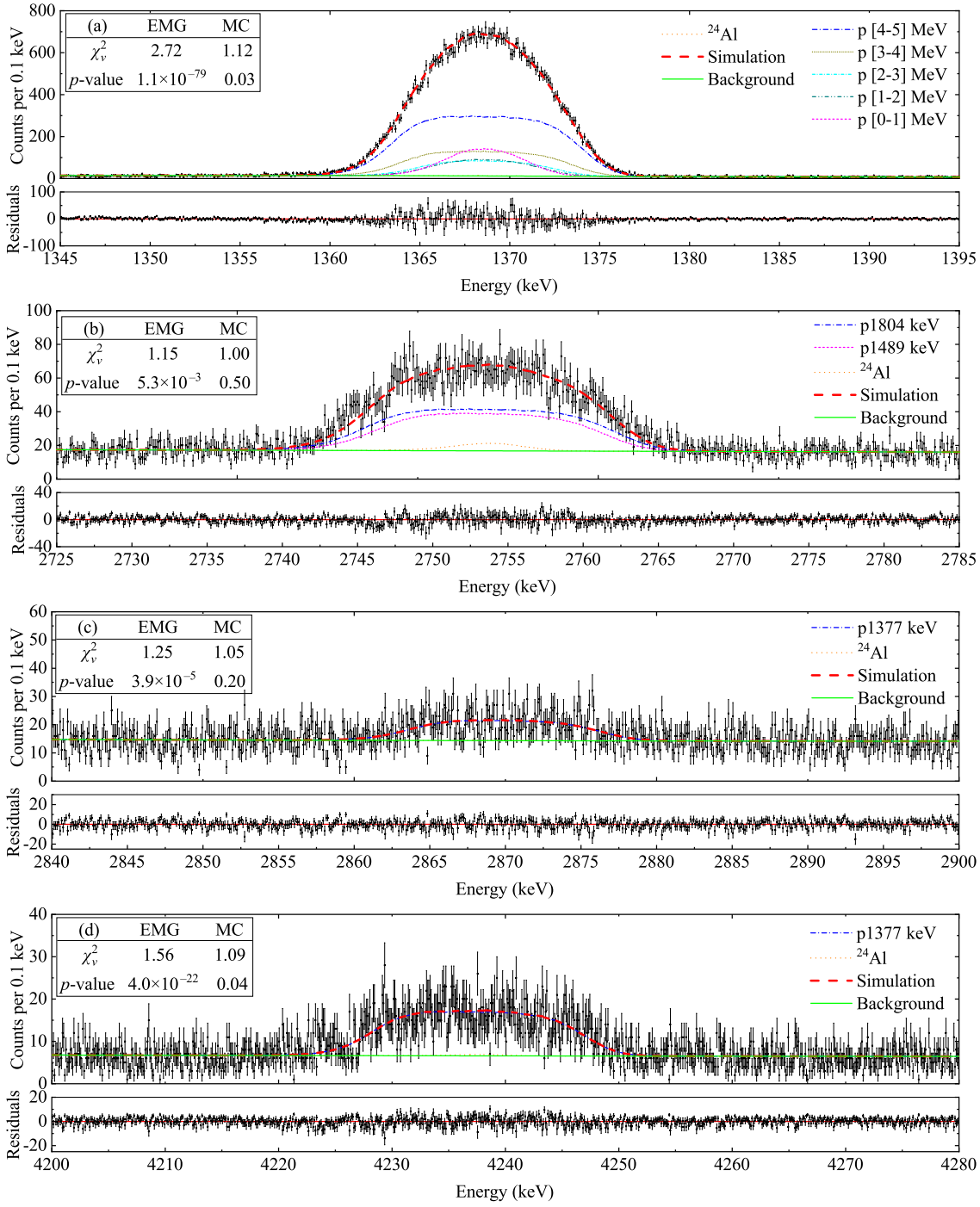

Figure 38: γ-ray spectrum measured by the SeGA detectors magnified at (a) 1369 keV, (b) 2754 keV, (c) 2870 keV, and (d) 4238 keV. We show the raw spectrum for panel (b), (c), and (d) and the Proton-Detector-gated spectrum for panel (a) to suppress the contribution from a room background line near the 1369-keV peak. Four upper panels: The Monte Carlo (MC) simulations of the (a) 1369-keV, (b) 2754-keV, (c) 2870-keV, and (d) 4238-keV γ-ray peaks are produced by using lifetimes adopted from the data evaluation [204] and the proton energies and relative proton feeding intensities measured by Thomas *et al.* [178]. The black dots represent the data, the solid green lines denote the background model, the dashed red lines denote the simulated line shapes including different contributions of proton feedings. Each proton feeding is represented by a colored line, and in the legend it is labeled with a letter p followed by its center-of-mass energy. The dotted orange lines denote the small unbroadened contribution of the contaminant decay ^{24}Al($\beta\gamma$)^{24}Mg. Four lower panels: The residual plots show the data subtracted from the simulation. Compared with a regular EMG fit of each peak, our Doppler broadening analysis substantially improved the χ^2_ν and p values, which are shown in the top-left corner of each panel.

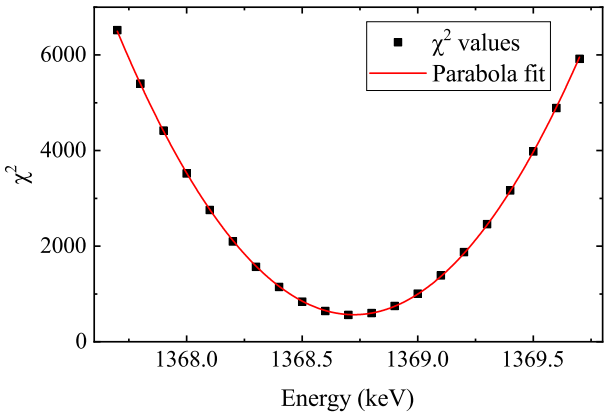

Figure 39: χ^2 distribution of the 1368.672(5)-keV γ-ray line as a function of input γ-ray energy (black squares). A quadratic polynomial fit (solid red line) was used to determine the best-fit energy and uncertainty.

can only be produced by ^{24}Al($\beta\gamma$)^{24}Mg. Based on the number of counts and intensity of the 7070-keV γ ray [214], we estimate that the beam contaminant ^{24}Al comprised 0.13(4)% of the implanted beam ions. Thus, the number of counts in the 1369-, 2754-, 2870-, and 4238-keV γ-ray peaks contributed by ^{24}Al($\beta\gamma$)^{24}Mg are quantified based on the SeGA efficiency at these energies and their known intensities relative to the 7070-keV γ-ray peak [204, 214].

For the 4238-keV ^{24}Mg state, a further correction is required. Since the 4238-keV state has two γ decay paths to the ground state, the 2870-1369 cascade that does not directly decay to the ground state will yield a small portion of counts in the 4238-keV peak due to summing in a single SeGA detector. The number of counts in the 4238-keV peak due to the summing effect is calculated from the number of counts in the 2870-keV peak and the SeGA efficiency for a 1369-keV γ ray. The loss of photopeak counts for the 1369- and 2870-keV γ rays due to the summing effect is corrected likewise. After correcting the contaminant counts and the summing counts for the ^{25}Si($\beta p\gamma$)^{24}Mg peak integral, we determine the final ^{25}Si($\beta p\gamma$)^{24}Mg intensities and γ-ray branching ratios (see Table 5).

The two γ rays emitted from the 4238.24(3)-keV ^{24}Mg state at 4237.96(6) and 2869.50(6) keV are measured to have branching ratios of 75(3) and 25(3)%, respectively. The branching ratios are in agreement with the evaluated values of 78.2(10) and 21.8(10)% [215], which took a weighed average of the results in Refs. [214, 216] with inflated uncertainty. We obtain the β-delayed proton feedings to the 1369-, 4123-, 4238-keV ^{24}Mg states per ^{25}Si decay of $I_{\beta p}$ = 21.0(9), 0.94(6), and 0.59(3)%, respectively, by adding all γ-ray decays originating from each state and subtracting feeding from higher-lying states. The proton feeding to the ^{24}Mg ground state accounts for 41.0(5)% of the total ^{25}Si(βp)^{24}Mg intensity [176, 177, 178]. Combining this branching ratio and our measured ^{25}Si($\beta p\gamma$)^{24}Mg intensities yields an $I_{\beta p}$ = 15.7(7)% for the ^{24}Mg ground state. Thomas *et al.* [178] reported $I_{\beta p}$ = 14.3(10), 18.7(15), 1.06(20), and 0.41(12)% and Robertson *et al.* [177] reported $I_{\beta p}$ = 14.96(5), 20.27(5), 1.105(9), and 0.378(8)% for the ^{24}Mg ground state and excited states at 1369, 4123, and 4238 keV, respectively. The consistency of intensities further confirms the literature interpretation of ^{25}Si β-delayed proton branches.

24.3. ^{25}Si($\beta\gamma$)^{25}Al

Figure 40 shows the full γ-ray spectrum measured by the SeGA detectors. The Proton-Detector-coincident γ-ray spectrum is also shown for comparison. This coincidence gate reduced the statistics for the ^{25}Si($\beta p\gamma$)^{24}Mg peaks approximately by a factor of 4, which is related to the implant-decay cycle and the trigger efficiencies of the Proton Detector for protons. As can be seen from Fig. 40, the relative statistics for the ^{25}Si($\beta\gamma$)^{25}Al peaks are even lower. This can be understood by considering the low trigger efficiency of the Proton Detector for β particles. The coincidence condition suppresses the room background lines substantially and helps verify the origins of the γ-ray lines. Eight new β-delayed γ rays are clearly observed in the β-decay of ^{25}Si, and the results are summarized in Table 6. The uncertainty associated with the energy calibration of the SeGA detector and the statistical uncertainty from peak fitting were added in quadrature to obtain the total uncertainty of each γ ray. For all the ^{25}Si($\beta\gamma$)^{25}Al peaks reported in this paper, the dominant source of the γ-ray energy uncertainty is the statistical uncertainty. The absolute intensity

Table 5: ^{25}Si($\beta p\gamma$)^{24}Mg measured in the present paper. The ^{24}Mg ground state and three lowest-lying excited states are observed to be populated by ^{25}Si(βp). The well-known ^{24}Mg excitation energies (column 1) and γ-ray energies (column 3) are adopted from the data evaluation [204]. Column 2 reports the measured ^{25}Si(βp)-feeding intensities to each ^{24}Mg state. Column 4 reports the intensity of each γ-ray transition per ^{25}Si decay. Column 5 reports the γ-ray branching ratios for each ^{24}Mg excited state.

E_x (keV) [204]	$I_{\beta p}$ (%)	E_γ (keV) [204]	$I_{\beta p\gamma}$ (%)	B.R. (%)
0	15.7(7)	–	–	–
1368.672(5)	21.0(9)	1368.626(5)	22.1(9)	100
4122.889(12)	0.94(6)	2754.007(11)	0.94(6)	100
4238.24(3)	0.59(3)	2869.50(6)	0.147(14)	25(3)
		4237.96(6)	0.44(3)	75(3)

of each γ ray in the β decay of ^{25}Si is determined using the number of counts in the γ-ray peak, the γ-ray detection efficiency of the SeGA detectors, and the aforementioned total γ-ray intensity. A further correction for the summing effect is applied whenever necessary. The statistical uncertainty associated with the peak area is obtained from the peak-fitting procedure. The statistical uncertainty and the systematic uncertainties associated with the SeGA efficiency simulation are propagated through the calculation of each γ-ray intensity.

The 452- and 1612-keV γ rays correspond to the 100% transitions from the 452- and 1612-keV states to the ^{25}Al ground state, respectively. The intensity of the 1612-keV γ ray is corrected for the contribution of a nearby 1611.7-keV β-delayed γ ray of ^{25}Al [202, 217]. There are two γ rays which are emitted from the 945-keV state at 493 and 945 keV, and they are expected to have branching ratios of 61(4) and 39(4)%, respectively [203, 202]. We have improved these branching ratios to be 58.4(16) and 41.6(16)% in this paper. The 1789-keV state is observed to be populated by the β decay of ^{25}Si for the first time. There are three γ rays which are emitted from this state with energies of 844.6(7), 1337.4(16), and 1789.4(9) keV, and their branching ratios are measured to be 44(3), 30.6(20), and 25.2(19)%, respectively. The measured energies are consistent with the evaluated literature values of 844.6(7), 1337.8(7), and 1789.4(5) keV [202]. The three branching ratios are consistent with the literature values of 39.6(21), 36.1(18), and 23.3(10)%, which are the weighted averages of five previous measurements with inflated uncertainty [203, 218, 219, 220, 221]. The excitation energy is determined to be 1789.2(6) keV by combining the three γ-ray energies. This value is of comparable precision to the excitation energy of 1789.5(5) keV reported in the data evaluation [202], and we have reevaluated the excitation energy to be 1789.4(4) keV by taking a weighted average of the two values.

In all the previous ^{25}Si decay measurements [169, 170, 171, 172, 173, 174, 175, 176, 177, 178], the proton-unbound states in ^{25}Al were observed to decay only by proton emission. For the first time, we have observed the β-delayed γ rays through two unbound ^{25}Al states at 2673 and 7902 keV.

There are four known γ rays which are emitted from the 2673-keV state at 883.8(8), 1728.3(8), 2221.5(8), 2673.1(6) keV [202], and they are expected to have branching ratios of 42.8(8), 0.5(2), 31.4(7), and 25.3(5)%, respectively [222]. We have observed three γ-ray branches from this state. As can be seen from Table 6, we have measured their energies and branching ratios to be 883.8(6) keV [37(5)%], 2221.4(18) keV [36(4)%], and 2673.6(6) keV [26(3)%], respectively, which agree with the literature values [202, 222] at the 2σ level. However, our sensitivity does not allow us to see the weakest 1728.3(8)-keV γ ray from this state. The excitation energy is obtained to be 2673.4(5) keV from the three γ-ray energies. Combining our result with the excitation energy of 2673.3(6) keV from the data evaluation [202] yields a weighted average of 2673.4(4) keV.

The $5/2^+$ isobaric analog state (IAS) with isospin $T = 3/2$ in ^{25}Al is predicted to decay by 36 or 37 γ-ray branches by our shell-model calculations using the USDC or USDI Hamiltonian, respectively. The three most intense γ-ray branches at 6288(2), 6955(2), and 7900(2) keV account for 92.4(15)% of its total theoretical γ-ray branch. Their branching ratios measured by a ^{24}Mg$(p,\gamma)^{25}$Al reaction experiment [202, 223] are normalized to be 34(3), 12.0(19), and 46(3)%, respectively. A theoretical percentage of 80.7(13)% is used to normalize the branching ratios for the two γ rays at 6289(3) and 7902(3) keV observed in our work. Their branching ratios are determined to be 36(10) and 45(10)%, respectively, in agreement with the previous measurement [223]. The highest-energy γ ray at 7902(3) keV is assigned as the deexcitation from the IAS to the ground state of ^{25}Al. Its single escape and double escape peaks are also observed, and the excitation energy of the IAS is determined to be 7903(2) keV by combining the full photopeak

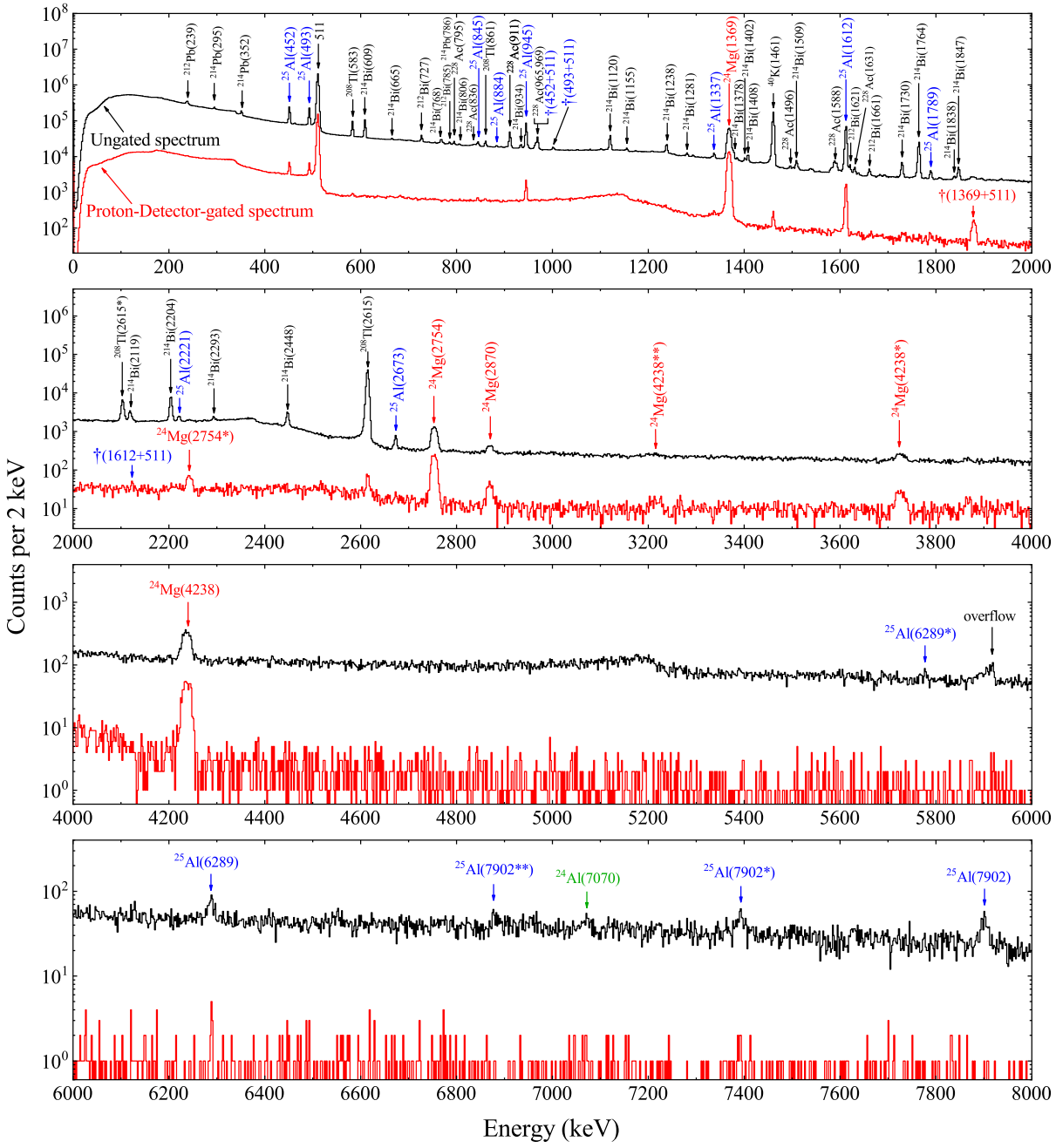

Figure 40: γ-ray spectrum (upper; black) measured by the SeGA detectors showing the assignments for the photopeaks used to construct the ^{25}Si decay scheme as well as those from room background. To reduce the room background contribution, a Proton-Detector-coincident γ-ray spectrum (lower; red) is produced by requiring coincidences with particle signals from the Proton Detector. Each photopeak is labeled by the emitting nucleus and its energy rounded to the closest integer in units of keV. Peaks labeled with one or two asterisks (*) correspond to single and double escape peaks, respectively. Peaks labeled with a single dagger (†) are sum peaks with the summation noted. The bump at ~5910 keV is caused by the overflow of one detector with unusual gain.

Table 6: Results from the ^{25}Si($\beta\gamma$)^{25}Al and ^{25}Si(βp)^{24}Mg decays obtained in the present paper. Columns 1−3 report the spin and parity (J_i^π), excitation energies (E_i), and β-feeding intensities (I_β) of each ^{25}Al level populated by the β decay of ^{25}Si, respectively. Columns 4−7 report the excitation energies of the final states populated by γ-ray transitions (E_f) from each ^{25}Al state, the laboratory frame energies of each γ-ray branch (E_γ), relative γ-ray branching ratios (B.R.), and γ-ray intensities per ^{25}Si β decay (I_γ), respectively. Columns 8−10 report the excitation energies (E_f) of the ^{24}Mg states fed by proton emissions from each ^{25}Al state, the energies of the emitted protons in the center-of-mass frame [E_p(c.m.)], and proton intensities (I_p) per ^{25}Si β decay, respectively.

			γ-ray transition				Proton emission		
J_i^π [202]	E_i (keV)	I_β (%)[3]	E_f (keV)	E_γ (keV)	B.R. (%)	I_γ (%)	E_f (keV)	E_p(c.m.) (keV)	I_p (%)[16]
$5/2^+$	0	21.5(12)[4]							
$1/2^+$	451.7(5)[1]	–	0	451.7(5)[1]	100	15.0(6)			
$3/2^+$	944.9(5)[1]	22.6(7)	452	493.3(7)[1]	58.4(16)	13.6(5)			
			0	944.9(5)[1]	41.6(16)	9.7(4)			
$(7/2)^+$	1612.5(5)[1]	15.2(9)	0	1612.4(5)[1]	100	15.3(9)			
$5/2^+$	1789.4(4)	1.46(7)	945	844.6(7)	44(3)	0.76(4)			
			452	1337.4(16)	30.6(20)	0.52(3)			
			0	1789.4(9)	25.2(19)	0.43(3)			
$3/2^+$	2673.4(4)	6.8(15)	1789	883.8(6)	37(5)	0.26(3)	0	402.0(9)[6]	6.1(15)[6]
			945	1728.3(8)[1]	0.5(2)[1]	–[5]			
			452	2221.4(18)	36(4)	0.25(3)			
			0	2673.6(6)	26(3)	0.184(17)			
$5/2^+$	3859.1(8)[1]	0.30(16)	–	–	–	–	0	1584(3)[7]	0.30(16)[7]
$3/2^+$	4192(4)[1]	3.1(7)	–	–	–	–	1369	554(10)[8]	0.49(25)[8]
							0	1924.3(20)[7]	2.6(7)[7]
$5/2^+$	4582(2)[1]	3.2(5)	–	–	–	–	1369	943.7(11)[7]	1.7(5)[7]
							0	2310.0(9)[7]	1.5(3)[7]
$(7/2)^+$	4906(4)[1]	0.45(22)	–	–	–	–	1369	1268(5)[9]	0.41(22)[9]
							0	2632(10)[10]	0.048(10)[10]
$(3/2, 5/2, 7/2)^+$	5597(6)[1]	0.5(3)	–	–	–	–	0	3327(4)[7]	0.5(3)[7]
$(3/2, 5/2, 7/2)^+$	5804(4)[1]	1.7(4)	–	–	–	–	1369	2164(3)[7]	1.7(4)[7]
–	6063(7)[1]	0.040(11)	–	–	–	–	1369	2453(25)[11]	0.040(11)[11]
$(3/2, 5/2, 7/2)^+$	6170(2)[1]	0.4(3)	–	–	–	–	1369	2486(25)[11]	0.10(3)[11]
							0	3896(8)[6]	0.3(3)[6]
$5/2^+$	6650(5)[1]	0.42(25)	–	–	–	–	1369	3006(11)[7]	0.42(25)[7]
$(3/2, 5/2, 7/2)^+$	6877(7)[1]	0.42(16)	–	–	–	–	1369	3236(6)[7]	0.42(16)[7]
$3/2^+$	6909(10)[1]	0.035(11)	–	–	–	–	0	4614(9)[10]	0.035(11)[10]
$3/2^+$	7118(5)[1]	4.8(16)	–	–	–	–	1369	3464(3)[7]	3.6(15)[7]
							0	4845(4)[7]	1.1(8)[7]
$5/2^+$	7240(3)[1]	1.3(5)	–	–	–	–	4238	724(4)[12]	0.036(15)[12]
							1369	3606(4)[7]	1.0(5)[7]
							0	4980(4)[7]	0.28(23)[7]
$(7/2)^+$	7422(5)[1]	0.16(6)	–	–	–	–	4123	1037(16)[13]	0.16(6)[13]
$(3/2, 5/2, 7/2)^+$	7646[1]	0.23(14)	–	–	–	–	0	5382(11)[7]	0.23(14)[7]
–	7819(20)[1]	0.32(9)	–	–	–	–	0	5549(15)[11]	0.32(9)[11]
$5/2^+$	7902.0(14)	13.4(16)	1612	6289(3)	36(10)	0.086(20)	4238	1380(5)[9]	0.38(14)[9]
			945	6955(2)[1]	<15[5]	<0.037[5]	4123	1492(6)[9]	0.26(13)[9]
			0	7902(3)	45(10)	0.110(19)	1369	4257(3)[7]	10.3(14)[7]
							0	5628.8(15)[7]	2.2(6)[7]
–	7936(20)[1]	0.45(13)	–	–	–	–	1369	4345(17)[14]	0.45(13)[14]
$(3/2, 5/2, 7/2)^+$	8186(3)[1]	1.0(4)	–	–	–	–	4238	1684(12)[13]	0.18(10)[13]
							4123	1794(3)[7]	0.51(19)[7]
							1369	4551(5)[7]	0.3(3)[7]
$(3/2, 5/2, 7/2)^+$	9073(7)[1]	0.13(10)	–	–	–	–	0	6798(5)[15]	0.13(10)[15]
–	9275(25)[2]	0.0127(17)	–	–	–	–	0	7000(25)[2]	0.0127(17)[2]
–	9415(30)[2]	0.0127(17)	–	–	–	–	0	7141(30)[2]	0.0127(17)[2]

energy and escape-peak energies. This value is of comparable precision to the excitation energy of 7901(2) keV reported in the data evaluation [202], and we have reevaluated the excitation energy of the IAS to be 7902.0(14) keV by taking a weighted average of the two values. The weakest 6955-keV γ-ray line is less than 3σ above the background level in our spectrum, and we estimate the 90% confidence upper limit for its branching ratio to be <15%, in agreement with the literature value of 12.0(19)% [202, 223].

24.4. $^{25}Si(\beta p)^{24}Mg$

The β-delayed proton spectrum of ^{25}Si is shown in Fig. 41. The event-level summing of three central pads (A+C+D) and an individual spectrum for pad A are shown for comparison. The single pad spectrum is generated with anticoincidence cuts on all other pads, resulting in a lower background and a fast-declining efficiency as a function of proton energy. Robertson *et al.* [177] observed 13 proton peaks below 2310 keV. Hatori *et al.* [176] did not observe six of them, and Thomas *et al.* [178] did not observe two of them at 1037 and 1684 keV. In the present work, all 13 known proton peaks below 2310 keV have been observed. We have reevaluated the proton energies by taking a weighted average of available literature proton energies with inflated uncertainty. The proton intensities are reevaluated by taking a weighted average of available literature proton relative intensities and then normalized to the ^{25}Si($\beta p\gamma$)^{24}Mg intensities determined in Sec. 24.2. A total of 34 proton energies and intensities are evaluated and listed in Table 6. The uncertainties of proton intensities reported by Robertson *et al.* [177] were unrealistically small [168], and therefore, we take an unweighted average of literature relative intensities and assign an uncertainty that covers all literature central values. For the three proton emissions at 2453, 2486, and 5549 keV only observed by Robertson *et al.* [177], the uncertainties evaluated in this way become zero. Hence, we extract the residuals between the averaged literature relative intensities and those measured by Robertson *et al.* [177] based on all other proton emissions. We derive a standard deviation of all the residuals, and this standard deviation is then factored into the uncertainties of the intensities for the 2453-, 2486-, and 5549-keV protons. As shown in Fig. 41, the β-particle background in our proton spectrum is suppressed to as low as 100 keV, enabling the clear identification of a new proton peak at 724(4) keV. We derive a detection efficiency curve for all other protons based on the number of counts in each peak observed in the proton spectrum and its corresponding intensity. We then interpolate the efficiency at 724 keV and determine the intensity for the 724-keV proton emission to be 0.036(15)%.

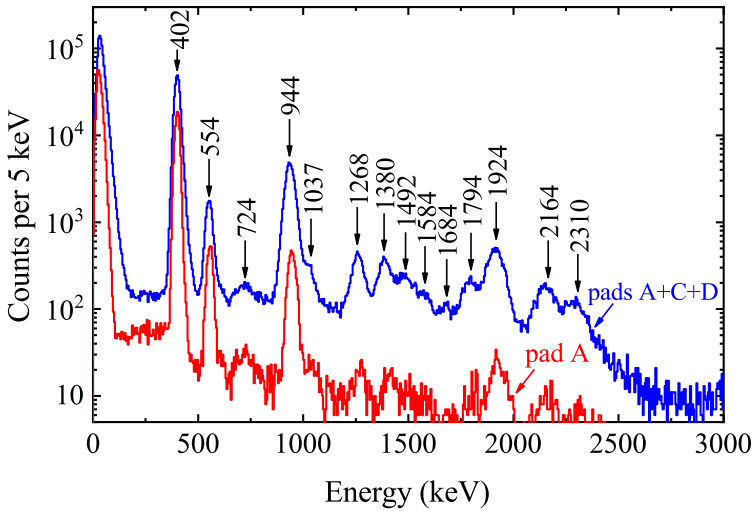

Figure 41: Proton spectra measured by three central pads A+C+D (upper; blue) and central pad A (lower; red). Each proton peak from the β-delayed proton decay of ^{25}Si is labeled with its center-of-mass energy rounded to the closest integer in units of keV.

24.5. Proton-γ coincidences and decay scheme

In order to reliably construct the decay scheme, it is desirable to conduct a $p\gamma$ coincidence analysis. Only two previous measurements showed a handful of $p\gamma$ coincidences. García *et al.* reported the coincidences between

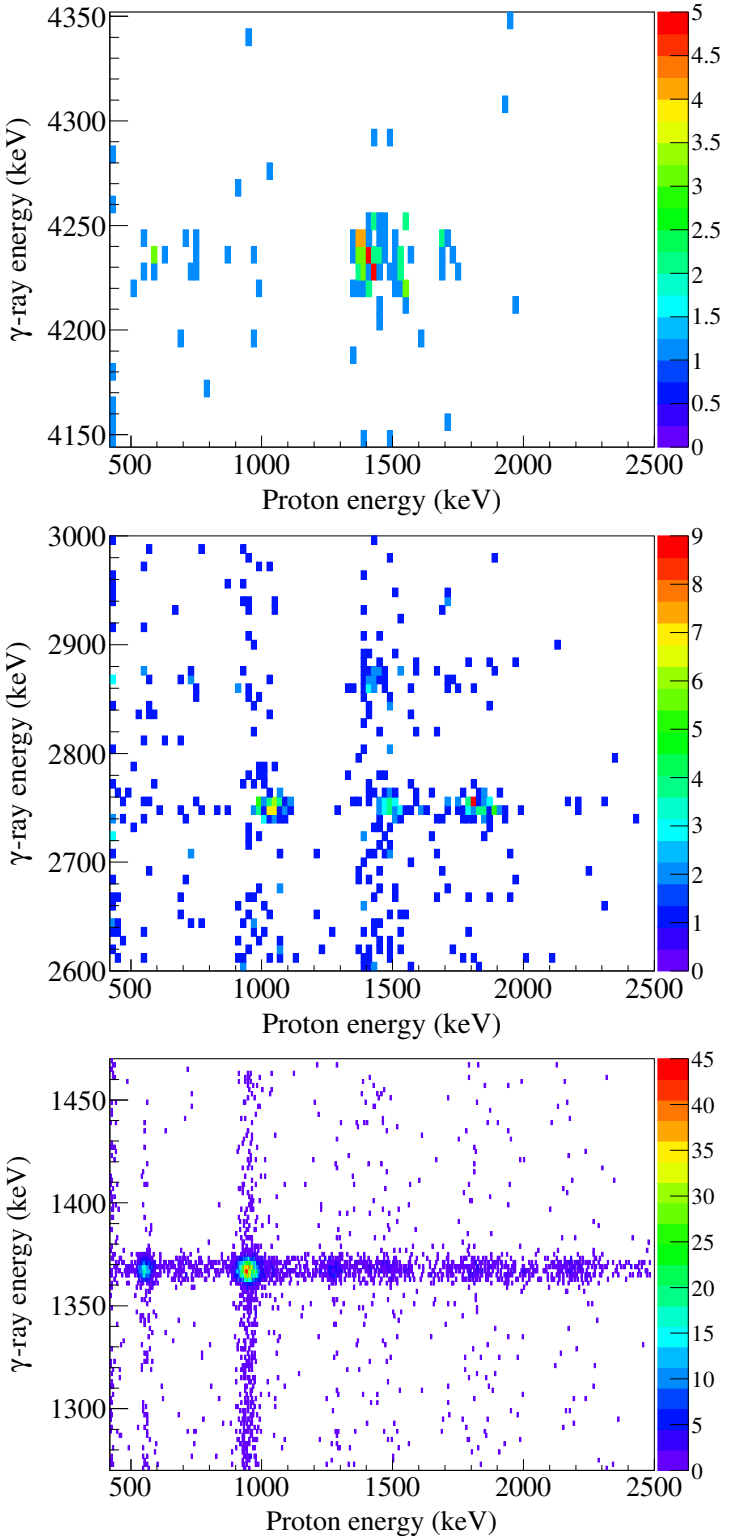

Figure 42: Coincidence spectrum between the Proton Detector and SeGA detection for ^{25}Si decay. The γ-ray spectrum is magnified at 4238 keV (top panel), 2754 and 2870 keV (middle panel), and 1369 keV (bottom panel), corresponding to the four γ rays originating from the three lowest-lying ^{24}Mg states.

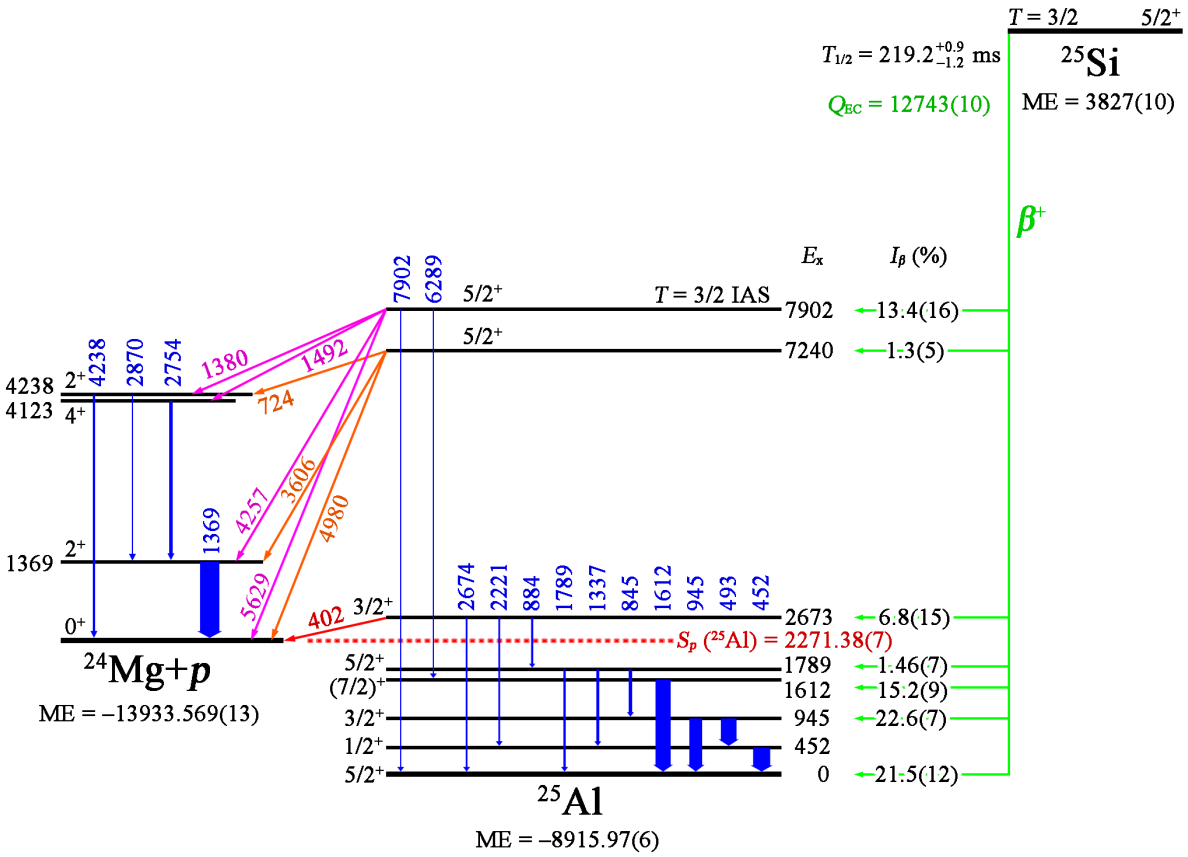

Figure 43: Simplified decay scheme of ^{25}Si. The mass excesses, separation energies, Q values, spins, and parities are adopted from the data evaluations [202, 204, 230]. The half-life is the weighted average of Refs. [170, 172, 176, 177] and the present paper. The γ-ray energies and the excitation energies deduced from these γ-ray energies are rounded to the nearest keV. Each γ-ray transition is denoted by a vertical arrow followed by its γ-ray energy, and the corresponding γ-ray transition intensity is denoted by the thicknesses of the arrow. Each β-decay transition is depicted by an arrow on the right side of the figure followed by its feeding intensity. The 2673- and 7902-keV ^{25}Al states are observed to decay by both proton and γ-ray emissions. The newly observed 724-keV proton is emitted from the 7240-keV ^{25}Al state. Each proton transition is denoted by an arrow between its initial and final states labeled alongside by its center-of-mass energy. For the sake of brevity, we omit other unbound ^{25}Al states. All the energies and masses are given in units of keV. See Table 6 for details.

Table 7: Coincidence matrix of the protons and γ rays measured in the β decay of ^{25}Si. The first row corresponds to the γ-ray energy on which the gate is set. The following rows indicate the protons observed in the gated spectrum. Protons observed in coincidence are indicated with a checkmark (✓) if the signal is statistically significant. All the energies are rounded to the closest integer and are given in units of keV.

	1369	2754	2870	4238
402				
554	✓			
724			✓	✓
944	✓			
1037	✓	✓		
1268	✓			
1380	✓		✓	✓
1492	✓	✓		
1584				
1684			✓	✓
1794	✓	✓		
1924				
2164	✓			
2310				

the 1369-keV γ ray and 3464-, 3606-, and 4257-keV protons [175]. Thomas *et al.* confirmed the 4257-1369 $p\gamma$ coincidence [178]. In the present work, many more $p\gamma$ coincidences have been directly observed. Figure 42 shows three regions of the two-dimensional coincidence spectrum between the protons and γ rays from ^{25}Si decay. The protons and γ rays detected in coincidence are summarized in Table 7 in the form of a coincidence matrix.

The newly identified 724-keV proton is observed in coincidence with the 2870- and 4238-keV γ rays. Hence, we assign it as a proton transition to the 4238-keV excited state of ^{24}Mg and obtain an excitation energy of E_x = 7234(4) keV for its proton-emitting state in ^{25}Al. The excitation energy is consistent with a $5/2^+$ proton-emitting state, which was previously measured to be 7240(7) keV [224], 7240(3) keV [225], and 7239(5) keV [226], 7243(12) keV [173], 7248(5) keV [176], 7245(8) keV [177], and 7255(7) keV [178], respectively. A decay width of 19(4) keV was reported in a polarized proton scattering experiment [225], which explains the broad peak shape at 724 keV observed in our proton spectrum. Previous ^{25}Si decay experiments [173, 176, 177, 178] observed two proton peaks at 3606 and 4980 keV, corresponding to the proton transitions from this state to the first excited state and ground state of ^{24}Mg, respectively. Our Proton Detector is not sensitive to those high-energy protons. Hence, we have determined the I_p = 1.0(5)% and 0.28(23)% for the 3606- and 4980-keV proton branches, respectively, based on the relative proton intensities measured in previous ^{25}Si decay experiments [173, 176, 177, 178] and the aforementioned proton feedings to each ^{24}Mg state (Table 5). No γ-ray branches populating or deexciting the 7240-keV state have been observed; therefore, the β feeding of the 7240-keV state is determined by adding up the intensities of the three proton branches from this state.

The γ-ray transitions are placed in the decay scheme shown in Fig. 43 based on the known level scheme in the database [202, 204], as well as including consideration of spin and parity selection rules and the γ-ray energy relationships. The level scheme is also verified using $\gamma\gamma$ coincidences. Except for the $\gamma\gamma$ coincidences associated with the two relatively weak γ rays originating from the IAS, all the expected $\gamma\gamma$ coincidences between other γ-ray transitions are observed in our paper. All the bound states of ^{25}Al are observed to be populated in the β decay of ^{25}Si. The β-feeding intensity to a ^{25}Al bound state is determined by subtracting the intensity of the γ rays feeding this level from the intensity of the γ rays deexciting this level. The feeding of the first excited state of ^{25}Al with $J^\pi = 1/2^+$ is consistent with its population by $\beta\gamma$ decay rather than directly by a second-forbidden β transition. It is possible that there exist weak, unobserved γ feedings from high-lying states, and the apparent β feedings for low-lying states are thus higher than the true β feedings due to the pandemonium effect [227]. We have assessed the extent of this effect based on the shell-model calculations, and the unobserved γ feedings from high-lying states to each low-lying state are expected to be negligible ($<10^{-4}$) due to the dominance of proton emission. The β-feeding intensity to a ^{25}Al unbound state is determined by adding up the intensities of the proton and γ-ray branches from this state. The

Table 8: Comparison of the mirror transitions in ^{25}Si and ^{25}Na β decays. Column 1 lists the excitation energies of each ^{25}Al state. Columns 2 and 3 report the log ft and B(GT) values for the each ^{25}Si β transition. Column 4 shows the J^π assignments [202]. Columns 5−7 list the results of the mirror ^{25}Na β-decay transitions. The mirror-asymmetry parameters δ are reported in the last column. The USDC and USDI shell-model calculated results for both ^{25}Si and ^{25}Na decays are shown for comparison.

^{25}Si→^{25}Al Present experiment				^{25}Na→^{25}Mg [195, 196]			
^{25}Al E_x (keV)	log ft	B(GT)	J^π [202]	^{25}Mg E_x (keV)	log ft	B(GT)	δ
0	5.306(25)	0.0187(11)	$5/2^+$	0	5.251(15)	0.0212(7)	0.14(8)
944.9(5)	5.109(14)	0.0294(9)	$3/2^+$	974.749(24)	5.043(6)	0.0342(5)	0.16(4)
1612.5(5)	5.15(3)	0.0269(19)	$7/2^+$	1611.772(11)	5.030(8)	0.0352(7)	0.31(9)
1789.4(4)	6.131(22)	0.00279(14)	$5/2^+$	1964.620(24)	6.045(9)	0.00340(7)	0.22(7)
2673.4(4)	5.27(10)	0.020(5)	$3/2^+$	2801.46(3)	5.246(9)	0.0214(5)	0.05(24)
^{25}Si→^{25}Al USDC				^{25}Na→^{25}Mg USDC			
^{25}Al E_x (keV)	log ft	B(GT)		^{25}Mg E_x (keV)	log ft	B(GT)	δ
0	5.314	0.0183	$5/2^+$	0	5.312	0.0184	0.01
1015	5.093	0.0305	$3/2^+$	1072	5.087	0.0309	0.01
1723	5.208	0.0234	$7/2^+$	1708	5.183	0.0248	0.06
1882	6.070	0.0032	$5/2^+$	2012	6.140	0.0027	−0.15
2739	5.127	0.0282	$3/2^+$	2834	5.135	0.0277	−0.02
^{25}Si→^{25}Al USDI				^{25}Na→^{25}Mg USDI			
^{25}Al E_x (keV)	log ft	B(GT)		^{25}Mg E_x (keV)	log ft	B(GT)	δ
0	5.293	0.0192	$5/2^+$	0	5.291	0.0193	0.01
1013	5.113	0.0291	$3/2^+$	1068	5.107	0.0295	0.01
1722	5.206	0.0235	$7/2^+$	1707	5.181	0.0249	0.06
1890	6.084	0.0031	$5/2^+$	2020	6.173	0.0025	−0.18
2761	5.139	0.0274	$3/2^+$	2854	5.147	0.0269	−0.02

excitation energies and β-feeding intensities of all the ^{25}Al levels populated by ^{25}Si β decay are tabulated in Table 6.

24.6. Shell-model calculations

We have performed the theoretical calculations using the shell-model code NuShellX [540] in the *sd*-shell-model space involving the $\pi 0d_{5/2}$, $\pi 1s_{1/2}$, $\pi 0d_{3/2}$, $\nu 0d_{5/2}$, $\nu 1s_{1/2}$, and $\nu 0d_{3/2}$ valence orbits. Two modified universal *sd* (USD) Hamiltonian [228], USDC and USDI, which directly incorporate Coulomb and other isospin-breaking interactions [120] were used. A quenching factor $q = 0.6$ for the Gamow-Teller strength was used in our theoretical calculation based on the average over the whole *sd* shell. Given the quenching factors in *sd* shell ranging from 0.5 near ^{40}Ca to 0.7 near ^{16}O, the theoretical uncertainty associated with the $A = 25$, $q = 0.6$ is estimated to be ±0.1. The theoretical log ft and B(GT) values are reported in Table 8. In general, the characteristics of the decay scheme measured in the present paper including the excitation energies, β-feeding intensities, log ft, B(GT), and γ-ray and proton partial widths for the states of ^{25}Al can be reproduced well within the framework of the nuclear shell model.

Low-lying states and the $T = 3/2$ IAS in ^{25}Al have been unambiguously identified and their excitation energies have been well measured. Given that decay widths and intensities are very sensitive to energies, we have applied a correction to the theoretical β feedings, γ-ray partial widths (Γ_γ), and proton partial widths (Γ_p) based on the experimental energies. The $I_\beta = T/t$ is determined using the half-life of ^{25}Si, T, and the individual partial half-life for each transition, t. The latter is scaled from the theoretical t by the phase space factor f using the experimental β-decay energy of ^{25}Si and the excitation energy of each ^{25}Al state under the assumption of constant ft value. Each theoretical Γ_p is calculated by using the theoretical spectroscopic factor and the barrier-penetration factor [229] corrected for the experimental resonance energy. Each theoretical Γ_γ is obtained using the effective $M1$ and $E2$ transition operators from Ref. [121] and then scaled for the E_γ^{2L+1} energy dependence, where L denotes the multipolarity of the radiation.

24.7. Mirror asymmetry

With the β-decay energy of ^{25}Si $Q_{EC}(^{25}\text{Si}) = 12743(10)$ keV [230], the ^{25}Si half-life of $219.2^{+0.9}_{-1.2}$ ms, the excitation energies of ^{25}Al states, and the β-feeding intensities to ^{25}Al states measured in the present paper, the corresponding

Table 9: Decay properties of the 2673-keV $3/2^+$ state in ^{25}Al.

Reference	Γ_γ (meV)	Γ_p (meV)	Γ_γ/Γ_p	$\omega\gamma$ (meV)	τ (fs)
[222, 233]	23.8(15)	166(16)	0.143(16)	41.6(26)	$6.1^{+4.8}_{-3.7}$
USDC	20.6	173	0.119	36.8	3.4
USDI	21.2	173	0.123	37.7	3.4
Present	23(8)[1]	202(48)[1]	0.11(3)	41.6(26)[2]	2.9(7)

log ft values for each ^{25}Al state can be calculated through the LOGFT analysis program provided by the National Nuclear Data Center website [231]. The corresponding Gamow-Teller transition strengths, B(GT), are calculated from the ft values using the following relation:

$$ft = \frac{K}{g_V^2 B(\mathrm{F}) + g_A^2 B(\mathrm{GT})}, \tag{11}$$

where $K/g_V^2 = 6144.48 \pm 3.70$ s [232] and $(g_A/g_V)^2 = (-1.2756 \pm 0.0013)^2$ [82], with g_V and g_A being the free vector and axial-vector coupling constants of the weak interaction. Our shell-model calculations predict that the Fermi transition strengths B(F) are negligible for low-lying ^{25}Al states.

The degree of isospin-symmetry breaking can be quantified by the mirror-asymmetry parameter $\delta = ft^+/ft^- - 1$, where the ft^+ and ft^- values are associated with the β^+ decay of ^{25}Si and the β^- decay of ^{25}Na, respectively. $\delta = 0$ denotes perfect isospin symmetry. The log ft and B(GT) values for each β-decay transition and the corresponding mirror-asymmetry parameter are summarized in Table 8. Limited by the $Q_{\beta^-} = 3835.0(12)$ keV, only five ^{25}Mg states were observed to be populated by ^{25}Na β decay [194, 195, 196], and each one of them can be matched with a specific ^{25}Al state measured in our paper. Thomas *et al.* [178] compared four transitions between the mirror nuclei ^{25}Si and ^{25}Na, and their mirror-asymmetry parameters for three bound states are consistent with but less precise than our values. We did not observe mirror asymmetry between the transitions to the second $3/2^+$ state. We observed some small but significant asymmetries for the other four low-lying states. The theoretical B(GT) values for ^{25}Si decay are in agreement with our experimental values considering the theoretical uncertainties. Our shell-model calculations somewhat underestimated the B(GT) value for the $7/2^+$ state but slightly overestimated that for the second $3/2^+$ state compared with ^{25}Na β-decay measurements [194, 195, 196], suggesting that a more careful theoretical treatment is needed, e.g., using the shell model in conjunction with more realistic radial wave functions and sums over parentages in the $A-1$ nuclei, including a change in the radial wave function overlap factors and how this is connected to the Thomas-Ehrman shifts. These calculations call for more theoretical efforts in the future.

24.8. ^{25}Al 2673-keV state

The β feeding of the 2673-keV state of ^{25}Al is measured to be $I_\beta = 6.8(15)\%$ by the sum of the intensities of the four β-delayed γ rays deexciting the 2673-keV state $I_\gamma = 0.70(4)\%$ and the intensity of the 402-keV proton $I_p = 6.1(15)\%$. The β feeding of the 2673-keV state is in agreement with the previous measured values of $I_\beta = 6.93(76)\%$ [176] and $I_\beta = 8.2(15)\%$ [177]. Thomas *et al.* reported a smaller $I_\beta = 4.8(3)\%$ [178], in which the 2673-keV state was assumed to decay only via proton emission. The ratio I_γ/I_p is equal to the ratio Γ_γ/Γ_p. We determine an experimental value of $\Gamma_\gamma/\Gamma_p = 0.11(3)$, in agreement with the $\Gamma_\gamma/\Gamma_p = 0.143(16)$ derived from a ^{24}Mg$(p,\gamma)^{25}$Al reaction measurement [233].

Another ^{24}Mg$(p,\gamma)^{25}$Al reaction measurement determined the resonance strength of the 2673-keV state to be $\omega\gamma = 41.6(26)$ meV [222]. The total decay width Γ_{tot} is the sum of the Γ_p and Γ_γ since they represent the only two open decay channels for the 402-keV resonance in ^{25}Al. The Γ_{tot} and $\omega\gamma$ are related by the following expression:

$$\omega\gamma = \frac{2J_r + 1}{(2J_p + 1)(2J_T + 1)} \frac{\Gamma_p \times \Gamma_\gamma}{\Gamma_{\mathrm{tot}}}, \tag{12}$$

where $J_r = 3/2$ is the spin of the 402-keV resonance, $J_p = 1/2$ is the spin of the proton, and $J_T = 0$ is the spin of the ground state of ^{24}Mg. The lifetime of the 2673-keV ^{25}Al state was previously measured to be $\tau = 6.1^{+4.8}_{-3.7}$ fs

Table 10: Decay properties of the 7902-keV $5/2^+$, $T = 3/2$ IAS in ^{25}Al.

Reference	Γ_γ (eV)	Γ_p (eV)	Γ_γ/Γ_p	$\omega\gamma$ (eV)
Ref. [237]	2.0(10)	111(17)[1]	0.018(9)	1.0(5)
Ref. [223]	0.50(13)	111(17)[1]	0.0045(13)	0.25(6)
USDC	2.98	111	0.027	1.49
USDI	2.45	111	0.022	1.22
Present	2.1(5)	111(17)[1]	0.019(3)	1.0(4)

using the Doppler shift attenuation method [233]. This value was converted to a half-life of 4(3) fs and adopted by the evaluation [202]. The lifetime is inversely proportional to the decay width by $\tau = \hbar/\Gamma_{\rm tot}$, where $\hbar$ is the Planck constant. Combining the branching ratio Γ_γ/Γ_p measured in this paper with the literature $\omega\gamma$ value yields a lifetime for the 2673-keV state of 2.9(7) fs, which is consistent with, as well as more precise than, the previously measured lifetime [233]. The decay properties of the 2673-keV state in ^{25}Al are summarized and compared to the USDC and USDI shell-model calculations in Table 9, and good agreement is obtained for all the quantities.

24.9. ^{25}Al $T = 3/2$ IAS at 7902 keV

The proton partial width of the lowest $T = 3/2$ IAS in ^{25}Al was determined to be $\Gamma_p = 155(50)$ eV [234, 235] and 105(18) eV [236], respectively, in two proton scattering measurements with polarized-proton beams. These two results agree, and a weighted average Γ_p is deduced to be 111(17) eV. The γ-ray partial width of the IAS was previously determined to be $\Gamma_\gamma = 2.0(10)$ eV in a ^{24}Mg$(p,\gamma)^{25}$Al reaction yield measurement [237] by adopting a proton branching ratio $I_{p0}/I_{p\rm tot} = 0.17$ from the ^{25}Si β-delayed proton measurement [172]. I_{p0} is the intensity of the proton emission from the IAS proceeding to the ground state of ^{24}Mg. $I_{p\rm tot}$ is the total intensity of the proton branches of the IAS. However, another ^{24}Mg$(p,\gamma)^{25}$Al reaction study [223] reported a much smaller $\Gamma_\gamma = 0.50(13)$ eV based on the measured resonance strength $\omega\gamma = 0.25(6)$ eV and the proton branching ratio $I_{p0}/I_{p\rm tot} = 0.168(13)$ from another ^{25}Si β-delayed proton measurement [173]. The ratio of the γ-ray partial width to the proton partial width is deduced to be either $\Gamma_\gamma/\Gamma_p = 0.018(9)$ by adopting the Γ_γ of Ref. [237] or $\Gamma_\gamma/\Gamma_p = 0.0045(13)$ by adopting the Γ_γ of Ref. [223].

The decay properties of the IAS obtained in the present paper are shown in Table 10. The sum of the intensities for the 7902- and 6289-keV β-delayed γ rays through the IAS is measured to be $I_\gamma = 0.20(3)\%$. The shell-model predicts a 19.3(13)% branch for unobserved weak γ rays, so we obtain a corrected $I_\gamma = 0.24(3)\%$. Based on the relative proton branching ratios measured in previous ^{25}Si decay experiments [173, 176, 177, 178] and normalized to our ^{25}Si$(\beta p\gamma)^{24}$Mg intensities, we have determined an $I_p = 13.1(16)\%$ for the IAS. Adding I_γ and I_p yields the total β feeding intensity $I_\beta = 13.4(16)\%$ for the IAS, corresponding to a log ft value of 3.23(6). The USDC and USDI shell-model calculations predicted the log $ft = 3.31$ and 3.39, respectively. The agreement between the measured and calculated values is good considering the theoretical uncertainties.

We extract the ratio of $\Gamma_\gamma/\Gamma_p = 0.019(3)$ from the I_γ and I_p values. Combining our Γ_γ/Γ_p ratio with the literature Γ_p value [234, 235, 236] yields a $\Gamma_\gamma = 2.1(5)$ eV. We have determined an $\omega\gamma = 1.0(4)$ eV by taking into account the $I_{p0}/I_{p\rm tot} = 0.17(5)$, deduced from the intensities of proton emission from the IAS (see Table 6). As can be seen from Table 10, our results are in good agreement with the results reported by Morrison *et al.* [237] and are more precise, but they deviate from the values reported by Rogers *et al.* [223] roughly by a factor of 4.

The USDC and USDI shell-model calculations estimate the Γ_γ to be 2.98 and 2.45 eV, respectively, in agreement with the $\Gamma_\gamma = 2.1(5)$ eV derived from our Γ_γ/Γ_p ratio and the Γ_p from Refs. [234, 235, 236]. The shell model also indicates that Γ_p of the IAS depends on the mixing with a predicted nearby $5/2^+$, $T = 1/2$ state that has a Γ_p of 50 keV. Unfortunately, this state has not yet been identified experimentally. The sum of Fermi and Gamow-Teller contributions is derived to be $B(\rm F) + (g_A/g_V)^2 B(\rm GT) = 3.6(5)$ from our measured log $ft = 3.23(6)$. Our shell-model calculations predict a $B(\rm GT) \approx 0.1$ for the IAS. The summed $B(\rm F)$ should fulfill the sum rule $\sum B(\rm F) = 3$, suggesting that the Fermi strength is mainly concentrated on the IAS. The fragmentation of the Fermi strength via isospin mixing is rather small compared with the strong mixing observed for some special cases [8, 238, 239, 240]. The USDC and USDI shell-model calculations predict that this state is 23 and 9 keV above the IAS, respectively, but there is an uncertainty of about 150 keV for the predicted energy of each state. It has been shown that this energy

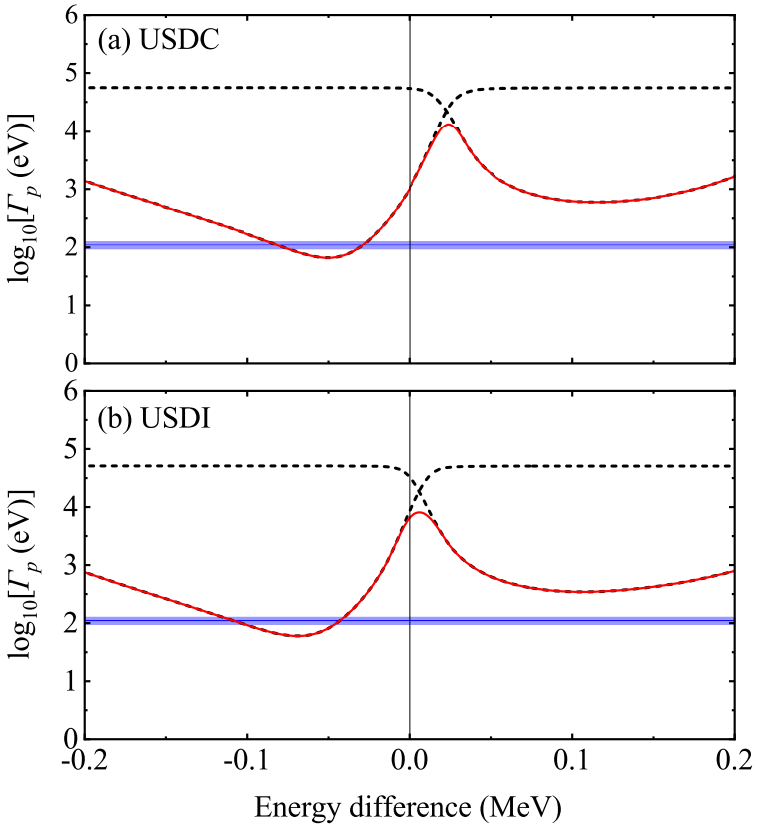

Figure 44: Γ_p for the $T = 3/2$ IAS in ^{25}Al and its neighboring $T = 1/2$ state as a function of the energy difference between the two states ($E_{x3/2} - E_{x1/2}$) calculated by the (a) USDC and (b) USDI shell models. The decay width for the state dominated by the $T = 3/2$ IAS is shown by the solid red line, and the decay width for the state dominated by the $T = 1/2$ state is shown by the dashed black line. The solid blue band corresponds to the uncertainty of the experimental Γ_p value for the $T = 3/2$ IAS [234, 235, 236].

uncertainty leads to uncertainties of about an order of magnitude for the proton and neutron decay width of IAS in the *sd* shell [241]. In order to assess the results for ^{25}Al, we move the relative location of the $T = 3/2$ and $1/2$ states by adding $b\hat{T}^2$ to the Hamiltonian, where $\hat{T}$ is the isospin operator. For states with good isospin, $b\hat{T}^2|T\rangle = bT(T+1)|T\rangle$. The $T = 3/2$ states are shifted by $3.75b$, and the $T = 1/2$ states are shifted by $0.75b$. The results obtained for the IAS and its neighboring $T = 1/2$ state obtained by adjusting the parameter b are shown in Fig. 44. If the IAS is moved down by a few keV, the Γ_p for the IAS comes into agreement with the well-measured Γ_p value [234, 235, 236]. This is equivalent to moving the $T = 1/2$ state up a few keV. An empirical two-state mixing formalism [238] predicts that the unperturbed and observed level spacing of the two states differ by less than 1 keV in this case. The USDC and USDI shell model predicts that the $T = 1/2$ state is approximately 30 and 44 keV above the $T = 3/2$ IAS, respectively, corresponding to 7932−7946 keV for the excitation energy of the $T = 1/2$ state.

25. Conclusion

By using the GADGET system at NSCL, simultaneous measurements of ^{25}Si β-delayed proton and γ decays were carried out. We have reported the most precise half-life of ^{25}Si to date. Eight new β-delayed γ-ray transitions were detected, leading to the population of three ^{25}Al states that have not been previously observed via ^{25}Si β-delayed γ decay. A total of 14 β-delayed proton branches have been identified, including a new proton peak at 724 keV. We have confirmed the placement of protons in the decay scheme of ^{25}Si reported by previous literature [177, 178] using both Doppler broadening line-shape analysis and proton-γ-ray coincidence analysis. We have reevaluated the energies and intensities for 34 ^{25}Si β-delayed proton emissions. A more precise lifetime for the ^{25}Al 2673-keV state has been extracted, and the discrepancy involving the γ-ray partial width of the 7902-keV $T = 3/2$ IAS in ^{25}Al in the literature has been resolved, which demonstrates the potential of utilizing complementary experimental approaches. The mirror-asymmetry parameters have been deduced for five transitions in the mirror β decays of ^{25}Si and ^{25}Na, which will contribute to the systematic understanding of the nature of mirror-symmetry breaking. Shell-model calculations using the USDC and USDI Hamiltonians both reproduce the experimental data well and predict a $5/2^+$, $T = 1/2$ state above the $T = 3/2$ IAS. It is desirable for future experiments with higher statistics to explore the fine structure near the IAS and search for the hypothetical $T = 1/2$ ^{25}Al state that exhibits weak isospin mixing with the IAS.

26. Doppler broadened γ-ray lines as a probe of neutron energies and lifetimes

Half of the nuclides heavier than iron are predicted to be produced in the rapid neutron capture process (*r*-process). The reproduction of the observed *r*-process abundance distribution in nucleosynthesis calculations relies on β-decay data such as half-lives and β-delayed neutron emission probabilities. Experimentally determined β-decay strength distributions provide stringent tests of models commonly used to predict global β-decay properties for *r*-process calculations. We propose to further develop a Doppler broadening line shape analysis method initiated at TRIUMF to obtain the β-delayed neutron energies and intensities for high-lying states, usually the most challenging region to access in conventional measurements. This will provide us with the full β-decay strength distributions in the Q_β windows for ^{29,30}Na. These will be the heaviest β-delayed nucleon emission cases ever measured using this method by a factor of three, representing a large step toward the longer-term goal of extending this method to the measurement of β-decays in the mass region of iron and beyond.

27. Scientific Motivations

The rapid neutron capture process (*r*-process) is known to be responsible for producing roughly half of the nuclides heavier than iron [242]. Modeling *r*-process nucleosynthesis requires β-decay properties such as half-lives [243] and β-delayed neutron emission probabilities (P_n) [244] of a wide range of nuclei across the neutron-rich side of the nuclear chart.

During the astrophysical *r*-process, β-decay half-lives set the time scale of the *r*-process and hence strongly influence the production of heavy elements in the universe. Theoretical calculations using the quasiparticle random phase approximation or shell model [245] are commonly employed to make global predictions of various β-decay properties for neutron-rich nuclei that are not presently accessible experimentally. These calculations are typically

tested against measured half-lives. The β-decay strength function has been demonstrated to be a more detailed benchmark of theoretical models than just half-lives [246, 247], but data is typically only available up to the neutron separation energy in the daughter nucleus. It would be valuable to improve data on the high-excitation-energy part of the β-decay strength to neutron-unbound states in the daughter nucleus, which becomes increasingly important towards the drip line.

A large number of the nuclei involved in the r-process are β-delayed neutron emitters. Delayed neutron emission has a twofold impact on the freezeout of the r-process: it is an important source of neutrons for late-time, non-equilibrium captures during freezeout and also finalizes the fine details of the abundance pattern [166, 248]. P_n values are only measured for less than half of the identified β-delayed neutron emitters [249, 250], so similarly, modeling of P_n values is essential and can benefit from measurements of the high-excitation-energy part of β-decay strength distributions. A realistic and robust description of the full β-decay strength distributions is crucial for our understanding of exotic nuclear structure as well as of r-process nucleosynthesis. Modeling of these P_n values also relies on accurate β-decay strength distributions including the portion to unbound states, as it contains the nuclear matrix elements for the Gamow-Teller, Fermi, and forbidden decay operators. Data on the β-decay strength distributions give much more detailed constraints In the past, ^{3}He proportional counters have been widely adopted for neutron counting, whereas they have low intrinsic efficiencies, limited time resolution and require special safety measures in their use due to toxicity, flammability or other aspects. In some cases, the neutron efficiency is assumed to be constant, which might induce systematic effects which cannot be corrected. Several neutron spectrometers based on liquid/plastic scintillators have been built in recent years. The efficiency is dependent on the neutron energy and is usually determined with the help of a Monte Carlo simulation, which poses a serious difficulty in the accurate determination of the P_n values. The overall efficiency of neutron detectors in P_n-value measurements depends on the assumed β-decay strength distribution, influencing the systematic scatter often observed in reported P_n values. Therefore, measurements of the β-decay strength distributions will facilitate the accurate estimates of the neutron detection efficiency, leading to more accurate P_n-value measurements.

28. Methodology

Detecting neutrons is more challenging than detecting charged particles or γ rays, and the identification of the delayed neutron branches is often complicated due to poor energy resolution and limited statistics [251]. We have been developing a γ-ray Doppler-broadening technique to measure β-delayed nucleon emissions to excited final states, as γ rays are relatively easy to detect with good efficiency and resolution. As shown in Fig. 45, when a nucleon is emitted from a nucleus, following β decay, the momentum of the system must be conserved, so the daughter nucleus will recoil with equal and opposite momentum as the ejected nucleon. If a γ ray is emitted while the nucleus is still recoiling, it will be Doppler-shifted in the laboratory frame. For an ensemble of such decays, the resulting γ-ray line shape in the measured energy spectrum will be Doppler broadened. In 2003, Fynbo *et al.* made the first attempt to analyze Doppler-broadened γ-ray line shapes due to the ^{10}Be recoil induced by the ^{11}Li β-delayed one-neutron emission [206, 207]. Then, two experiments on ^{11}Li($\beta n\gamma$)^{10}Be [208, 209] were conducted by Sarazin *et al.* at the Isotope Separation and Acceleration (ISAC) facility using the 8π γ-ray spectrometer [252] at TRIUMF. They further demonstrated how information can be extracted from the broadened line shapes and achieved comparable precision in the neutron energies to those obtained from direct neutron spectroscopy experiments. Recently, the Wrede Group at NSCL extended the method to higher masses and applied it to proton-rich nuclei: ^{26}P($\beta p\gamma$)^{25}Al [210] and ^{20}Mg($\beta p\gamma$)^{19}Ne [526], and ^{25}Si($\beta p\gamma$)^{24}Mg [516]. Even though protons are relatively easy to detect directly with good efficiency and resolution, some inconsistencies between conventional decay spectroscopy experiments [179, 180] were resolved with the Doppler broadening line shape analysis method [526]. This technique can also provide new information about unknown energies and intensities of nucleon feedings and previously unknown lifetimes of γ-ray emitting states.

It is desirable to apply this technique to heavier nuclei of astrophysical interest. However, doing so is more challenging because the recoil velocities and the corresponding Doppler shifts for γ rays get smaller with higher mass. So we propose a new experiment to extend this method to neutron-rich nuclei near $A = 30$, which is almost a factor of three heavier than ^{11}Li, the only neutron-rich nucleus ever measured using this method. Sodium isotopes are rather easy to produce in high quantities at Isotope Separation On-Line (ISOL) facilities such as ISAC. The existing β-delayed neutron information for ^{29,30}Na provides a strong foundation for this Doppler analysis technique,

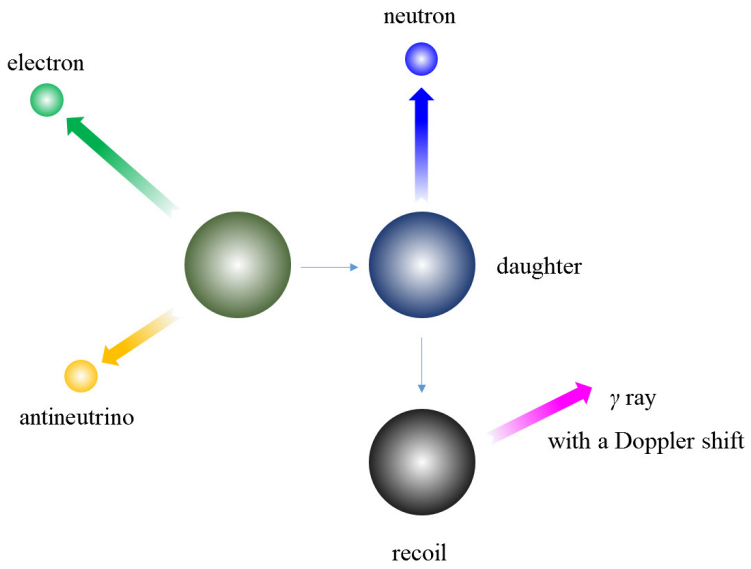

Figure 45: The γ ray following the β-delayed neutron emission is Doppler-shifted due to the recoil of the daughter nucleus.

but there is also substantial room for improvement in both decay schemes. The present measurement using the Doppler-broadening technique would be a beneficial complement to previous direct measurements of β-delayed neutrons of ^{29,30}Na. Additionally, the methodology has a wide range of possible other applications and offers the potential to be incorporated into the routine analysis procedure of future β-decay spectroscopies.

Figure 46 shows what the Doppler broadening of a γ-ray peak would look like with various neutron-feeding energies. Taking the 3081-keV γ-ray peak corresponding to the deexcitation from the ^{28}Mg 4054.6-keV state as an example, the energetically allowed neutrons feeding this state should be within $E_{\rm cm}$ = 5073 keV, and the known upper limit of the lifetime of the 4054.6-keV state is $T_{1/2}$ = 30 fs. By assuming a lifetime of τ = 30 fs and adopting a typical response function of the SeGA germanium detectors at NSCL and the stopping power of the implantation material of Polyvinyltoluene from a SRIM code [491], γ rays are emitted isotropically from the recoil positions and interact with germanium detectors to produce a simulated energy spectrum. The TIGRESS detectors are expected to have a similar response function to that of the SeGA detectors. After the experiment at TRIUMF, we will determine the real response function for each of the TIGRESS detectors by fitting unbroadened γ-ray peaks and update this simulation so that it can be compared to the observed experimental data using a χ^2-minimization or Bayesian-MCMC technique.

Compared with the ^{29}Na-decay spectroscopy [253], the ^{30}Na-decay spectroscopy [254] reported more n-γ coincidence information, whereas the lifetime information of neutron-emission daughter states populated is much less than that in the ^{29}Na case. Of the two key quantities in the Doppler broadening technique, the neutron branch and lifetime, the better known quantity is usually used to determine the lesser known quantity. Therefore, ^{29}Na and ^{30}Na provide a good opportunity to cross-check the analysis, to narrow down the various neutron-feeding possibilities, and to resolve the existing discrepancies.

It is worth mentioning that the ^{30}Na-decay spectroscopy also reported a piece of evidence for the observation of a 1474-keV γ ray corresponding to the deexcitation of the first excited state of ^{28}Mg following the β-delayed two-neutron emission of ^{30}Na. So far, the energy and the angular distributions for the β-delayed two-neutron emission of ^{30}Na have not yet been measured experimentally. Different two-neutron correlations may result in different Doppler-broadening of the γ-ray line following two-neutron emission. In this case, the measured Doppler-broadening features might preserve the information about the mechanism of the two-neutron correlation, which may shed more light on the pairing of nucleons inside the nucleus.

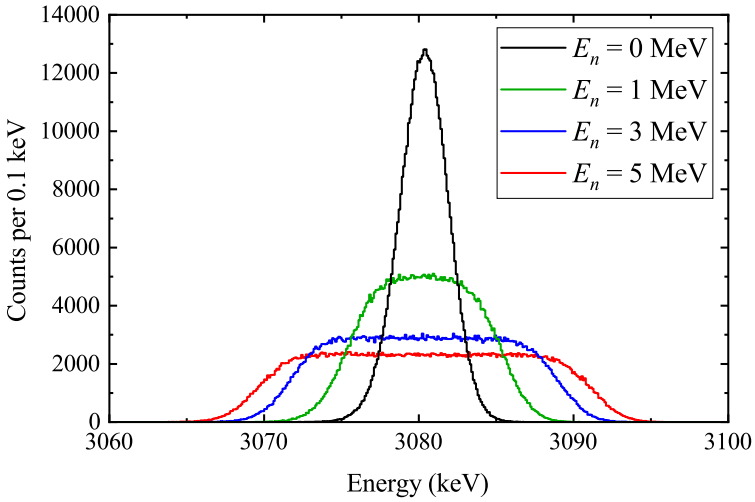

Figure 46: Doppler-broadened 3081-keV γ-ray line shape simulated by assuming four different β-delayed neutron branches of ^{29}Na that feed the ^{28}Mg 4054.6-keV state. The neutron energies are center-of-mass energies.

28.1. Doppler broadening technique for FDSi

^{43}P($\beta n\gamma$)^{42}S data from FRIB E21062 would be a good case. This technique works both ways; either with well-known lifetimes to constrain neutron feeding branchings/energies or with well-known neutron feedings to constrain lifetimes. For most FDSi data, the latter seems applicable, as there are no known lifetimes for most of the excited states in neutron emission daughters, but there is neutron information from the VANDLE measurement. Considering FDSi experiments typically are not able to measure short lifetimes (below picoseconds), extracting lifetimes using this technique will enhance the results we can obtain from the data sets acquired by the FDSi collaboration. It is important to emphasize that this method does not overlap with existing analysis efforts; rather, it serves as a complementary approach to direct measurements. This advancement will only contribute and strengthen the FDSi research outcomes. Given that this issue involves fitting the model to the data and constraining model parameters based on observations, we can leverage Bayesian analysis techniques.

Part III
LIBRA

29. Extension of the Particle X-Ray Coincidence Technique: The Lifetimes and Branching Ratios Apparatus

The particle x-ray coincidence technique (PXCT) was originally developed to measure average lifetimes in the 10^{-17} – 10^{-15} s range for proton-unbound states populated by electron capture (EC). We have designed and built the Lifetimes and Branching Ratios Apparatus (LIBRA) to be used in the stopped-beam area at the Facility for Rare Isotope Beams that extends PXCT to measure lifetimes and decay branching ratios of resonances populated by EC/β^+ decay. The first application of LIBRA aims to obtain essential nuclear data from ^{60}Ga EC/β^+ decay to constrain the thermonuclear rates of the ^{59}Cu$(p,\gamma)^{60}$Zn and ^{59}Cu$(p,\alpha)^{56}$Ni reactions, and in turn, the strength of the NiCu nucleosynthesis cycle, which is predicted to significantly impact the modeling of type I x-ray burst light curves and the composition of the burst ashes. Detailed theoretical calculations, Monte Carlo simulations, and performance tests with radioactive sources have been conducted to validate the feasibility of employing LIBRA for the ^{60}Ga experiment. LIBRA can be utilized to measure most essential ingredients needed for charged-particle reaction rate calculations in a single experiment, in the absence of direct measurements, which are often impractical for radioactive reactants.

30. Introduction

Direct measurements of charged-particle thermonuclear reaction rates are challenging, especially when radioactive reactants are involved. Small cross sections at stellar energies, limited beam intensities, target degradation under bombardment, and low signal-to-background ratios may render a direct measurement infeasible. Successful direct measurements at astrophysical energies have been achieved only in a few instances [394]. Consequently, direct measurements of thermonuclear reaction rates are often performed at higher energies and then extrapolated to stellar energies with the aid of nuclear theories. Alternatively, various indirect approaches, such as elastic scattering, transfer reactions, surrogate reactions, charge-exchange reactions, Coulomb dissociation, in-beam γ-ray spectroscopy, and β-decay spectroscopy have also played a major role in achieving a comprehensive understanding of thermonuclear reactions [395, 396, 397]. However, these methods typically yield only a fraction of the necessary nuclear data, and results from multiple experiments still need to be pieced together to infer the reaction rates of interest [398].

Thermonuclear charged-particle reactions are often dominated by narrow and isolated resonances if the level density of the compound nucleus in the Gamow window is not too high. The resonant reaction rate $N_A\langle\sigma\nu\rangle_r$ can be calculated using the well-known expression [399, 400]

$$N_A\langle\sigma\nu\rangle_r = 1.5394\times10^{11}(\mu T_9)^{-3/2}\times\omega\gamma \times\exp\left(-\frac{11.605E_r}{T_9}\right)(\mathrm{cm^3s^{-1}mol^{-1}}), \tag{13}$$

where N_A denotes the Avogadro constant and $\langle\sigma\nu\rangle_r$ is the velocity-averaged product of the cross section and relative velocity. $\mu = A_pA_T/(A_p + A_T)$ is the reduced mass in atomic mass units, with A_p and A_T as the mass numbers of the incoming particle and the target nucleus, respectively. E_r is the resonance energy in the center-of-mass system in units of MeV. T_9 is the temperature in units of giga kelvin (GK), and $\omega\gamma$ is the resonance strength in units of MeV. For a (p,γ) resonance,

$$\omega\gamma = \frac{2J_r+1}{(2J_p+1)(2J_T+1)}\frac{\Gamma_p\Gamma_\gamma}{\Gamma_{\mathrm{tot}}}, \tag{14}$$

where J_r is the spin of the resonance, $J_p = 1/2$ is the spin of proton, and J_T is the spin of the ground state of the target nucleus. The total decay width Γ_{tot} of the resonance is the sum of the partial widths for open decay channels, typically including proton width (Γ_p), γ width (Γ_γ), and α width (Γ_α). Equivalently, the resonance strength can be constructed by combining the proton branching ratio $B_p = \Gamma_p/\Gamma_{\mathrm{tot}}$, the γ-ray branching ratio $B_\gamma = \Gamma_\gamma/\Gamma_{\mathrm{tot}}$, and the lifetime τ using the following expression:

$$\omega\gamma = \frac{2J_r + 1}{(2J_p + 1)(2J_T + 1)} B_p B_\gamma \frac{\hbar}{\tau}, \tag{15}$$

where $\hbar$ is the reduced Planck constant. These relations are also applicable to a (p, α) resonance by replacing the terms Γ_γ and B_γ with Γ_α and B_α, respectively. Therefore, important quantities to determine the reaction rates include the resonance energies, the spins, the proton-, γ-, and α-decay branching ratios, and the lifetimes of the resonances.

In cases where the level density of resonances in the compound nucleus is sufficiently high to justify a statistical treatment, the (p, γ) reaction cross section $\sigma_{p\gamma}$ can be estimated within the Hauser-Feshbach statistical model framework:

$$\sigma_{p\gamma} = \frac{\pi\hbar^2}{2\mu E_r (2J_p + 1)(2J_T + 1)} \sum_{J,\pi} (2J + 1) \frac{T_p^{J^\pi} T_\gamma^{J^\pi}}{\sum_k T_k^{J^\pi}}, \tag{16}$$

where μ is the reduced mass, E_r, J, and π are the energy, spin, and parity of the resonance in the compound nucleus, and J_p and J_T are the spins of the proton and the state in the target nucleus, respectively. $T_p^{J^\pi}$ and $T_\gamma^{J^\pi}$ are the transmission coefficients for the proton and γ channels, respectively, of a given resonance with J, π at E_r. $\sum_k T_k^{J^\pi}$ represents the sum of the transmission coefficients over all possible decay channels k of the resonance, including proton, α, and γ emissions. The statistical model assumes that a large number of resonances with all spins and parities are available at each energy, and hence, Eq. (16) includes the summation over J, π. Transmission coefficients quantify the probability of particles or photons transmitting through the nuclear potential barrier, and are related to the average decay widths through the number of resonances with J, π per energy interval, i.e., the nuclear level density. Therefore, obtaining average resonance properties, including decay branching ratios and lifetimes (or total widths) of excited states in the compound nucleus, is valuable for calculating reaction rates within the statistical model [401, 402].

In this paper, we introduce the Lifetimes and Branching Ratios Apparatus (LIBRA) that applies and extends the Particle X-ray Coincidence Technique (PXCT) [403] to measure various essential ingredients for thermonuclear reaction rate calculations in a single experiment, potentially reducing uncertainties associated with combining quantities from separate experiments. We provide a comprehensive description of the experimental setup and its performance tests, demonstrating the feasibility of employing LIBRA in a case study to address the question of NiCu cycling in Type I X-ray bursts (XRBs).

Quote from [264]: In the absence of a direct measurement, experimental techniques focus on constraining the nuclear properties used by theory to calculate the reaction cross section using the Hauser-Feshbach statistical model. These properties are the particle-nucleus optical model potential (a description of the interaction between the particle and the nucleus), the nuclear level density - NLD (the number of energy levels per unit energy as a function of excitation energy, spin, and parity), and the γ-ray strength function - gSF (the reduced probability to emit a γ ray of a particular energy and multipolarity).

31. Case Study: NiCu Cycle in XRBs

Type I XRBs are the most frequent type of thermonuclear stellar explosions in the Galaxy [404]. They are powered by thermonuclear runaways in hydrogen- and/or helium-rich material accreted onto the surface of a neutron star in a low-mass X-ray binary system. The main nuclear reaction flow in the XRB is driven towards the proton drip line and to higher masses via a series of particle-induced reactions and β^+ decays. Accurate modeling of energy production and nucleosynthesis in XRBs requires precise nuclear physics inputs, including β decay rates, nuclear masses, and nuclear reaction rates of proton-rich rare isotopes along the path of the rapid proton (rp) capture process. Our understanding of XRBs has greatly expanded thanks to decades of work, yet many open questions remain [405, 406].

As illustrated in Fig. 47, under XRB conditions, the rp process beyond the waiting point ^{56}Ni may be affected by several cycles, such as the NiCu cycle. The ratio of ^{59}Cu$(p, \alpha)^{56}$Ni to ^{59}Cu$(p, \gamma)^{60}$Zn rate could lead to the formation of a NiCu cycle, returning the reaction flux to ^{56}Ni, strongly impeding the synthesis of heavier nuclei and affecting the XRB observables [407]. Currently, both rates recommended by REACLIB [408] are calculated by the Hauser-Feshbach statistical model [401, 409]. The variations in these rates have been identified as having a significant impact on the modeling of XRB light curves and the composition of the burst ashes [410, 411, 412]. At higher temperatures

(≈3 GK), the competition between ^{59}Cu$(p,\gamma)^{60}$Zn and ^{59}Cu$(p,\alpha)^{56}$Ni reactions is also found to significantly impact the νp-process nucleosynthesis in core-collapse supernovae [413, 414, 415].

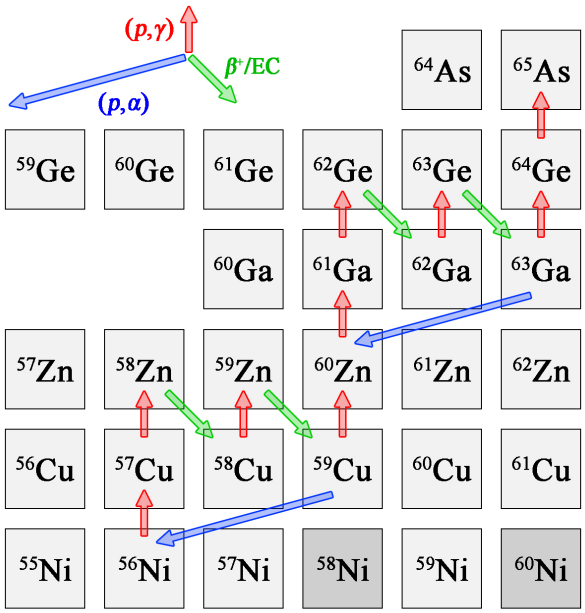

Figure 47: Portion of the rp-process reaction sequence featuring the NiCu cycle and ZnGa cycle one α cluster above. ^{58}Ni and ^{60}Ni (darker gray) are stable isotopes.

It is challenging to directly measure these two reactions at astrophysical energies because the predicted cross sections are too small, and intense low-energy radioactive ^{59}Cu beams are not currently available. A ^{59}Cu$(p,\alpha)^{56}$Ni reaction measurement using a ^{59}Cu beam with an intensity of 3.6×10^3 particle per second (pps) on a cryogenic solid H_2 target at an excitation energy of $E_x(^{60}\text{Zn}) = 11.1$ MeV found that ^{59}Cu(p,α) proceeds predominantly to the ^{56}Ni ground state, and standard statistical model calculations overestimate the cross section by a factor of 1.6–4 [416]. In a ^{58}Ni$(^3\text{He},n)^{60}$Zn reaction measurement [417], the nuclear level density of ^{60}Zn was extracted from the neutron evaporation spectrum. At an excitation energy of 6 MeV, the level density was estimated to be $\approx$18 MeV^{-1}. Taking into account the spin and parity range relevant to $\ell = 0, 1$ proton captures (Table 11), it was concluded that the level density could be too low to accurately apply the Hauser-Feshbach statistical model. Kim *et al.* [418] evaluated available experimental data on ^{60}Zn resonances, supplemented with theoretical calculations. They found the ^{59}Cu$(p,\alpha)^{56}$Ni reaction rate to be lower than the REACLIB rate [408] at XRB temperatures, implying a weaker NiCu cycle strength than previously estimated [410, 411, 412].

There are many ongoing efforts to address this problem both directly and indirectly:

1) ^{56}Ni$(\alpha,p)^{59}$Cu reaction cross section measurement using a ^{56}Ni beam of 3×10^3 pps on a He jet target at $E_x(^{60}\text{Zn}) = 11.1, 11.7, 12.6$ MeV with the Jet Experiments in Nuclear Structure and Astrophysics setup [419];

2) ^{59}Cu$(p,\alpha)^{56}$Ni reaction cross section measurement using a ^{59}Cu beam of 2×10^4 pps on CH_4 gas within the Multi-Sampling Ionization Chamber at $E_x(^{60}\text{Zn}) = 7.3 - 11.0$ MeV [420];

3) ^{59}Cu$(p,\alpha)^{56}$Ni reaction cross section measurement using a ^{59}Cu beam of 5.5×10^5 pps on a CH_2 target at $E_x(^{60}\text{Zn}) = 8.3 - 10.1$ MeV with circular double-sided silicon detectors [421];

4) ^{60}Zn γ-ray spectroscopy via the ^{59}Cu$(d,n)^{60}$Zn transfer reaction using Gamma-Ray Energy Tracking In-beam Nuclear Array [422];

5) ^{58}Ni$(^3\text{He},n)^{60}$Zn reaction using a ^{3}He beam on a ^{58}Ni target and measuring neutron angular distributions using liquid scintillators to determine the spins and parities of ^{60}Zn states [423];

6) ^{59}Cu$(^3\text{He},d)^{60}$Zn reaction using a ^{59}Cu beam to populate ^{60}Zn states and to measure the decay branching ratios [424];

7) ^{60}Ga β-delayed γ decay total absorption spectroscopy using the Summing NaI detector to determine the β-decay strength distribution and γ-ray strength functions [425];

8) ^{60}Ga decay using the Gaseous Detector with Germanium Tagging II to discover resonances and to measure decay branching ratios [426].

To date, experimental constraints on the ^{59}Cu$(p,\gamma)^{60}$Zn and ^{59}Cu$(p,\alpha)^{56}$Ni are still scarce and preclude a robust understanding of their astrophysical impacts.

Table 11 summarizes the spins and parities of ^{59}Cu + p resonances in ^{60}Zn. We also include captures on the first excited state of ^{59}Cu, which can be thermally populated at XRB temperatures [401]. Only positive parity states associated with $\ell = 1$ proton captures are accessible via allowed ^{60}Ga β transitions, also indicating a lower density of levels populated in the β decay than in the previous ^{58}Ni$(^3$He$, n)^{60}$Zn reaction measurement [417].

Table 11: Properties of ^{60}Zn states populated via proton captures on the $3/2^-$ ^{59}Cu ground state and the $1/2^-$ ^{59}Cu first excited state, and the allowed β transitions of the 2^+ ^{60}Ga ground state.

Population	^{60}Zn states
$\ell = 0$ p on $3/2^-$	1^-, 2^-
$\ell = 1$ p on $3/2^-$	0^+, 1^+, 2^+, 3^+
$\ell = 2$ p on $3/2^-$	0^-, 1^-, 2^-, 3^-, 4^-
$\ell = 0$ p on $1/2^-$	0^-, 1^-
$\ell = 1$ p on $1/2^-$	0^+, 1^+, 2^+
$\ell = 2$ p on $1/2^-$	1^-, 2^-, 3^-
β from 2^+	1^+, 2^+, 3^+

The Gamow energies and windows for the ^{59}Cu$(p,\gamma)^{60}$Zn and ^{59}Cu$(p,\alpha)^{56}$Ni reactions shown in Table 12 are calculated from a numerical study of the relevant energy ranges for astrophysical reaction rates [427]. For XRB, the most relevant Gamow windows are those calculated at temperatures of 0.5−1.5 GK [400]. Combined with the proton-separation energy of ^{60}Zn $S_p(^{60}\text{Zn}) = 5105.0(4)$ keV [428] and α-separation energy of ^{60}Zn $S_\alpha(^{60}\text{Zn}) = 2691.7(5)$ keV [428], ^{60}Zn resonances of interest are energetically accessible in ^{60}Ga β decay owing to the large $Q_{\text{EC}}(^{60}\text{Ga}) = 14160(15)$ keV [429, 430, 431].

Table 12: Gamow windows $\widetilde{E}_{\text{hi}} - \widetilde{\Delta} \le E \le \widetilde{E}_{\text{hi}}$ and Gamow peaks $\widetilde{E}_0$ for the ^{59}Cu$(p,\gamma)^{60}$Zn and ^{59}Cu$(p,\alpha)^{56}$Ni reactions at a temperature T [427].

	^{59}Cu$(p,\gamma)^{60}$Zn			^{59}Cu$(p,\alpha)^{56}$Ni		
T (GK)	$\widetilde{E}_{\text{hi}} - \widetilde{\Delta}$ (MeV)	$\widetilde{E}_0$ (MeV)	$\widetilde{E}_{\text{hi}}$ (MeV)	$\widetilde{E}_{\text{hi}} - \widetilde{\Delta}$ (MeV)	$\widetilde{E}_0$ (MeV)	$\widetilde{E}_{\text{hi}}$ (MeV)
0.5	0.51	0.71	0.92	0.55	0.74	0.98
1.0	0.67	0.91	1.26	0.73	1.01	1.48
1.5	0.75	1.01	1.57	0.87	1.27	2.11
2.0	0.82	1.14	1.83	1.01	1.74	2.80
2.5	0.85	1.40	2.05	1.24	2.19	3.52
3.0	0.89	1.49	2.26	1.51	2.66	4.16
3.5	0.93	1.57	2.46	1.79	3.10	4.70
4.0	0.97	1.64	2.66	2.04	3.48	5.16

In the first ^{60}Ga decay study, Mazzocchi *et al.* observed 802 protons and reported a total ^{60}Ga βp intensity of $I_p = 1.6(7)\%$ and an upper limit for $\beta\alpha$ intensity $I_\alpha \le 0.023(20)\%$. They also observed five ^{60}Ga$(\beta\gamma)$ transitions through three ^{60}Zn bound states [432]. Orrigo *et al.* [429] confirmed these five $\beta\gamma$ transitions and the three proton-bound states, and reported 24 new $\beta\gamma$ transitions that are correlated with ^{60}Ga implants. However, these new transitions were not placed in the decay scheme, nor were β-feeding intensities provided. Individual proton peaks were not resolved in either work [432, 429, 433]. The Evaluated Nuclear Structure Data File (ENSDF) for mass 60 is 12 years

old, and we present an up-to-date ^{60}Ga decay data evaluation to facilitate an accurate understanding of the pertinent nuclear structure properties (Fig. 48). However, the evaluated decay scheme remains incomplete, with substantial unplaced $\beta\gamma$ intensities. The five γ intensities reported by both studies [429, 432] are in good agreement, and if we deduce the corresponding β-feeding intensities, unplaced $\beta\gamma$ transitions likely account for >20% of total β-feeding intensities. A recent ^{60}Ga total absorption γ-ray spectroscopy experiment observed β-feeding intensities above the ^{60}Zn proton separation energy [425], indicating the need for further studies.

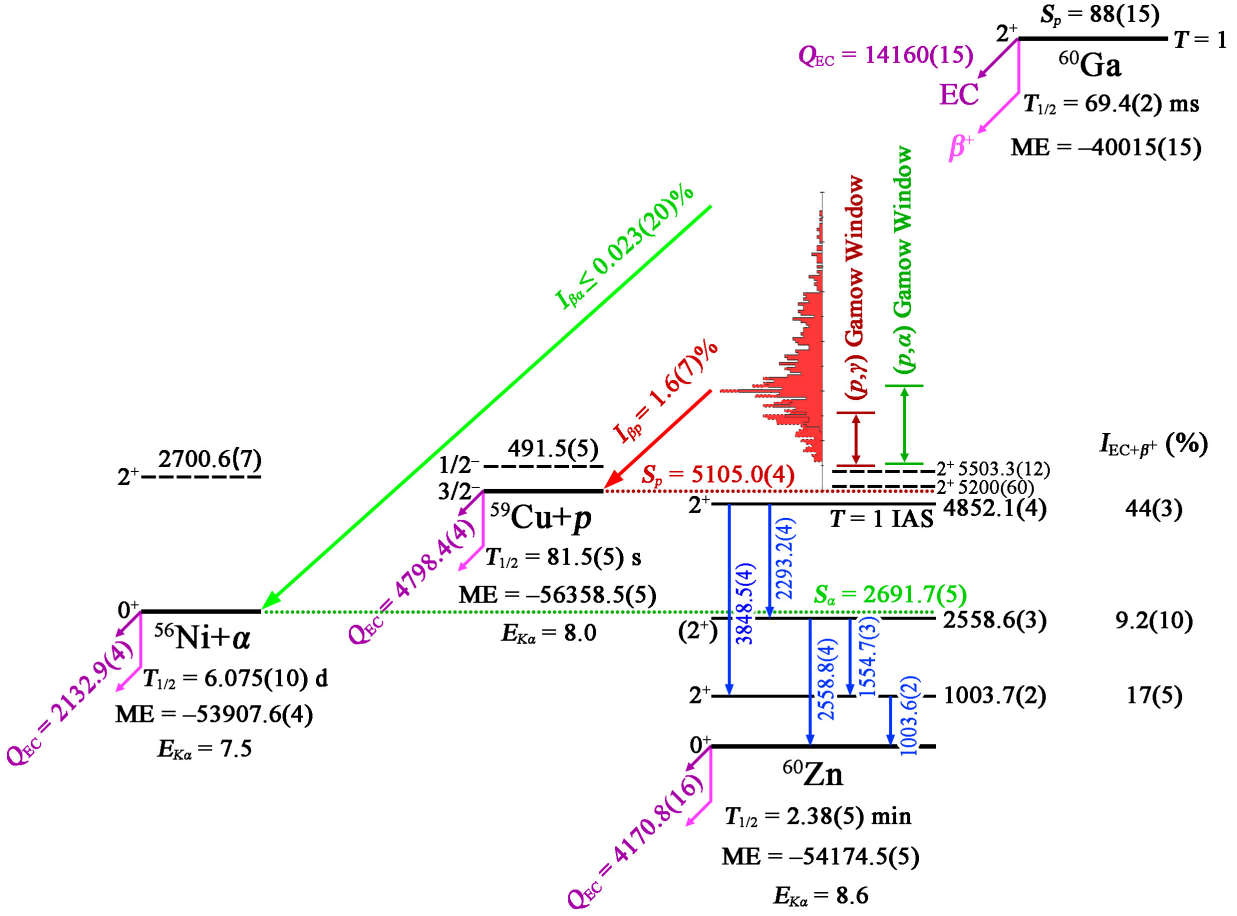

Figure 48: Evaluated decay scheme of ^{60}Ga. All energies are given in units of keV. The mass excesses, Q_{EC} values, and particle separation energies of ^{56}Ni, ^{59}Cu, and ^{60}Zn are from AME2020 [428], while for ^{60}Ga the data are evaluated based on Refs. [429, 430, 431]. The half-lives of ^{56}Ni, ^{59}Cu, and ^{60}Zn are from ENSDF evaluations [434, 435, 436], respectively. The half-life of ^{60}Ga is evaluated based on Refs. [432, 437, 438, 433, 439, 429]. All spins and parities are adopted from ENSDF evaluations [434, 435, 436], with the 4852-keV state in ^{60}Zn revised from (2^+) to 2^+ based on the unambiguous $T = 1$ isobaric analog state argument [429, 432]. The γ-ray energies, excitation energies, and β feedings of ^{60}Zn states are evaluated [440] based on all available measurements [429, 432, 441, 442]. The proton spectrum and β-delayed proton and α branchings are adopted from Ref. [432]. Dashed lines represent two 2^+ resonances in ^{60}Zn and the first excited states of ^{56}Ni and ^{59}Cu, which are expected to be accessible but have not yet been observed in ^{60}Ga decay. Double-headed arrows indicate the Gamow windows for the ^{59}Cu$(p,\gamma)^{60}$Zn and ^{59}Cu$(p,\alpha)^{56}$Ni reactions at 0.5−1.5 GK (Table 12).

High-statistics ^{60}Ga β decay measurements with proton, α, and γ-ray coincidences will allow for the construction of a more comprehensive decay scheme, including the proton/α-emitting states in ^{60}Zn to the ground and excited states of ^{59}Cu/^{56}Ni. This will provide crucial insights into the entrance and exit channels of the thermonuclear ^{59}Cu$(p,\gamma)^{60}$Zn and ^{59}Cu$(p,\alpha)^{56}$Ni reactions. Although β-decay spectroscopy has proven to be a powerful method for obtaining decay branching ratios, it typically does not yield lifetimes or widths of resonances [443, 444]. Therefore, incorporating lifetime measurement capabilities into β-decay spectroscopy would be a significant advancement,

allowing most essential information to be gathered in a single experiment.

The mass excesses and particle separation energies of ^{56}Ni, ^{59}Cu, and ^{60}Zn reported by AME2020 [428] are all of sub-keV precision, while the mass of ^{60}Ga is estimated to be −39590(200) keV. A recent ^{60}Ge β-decay study measured the energies of protons and γ rays emitted from the $T = 2$ isobaric analog state in ^{60}Ga. Combining with the known mass of ^{59}Zn [428], the mass excess of ^{60}Ga is determined to be −40016(15) keV, where the dominant uncertainty is from their measured proton energies [429]. At the Ion Trap for Atomic and Nuclear Science of TRIUMF, a direct mass measurement using the multiple-reflection time-of-flight mass spectrometer reported a consistent ^{60}Ga mass value of −40005(30) keV [430]. At the cooler storage ring of the Heavy Ion Research Facility in Lanzhou (HIRFL), ^{60}Ga mass of −40034(46) keV was measured using isochronous mass spectrometry [431].

We obtain the mass of ^{60}Ga to be −40015(15) keV by taking a weighted average of Refs. [429, 430, 431]. The corresponding proton-separation energy and the β-decay Q-value of ^{60}Ga are obtained to be $S_p = 88(15)$ keV and $Q_{\rm EC} = 14160(15)$ keV, respectively, which are input to our shell-model calculations.

^{56}Ni, ^{59}Cu, and ^{60}Zn decay via low-energy $\beta\gamma$ only.

The half-life of ^{60}Ga has been measured to be $T_{1/2} = 70(15)$ ms [432], 70(13) ms [437], 76(3) ms [438], and 69.4(2) ms [429], and we obtain the weighted average to be 69.4(2) ms.

Orrigo *et al*. [429] is the only new measurement on ^{60}Zn performed after the cutoff date of $A = 60$ evaluation [436].

Fig. 48 includes the 5 confirmed ^{60}Zn γ-ray energies by taking the weighted average of all available measurements [429, 432, 441, 442].

We incorporate these newly evaluated γ-ray energies into the $A = 60$ evaluation [436] and perform a least-squares fit to γ-ray energies to obtain adjusted excitation energies [440].

32. Particle X-ray Coincidence Technique

In the 1970s, PXCT was introduced and applied to measure the average lifetimes of proton-unbound states in ^{69}As populated by the electron capture (EC) of ^{69}Se [403]. The principle of PXCT is illustrated in Fig. 49. In the process of an EC-delayed proton emission, a proton-rich precursor with an atomic number of Z decays by EC to the proton emitter $(Z-1)$. Once EC occurs, a proton-unbound nuclear state and an atomic shell vacancy are created simultaneously. The vacancy is primarily created in the K shell. An electron from an outer shell fills the K shell vacancy and may yield X-ray photons corresponding to the binding energy difference between the outer and the K shells. Meanwhile, the proton-unbound state with a comparable lifetime $\tau_{p-\rm emit}$ emits a proton to a state of the daughter $(Z-2)$. If the proton is emitted before the X-ray emission, then the X-ray energy will be characteristic of the daughter $(Z-2)$. If the proton is emitted after the X-ray emission, then the X-ray energy will be characteristic of the proton emitter $(Z-1)$. By measuring X rays in coincidence with protons, the relative intensities of the $(Z-1)$ and $(Z-2)$ X-ray peaks, primarily $I_{K_\alpha(Z-1)}/I_{K_\alpha(Z-2)}$, can be used to establish the relationship between the nuclear and atomic lifetimes:

$$\frac{\tau_{p-\rm emit}}{\tau_{K\rm shell(Z-1)}} = \frac{\Gamma_{K\rm shell(Z-1)}}{\Gamma_{p-\rm emit}} = \frac{I_{K_\alpha(Z-1)}}{I_{K_\alpha(Z-2)}}, \tag{17}$$

where the level widths $\Gamma_{K\rm shell}$ and $\Gamma_{p-\rm emit}$ are the equivalent of $\hbar/\tau_{K\rm shell}$ and $\hbar/\tau_{p-\rm emit}$, respectively, as they both follow the exponential decay law. The lifetimes of proton-emitting states can be determined by measuring X-ray intensity ratios combined with known atomic K-shell vacancy lifetimes, ranging from 1.1×10^{-14} s for C $(Z = 6)$ down to 5×10^{-18} s for Fm $(Z = 100)$ [446, 447, 448, 449, 450]. This also defines the PXCT applicable lifetime range, where conventional approaches are limited [451, 452]. The preceding discussion is also generalizable to EC-delayed α-particle emission, where the proton-decay daughter $(Z-2)$ is replaced by α-decay daughter $(Z-3)$. Another decay channel is EC-delayed γ-ray emission, which can occur either before or after the filling of atomic shell vacancies. However, the resulting X rays are always characteristic of $(Z-1)$ and are therefore insensitive for determining nuclear lifetimes.

So far, PXCT has been applied in the decay studies of six nuclei, as summarized in Table 13. A variation of PXCT has also been applied in p+^{112}Sn [474, 475] and p+^{106}Cd [476] inelastic scattering measurements at 10 and 12 MeV proton incident energies. By measuring X-rays in coincidence with inelastically and elastically scattered protons, the lifetimes of compound nuclear states can be deduced. However, an uncertain factor in this reaction process is

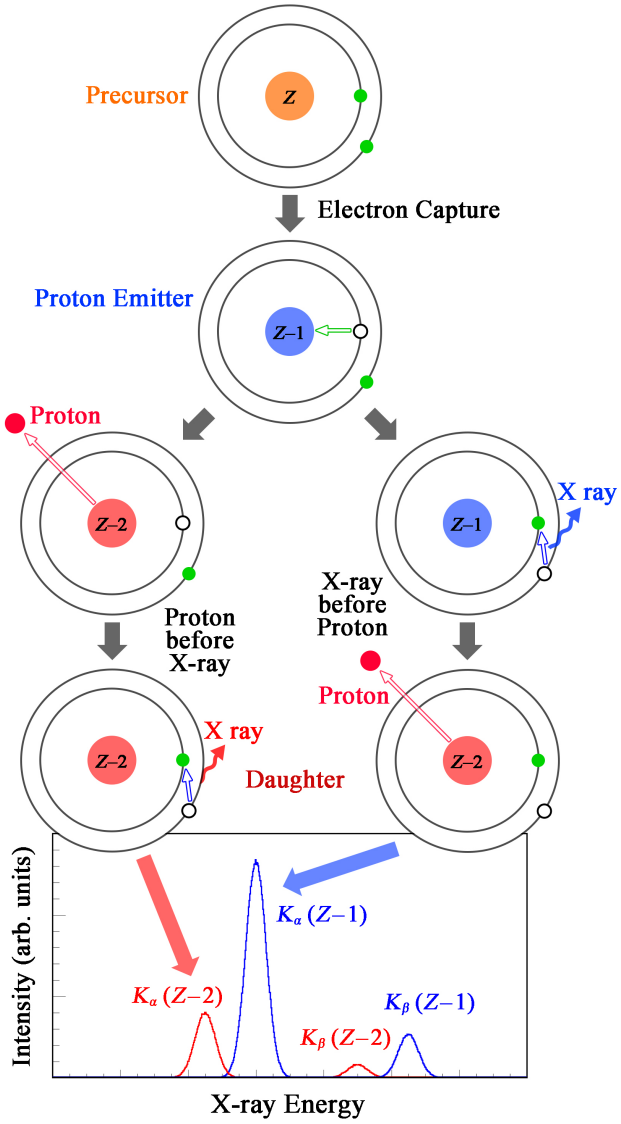

Figure 49: Schematic illustrating electron capture to a proton-unbound excited state and the Particle-X-ray Coincidence Technique.

Table 13: Properties of all nuclei that have been measured with PXCT. Columns 1−7 present the EC/β^+ decay, the half-life ($T_{1/2}$) of the precursor, the β-decay energy ($Q_{\rm EC}$), the proton-separation energy of the EC/β^+-decay daughter (S_p), the total intensity of EC/β^+-delayed protons (I_p), the primary X-ray energies that need to be distinguished, the known lifetime of the K-shell vacancy, and the lifetime range of proton-emitting states of the EC/β^+-decay daughter obtained in each study, respectively. The two K_α energies listed in column 6 correspond to the proton-emission daughter ($Z-2$) and proton emitter ($Z-1$), respectively, which are adopted from Ref. [517] rounded to the nearest 0.1 keV. The last two rows list the properties of ^{60}Ga and ^{64}As for comparison.

EC/β^+-decay	$T_{1/2}$ (s)	$Q_{\rm EC}$ (keV) [428]	S_p (keV) [428]	I_p (%)	$E_{K\alpha}$ (keV) [517]	$\tau_{K\rm shell}$ (fs) [450]	$\tau_{p-\rm emit}$ (fs)
^{65}Ge→^{65}Ga	30.9(5) [453]	6179.3(23)	3942.4(6)	0.011(3) [454, 455, 456]	8.6, 9.2	0.374	≈1.7 [457]
^{69}Se→^{69}As	27.4(2) [458]	6680(30)	3420(30)	0.052(10) [459, 460]	9.9, 10.5	0.315	0.3–3.3 [403, 454, 459]
^{73}Kr→^{73}Br	27.3(10) [461]	7094(9)	3067(7)	0.47(22) [462, 463]	11.2, 11.9	0.264	0.3–2.7 [454, 464, 465]
^{77}Sr→^{77}Rb	9.0(2) [466]	7027(8)	3106(4)	0.08(3) [454, 455]	12.6, 13.4	0.222	≈1.5 [454]
^{113}Xe→^{113}I	2.74(8) [467]	8916(11)	841(12)	7(4) [468]	27.5, 28.6	0.062	0.3–2.9 [468]
^{117}Ba→^{117}Cs	1.75(7) [469]	9040(260)	740(60)	16(3) [470]	29.8, 31.0	0.054	>4.7 [470]
^{60}Ga→^{60}Zn	0.0694(3)[1]	14160(15)[1]	5105.0(4)	1.6(7) [432]	8.0, 8.6	0.406	
^{64}As→^{64}Ge	0.0690(14) [471]	14606(110)[2]	5057(4)	unreported [473]	9.2, 9.9	0.343	

the ionization probability of the K shell during the incoming and outgoing parts of the collision [477, 478]. In the following discussion, we focus on the application of PXCT to EC decay.

In the previous PXCT studies, the proton energy distribution and the X-ray count ratios as a function of coincident proton energies are the most important observables. By tuning the statistical model parameters to reproduce the experimental observables, the model parameters, such as average proton partial widths ($\langle\Gamma_p\rangle$), average γ-ray partial widths ($\langle\Gamma_\gamma\rangle$), and level densities ($\rho$), can be constrained [457, 459, 465, 454].

The initial ρ is typically estimated using the back-shifted Fermi gas model [479, 480]. The initial $\langle\Gamma_\gamma\rangle$ is calculated using γ-ray strength functions [481], which can be parametrized by Lorentzian fits to giant resonance cross-section data [482, 483]. The initial $\langle\Gamma_p\rangle$ is calculated using

$$\langle\Gamma_p\rangle = \frac{\sum_\ell T_\ell(E_p)}{2\pi\rho(E_x, J, \pi)}, \tag{18}$$

where $T_\ell(E_p)$ is the transmission coefficient for protons with energy E_p and angular momentum ℓ, and $\rho(E_x, J, \pi)$ is the level density with spin and parity J, π at excitation energy E_x. $T_\ell(E_p)$ is typically calculated using the optical model. The PXCT experimentally constrained particle transmission coefficients will help benchmark the local optical model potentials in this mass region [484].

In all six cases studied using PXCT (Table 13), only the average lifetimes of proton-unbound states populated by EC were obtained. Individual proton-emitting states could not be fully resolved due to high level densities. Moreover, the applicability of this technique has not been explored in an astrophysical context. We have designed, built, and tested LIBRA to extend PXCT to measure most essential ingredients for calculating reaction rates with the Hauser-Feshbach statistical model Eq. (16) [401]. LIBRA may also be able to identify individual resonances, providing spins and parities, excitation/resonance energies, lifetimes, and p, α, γ decay branching ratios for calculating narrow resonance reaction rates using Eqs. (13) and (15).

EC/β^+ ratios are energy dependent, and in the center of the ^{59}Cu$(p,\gamma)^{60}$Zn Gamow window, when a 1-MeV resonance is populated by allowed ^{60}Ga β transitions, $R_{\rm EC/\beta^+} = 2.0\times10^{-3}$ [445]. The fractional probability of EC occurring in the K shell is 89% [445]. The K-shell fluorescence yield for Zn is 47%, with the remaining 53% attributed to Auger electrons [446]. Additionally, $K_{\alpha1}$ and $K_{\alpha2}$ X rays constitute 59% and 30%, respectively, of the total K X-ray emission [446]. Since their energies are generally indistinguishable in experiments, we collectively refer to these X rays as K_α. Combining these decay probabilities, we estimate that for a 1-MeV resonance in ^{60}Zn populated in ^{60}Ga decay, approximately 7.4×10^{-4} of such events will produce X rays suitable for lifetime analysis.

33. Experimental Setup

33.1. Beam delivery

For the future experiment case study under consideration, the Facility for Rare Isotope Beams (FRIB) linear accelerator [485] will accelerate ^{70}Ge to 249 MeV/nucleon. The reaction products from ^{70}Ge impinging on a rotating carbon transmission target will be separated in flight by the Advanced Rare Isotope Separator [486]. A cocktail fast beam containing ^{60}Ga and some nearby isotones will be slowed down in metal degraders with momentum compression and thermalized in gas stoppers filled with helium [487, 488]. The thermalized ^{60}Ga ions will be drifted by a combination of radio-frequency and direct-current fields towards a nozzle and exit into a radio-frequency quadrupole ion-guide system. The ions will be guided and accelerated to 30 keV before being delivered to the stopped beam area [489]. The scientific user program involving stopped and reaccelerated beams started in 2023, and the beam intensities will continue increasing as the primary beam power gradually ramps up to 400 kW over the coming years. The FRIB beam rate calculator yields a stopped-beam rate of ^{60}Ga of 3×10^5 pps. It should be noted that the calculator assumes optimal conditions and actual rates are likely to be lower than the calculated values [490].

A mechanical design drawing and photograph of LIBRA are shown in Fig. 50. Prior to the experiment, a stable beam around the $A = 60$ region will be tuned into the Faraday cup at the center of the vacuum chamber. After maximizing the beam current, the chamber will be vented and the Faraday cup will be replaced by a thin aluminized Mylar foil tilted at a 45° angle with respect to the beam direction. The ^{60}Ga beam will then be directed into the center of the foil using the previously established beam tune. A 30-keV ^{60}Ga beam can be fully stopped by a Mylar foil as thin as 50 nm [491], in contrast to the 6.5 mm needed to stop a 130-MeV/nucleon ^{60}Ga fast beam [426]. Since fast beams penetrate deeply into materials and would block the emitted X rays and charged particles, we have chosen to use stopped beams instead of fast beams to effectively utilize PXCT.

The highest vacuum reached in our lab testing environment is 1.47×10^{-7} torr.

33.2. Detectors

The detection system consists of a planar germanium detector for X-ray detection, two large-volume coaxial germanium detectors for γ-ray detection, and a silicon telescope for charged-particle detection via energy-loss and residual energy (ΔE-E).

For X-ray detection, we selected a disk-shaped Low Energy Germanium detector (LEGe), Mirion GL0510 [492]. The LEGe detector comprises a Ge crystal with a diameter of 25.0 mm and a thickness of 10.5 mm. LEGe is housed in a flanged-style cryostat with a diameter of 38.1 mm and a 0.13-mm thick Be entrance window. The endcap is inserted into the vacuum chamber with its entrance window 11.0 mm from the center of the chamber. The Ge crystal is positioned 5.6 mm from the entrance window, subtending 10.1% of the 4π solid angle with respect to the center of the chamber. LEGe is fabricated with a thin p^+ contact on the front and side, and a rear n^+ contact that covers less than the full area, resulting in lower capacitance than a similar-sized planar device. Since preamplifier noise is a function of detector capacitance, the low capacitance feature makes LEGe ideally suited for X-ray spectroscopy down to 3 keV.

For γ-ray detection, we selected two Extended Range Coaxial Germanium Detectors (XtRa), Mirion GX10020 [493]. The active volume of XtRa1 has a diameter of 84.8 mm and a thickness of 65.2 mm, while XtRa2 has a diameter of 79.8 mm and a thickness of 80.0 mm. The Ge crystals are positioned 6.8 and 6.3 mm, respectively, from their 0.6-mm-thick carbon composite windows. The XtRa detectors feature a thin window contact on the front surface and an n^+ contact on the periphery, providing a good low-energy response.

All three Ge detectors are equipped with the Cryo-Pulse 5 Plus electrically refrigerated cryostat [494, 495]. The detector housing is connected to a compact cold-head assembly containing a 5-watt pulse tube cooler. The assembly is powered by a bench-top controller, which contains the necessary logic to ensure the safe and reliable operation of the cryostat. During normal operations, the cold tip is maintained at the preset −185 °C. Additionally, a control panel application provides remote control, monitoring, and logging of cryostat status.

If the cold tip temperature rises above −160 °C, the controller will trigger the high-voltage inhibit. If it further rises above −150 °C, the controller will shut down the cooler, forcing the Ge to undergo a full thermal cycle. Once the cold tip temperature reaches 0 °C, the cooler will restart.

A 5-watt pulse tube cooler is integrated into a compact coldhead assembly, which is directly attached to the detector housing. The assembly is connected to a bench-top power controller that provides the required output voltage

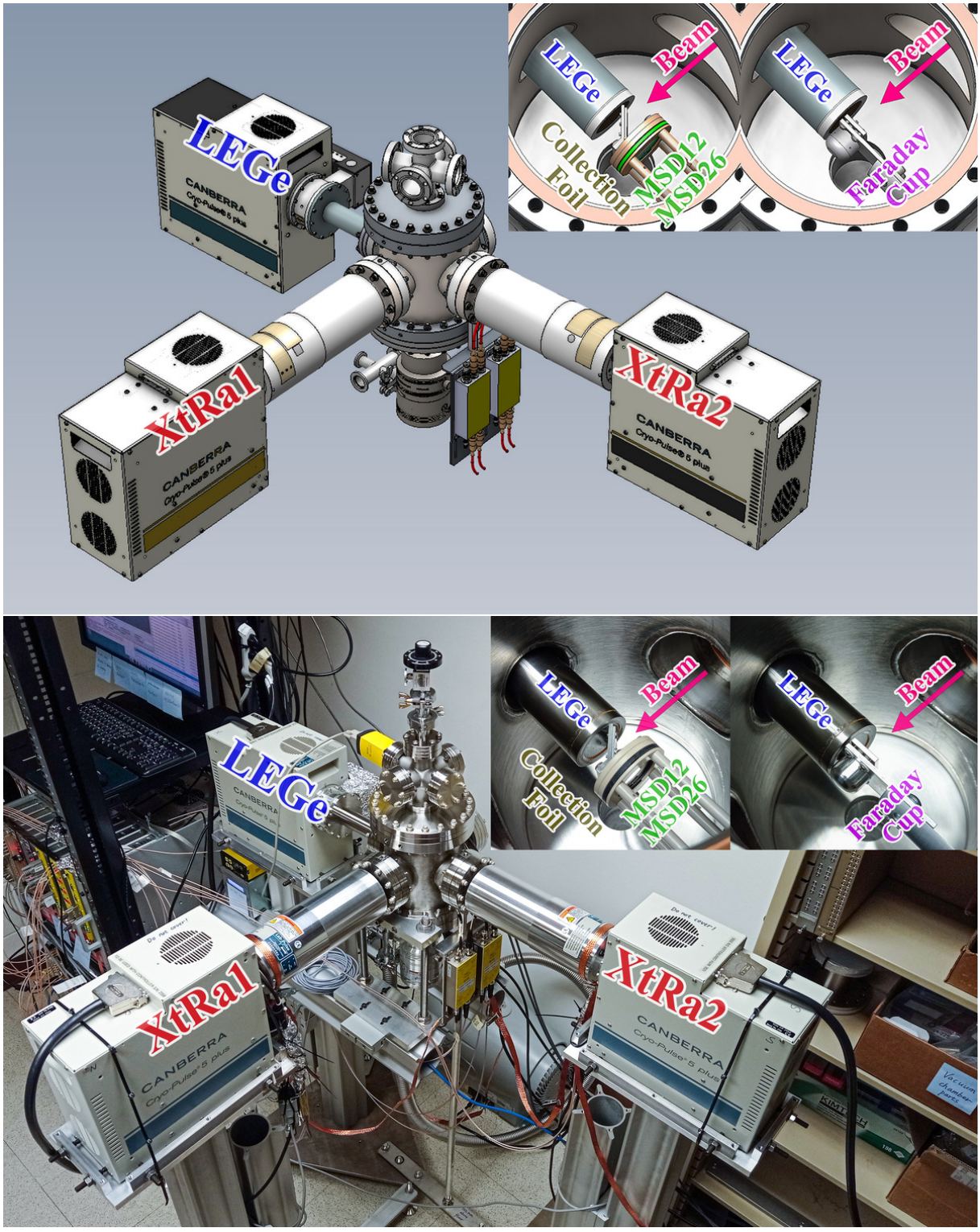

Figure 50: Mechanical design drawing and photograph of LIBRA. The insets highlight two configurations for the detectors inside the central chamber: a Faraday cup with a collimator for beam tuning or a collection foil and Si detectors for decay measurements.

to drive the compressor. The controller also contains the necessary logic to ensure the safe and reliable operation of the cryostat. An RS-232 serial interface and CP5-Plus control panel application are also included, allowing for remote monitoring of the cooler status. The CP5-Plus is extremely reliable, with estimated Mean Time To Failure of 3 million hours [495]. The Cryo-Pulse 5 Plus cryostat is equipped with an active vibration reduction system. An accelerometer inside the coldhead measures the vibrations generated by the compressor and feeds this signal back to the controller. The controller then adjusts the drive signal to the cooler so that vibrations are minimized. The system is even self-tuning such that it adapts to possible changes of the system's vibration characteristics over time. It is currently the best available technology in the field.

For the ΔE-E charged-particle telescope, we selected two single-sided, single-area circular Si detectors manufactured by Micron Semiconductor Ltd. The active volume of MSD12 is 12 μm in thickness and 12 mm in diameter [496], and MSD26 is 1000 μm thick and 26 mm in diameter [497]. The junction side of both MSDs features a 50-nm thick boron-doped silicon dead layer and a 30-μm wide peripheral metal band for wire bonding, leaving the majority of the active area without metal coverage. The Ohmic side of MSD12 has a thicker dead layer of 300 nm with no metal coverage. The Ohmic side of MSD26 has little impact on charged-particle signals, and thus, we opt for the standard 500-nm thick dead layer and 300-nm thick aluminum coverage. Both silicon chips are assembled onto an FR4 printed circuit board. MSD26 is positioned 15.7 mm from the center of the chamber and covers 11.5% of the 4π solid angle. MSD12 is 11.2 mm from the center and defines the solid angle coverage of the ΔE-E telescope at 5.9% of 4π.

The numbers following "MSD" indicate in millimeters. The dead layer window and metallization type for MSD12 are 9.5P/7P, and for MSD26 are 9.5P/2M. Here, 9.5 represents a boron-doped silicon dead layer with a thickness of 50 nm, 7 represents a dead layer with a thickness of 300 nm, and 2 represents a dead layer with a thickness of 500 nm. "P" denotes a periphery metal band with a width of 30 μm around the edge of the active areas and contact pads for wire bonding. The majority of the active area does not have metal coverage. "M" denotes a continuous aluminum coverage with a thickness of 300 nm over the entire active area region.

33.3. Electronics

All three Ge detectors are equipped with Intelligent Preamplifiers (iPA) [498], which incorporate a low-noise field-effect transistor (FET) input circuit optimized for the ultra-high source impedance of Ge detectors. The first stage of the iPA functions as an integrator, providing an output voltage proportional to the accumulated charge. The second stage of the iPA acts as an output buffer and offers four selectable gain settings. The output signal is split into two channels with termination impedances of 93 and 50 Ω, respectively. The iPA memory stores detector leakage currents, temperatures, and preamplifier operating voltages. A control panel application allows for remote monitoring and logging of these parameters. Each iPA is equipped with two 100-Ω Pt resistance temperature detectors thermally connected to the crystal holder (PRTD1) and the cold tip (PRTD2), respectively [499]. The PRTD1 reading represents the temperature of the Ge crystal when they are in thermal equilibrium. If either PRTD exceeds its preset threshold, it can trigger the high-voltage inhibit via the iPA. This mechanism operates independently of the inhibit function via the controller, providing enhanced protection for the detector.

In our lab testing environment, the observed PRTD1 temperatures are −182.7 °C (LEGe), −158.1 °C (XtRa1), and −168.2 °C (XtRa2), which represent the temperatures of the Ge crystals when they are in thermal equilibrium. The nominal PRTD1 temperatures are −182.6 °C (LEGe), −163.6 °C (XtRa1), and −170.9 °C (XtRa2). If either PRTD exceeds its nominal value by 10 °C, it can trigger the high-voltage inhibit via the iPA. This mechanism operates independently of the inhibit function via the controller, providing enhanced protection for the detector.

The Ge is connected to the Intelligent Preamplifier (iPA) [498], which incorporates a low-noise field-effect transistor (FET) input circuit optimized for the ultra-high source impedance of germanium detectors. The input circuits are cooled by mounting them inside the cryostat. The first stage of iPA serves as an integrator, providing an output voltage proportional to the accumulated charge from the detector, and also functions as an electrometer for measuring the leakage current of the detector. The second stage acts as an output buffer and allows for four conversion factors of 50, 100, 250, and 500 mV/MeV.

The included iPA control panel application provides the user with real-time monitoring of the detector current and temperature, along with pertinent internal preamplifier operating voltages. The integrated data logging feature continuously records several of these key operating parameters on a periodic basis, and stores them within the iPA

mass storage memory. The stored data log files can be readily downloaded and viewed. This allows the user to take preventative measures if a key parameter starts to shift and ultimately improves equipment availability and productivity.

The four output gains, as well as external or internal test pulsers, are selectable via the control panel application. iPA is equipped with a warm-up sensor that is thermally connected to the detector. The coldhead is also equipped with temperature sensors. In the event that the temperature exceeds the normal operating range, these sensors trigger the high-voltage inhibit signal from either the preamplifier or the cryostat controller, respectively, providing protection to the Ge detectors.

Two ORTEC 660 Dual Bias Supply modules [500] are used to provide bias voltages to the three Ge detectors. We apply a negative bias to the p^+ contacts of LEGe and a positive bias to the n^+ contacts of XtRa. LEGe becomes fully depleted at −600 V and is recommended to be operated at −1100 V. XtRa1 and XtRa2 become fully depleted at bias voltages of +4000 V and +2200 V, respectively, and both operate at +4500 V. The bias shutdown mode of the ORTEC 660 is set to transistor-transistor logic (TTL) to be compatible with the iPA high-voltage inhibit mode. The typical leakage currents of the two XtRa detectors are below 20 pA and below 100 pA for LEGe. The tail pulses from iPAs exhibit rise times of ≈150 ns (LEGe) and ≈250 ns (XtRa), with a 50-μs decay constant.

A Mesytec MHV 4-channel bias supply module with remote control features provides the bias voltages to the two MSD Si detectors. We apply a negative bias to the p^+ contacts of both MSD detectors through MPR-1 charge-sensitive preamplifiers [501], and the n^+ contacts are grounded. MSD12 has a depletion voltage of −1.5 V and is operated at −3.0 V, and MSD26 has a −90 V depletion voltage and is operated at −130 V. MHV offers a ramp speed as low as 5 V/s to protect the circuits of preamplifiers [502]. MSD12 exhibits a leakage current of approximately 1 nA, while MSD26 exhibits a leakage current of approximately 60 nA. The energy and timing outputs of the MPR-1 are both terminated with 50 Ω impedance. The tail pulses from MPR-1 exhibit rise times of ≈400 ns (MSD12) and ≈70 ns (MSD26), with a 120 μs decay constant. All preamplifiers are powered by two Mesytec MNV-4 NIM power distribution and control modules [503].

33.4. Data acquisition

All preamplifier signals are transmitted through double-shielded RG316 coaxial cables of equal length and then digitized by a 16-bit, 250 MHz Pixie-16 module manufactured by XIA LLC [504] (Fig. 51). The input impedance of each channel in Pixie-16 is switchable between 50 Ω and 1 kΩ. The Digital Data Acquisition System (DDAS) [505, 506] is used for recording and processing data. Trapezoidal filtering algorithms are implemented in both the slow filter for pulse amplitude measurement and the fast filter for leading-edge triggering. The DDAS filter parameters (Table 14) are optimized based on Refs. [506, 507, 508, 509].

The system operates in an internally triggered mode: recording data on a channel-by-channel basis whenever the trigger filter crosses the user-defined threshold. Data from all channels are ordered in time and subsequently assembled into events in software based on a user-defined event window length. Each event is timestamped using a Constant Fraction Discriminator (CFD) algorithm based on the trigger filter response. The event timestamp is counted with 125 MHz clock ticks, i.e., 8 ns intervals.

The pulse amplitude is extracted from the energy filter amplitude at approximately rise time plus gap time after triggering. If a second trigger arrives within the rise time plus gap time window, both events will be flagged as pileup. In the tests conducted in the next section, pileup rejection is turned off in DDAS. As a result, the timestamp of the first event is preserved while the second is discarded for all the tests conducted in the next section. The amplitude of the second event is partially added to that of the first event, with the addition diminishing as the time interval between them increases. The count rate capacity of the detection system is primarily determined by the energy filter parameters selected for each detector.

To assess DDAS live time under our parameter setting, a DB-2 Random Pulser [510] is used to generate pulses with time intervals following a Poisson distribution. The recorded count rates are shown in Fig. 52, and are consistent with the pileup rates defined by the energy filter settings [505]. Furthermore, DDAS can provide real-time spectra for identifying characteristic charged particles and γ rays from decay, aiding in the online identification of radioactive beams.

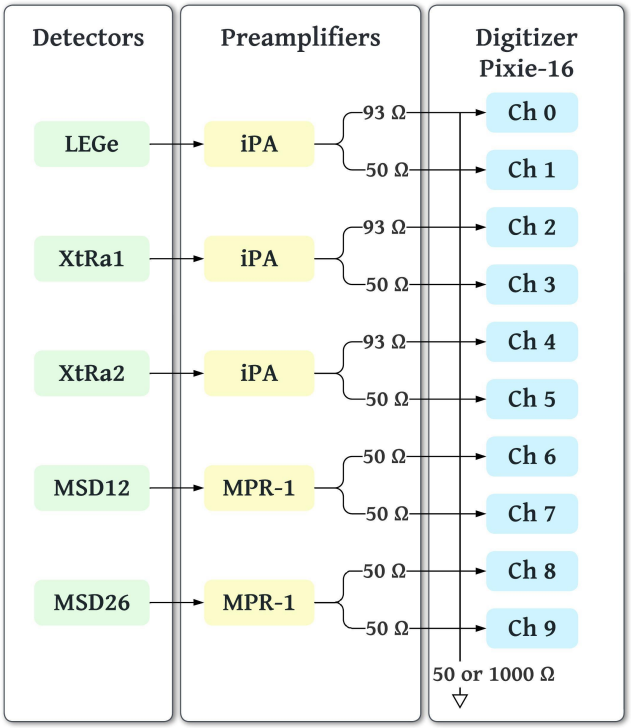

Figure 51: Schematic diagram of the electronics setup. The two arrows following each preamplifier indicate dual outputs with their respective impedance.

Table 14: DDAS trapezoidal filter parameter settings for each detector.

Parameter	LEGe	XtRa1	XtRa2	MSD12	MSD26
Energy T_{Rise} (μs)	7.168	10.240	10.752	9.984	2.048
Energy T_{Gap} (μs)	0.768	1.792	1.280	2.944	1.024
Trigger T_{Rise} (μs)	0.064	0.064	0.064	0.016	0.016
Trigger T_{Gap} (μs)	0.952	0.952	0.952	1.000	1.000
CFD Delay (μs)	0.304	0.304	0.304	0.304	0.304
CFD Scale (μs)	7	7	7	7	7
Tau (μs)	50	50	50	120	120

Table 15: LIBRA detector and instrument specifications.

Specifications	LEGe	XtRa1/North	XtRa2/South	ΔE Si	E Si
Detector Model	GL0510	GX10020	GX10020	MSD012	MSD026
Detector S/N	13725	5593	5596	3/1/3506	3498−25−2
Preamplifier Model	iPA P10	iPA SlimLine10	iPA SlimLine10	MPR−1	MPR−1
Preamplifier S/N	13000040	201216−0207	210610−0560	1021511	1021512
Cryostat Model	Cryo−Pulse 5 Plus FM	Cryo−Pulse 5 Plus SL	Cryo−Pulse 5 Plus SL		
Cryocooler S/N	2751	2749	2750		
Controller S/N	2402	2358	2355		
Endcap Diameter (mm)	38.1	101.6	101.6		
Endcap Length (mm)	203.2	171.45	171.45		
Crystal Diameter (mm)	25.0	84.8	79.8	12	26
Crystal Length (μm)	10.5	65.2	80.0	12	1
Distance from Window (mm)	5.6	6.8	6.3		
Solid Angle Coverage (%)	10.10	1.70	1.51	5.90	11.50
Dead Layer (μm)	5			50 nm/300 nm	50 nm/800 nm
Entrance Window	0.13 mm Be	0.6 mm C	0.6 mm C		
Depletion Voltage (V)	−600	+4000	+2200	−1.5	−90
Recommended Bias Voltage (V)	−1100	+4500	+4500	−3.0	−130
Reported Test Point Voltage (V)	−1.70	−2.40	−0.66		
Measured Test Point Voltage (V)	−1.71	−0.40	−0.66		
Bias Supply	ORTEC 660 Ch A	ORTEC 660 Ch A	ORTEC 660 Ch B	MHV−4 Ch 0	MHV−4 Ch 1
Bias Supply S/N	22004180	22004181	22004181	721242	721242
Power Supply	MNV−4 Ch 4	MNV−4 Ch 1	MNV−4 Ch 2	MNV−4 Ch 4	MNV−4 Ch 3
Power Supply S/N	1021266	1021266	1021266	122278	122278
Measured Leakage Current	0−100 pA	0−20 pA	0−20 pA	1−2 nA	50−100 nA
Measured Leakage Current w/ Source	10−140 pA	50−70 pA	50−70 pA	1−2 nA	50−100 nA
Preamp Output Polarity	Positive	Negative	Negative	Positive	Positive
Preamp Output Gain	x1, x2, x5, x10	x1, x2, x5, x10	x1, x2, x5, x10	40/200 MeV	40/200 MeV
Preamp Output Rise Time	150 ns	250 ns	250 ns	500 ns	70 ns
Preamp Output Fall Time	120 μs	120 μs	120 μs	280 μs	280 μs
Digital Shaping Time Rise Time	7.2 μs	10.2 μs	10.8 μs		
Digital Shaping Time Flat Top	0.8 μs	1.8 μs	1.2 μs		
Capacitance at Recommended Bias	6 pF	23 pF	28 pF		
Maximum Controller Power	180 W	180 W	180 W		
Operating Controller Power	54−70 W	120−160 W	90−120 W		
Nominal PRTD1	−182.6°C	−163.6°C	−170.9°C		
PRTD1 HV−inhibit Threshold	−172.6°C	−153.5°C	−160.9°C		
Measured PRTD1	−182.7°C	−158.1°C	−168.2°C		
Nominal PRTD2	−190.7°C	−198.3°C	−197.6°C		
PRTD2 HV−inhibit Threshold	−180.7°C	−188.2°C	−187.3°C		
Measured PRTD2	−190.7°C	−198.9°C	−197.4°C		
Cold−tip Setpoint	−185°C	−185°C	−185°C		
Nominal Cold−tip Temperature	−185°C	−185°C	−185°C		
Cold−tip HV−inhibit Threshold	−160°C	−160°C	−160°C		
Cold−tip cooler shutdown Threshold	−150°C	−150°C	−150°C		
Recommended Cool−down Time	12 hours	24 hours	24 hours		
Typical Warm−up Time	12−24 hours	12−24 hours	12−24 hours		
Digitizer	XIA Pixie−16 Ch 1	XIA Pixie−16 Ch 3	XIA Pixie−16 Ch 5	XIA Pixie−16 Ch 6	XIA Pixie−16 Ch 8

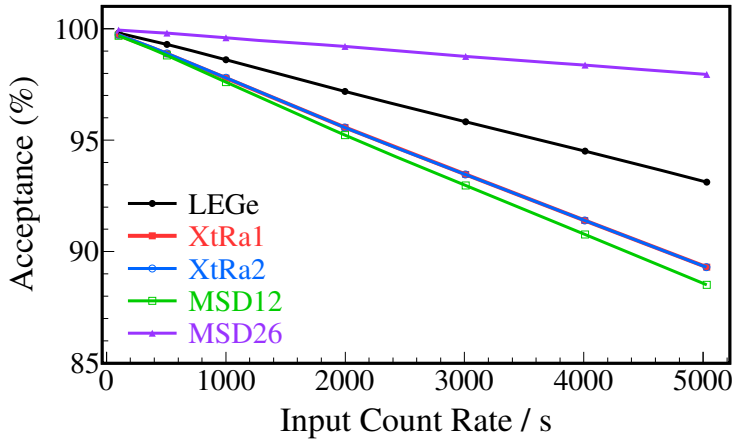

Figure 52: Count rate performance of each detector.

34. Performance Tests

We performed offline tests on LIBRA using the radioactive sources listed in Table 16. An event-build window of ± 1 μs was set, and the count rate of each detector remained below 1500 events per second throughout all conducted tests, except for a LEGe test with the ^{152}Eu source.

34.1. X-ray measurements

We evaluated the performance of LEGe using the ^{55}Fe, ^{152}Eu, and ^{241}Am sources, as shown in Fig. 53. ^{55}Fe EC decays to ^{55}Mn ground state, and the subsequent filling of atomic shell vacancies results in X rays characteristic of Mn. Similarly, Sm X rays mainly result from ^{152}Eu EC. ^{152}Eu decay populates ^{152}Sm/^{152}Gd excited states, which can deexcite via internal conversion (IC), followed by filling of atomic shell vacancies and the emission of X rays characteristic of Sm/Gd. This explains why the observed Gd X rays are much weaker compared to Sm X rays that have two production mechanisms: EC and IC. For ^{241}Am, α decay populates ^{237}Np excited states, where IC serves as the primary mechanism leading to Np X rays. A trace amount of X rays may also arise from inner-shell ionization and excitation caused by perturbations in the electron cloud during nuclear decays [512, 513, 514]. The 0.13-mm-thick Be entrance window is sufficient to block electrons below 125 keV [515], rendering the LEGe detector insensitive to Auger electrons.

The overall energy resolution achieved by LEGe is characterized by fitting X-ray or γ-ray lines with an exponentially modified Gaussian (EMG) function [516] to account for incomplete charge collection at 5.90 keV (Mn $K_{\alpha 1}$), 6.49 keV (Mn $K_{\beta 1}$), 11.89 keV (Np L_{ℓ}), 13.76 keV (Np $L_{\alpha 2}$), 13.95 keV (Np $L_{\alpha 1}$), 26.34 keV (^{237}Np γ),

Table 16: Characteristics of the radioactive sources used in the LIBRA detector tests. Columns 2–7 present the source nuclides, main decay modes, actual activities (A), relative uncertainties of the activities (σA), active diameters (D), and half-lives ($T_{1/2}$), respectively.

No.	Nuclide	Decay	A (Bq)	σA (%)	D (mm)	$T_{1/2}$ (yr)[1]
SS Z7212	^{55}Fe	EC	1.11×10^4	–[2]	9.5	2.756
I7281	^{60}Co	β^-	3.73×10^4	3	1	5.271
M4038	^{137}Cs	β^-	3.00×10^3	3	3	30.007
C169729	^{148}Gd	α	2.86×10^4	–[2]	5	86.9
Z2707	^{152}Eu	EC/β^-	3.10×10^4	1.4	3	13.517
Z7117	^{241}Am	α	3.44×10^3	2.7	3	432.6

33.20 keV (^{237}Np γ), 39.52 keV (Sm $K_{\alpha 2}$), 40.12 keV (Sm $K_{\alpha 1}$), 45.29 keV (Sm $K_{\beta 3}$), 45.41 keV (Sm $K_{\beta 1}$), and 59.54 keV (^{237}Np γ). The manufacturer specifies the full width at half maximum (FWHM) values for LEGe as 0.218 keV at 5.9 keV (^{55}Fe) and 0.514 keV at 122 keV (^{57}Co), respectively. Figure 53 demonstrates that the observed energy resolution aligns with these specifications. We then interpolated the FWHM values at the energies of interest, 8.05 keV (Cu $K_{\alpha 1}$) and 8.64 keV (Zn $K_{\alpha 1}$), to be 0.238(8) and 0.241(7) keV, respectively, demonstrating sufficient resolution to distinguish between the key X rays of Zn and Cu in our case study.

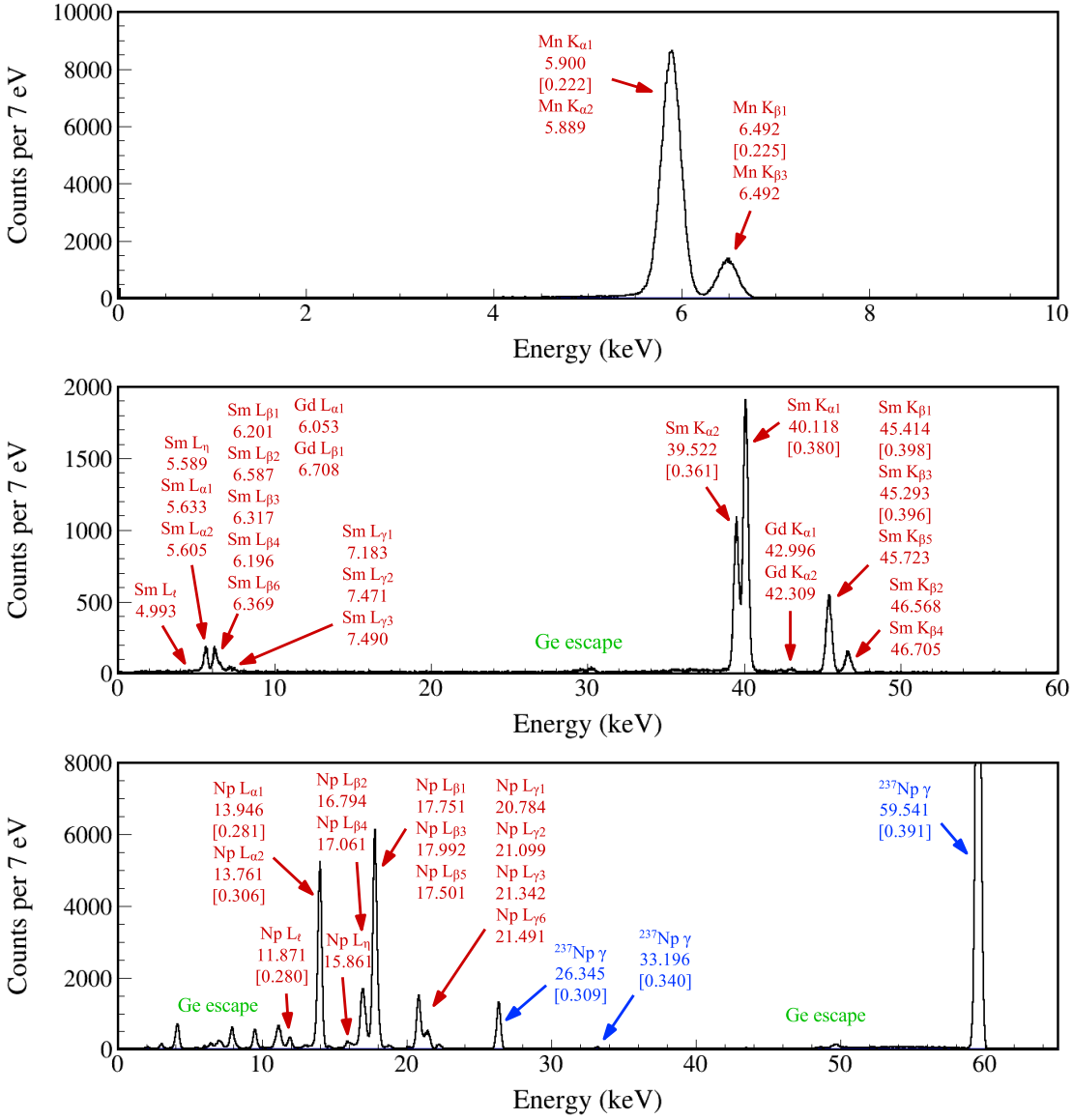

Figure 53: X-ray and/or γ-ray spectra measured by the LEGe detector using the ^{55}Fe (top), ^{152}Eu (middle), and ^{241}Am (bottom) sources. X-ray energy values are adopted from Ref. [517] rounded to the nearest 0.001 keV. γ-ray energy values are adopted from Ref. [518] rounded to the nearest 0.001 keV. FWHM values used to characterize the energy resolution of LEGe are indicated within brackets.

For photons below 100 keV interacting with Ge, the photoelectric effect is predominant, i.e., the photon is absorbed, and a photoelectron is ejected by the Ge atom. When the resulting atomic shell vacancy is filled, X rays characteristic of Ge may be created. A full-energy peak is still observed if these X rays are reabsorbed near the

original interaction site. However, if the photoelectric interaction occurs near the surface of Ge, the X rays are more likely to escape, which results in peaks usually at 9.89 and 10.98 keV below the photopeaks, known as the Ge escape peaks (Fig. 53). These energy differences correspond to the characteristic K_α and K_β X-ray energies for Ge, respectively [517].

We evaluated the detection efficiency of LEGe using the X rays from the ^{152}Eu source placed at the center of the chamber tilted at a 45° angle with respect to LEGe. ^{152}Eu emits Sm L X rays at 5.0 keV (L_ℓ), 5.6 keV (L_η, L_α), 6.2 keV (L_β), and 7.2 keV (L_γ). The Gd L X rays are approximately half a keV higher but with two orders of magnitude lower intensities. We adopted the total L X-ray emission probability from Ref. [519] and deduced the absolute intensities for each of the 4 groups of X rays based on the relative emission probabilities reported by Ref. [520]. The corresponding efficiencies are indicated by the four low-energy data points in Fig. 54. We also measured the X rays from the ^{241}Am source placed at the center of the chamber. ^{241}Am emits Np L X rays at 11.9 keV (L_ℓ), 13.9 keV (L_α), 15.9 keV (L_η), and 17.0 keV (L_β) [521]. The corresponding efficiencies are indicated by the four high-energy data points in Fig. 54.

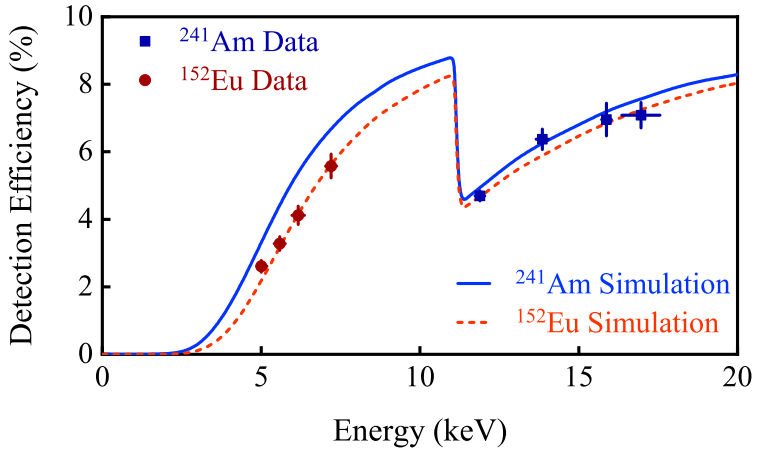

Figure 54: Absolute X-ray photopeak detection efficiency of the LEGe detector obtained using the Sm L_ℓ, L_η + L_α, L_β, and L_γ X rays from the ^{152}Eu source and Np L_ℓ, L_α, L_η, and L_β X rays from the ^{241}Am source, each placed at the center of the chamber. The red dashed and blue solid curves represent the GEANT4 simulated efficiencies according to the ^{152}Eu and ^{241}Am source configurations, respectively. The error bars along the x-axis also reflect the energy span for the multiple X rays within each group.

We simulated the X-ray detection efficiencies using GEANT4 [522, 523]. The simulation incorporates the geometric configuration of the setup and the LEGe detector response, which was characterized by fitting the measured X-ray lineshapes in Fig. 53 with the EMG function. Monoenergetic X rays are emitted isotropically from the source position and interact with the surrounding materials. The simulation outputs an energy spectrum, from which we obtain the detection efficiency by dividing the counts in the X-ray peak by the number of emitted X rays. This process was repeated at different energies to generate the efficiency curves shown in Fig. 54.

For photon energies just above the K-shell binding energy of Ge, 11.1030(20) keV [517], the incident photon is strongly absorbed without deep penetration beyond the detector surface. The subsequent characteristic K X rays of 9.7−11.1 keV tend to escape. However, for photons just below the Ge K-shell binding energy, K-shell absorption is no longer possible, and L-shell interactions dominate. In this case, incident photons tend to penetrate somewhat deeper, and the chance of escape of the fluorescent Ge L X rays of 1.0−1.4 keV is significantly lower. This phenomenon abruptly changes the full-energy detection efficiency of X rays near the K-shell absorption edge [524]. The ^{241}Am source used for this test is an open source, while the ^{152}Eu source is encapsulated between two 60-μm-thick Mylar tapes. The Mylar layer attenuates low-energy X-rays, but its impact diminishes for X rays above 10 keV. Additionally, the LEGe count rate was ≈3000 pps during the ^{152}Eu test but only ≈200 pps during the ^{241}Am test, resulting in different DDAS live time (Fig. 52). Therefore, the ^{152}Eu efficiency curve represents a lower limit, while the ^{241}Am efficiency curve represents an ideal setting. The ^{60}Ga experimental condition is expected to fall between these two scenarios, and we estimate the X-ray efficiencies at 8.0 and 8.6 keV to be 6.5−7.4% and 7.0−7.8%, respectively.

34.2. γ-ray measurements

Figure 55 shows the γ-ray spectra measured by XtRa1 and XtRa2 using the ^{152}Eu source. We first placed the source at the midpoint between the two XtRa detectors that were facing each other, with a distance of 28 cm between them. Both XtRa detectors exhibit good low-energy response to the ^{152}Sm X rays at 40 keV. We then placed the source at the center of the vacuum chamber to determine the absolute γ-ray detection efficiencies. The two XtRa detectors were placed as close as possible to the two flanges (Fig. 50), with their entrance windows about 12 mm from the flange surface. The XtRa1 Ge crystal has a slightly larger diameter than that of XtRa2. Both Ge crystals are 158.5 mm from the target center, covering 1.70% and 1.51% of the 4π solid angle, respectively. Both XtRa detectors record an average of ≈300 room background γ rays per second in our laboratory test environment. The manufacturer specifies the FWHM values for XtRa1 and XtRa2 as 0.998 and 1.065 keV at 122 keV (^{57}Co), and 1.879 and 1.926 keV at 1332 keV (^{60}Co), respectively. The insets of Fig. 55 demonstrate that the observed energy resolution using the ^{152}Eu source aligns with these specifications. The absence of X-ray peaks in the second test (lower panel of Fig. 55) is due to the 3.175-mm-thick stainless steel flanges of the chamber effectively blocking the X rays.

We also measured the γ-ray detection efficiencies using the ^{60}Co and ^{137}Cs sources placed at the center of the chamber. MSD12 was not in place during these tests due to its fragility. MSD26 and the Si detector holders attenuated the γ rays from the source to XtRa2 but had little effect on XtRa1. Based on an exponential function that contains a polynomial of degree i with the natural logarithm of the energy E, $\varepsilon(E) = \exp\left[\sum_{i=0}^{6} p_i \ln(E)^i\right]$ [526], fit on all the data points, we obtain the photopeak efficiencies of 0.334(3)% and 0.286(3)% at 1 MeV, respectively, for XtRa1 and XtRa2. The error bars on the data points reflect the uncertainty of the γ-ray yields and the source activities, with an additional 2.5% uncertainty to account for the true coincidence summing effect [527, 528], which was estimated based on the observed 1173-1332-keV γ cascade from ^{60}Co.

We used GEANT4 simulation [522, 523] to extend the γ-ray detection efficiency curve to high energies (Fig. 56). The simulation takes into account the geometry of the setup and the detector response characterized by fitting the measured γ-ray lineshapes with the EMG function. Monoenergetic γ rays were emitted isotropically according to the source distribution and interacted with the surrounding materials. The photopeak efficiency was extracted from the output spectrum. We then fit the ratio of the simulated efficiency to the measured efficiency in the range 0.5−1.5 MeV and obtained energy-independent ratios of 0.875(10) and 0.837(10) for XtRa1 and XtRa2, respectively, which serve as the normalization factors to match the simulation with the experimental data. One of the factors that reduces the measured efficiency is the data acquisition event loss, which is estimated to be 3.3%, 0.7%, and 2.1% based on the count rates during the ^{60}Co, ^{137}Cs, and ^{152}Eu tests, respectively (Fig. 52).

34.3. Charged-particle measurements

Figure 57 shows the α spectrum measured by MSD26 alone using the ^{241}Am source, with a 2-mm-diameter aperture installed in front. An EMG fit of the main peak at 5485.56 keV yields a FWHM value of 17.0 keV, corresponding to an energy resolution of 0.31%. For comparison, the manufacturer specifies the FWHM values for MSD26 as 26.7 and 35.4 keV, respectively, with different bias settings. MSD12 alone is too thin to stop α particles above 3 MeV, and we demonstrate the ΔE-E α spectra measured by the telescope formed by MSD12 and MSD26 in Fig. 58. An EMG fit of the energy-sum peak yields a FWHM value of 52.1 keV, corresponding to an energy resolution of 0.95%. This resolution is better than that of the Si telescopes used in the previous ^{60}Ga experiment [432], where FWHM values for ^{148}Gd (E_α = 3182.68 keV [529]) were reported to be 100 and 90 keV for the ΔE and 50 and 60 keV for the E detectors.

MSD26 was calibrated using the ^{148}Gd and ^{241}Am sources. We then measured the residual energy of ^{241}Am α particles in MSD26 with MSD12 installed in front of it. This allowed us to accurately determine the effective thickness of MSD12 to be 11.65(8) μm after subtracting the 0.35 μm dead layer thickness [491]. The total thickness of MSD12 is in agreement with the nominal value of 12 μm specified in the Micron datasheet [496].

34.4. Electron measurements

Figure 59 shows the electron spectra measured by MSD26 using the ^{137}Cs source placed at the center of the chamber facing MSD26. The source is deposited on a 64.4-μm-thick aluminized Mylar disk and covered with a 6.3-μm-thick Kapton window. The spectrum exhibits a continuum of electrons from ^{137}Cs β^- decay, along with distinct electron peaks from IC. The main β^- decay branch has an endpoint energy of 514 keV and the IC peaks

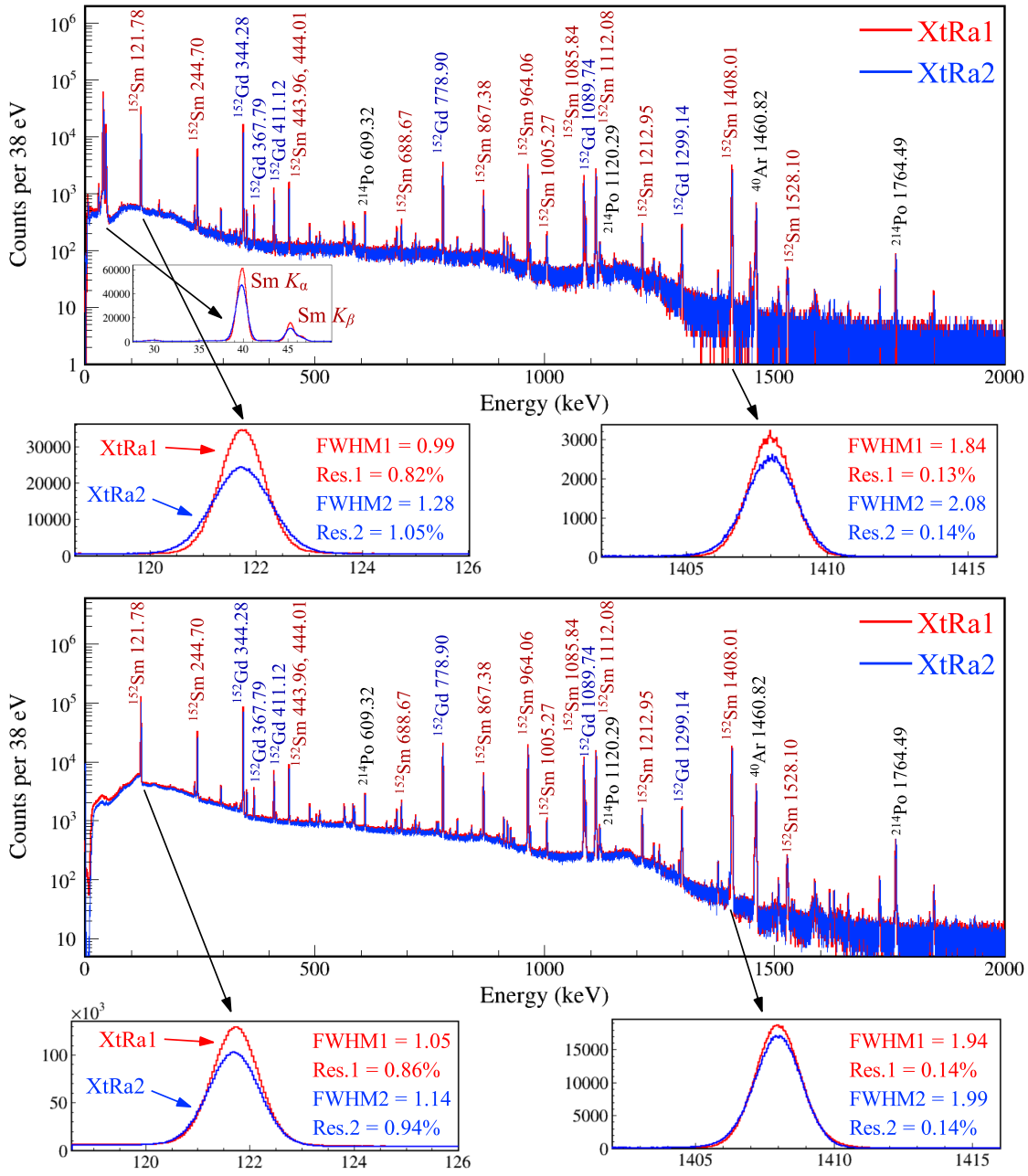

Figure 55: γ-ray spectra measured by XtRa1 (red) and XtRa2 (blue) using the ^{152}Eu source. Upper panel: the ^{152}Eu source is placed in the middle of the two XtRa facing each other. Lower panel: the ^{152}Eu source is placed at the center of the vacuum chamber, with the two XtRa detectors positioned according to the Fig. 50 configuration. All the γ-ray energy values are adopted from Ref. [525] rounded to the nearest 0.01 keV. The insets demonstrate the detector responses at 122 and 1408 keV.

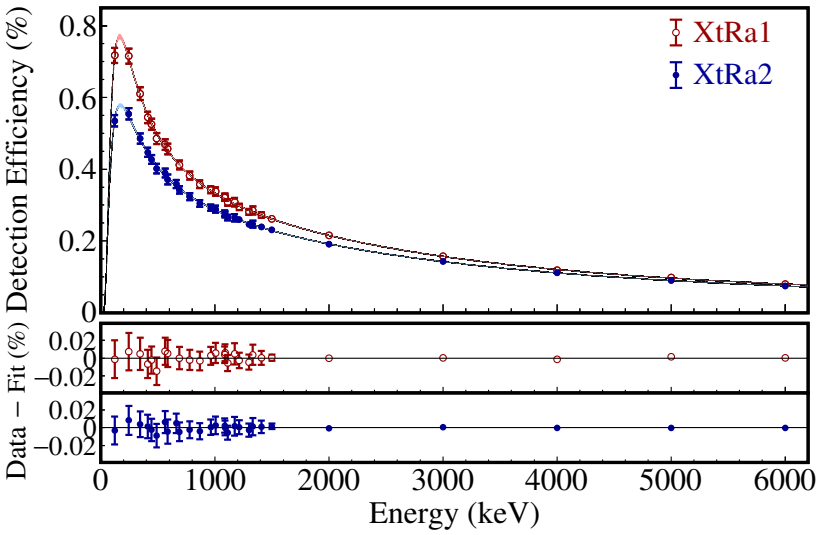

Figure 56: Absolute γ-ray photopeak detection efficiency of the two XtRa detectors obtained using the ^{152}Eu, ^{137}Cs, and ^{60}Co sources placed at the center of the chamber. The ^{137}Cs data point at 662 keV is only applicable to XtRa2 due to the source placement. The six data points above 1408 keV are GEANT4 simulated efficiencies scaled by a factor to match the low-energy source data. The efficiency curves are generated by fitting all measured and simulated data points.

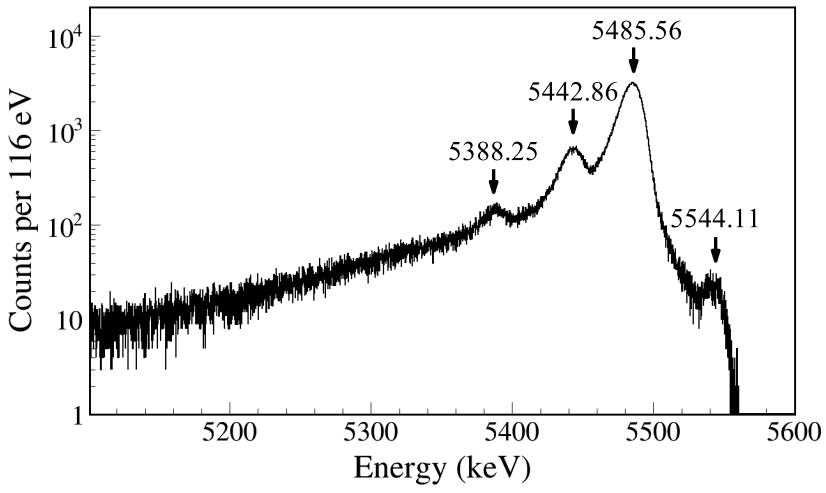

Figure 57: α spectrum measured by MSD26 using the ^{241}Am source. The α energy values are adopted from Ref. [521] rounded to the nearest 0.01 keV. The FWHM value at 5485.56 keV is 17.0 keV, corresponding to an energy resolution of 0.31%.

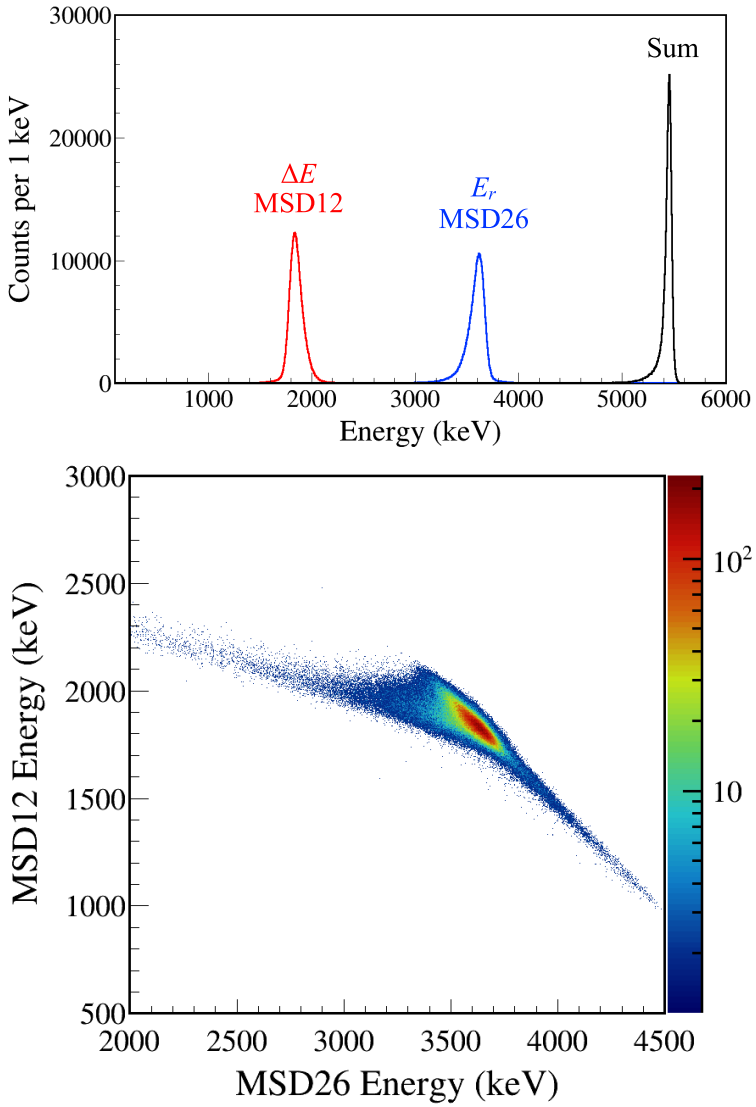

Figure 58: Upper panel: ^{241}Am α-energy spectra measured by MSD12 (energy loss) and MSD26 (residual energy). The FWHM value of the sum peak is 52.1 keV, corresponding to an energy resolution of 0.95%. Lower panel: ΔE-E 2D plot.

are characterized by the energy differences between the 662-keV ^{137}Ba isomeric transition and the Ba atomic shell binding energies. Using the counts in the IC peaks measured by MSD26 alone, the total IC electron emission intensity of 9.56(14)% per ^{137}Cs decay [530], and the source activity (Table 16), we estimate the detection efficiency of MSD26 for ^{137}Ba IC electrons to be 9.0(3)%.

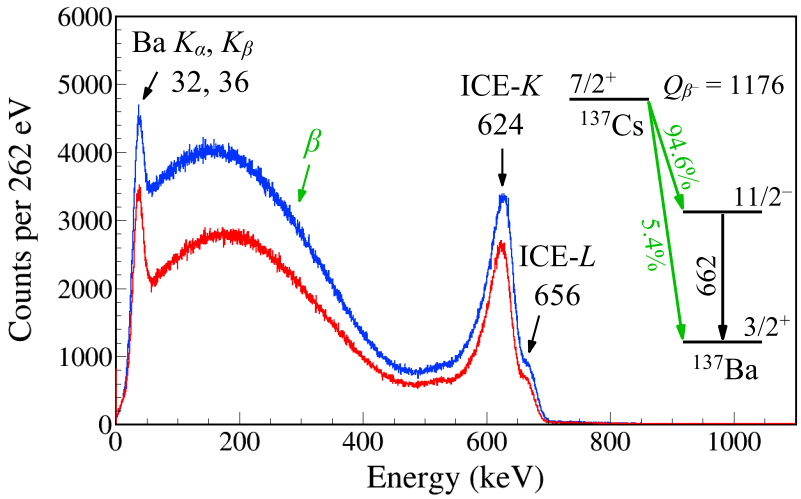

Figure 59: Electron spectra measured by MSD26 using the ^{137}Cs source. The spectrum with lower statistics (red) was obtained with MSD12 installed between the source and MSD26. The spectrum with higher statistics (blue) was acquired over an equal time period with MSD12 removed. Electrons from ^{137}Cs β^- decay form the continuum. ICE-K and ICE-L denote the internal conversion electrons ejected from Ba K and L atomic shells, respectively. The low-energy peak is mainly from Ba K_α X rays at 32 keV and K_β X rays at 36 keV. All energy values are adopted from Ref. [530] rounded to the nearest keV. A simplified ^{137}Cs decay scheme shows the main decay branches.

34.5. Coincidence measurements

Figure 60 shows the α-γ coincidence spectrum between the MSD telescope and LEGe with the ^{241}Am source placed at the center of the chamber. The source faces the MSD, and its 127-μm-thick Pt substrate attenuates most of the low-energy photons emitted towards LEGe, leaving mainly the 59.5-keV ^{237}Np γ ray and its escape peaks observable.

We placed the ^{152}Eu source at the center of the chamber. Figure 61 shows the XtRa1 γ spectra gated by the Sm K X rays measured by LEGe and gated by the electrons measured by MSD26. By applying the characteristic X-ray coincidence condition, both the room background γ rays and the ^{152}Gd γ rays are substantially suppressed. Conversely, the electron coincidence condition suppresses the room background and the ^{152}Sm γ rays. Quantitatively, at 1 MeV, the background levels per 152-eV bin decrease from approximately 625 counts in the raw spectrum to 21 and 3 counts in the X-ray-gated and electron-gated spectra, respectively. Having the ability to detect electrons and positrons will help clean up the spectrum in radioactive beam measurements, thereby facilitating the identification of γ ray origins.

34.6. Timing performance

The timing performance of the electronics was first tested using a Canberra Model 1407P Pulse Pair Generator [531]. The dual pulses were separately fed into two Pixie-16 channels. The FWHM resolution of the time-difference distribution is estimated to be 0.46 ns. Then, the primary pulse was split and fed to each test input of preamplifiers, and the resulting FWHM timing resolutions are 37.4 ns (MSD12), 4.4 ns (MSD26), 1.2 ns (XtRa1), and 1.8 ns (XtRa2).

The timing performance of the detectors was studied using each of the ^{60}Co, ^{152}Eu, ^{241}Am sources placed at the center of the chamber. ^{60}Co provides γ-γ coincidences to test the two XtRa detectors, ^{152}Eu provides X-γ coincidences to test LEGe and XtRa, and ^{241}Am provides α-γ coincidences to test MSD and LEGe. Figure 62 shows the time

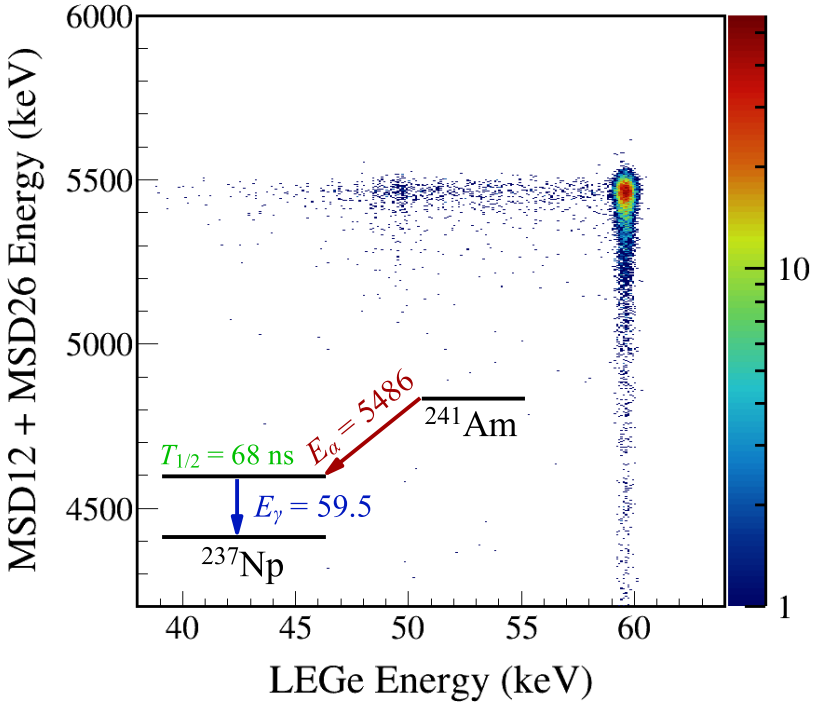

Figure 60: Coincidence spectrum between the MSD detector telescope and LEGe obtained using the ^{241}Am source placed at the center of the chamber. A simplified ^{241}Am decay scheme shows the dominant α-γ sequence.

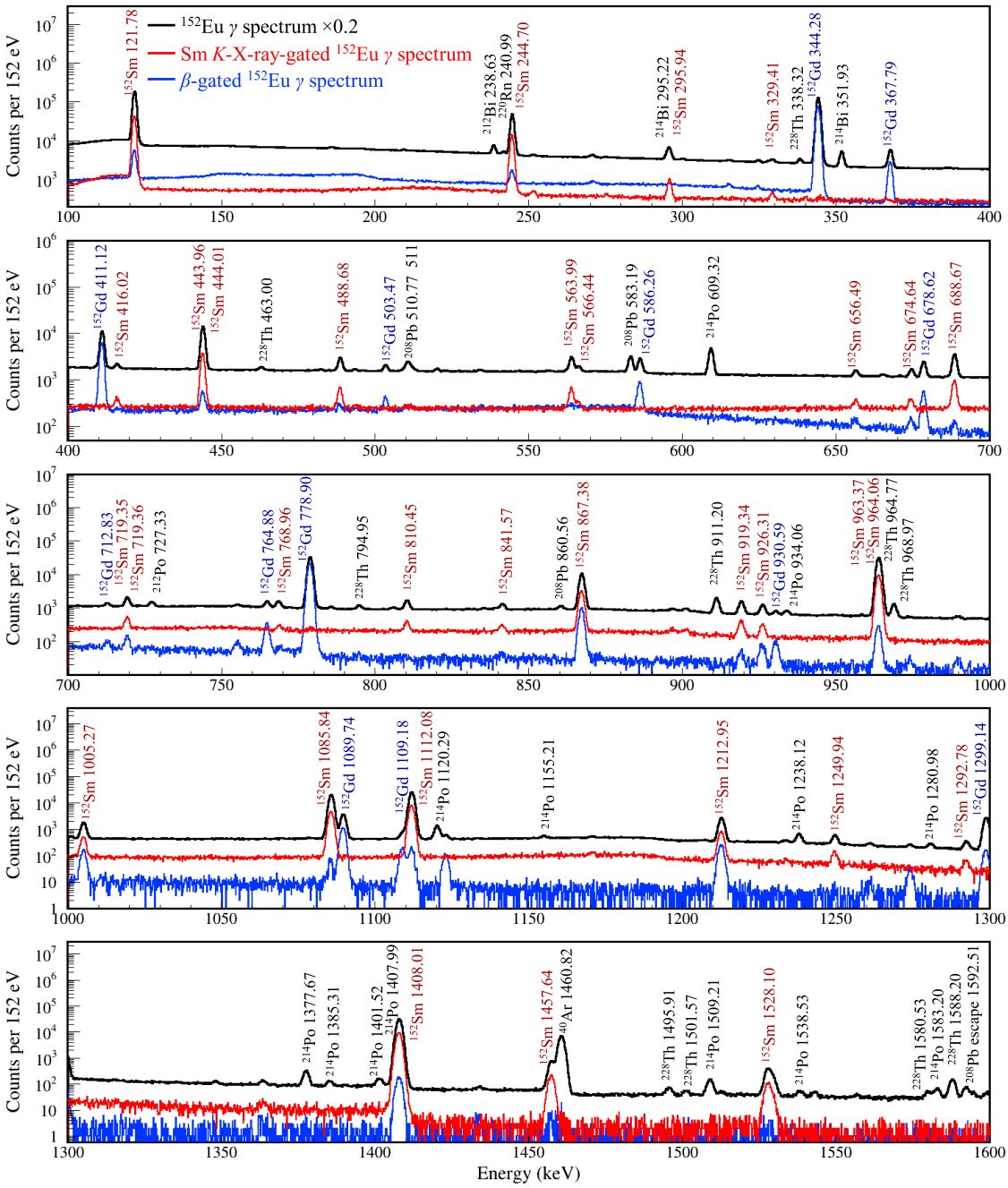

Figure 61: Black spectrum with the highest statistics represents the raw γ-ray spectrum measured by XtRa1 using the ^{152}Eu source placed at the center of the chamber. The red spectrum with intermediate statistics represents the XtRa1 γ-ray spectrum gated by the Sm K_α and K_β X rays measured by LEGe. The blue spectrum with the lowest statistics represents the XtRa1 γ-ray spectrum gated by the electrons measured by MSD26. The raw (black) spectrum is scaled down by a factor of 5 for better comparison.

difference distributions between each coincidence. Based on these measurements, an event-build window of a few hundred ns can be defined to capture all prompt coincidences and some chance continuum for background subtraction in offline analysis. The asymmetric tail in both α-γ time difference distributions is attributed to the relatively long-lived 59.5-keV excited state of ^{237}Np.

Figure 63 shows the α-γ time difference distribution constructed by the start timestamps from 5486-keV α measured by the two MSDs and the stop timestamps from the 59.5-keV γ ray deexciting the 59.5-keV state in ^{237}Np measured by LEGe. By fitting the time spectra with a function

$$f(t; N, T_{1/2}, B) = \frac{N \ln(2)}{T_{1/2}} \exp\left[-\frac{t \ln(2)}{T_{1/2}}\right] + B \tag{19}$$

composed of the total number of decays (N), the exponential decay half-life ($T_{1/2}$), and a constant background (B), we obtained the half-life of the 59.5-keV excited state in ^{237}Np to be $T_{1/2}$ = 68.1(6) ns (MSD12) and 67.9(5) ns (MSD26), respectively. The results obtained from both Si detectors are consistent with recent precision measurements of 67.86(9) ns [532], 67.60(25) ns [533], and 67.60(20) ns [534].

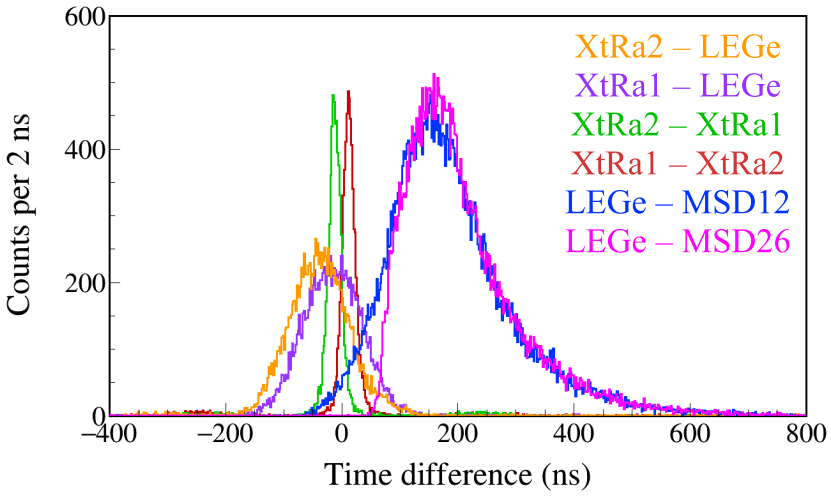

Figure 62: Coincidence time spectra between each detector pair. From left to right: the six time peaks correspond to three decay sequences: the ^{152}Eu 40–46-keV and 1408-keV X-γ coincidences measured by XtRa-LEGe, the ^{60}Co 1173-keV and 1332-keV γ-γ coincidences measured by XtRa-XtRa, and the ^{241}Am 5486-keV and 59.5-keV α-γ coincidences measured by LEGe-MSD. In each decay sequence, the timestamp of the prior event is subtracted from the timestamp of the subsequent event.

In summary, the detectors selected for our setup all feature minimal or zero dead layers in front of their active regions. The mechanical assembly is designed to be compact and employs thin materials in the transmission path to mitigate attenuation, thereby maximizing detection efficiencies. Furthermore, the design also allows for the flexible combination of individual detectors for various experimental purposes. The two XtRa detectors have been coupled with a silicon cube [535, 536] and with a Time Projection Chamber [537]. We also have the option to engineer the integration of LEGe and the central chamber with larger detector arrays, such as the DEcay Germanium Array initiator (DEGAi) and ultimately DEGA of the FRIB Decay Station [538], to achieve a higher γ-ray detection efficiency.

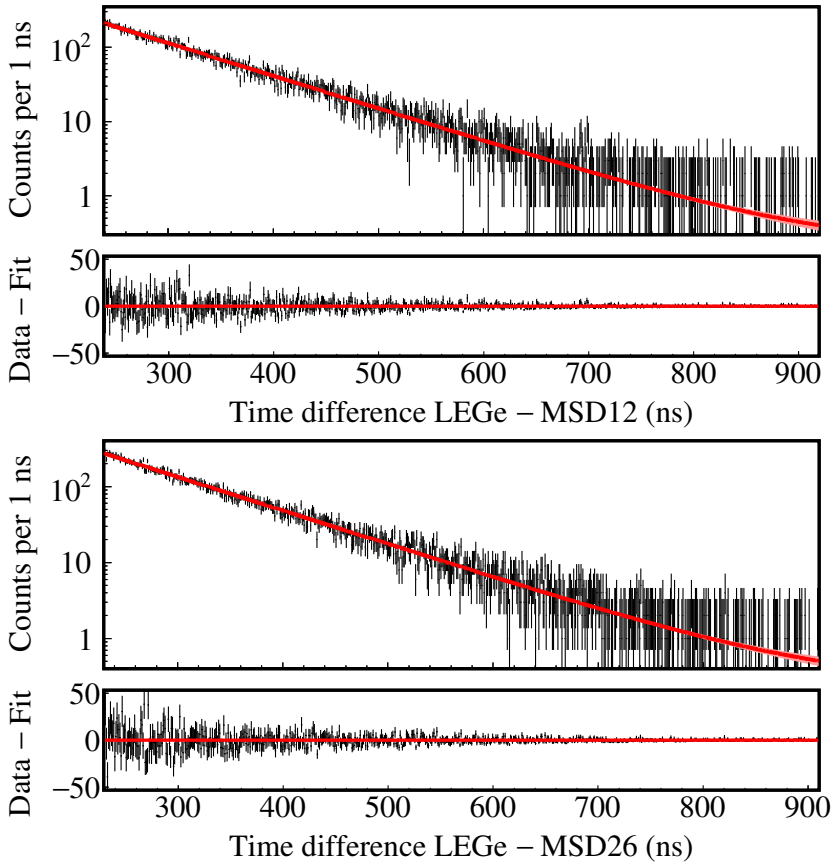

Figure 63: Time differences between the 59.5-keV ^{237}Np γ-ray signals in LEGe and the 5486-keV ^{241}Am α signals in the MSD silicon detector telescope. By fitting the LEGe-MSD12 time difference (upper), we obtain the half-life of the second excited state of ^{237}Np to be $T_{1/2}$ = 68.1(6) ns with p value = 0.34 and χ^2_ν = 1.02, by dividing the χ^2 value by the number of degrees of freedom. From the LEGe-MSD26 time difference (lower), we obtain $T_{1/2}$ = 67.9(5) ns, p value = 0.88, and χ^2_ν = 0.94.

35. Calculations

Table 17: Properties of potentially important ^{59}Cu$(p,\gamma)^{60}$Zn resonances predicted by the shell model. The values in the first through tenth columns represent the spin and parity (J^π), excitation energy (E_x), resonance energy (E_r), partial decay widths (Γ_γ, Γ_p, Γ_α), lifetime (τ), log ft value and β-feeding intensity (I_β) for ^{60}Ga decay, and ratio of EC/β^+ feeding [445].

J^π	E_x (keV)	E_r (keV)	Γ_γ (eV)	Γ_p (eV)	Γ_α (eV)[1]	τ (fs)	log ft	I_β (%)	R_{EC/β^+}
2^+	5501	396	3.8×10^{-2}	7.4×10^{-10}	2.9×10^{-7}	17.3	5.463	0.314	1.6×10^{-3}
1^+	5566	461	6.4×10^{-2}	1.5×10^{-7}	0	10.3	4.708	1.713	1.6×10^{-3}
2^+	5645	540	1.9×10^{-1}	2.1×10^{-6}	1.1×10^{-6}	3.5	6.146	0.060	1.7×10^{-3}
2^+	5989	884	3.3×10^{-2}	4.7×10^{-3}	1.6×10^{-5}	17.5	5.367	0.287	1.9×10^{-3}
2^+	6072	967	2.5×10^{-1}	5.7×10^{-2}	2.9×10^{-5}	2.1	5.536	0.184	2.0×10^{-3}
1^+	6305	1200	2.0×10^{-1}	2.1×10^{-1}	1.3×10^{-27}	1.6	7.035	0.005	2.2×10^{-3}

To enhance our understanding of ^{60}Ga decay properties, we performed shell-model calculations in the truncated fp-shell model space with the GPFX1A Hamiltonian [539] using the NuShellX@MSU code [540]. The newly evaluated ^{60}Ga Q_{EC} = 14160(15) keV [429, 430, 431] was incorporated into the calculation. We obtained 900 ^{60}Zn states populated by ^{60}Ga decay up to E_x = 12.6 MeV, with 300 states each for $J^\pi = 1^+, 2^+, 3^+$. A quenching factor q^2 = 0.6 for the matrix elements of the Gamow-Teller operator was used to calculate the β feedings in ^{60}Ga decay. We calculated the decay widths Γ_γ and Γ_p for 128 resonances with $J^\pi = 0^+, 1^+, 2^+, 3^+, 4^+, 5^+$ up to E_x = 7.3 MeV, corresponding to the upper end of the ^{59}Cu(p,α) Gamow window at 1.5 GK. We also calculated the average decay widths Γ_γ, Γ_p, and Γ_α using the statistical model code SMARAGD [541, 542]. We adopted the shell-model calculated Γ_γ and Γ_p and the statistical-model calculated Γ_α to calculate the ^{59}Cu$(p,\gamma)^{60}$Zn and ^{59}Cu$(p,\alpha)^{56}$Ni reaction rates by combining all 128 positive parity resonances. The fractional contributions of each resonance are shown in Fig. 64. The statistical model calculation indicates that the level densities for 1^- and 2^- states in ^{60}Zn fall below 1 MeV^{-1} at excitation energies of 7.2 and 6.9 MeV, respectively. This suggests that $\ell = 0$ resonances are less likely to be present within the Gamow window and to significantly contribute to the total reaction rate. Table 17 summarizes the properties of the six most influential ^{59}Cu$(p,\gamma)^{60}$Zn $\ell = 1$ resonances. It should be noted that the uncertainties of the excitation/resonance energies are on the order of 200 keV. The resonances listed in Table 17 are not necessarily the specific resonances that our experiment aims to identify but rather represent a typical potential scenario that we may encounter. As realistic Γ_α values vary much more than the average Γ_α calculated by the statistical model, it is likely that the influential ^{59}Cu$(p,\alpha)^{56}$Ni resonances are fewer than those labeled in the lower panel of Fig. 64. Any ^{60}Zn resonances that we are able to discover through ^{60}Ga β decay will provide valuable experimental constraints on the ^{59}Cu$(p,\gamma)^{60}$Zn and ^{59}Cu$(p,\alpha)^{56}$Ni reaction rates.

A theoretical reaction rate calculation with principled uncertainty quantification will be discussed in a forthcoming paper [543], in which all the nuclear physics properties entering into the reaction rate calculation will be sampled according to appropriate probability density functions [544, 545, 546, 547, 548].

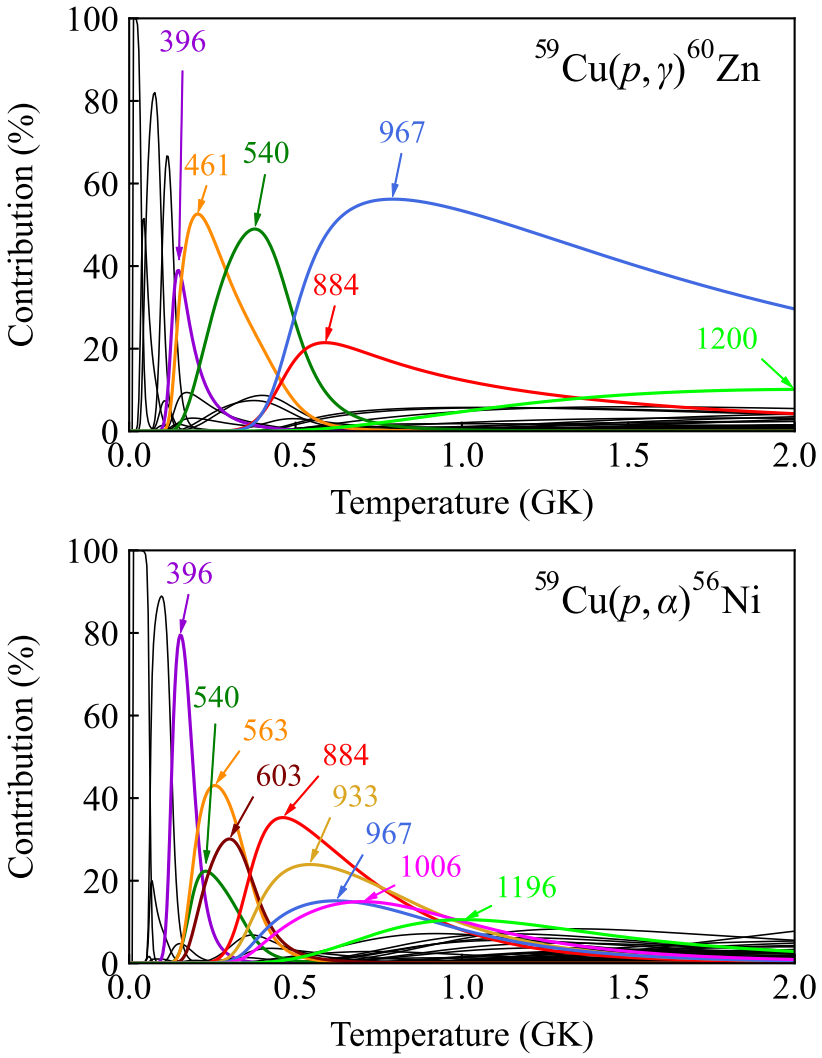

Figure 64: Fractional contributions of 128 shell-model predicted resonances to the ^{59}Cu$(p,\gamma)^{60}$Zn (upper) and ^{59}Cu$(p,\alpha)^{56}$Ni (lower) reaction rates. The most influential resonances are labeled with their corresponding resonance energies in keV.

36. Simulations

To assess the feasibility of the ^{60}Ga decay measurement with LIBRA, we have developed GEANT4 simulations incorporating the theoretical ^{60}Ga decay scheme and the known decay schemes of the daughter nuclei [434, 435, 436], the detector responses characterized based on radioactive source tests, and the integrated ^{60}Ga beam intensity over a six-day period (1.5×10^{10}). The resulting simulated proton and α particle identification spectrum by the ΔE-E telescope and the proton-gated X-ray spectrum by LEGe are shown in Fig. 65. As demonstrated in the charged-particle ΔE-E spectrum, our setup enables clear separation of most proton and α emission branches, allowing for accurate determination of their respective decay branching ratios.

One of the key observables offered by LIBRA is the proton-X-ray coincidence. The Cu/Zn K_α X-ray count ratio can be determined by integrating the 8.0- and 8.6-keV X-ray peaks observed in coincidence with protons. The Zn K_α radiative transition probability is 41.4%, compared to 38.7% for Cu [446], and the LEGe detection efficiency for 8.6-keV photons is 7.8%, compared to 7.4% at 8.0 keV (Fig. 54). Consequently, we need to apply two correction factors of $F = 1.07$ for fluorescence yields and $E = 1.05$ for efficiencies when extracting the lifetime of the proton-emitting state in ^{60}Zn from the observed Cu/Zn K_α X-ray count ratio:

$$\tau_{p-\mathrm{emit}} = \frac{\tau_{K\mathrm{shell(Zn)}}}{R_{\mathrm{Cu/Zn}}}, \tag{20}$$

$$R_{\mathrm{Cu/Zn}} = \frac{I_{K_\alpha(\mathrm{Cu})} \times F \times E}{I_{K_\alpha(\mathrm{Zn})}}, \tag{21}$$

The bottom panel of Fig. 65 shows the Cu/Zn K_α X-ray count ratios as a function of coincident proton energies, along with the corresponding lifetimes of proton-emitting states in ^{60}Zn. Only the X-ray count statistical uncertainty is taken into account. The integrated X-ray ratio of $R_{\mathrm{Cu/Zn}} = 3.2(3)$ corresponds to a lifetime $\tau_{p-\mathrm{emit}} = 0.126(11)$ fs, which is an average for all ^{60}Zn proton-emitting states. The main source of systematic uncertainty is the recommended Zn K-shell vacancy width $\Gamma_{K\mathrm{shell(Zn)}} = 1.62$ eV [450], adjusted based on the calculated $\Gamma_{K\mathrm{shell(Zn)}} = 1.56$ eV from Ref. [446]. A resonant Raman scattering measurement reported $\Gamma_{K\mathrm{shell(Zn)}} = 1.9(1)$ eV [549], which is consistent with the recommended value, considering the estimated uncertainty of 5−25% for atomic numbers below 30 [450].

Notably, the nuclear lifetimes can be reliably determined within a sensitivity range that spans approximately one order of magnitude above and below the Zn K-shell vacancy lifetime of 0.4 fs (Table 13). This timescale is typical for most nuclear resonances but extremely challenging for conventional lifetime measurement techniques. Should the experimental statistics fall short of the current estimates, we may obtain only upper or lower limits on certain branches, which would still be meaningful for constraining the astrophysical reaction rates.

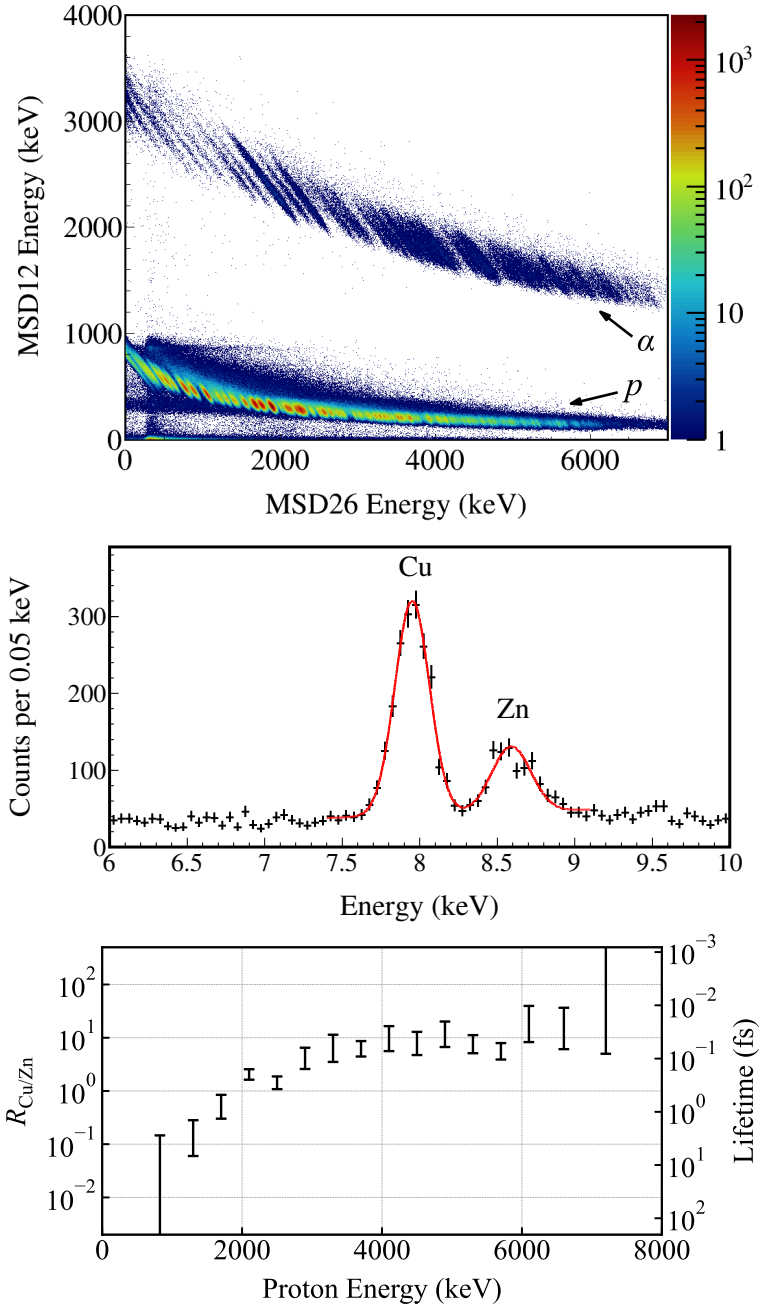

Figure 65: Top panel: charged-particle ΔE-E spectrum simulated by incorporating the theoretical decay properties of ^{60}Ga and the measured detector responses. Middle panel: X-ray spectrum gated by all protons in the ΔE-E spectrum, yielding a total X-ray ratio of $R_{Cu/Zn}$ = 3.2(3). A double-Gaussian with a linear background fit is superimposed on the Cu and Zn K_α peaks. Bottom panel: Cu/Zn K_α X-ray count ratio and the inferred lifetime as a function of coincident proton energy. The error bars represent statistical uncertainties, where the leftmost and rightmost error bars indicate upper or lower limits.

37. Summary & Outlook

We present the design, construction, simulation, and radioactive source testing of LIBRA. The system is capable of detecting all types of charged particles and photons emitted in EC/β^+ decay, which will enable us to measure the energies, proton-, α-, and γ-decay branching ratios of resonances. We will also utilize PXCT to determine the lifetimes of resonances populated by EC. Proton/α-γ coincidences provide information on the proton/α-emitting states in the compound nucleus and the ground and excited states of daughter nuclei, pertinent to both the entrance and exit channels for particle-induced reactions. LIBRA data can also provide nuclear level densities and transmission coefficients needed for calculating reaction rates using the Hauser-Feshbach statistical model.

Utilizing LIBRA for ^{60}Ga EC/β^+ decay offers the unique advantage of obtaining a comprehensive set of nuclear data in a single experiment. This capability efficiently addresses a key limitation of traditional indirect methods that they often yield only partial necessary nuclear data and thus require multiple experiments. By combining the nuclear data acquired through LIBRA, we may provide experimentally constrained thermonuclear rates of the ^{59}Cu$(p,\gamma)^{60}$Zn and ^{59}Cu$(p,\alpha)^{56}$Ni reactions to XRB models. The results could help us better understand the NiCu cycle, reduce the nuclear physics uncertainties in modeling the light curves and nucleosynthesis of XRBs, and ultimately facilitate the comparisons between model predictions and astronomical observations.

LIBRA holds the potential for studying other important reaction rates in the *rp* process. As shown in Fig. 47, ^{64}Ge plays an analogous role in the ZnGa cycle to that of ^{60}Zn in the NiCu cycle [411, 412, 550]. A notable difference is that the allowed β transitions of the 0^+ ^{64}As ground state populate the 0^+ and 1^+ states in ^{64}Ge [471]. Given the comparable $Q_{\rm EC}$, half-lives, proton/α-separation energies, and key X-ray energies (Table 13), it is technically feasible to utilize LIBRA for the ^{64}As EC/β^+ decay experiment to address the competition between the ^{63}Ga$(p,\gamma)^{64}$Ge and ^{63}Ga$(p,\alpha)^{60}$Zn reactions.

References

[1] J. José, *Stellar Explosions: Hydrodynamics and Nucleosynthesis*, CRC Press: Boca Raton, USA, (2016).
[2] C. Iliadis, *Nuclear Physics of Stars*, Wiley-VCH, Verlag, Wenheim, Germany, (2015).
[3] J. José, M. Hernanz, and C. Iliadis, Nucl. Phys. A **777**, 550 (2006).
[4] J. José, M. Hernanz, S. Amari, K. Lodders, and E. Zinner, Astrophys. J. **612**, 414 (2004).
[5] Lori N. Downen, Christian Iliadis, Jordi José, and Sumner Starrfield, Astrophys. J. **762**, 105 (2013).
[6] Keegan J. Kelly, Christian Iliadis, Lori Downen, Jordi José, and Art Champagne, Astrophys. J. **777**, 130 (2013).
[7] C. Wrede, AIP Advances **4**, 041004 (2014).
[8] M. B. Bennett, C. Wrede, B. A. Brown, S. N. Liddick, D. Pérez-Loureiro, D. W. Bardayan, A. A. Chen, K. A. Chipps, C. Fry, B. E. Glassman, C. Langer, N. R. Larson, E. I. McNeice, Z. Meisel, W. Ong, P. D. O'Malley, S. D. Pain, C. J. Prokop, H. Schatz, S. B. Schwartz, S. Suchyta, P. Thompson, M. Walters, and X. Xu, Phys. Rev. Lett. **116**, 102502 (2016).
[9] M. B. Bennett, C. Wrede, S. N. Liddick, D. Pérez-Loureiro, D. W. Bardayan, B. A. Brown, A. A. Chen, K. A. Chipps, C. Fry, B. E. Glassman, C. Langer, N. R. Larson, E. I. McNeice, Z. Meisel, W. Ong, P. D. O'Malley, S. D. Pain, C. J. Prokop, H. Schatz, S. B. Schwartz, S. Suchyta, P. Thompson, M. Walters, and X. Xu, Phys. Rev. C **97**, 065803 (2018).
[10] T. Budner, M. Friedman, C. Wrede, B. A. Brown, J. José, D. Pérez-Loureiro, L. J. Sun, J. Surbrook, Y. Ayyad, D. Bardayan, K. Chae, A. Chen, K. Chipps, M. Cortesi, B. Glassman, M. R. Hall, M. Janasik, J. Liang, P. O'Malley, E. Pollacco, A. Psaltis, J. Stomps, and T. Wheeler, Phys. Rev. Lett. **128**, 182701 (2022).
[11] R. Engmann, E. Ehrmann, F. Brandolini, and C. Signorini, Nucl. Phys. A **162**, 295 (1971).
[12] P. Doornenbal, P. Reiter, H. Grawe, T. Saito, A. Al-Khatib, A. Banu, T. Beck, F. Becker, P. Bednarczyk, G. Benzoni, A. Bracco, A. Bürger, L. Caceres, F. Camera, S. Chmel, F.C.L. Crespi, H. Geissel, J. Gerl, M. Górska, J. Gre,bosz, H. Hübel, M. Kavatsyuk, O. Kavatsyuk, M. Kmiecik, I. Kojouharov, N. Kurz, R. Lozeva, A. Maj, S. Mandal, W. Meczynski, B. Million, Zs. Podolyák, A. Richard, N. Saito, H. Schaffner, M. Seidlitz, T. Striepling, J. Walker, N. Warr, H. Weick, O. Wieland, M. Winkler, and H.J. Wollersheim, Nucl. Instrum. Methods Phys. Res. A **613**, 218 (2010).
[13] Clemens Herlitzius, Ph.D. Thesis, Technische Universität München, Germany, 2013.
[14] D. Tonev, G. de Angelis, I. Deloncle, N. Goutev, G. De Gregorio, P. Pavlov, I.L. Pantaleev, S. Iliev, M.S. Yavahchova, P.G. Bizzeti, A. Demerdjiev, D.T. Dimitrov, E. Farnea, A. Gadea, E. Geleva, C.Y. He, H. Laftchiev, S.M. Lenzi, S. Lunardi, N. Marginean, R. Menegazzo, D.R. Napoli, F. Nowacki, R. Orlandi, H. Penttilä, F. Recchia, E. Sahin, R.P. Singh, M. Stoyanova, C.A. Ur, H.-F. Wirth, Phys. Lett. B **821**, 136603 (2021).
[15] N. S. Pattabiraman, D. G. Jenkins, M. A. Bentley, R. Wadsworth, C. J. Lister, M. P. Carpenter, R. V. F. Janssens, T. L. Khoo, T. Lauritsen, D. Seweryniak, S. Zhu, G. Lotay, P. J. Woods, Krishichayan, and P. Van Isacker, Phys. Rev. C **78**, 024301 (2008).
[16] L. G. Elliott and R. E. Bell, Phys. Rev. **74**, 1869 (1948).
[17] S. Devons, G. Manning and D. St. P. Bunbury, Proc. Phys. Soc. A **68**, 18 (1955).
[18] S. Devons, G. Manning, and J. H. Towle, Proc. Phys. Soc. A **69**, 173 (1956).
[19] G. B. King, A. E. Lovell, L. Neufcourt, and F. M. Nunes, Phys. Rev. Lett. **122**, 232502 (2019).
[20] M. Catacora-Rios, G. B. King, A. E. Lovell, and F. M. Nunes, Phys. Rev. C **104**, 064611 (2021).

[21] A. E. Lovell, F. M. Nunes, M. Catacora-Rios, and G. B. King, J. Phys. G: Nucl. Part. Phys. **48**, 014001 (2021).
[22] Fox Colin, Haario Heikki, Christen J Andrés, *Inverse problems* in Paul Damien and others (eds), *Bayesian Theory and Applications* (Oxford University Press, 2013).
[23] Thomas Bayes and Richard Price, Philos. Trans. **53**, 370 (1763).
[24] H. Jeffreys, *The Theory of Probability* (Oxford, UK: Oxford Univ. Press, 1939).
[25] Rens van de Schoot, Sarah Depaoli, Ruth King, Bianca Kramer, Kaspar Märtens, Mahlet G. Tadesse, Marina Vannucci, Andrew Gelman, Duco Veen, Joukje Willemsen, and Christopher Yau, Nat. Rev. Methods Primers **1**, 1 (2021).
[26] N. Metropolis, A. W. Rosenbluth, M. N. Rosenbluth, A. H. Teller, and E. Teller, J. Chem. Phys. **21**, 1087 (1953).
[27] W. K. Hastings, Biometrika **57**, 97 (1970).
[28] Sanjib Sharma, Annu. Rev. Astron. Astrophys. **55**, 213 (2017).
[29] J. Novak, K. Novak, S. Pratt, J. Vredevoogd, C. E. Coleman-Smith, and R. L. Wolpert, Phys. Rev. C **89**, 034917 (2014).
[30] Scott Pratt, Evan Sangaline, Paul Sorensen, and Hui Wang, Phys. Rev. Lett. **114**, 202301 (2015).
[31] Jonah E. Bernhard, J. Scott Moreland, Steffen A. Bass, Jia Liu, and Ulrich Heinz, Phys. Rev. C **94**, 024907 (2016).
[32] Jonah E. Bernhard, J. Scott Moreland, and Steffen A. Bass, Nat. Phys. **15**, 1113 (2019).
[33] P. Morfouace, C.Y. Tsang, Y. Zhang, W.G. Lynch, M.B. Tsang, D.D.S. Coupland, M. Youngs, Z. Chajecki, M.A. Famiano, T.K. Ghosh, G. Jhang, Jenny Lee, H. Liu, A. Sanetullaev, R. Showalter, and J. Winkelbauer, Phys. Lett. B **799**, 135045 (2019).
[34] J. Scott Moreland, Jonah E. Bernhard, and Steffen A. Bass, Phys. Rev. C **101**, 024911 (2020).
[35] Wen-Jie Xie and Bao-An Li, J. Phys. G: Nucl. Part. Phys. **48**, 025110 (2021).
[36] Dananjaya Liyanage, Ö. Sürer, Matthew Plumlee, Stefan M. Wild, and Ulrich Heinz, Phys. Rev. C **108**, 054905 (2023).
[37] L. Vermunt, Y. Seemann, A. Dubla, S. Floerchinger, E. Grossi, A. Kirchner, S. Masciocchi, and I. Selyuzhenkov, Phys. Rev. C **108**, 064908 (2023).
[38] C.Y. Tsang, M. Kurata-Nishimura, M.B. Tsang, W.G. Lynch, Y.X. Zhang, J. Barney, J. Estee, G. Jhang, R. Wang, M. Kaneko, J.W. Lee, T. Isobe, T. Murakami, D.S. Ahn, L. Atar, T. Aumann, H. Baba, K. Boretzky, J. Brzychczyk, G. Cerizza, N. Chiga, N. Fukuda, I. Gasparic, B. Hong, A. Horvat, K. Ieki, N. Inabe, Y.J. Kim, T. Kobayashi, Y. Kondo, P. Lasko, H.S. Lee, Y. Leifels, J. Łukasik, J. Manfredi, A.B. McIntosh, P. Morfouace, T. Nakamura, N. Nakatsuka, S. Nishimura, H. Otsu, P. Pawłowski, K. Pelczar, D. Rossi, H. Sakurai, C. Santamaria, H. Sato, H. Scheit, R. Shane, Y. Shimizu, H. Simon, A. Snoch, A. Sochocka, T. Sumikama, H. Suzuki, D. Suzuki, H. Takeda, S. Tangwancharoen, H. Törnqvist, Y. Togano, Z.G. Xiao, S.J. Yennello, Y. Zhang, Phys. Lett. B **853**, 138661 (2024).
[39] M. Heffernan, C. Gale, S. Jeon, and J.-F. François Paquet, Phys. Rev. C **109**, 065207 (2024).
[40] A. E. Lovell and F. M. Nunes, Phys. Rev. C **97**, 064612 (2018).
[41] L. Yang, C.J. Lin, Y.X. Zhang, P.W. Wen, H.M. Jia, D.X. Wang, N.R. Ma, F. Yang, F.P. Zhong, S.H. Zhong, T.P. Luo, Phys. Lett. B **807**, 135540 (2020).
[42] C. Marshall, P. Morfouace, N. de Séréville, and R. Longland, Phys. Rev. C **102**, 024609 (2020).
[43] C. D. Pruitt, R. J. Charity, L. G. Sobotka, J. M. Elson, D. E. M. Hoff, K. W. Brown, M. C. Atkinson, W. H. Dickhoff, H. Y. Lee, M. Devlin, N. Fotiades, and S. Mosby, Phys. Rev. C **102**, 034601 (2020).
[44] Daniel Odell, Carl R. Brune, and Daniel R. Phillips, Phys. Rev. C **105**, 014625 (2022).
[45] Christian Iliadis, Vimal Palanivelrajan, and Rafael S. de Souza, Phys. Rev. C **106**, 055802 (2022).
[46] Liyong Zhang, Jianjun He, Richard J. deBoer, Michael Wiescher, Alexander Heger, Daid Kahl, Jun Su, Daniel Odell, Yinji Chen, Xinyue Li, Jianguo Wang, Long Zhang, Fuqiang Cao, Hao Zhang, Zhicheng Zhang, Xinzhi Jiang, Luohuan Wang, Ziming Li, Luyang Song, Hongwei Zhao, Liangting Sun, Qi Wu, Jiaqing Li, Baoqun Cui, Lihua Chen, Ruigang Ma, Ertao Li, Gang Lian, Yaode Sheng, Zhihong Li, Bing Guo, Xiaohong Zhou, Yuhu Zhang, Hushan Xu, Jianping Cheng, and Weiping Liu, Nature **610**, 656 (2022).
[47] J. Hooker, J. Kovoor, K.L. Jones, R. Kanungo, M. Alcorta, J. Allen, C. Andreoiu, L. Atar, D.W. Bardayan, S.S. Bhattacharjee, D. Blankstein, C. Burbadge, S. Burcher, W.N. Catford, S. Cha, K. Chae, D. Connolly, B. Davids, N. Esker, F.H. Garcia, S. Gillespie, R. Ghimire, A. Gula, G. Hackman, S. Hallam, M. Hellmich, J. Henderson, M. Holl, P. Jassal, S. King, T. Knight, R. Kruecken, A. Lepailleur, J. Liang, L. Morrison, P.D. O'Malley, S.D. Pain, X. Pereira-Lopez, A. Psaltis, A. Radich, A.C. Shotter, M. Vostinar, M. Williams, O. Workman, Nucl. Instrum. Methods Phys. Res. B **512**, 6 (2022).
[48] J. Kovoor, K.L. Jones, J. Hooker, M. Vostinar, R. Kanungo, S.D. Pain, M. Alcorta, J. Allen, C. Andreoiu, L. Atar, D.W. Bardayan, S.S. Bhattacharjee, D. Blankstein, C. Burbadge, S. Burcher, W.N. Catford, S. Cha, K. Chae, D. Connolly, B. Davids, N. E. Esker, F.H. Garcia, S. Gillespie, R. Ghimire, A. Gula, G. Hackman, S. Hallam, M. Hellmich, J. Henderson, M. Holl, P. Jassal, S. King, T. Knight, R. Kruecken, A. Lepailleur, J. Liang, L. Morrison, P.D. O'Malley, X. Pereira-Lopez, A. Psaltis, A. Radich, J. Refsgaard, A.C. Shotter, M. Williams, O. Workman, Phys. Rev. C **108**, 034601 (2023).
[49] H. Zhang, J. Su, Z. H. Li, Y. J. Li, E. T. Li, C. Chen, J. J. He, Y. P. Shen, G. Lian, B. Guo, X. Y. Li, L. Y. Zhang, Y. D. Sheng, Y. J. Chen, L. H. Wang, L. Zhang, F. Q. Cao, W. Nan, W. K. Nan, G. X. Li, N. Song, B. Q. Cui, L. H. Chen, R. G. Ma, Z. C. Zhang, T. Y. Jiao, B. S. Gao, X. D. Tang, Q. Wu, J. Q. Li, L. T. Sun, S. Wang, S. Q. Yan, J. H. Liao, Y. B. Wang, S. Zeng, D. Nan, Q. W. Fan, and W. P. Liu, Phys. Rev. C **107**, 065801 (2023).
[50] M. Catacora-Rios, A. E. Lovell, and F. M. Nunes, Phys. Rev. C **108**, 024601 (2023).
[51] A. Chalil, C. Ducoin, O. Stézowski, N. Millard-Pinard, J. Dudouet, Y. Demane, and M. Chamseddine, Phys. Rev. C **110**, 024602 (2024).
[52] W.-J. Ong, H. Schatz, K. Kravvaris, S. Ahn, K. Childers, B. P. Crider, A. C. Dombos, C. Langer, R. Lewis, S. N. Liddick, S. Lyons, Z. Meisel, F. Montes, J. Pereira, D. Richman, K. Schmidt, and A. Spyrou, Phys. Rev. C **110**, 024321 (2024).
[53] D. R. Phillips, R. J. Furnstahl, U. Heinz, T. Maiti, W. Nazarewicz, F. M. Nunes, M. Plumlee, M. T. Pratola, S. Pratt, F. G. Viens, and S. M. Wild, J. Phys. G: Nucl. Part. Phys. **48**, 072001 (2021).
[54] Paulo Bedaque, Amber Boehnlein, Mario Cromaz, Markus Diefenthaler, Latifa Elouadrhiri, Tanja Horn, Michelle Kuchera, David Lawrence, Dean Lee, Steven Lidia, Robert McKeown, Wally Melnitchouk, Witold Nazarewicz, Kostas Orginos, Yves Roblin, Michael Scott Smith, Malachi Schram, Xin-Nian Wang, Eur. Phys. J. A **57**, 100 (2021).
[55] Amber Boehnlein, Markus Diefenthaler, Nobuo Sato, Malachi Schram, Veronique Ziegler, Cristiano Fanelli, Morten Hjorth-Jensen, Tanja Horn, Michelle P. Kuchera, Dean Lee, Witold Nazarewicz, Peter Ostroumov, Kostas Orginos, Alan Poon, Xin-Nian Wang, Alexander

Scheinker, Michael S. Smith, and Long-Gang Pang, Rev. Mod. Phys. **94**, 031003 (2022).
[56] N. Galinski, S. K. L. Sjue, G. C. Ball, D. S. Cross, B. Davids, H. Al Falou, A. B. Garnsworthy, G. Hackman, U. Hager, D. A. Howell, M. Jones, R. Kanungo, R. Kshetri, K. G. Leach, J. R. Leslie, M. Moukaddam, J. N. Orce, E. T. Rand, C. Ruiz, G. Ruprecht, M. A. Schumaker, C. E. Svensson, S. Triambak, and C. D. Unsworth, Phys. Rev. C **90**, 035803 (2014).
[57] B. Davids, Hyperfine Interact. **225**, 215 (2014).
[58] R. Kanungo, T. K. Alexander, A. N. Andreyev, G. C. Ball, R. S. Chakrawarthy, M. Chicoine, R. Churchman, B. Davids, J. S. Forster, S. Gujrathi, G. Hackman, D. Howell, J. R. Leslie, A. C. Morton, S. Mythili, C. J. Pearson, J. J. Ressler, C. Ruiz, H. Savajols, M. A. Schumaker, I. Tanihata, P. Walden, and S. Yen, Phys. Rev. C **74**, 045803 (2006).
[59] S. Mythili, B. Davids, T. K. Alexander, G. C. Ball, M. Chicoine, R. S. Chakrawarthy, R. Churchman, J. S. Forster, S. Gujrathi, G. Hackman, D. Howell, R. Kanungo, J. R. Leslie, E. Padilla, C. J. Pearson, C. Ruiz, G. Ruprecht, M. A. Schumaker, I. Tanihata, C. Vockenhuber, P. Walden, and S. Yen, Phys. Rev. C **77**, 035803 (2008).
[60] O. S. Kirsebom, P. Bender, A. Cheeseman, G. Christian, R. Churchman, D. S. Cross, B. Davids, L. J. Evitts, J. Fallis, N. Galinski, A. B. Garnsworthy, G. Hackman, J. Lighthall, S. Ketelhut, P. Machule, D. Miller, S. T. Nielsen, C. R. Nobs, C. J. Pearson, M. M. Rajabali, A. J. Radich, A. Rojas, C. Ruiz, A. Sanetullaev, C. D. Unsworth, and C. Wrede, Phys. Rev. C **93**, 025802 (2016).
[61] Cathleen Fry, Ph.D. Thesis, Michigan State University, Michigan, USA, 2018.
[62] L. J. Sun, C. Fry, B. Davids, N. Esker, C. Wrede, M. Alcorta, S. Bhattacharjee, M. Bowry, B. A. Brown, T. Budner, R. Caballero-Folch, L. Evitts, M. Friedman, A. B. Garnsworthy, B. E. Glassman, G. Hackman, J. Henderson, O. S. Kirsebom, J. Lighthall, P. Machule, J. Measures, M. Moukaddam, J. Park, C. Pearson, D. Pérez-Loureiro, C. Ruiz, P. Ruotsalainen, J. Smallcombe, J. K. Smith, D. Southall, J. Surbrook, L. E. Weghorn, and M. Williams, Phys. Lett. B **839**, 137801 (2023).
[63] ORTEC B Series Totally Depleted Silicon Surface Barrier Radiation Detector.
[64] U. Rizwan, A. B. Garnsworthy, C. Andreoiu, G. C. Ball, A. Chester, T. Domingo, R. Dunlop, G. Hackman, E. T. Rand, J. K. Smith, K. Starosta, C. E. Svensson, P. Voss, and J. Williams, Nucl. Instrum. Methods Phys. Res. A **820**, 126 (2016).
[65] A.B. Garnsworthy, C.E. Svensson, M. Bowry, R. Dunlop, A.D. MacLean, B. Olaizola, J.K. Smith, F.A. Ali, C. Andreoiu, J.E. Ash, W.H. Ashfield, G.C. Ball, T. Ballast, C. Bartlett, Z. Beadle, P.C. Bender, N. Bernier, S.S. Bhattacharjee, H. Bidaman, V. Bildstein, D. Bishop, P. Boubel, R. Braid, D. Brennan, T. Bruhn, C. Burbadge, A. Cheeseman, A. Chester, R. Churchman, S. Ciccone, R. Caballero-Folch, D.S. Cross, S. Cruz, B. Davids, A. Diaz Varela, I. Dillmann, M.R. Dunlop, L.J. Evitts, F.H. Garcia, P.E. Garrett, S. Georges, S. Gillespie, R. Gudapati, G. Hackman, B. Hadinia, S. Hallam, J. Henderson, S.V. Ilyushkin, B. Jigmeddorj, A.I. Kilic, D. Kisliuk, R. Kokke, K. Kuhn, R. Krücken, M. Kuwabara, A.T. Laffoley, R. Lafleur, K.G. Leach, J.R. Leslie, Y. Linn, C. Lim, E. MacConnachie, A.R. Mathews, E. McGee, J. Measures, D. Miller, W.J. Mills, W. Moore, D. Morris, L.N. Morrison, M. Moukaddam, C.R. Natzke, K. Ortner, E. Padilla-Rodal, O. Paetkau, J. Park, H.P. Patel, C.J. Pearson, E. Peters, E.E. Peters, J.L. Pore, A.J. Radich, M.M. Rajabali, E.T. Rand, K. Raymond, U. Rizwan, P. Ruotsalainen, Y. Saito, F. Sarazin, B. Shaw, J. Smallcombe, D. Southall, K. Starosta, M. Ticu, E. Timakova, J. Turko, R. Umashankar, C. Unsworth, Z.M. Wang, K. Whitmore, S. Wong, S.W. Yates, E.F. Zganjar, and T. Zidar, Nucl. Instrum. Methods Phys. Res. A **918**, 9 (2019).
[66] J. F. Ziegler, M. D.Ziegler, and J. P. Biersack, Nucl. Instrum. Methods Phys. Res. B **268**, 1818 (2010).
[67] Xiaolong Huang and Chunmei Zhou, Nucl. Data Sheets **104**, 283 (2005).
[68] J. Chen, Nucl. Data Sheets **149**, 1 (2018).
[69] D.R. Tilley, H.R. Weller, and C.M. Cheves, Nucl. Phys. A **564**, 1 (1993).
[70] D. Branford and I.F. Wright, Nucl. Instrum. Methods **106**, 437 (1973).
[71] T. K. Alexander and J. S. Forster, Adv. Nucl. Phys. **10**, 197 (1978).
[72] P. J. Nolan and J. F. Sharpey-Schafer, Rep. Prog. Phys. **42**, 1 (1979).
[73] B. Frentz, A. Aprahamian, A. M. Clark, R. J. deBoer, C. Dulal, J. D. Enright, J. Görres, S. L. Henderson, J. D. Hinnefeld, K. B. Howard, R. Kelmar, K. Lee, L. Morales, S. Moylan, Z. Rahman, W. Tan, L. E. Weghorn, and M. Wiescher, Phys. Rev. C **103**, 045802 (2021).
[74] S. Ritt and P. Amaudruz, Proceedings of the 10th IEEE Real Time Conference, Beaune, 1997, 309.
[75] A.B. Garnsworthy, C.J. Pearson, D. Bishop, B. Shaw, J.K. Smith, M. Bowry, V. Bildstein, G. Hackman, P.E. Garrett, Y. Linn, J.-P. Martin, W.J. Mills, C.E. Svensson, Nucl. Instrum. Methods Phys. Res. A **853**, 85 (2017).
[76] S. Agostinelli, J. Allison, K. Amako, J. Apostolakis, H. Araujo, P. Arce, M. Asai, D. Axen, S. Banerjee, G. Barrand, F. Behner, L. Bellagamba, J. Boudreau, L. Broglia, A. Brunengo, H. Burkhardt, S. Chauvie, J. Chuma, R. Chytracek, G. Cooperman, G. Cosmo, P. Degtyarenko, A. Dell'Acqua, G. Depaola, D. Dietrich, R. Enami, A. Feliciello, C. Ferguson, H. Fesefeldt, G. Folger, F. Foppiano, A. Forti, S. Garelli, S. Giani, R. Giannitrapani, D. Gibin, J. J. Gómez Cadenas, I. González, G. Gracia Abril, G. Greeniaus, W. Greiner, V. Grichine, A. Grossheim, S. Guatelli, P. Gumplinger, R. Hamatsu, K. Hashimoto, H. Hasui, A. Heikkinen, A. Howard, V. Ivanchenko, A. Johnson, F. W. Jones, J. Kallenbach, N. Kanaya, M. Kawabata, Y. Kawabata, M. Kawaguti, S. Kelner, P. Kent, A. Kimura, T. Kodama, R. Kokoulin, M. Kossov, H. Kurashige, E. Lamanna, T. Lampén, V. Lara, V. Lefebure, F. Lei, M. Liendl, W. Lockman, F. Longo, S. Magni, M. Maire, E. Medernach, K. Minamimoto, P. Mora de Freitas, Y. Morita, K. Murakami, M. Nagamatu, R. Nartallo, P. Nieminen, T. Nishimura, K. Ohtsubo, M. Okamura, S. O'Neale, Y. Oohata, K. Paech, J. Perl, A. Pfeiffer, M. G. Pia, F. Ranjard, A. Rybin, S. Sadilov, E. Di Salvo, G. Santin, T. Sasaki, N. Savvas, Y. Sawada, S. Scherer, S. Sei, V. Sirotenko, D. Smith, N. Starkov, H. Stoecker, J. Sulkimo, M. Takahata, S. Tanaka, E. Tcherniaev, E. Safai Tehrani, M. Tropeano, P. Truscott, H. Uno, L. Urban, P. Urban, M. Verderi, A. Walkden, W. Wander, H. Weber, J. P. Wellisch, T. Wenaus, D. C. Williams, D. Wright, T. Yamada, H. Yoshida, and D. Zschiesche, Nucl. Instrum. Methods Phys. Res. A **506**, 250 (2003).
[77] J. Allison, K. Amako, J. Apostolakis, P. Arce, M. Asai, T. Aso, E. Bagli, A. Bagulya, S. Banerjee, G. Barrand, B.R. Beck, A.G. Bogdanov, D. Brandt, J.M.C. Brown, H. Burkhardt, Ph. Canal, D. Cano-Ott, S. Chauvie, K. Cho, G.A.P. Cirrone, G. Cooperman, M.A. Cortés-Giraldo, G. Cosmo, G. Cuttone, G. Depaola, L. Desorgher, X. Dong, A. Dotti, V.D. Elvira, G. Folger, Z. Francis, A. Galoyan, L. Garnier, M. Gayer, K.L. Genser, V.M. Grichine, S. Guatelli, P. Guèye, P. Gumplinger, A.S. Howard, I. Hřivnáčová, S. Hwang, S. Incerti, A. Ivanchenko, V.N. Ivanchenko, F.W. Jones, S.Y. Jun, P. Kaitaniemi, N. Karakatsanis, M. Karamitros, M. Kelsey, A. Kimura, T. Koi, H. Kurashige, A. Lechner, S.B. Lee, F. Longo, M. Maire, D. Mancusi, A. Mantero, E. Mendoza, B. Morgan, K. Murakami, T. Nikitina, L. Pandola, P. Paprocki, J. Perl, I. Petrović, M.G. Pia, W. Pokorski, J.M. Quesada, M. Raine, M.A. Reis, A. Ribon, A. Ristić Fira, F. Romano, G. Russo, G. Santin, T. Sasaki, D. Sawkey, J.I. Shin, I.I. Strakovsky, A. Taborda, S. Tanaka, B. Tomé, T. Toshito, H.N. Tran, P.R. Truscott, L. Urban, V. Uzhinsky,

J.M. Verbeke, M. Verderi, B.L. Wendt, H. Wenzel, D.H. Wright, D.M. Wright, T. Yamashita, J. Yarba, H. Yoshida, Nucl. Instrum. Methods Phys. Res. A **835**, 186 (2016).
[78] M. Wang, W. J. Huang, F. G. Kondev, G. Audi, S. Naimi, Chin. Phys. C **45**, 030003 (2021).
[79] B. E. Glassman, D. Pérez-Loureiro, C. Wrede, J. Allen, D. W. Bardayan, M. B. Bennett, K. A. Chipps, M. Febbraro, M. Friedman, C. Fry, M. R. Hall, O. Hall, S. N. Liddick, P. O'Malley, W. -J. Ong, S. D. Pain, S. B. Schwartz, P. Shidling, H. Sims, L. J. Sun, P. Thompson, and H. Zhang, Phys. Rev. C **99**, 065801 (2019).
[80] L. J. Sun, M. Friedman, T. Budner, D. Pérez-Loureiro, E. Pollacco, C. Wrede, B. A. Brown, M. Cortesi, C. Fry, B. E. Glassman, J. Heideman, M. Janasik, A. Kruskie, A. Magilligan, M. Roosa, J. Stomps, J. Surbrook, and P. Tiwari, Phys. Rev. C **103**, 014322 (2021).
[81] J. Chen, Nucl. Data Sheets **140**, 1 (2017).
[82] P.A. Zyla *et al*. (Particle Data Group), Prog. Theor. Exp. Phys. **2020**, 083C01 (2020).
[83] C.E. Moss, Nucl. Phys. A **145**, 423 (1970).
[84] D. T. Doherty, G. Lotay, P. J. Woods, D. Seweryniak, M. P. Carpenter, C. J. Chiara, H. M. David, R. V. F. Janssens, L. Trache, and S. Zhu, Phys. Rev. C **108**, 262502 (2012).
[85] D. T. Doherty, P. J. Woods, G. Lotay, D. Seweryniak, M. P. Carpenter, C. J. Chiara, H. M. David, R. V. F. Janssens, L. Trache, and S. Zhu, Phys. Rev. C **89**, 045804 (2014).
[86] A. Kankainen, P.J. Woods, H. Schatz, T. Poxon-Pearson, D.T. Doherty, V. Bader, T. Baugher, D. Bazin, B.A. Brown, J. Browne, A. Estrade, A. Gade, J. José, A. Kontos, C. Langer, G. Lotay, Z. Meisel, F. Montes, S. Noji, F. Nunes, G. Perdikakis, J. Pereira, F. Recchia, T. Redpath, R. Stroberg, M. Scott, D. Seweryniak, J. Stevens, D. Weisshaar, K. Wimmer, R. Zegers, Phys. Lett. B **769**, 549 (2017).
[87] D. G. Jenkins, C. J. Lister, M. P. Carpenter, P. Chowdhury, N. J. Hammond, R. V. F. Janssens, T. L. Khoo, T. Lauritsen, D. Seweryniak, T. Davinson, P. J. Woods, A. Jokinen, and H. Penttila, Phys. Rev. C **72**, 031303(R) (2005).
[88] D. G. Jenkins, A. Meadowcroft, C. J. Lister, M. P. Carpenter, P. Chowdhury, N. J. Hammond, R. V. F. Janssens, T. L. Khoo, T. Lauritsen, D. Seweryniak, T. Davinson, P. J. Woods, A. Jokinen, H. Penttila, G. Martìnez-Pinedo, and J. José, Phys. Rev. C **89**, 045804 (2014).
[89] D. A. Testov, A. Boso, S. M. Lenzi, F. Nowacki, F. Recchia, G. de Angelis, D. Bazzacco, G. Colucci, M. Cottini, F. Galtarossa, A. Goasduff, A. Gozzelino, K. Hadyńska-Klek, G. Jaworski, P. R. John, S. Lunardi, R. Menegazzo, D. Mengoni, A. Mentana, V. Modamio, A. Nannini, D. R. Napoli, M. Palacz, M. Rocchini, M. Siciliano, and J. J. Valiente-Dobón, Phys. Rev. C **104**, 024309 (2021).
[90] K. Setoodehnia, A. A. Chen, J. Chen, J. A. Clark, C. M. Deibel, J. Hendriks, D. Kahl, W. N. Lennard, P. D. Parker, D. Seiler, and C. Wrede, Phys. Rev. C **102**, 045806 (2020).
[91] Jonah E. Bernhard, Ph.D. Thesis, Duke University, North Carolina, USA, 2018.
[92] ICRU Report 73, *Stopping of Ions Heavier than Helium*, International Commission on Radiation Units and Measurements, Oxford University Press, Oxford, 2005.
[93] Istem Fer, Ryan Kelly, Paul R. Moorcroft, Andrew D. Richardson, Elizabeth M. Cowdery, and Michael C. Dietze, Biogeosciences **15**, 5801 (2018).
[94] Cade R. Rodgers and Christian Iliadis, Nucl. Instrum. Methods Phys. Res. A **998**, 165172 (2021).
[95] Michael E. Tipping and Christopher M. Bishop, Neural Comput. **11**, 443 (1999).
[96] C. E. Rasmussen and C. K. I. Williams, *Gaussian Processes for Machine Learning* (Cambridge, MA: The MIT Press, 2006).
[97] Ö. Sürer, F. M. Nunes, M. Plumlee, and S. M. Wild, Phys. Rev. C **106**, 024607 (2022).
[98] H. Roch, S. A. Jahan, and C. Shen, Phys. Rev. C **110**, 044904 (2024).
[99] S. A. Jahan, H. Roch, and C. Shen, Phys. Rev. C **110**, 054905 (2024).
[100] Ö. Sürer, M. Plumlee, and S. M. Wild, Technometrics (2023).
[101] S. A. Miskovich, F. Montes, G. P. A. Berg, J. Blackmon, K. A. Chipps, M. Couder, C. M. Deibel, K. Hermansen, A. A. Hood, R. Jain, T. Ruland, H. Schatz, M. S. Smith, P. Tsintari, and L. Wagner, Phys. Rev. Accel. Beams **25**, 044601 (2022).
[102] Chenran Xu, Tobias Boltz, Akira Mochihashi, Andrea Santamaria Garcia, Marcel Schuh, and Anke-Susanne Müller, Phys. Rev. Accel. Beams **26**, 034601 (2023).
[103] R. Ghanem and P. Spanos, *Stochastic Finite Elements: A Spectral Approach* (Courier Dover Publications, Mineola, 2nd edition, 2003).
[104] J. L. Peterson, K. D. Humbird, J. E. Field, S. T. Brandon, S. H. Langer, R. C. Nora, B. K. Spears, and P. T. Springer, Phys. Plasmas **24**, 032702 (2017).
[105] Z. M. Niu, J. Y. Fang, and Y. F. Niu, Phys. Rev. C **100**, 054311 (2019).
[106] Edgard Bonilla, Pablo Giuliani, Kyle Godbey, and Dean Lee, Phys. Rev. C **106**, 054322 (2022).
[107] Pablo Giuliani, Kyle Godbey, Edgard Bonilla, Frederi Viens, Jorge Piekarewicz, Front. Phys. **10**, 54524 (2023).
[108] D. Odell, P. Giuliani, K. Beyer, M. Catacora-Rios, M. Y.-H. Chan, E. Bonilla, R. J. Furnstahl, K. Godbey, and F. M. Nunes, Phys. Rev. C **109**, 044612 (2024).
[109] C. Drischler, M. Quinonez, P.G. Giuliani, A.E. Lovell, and F.M. Nunes, Phys. Lett. B **823**, 136777 (2021).
[110] Rohit K.Tripathy and Ilias Bilionis, J. Comput. Phys. **375**, 565 (2018).
[111] Marc Verriere, Nicolas Schunck, Irene Kim, Petar Marević, Kevin Quinlan, Michelle N. Ngo, David Regnier, and Raphael David Lasseri, Front. Phys. **10**, 1028370 (2022).
[112] MADAI: Modeling and Data Analysis Initiative.
[113] Evaluation of measurement data - Supplement 1 to the *Guide to the expression of uncertainty in measurement - Propagation of distributions using a Monte Carlo method*. Joint Committee for Guides in Metrology, 101, 2008.
[114] Louis Lyons, *Statistics for nuclear and particle physicists* (Cambridge University Press, 1986).
[115] Surmise's documentation.
[116] Surmise's repository
[117] Moses Y.-H. Chan, Ph.D. Thesis, Northwestern University, Illinois, USA, 2023.
[118] B. A. Brown and W. D. M. Rae, Nucl. Data Sheets **120**, 115 (2014).
[119] B. Alex Brown and W. A. Richter, Phys. Rev. C **74**, 034315 (2006).
[120] A. Magilligan and B. A. Brown, Phys. Rev. C **101**, 064312 (2020).

[121] W. A. Richter, S. Mkhize, and B. A. Brown, Phys. Rev. C **78**, 064302 (2008).
[122] B. Alex Brown, W. A. Richter, and C. Wrede, Phys. Rev. C **89**, 062801(R) (2014).
[123] Jun Chen and Balraj Singh, Nucl. Data Sheets **184**, 29 (2022).
[124] M. Shamsuzzoha Basunia, Nucl. Data Sheets **111**, 2331 (2010).
[125] Tamas Budner, Ph.D. Thesis, Michigan State University, Michigan, USA, 2022.
[126] Alex Brown, private communication.
[127] E.O. de Neijs, G.D. Haasbroek, M.A. Meyer, R.S. Rossouw, D. Reitmann, Nucl. Phys. A **254**, 45 (1975).
[128] MIRCON W1 Double-sided Silicon Strip Detector.
[129] MIRCON MSX25 Single-side Large Area Silicon Detector.
[130] B. Davids, C. Wrede *et al.*, TRIUMF EEC S2193.
[131] Lexanne Weghorn, Ph.D. Thesis in progress, Michigan State University, Michigan, USA.
[132] R. Longland, C. Iliadis, A. E. Champagne, J. R. Newton, C. Ugalde, A. Coc, and R. Fitzgerald, Nucl. Phys. A **841**, 1 (2010).
[133] C. Iliadis, R. Longland, A. E. Champagne, A. Coc, and R. Fitzgerald, Nucl. Phys. A **841**, 31 (2010).
[134] C. Iliadis, R. Longland, A. E. Champagne, and A. Coc, Nucl. Phys. A **841**, 251 (2010).
[135] P. Mohr, R. Longland, and C. Iliadis, Phys. Rev. C **90**, 065806 (2014).
[136] C. Iliadis, R. Longland, A. Coc, F. X. Timmes, and A. E. Champagne, J. Phys. G: Nucl. Part. Phys. **42**, 034007 (2015).
[137] Richard Longland, Astron. Astrophys. **604**, A34 (2017).
[138] Richard Longland, Astron. Astrophys. **642**, A41 (2020).
[139] J. José and M. Hernanz, Astrophys. J **494**, 680 (1998).
[140] D. D. Clayton and F. Hoyle, Astrophys. J. Lett. **187**, L101 (1974).
[141] A. Weiss and J.W. Truran, Astron. Astrophys. **238**, 178 (1990).
[142] A. F. Iyudin ,K. Bennett, H. Bloemen, R. Diehl, W. Hermsen, G. G. Lichti, D. Morris, J. Ryan, V. Schonfelder, H. Steinle, A. Strong, M. Varendorff, and C. Winkler, Astron. Astrophys. **300**, 422 (1995).
[143] S. Seuthe, C. Rolfs, U. Schröder, W.H. Schulte, E. Somorjai, H.P. Trautvetter, F.B. Waanders, R.W. Kavanagh, H. Ravn, M. Arnould, G. Paulus, Nucl. Phys. A **514**, 471 (1990).
[144] F. Stegmüller, C. Rolfs, S. Schmidt, W.H. Schulte, H.P. Trautvetter, R.W. Kavanagh, Nucl. Phys. A **601**, 168 (1996).
[145] A. L. Sallaska, C. Wrede, A. García, D. W. Storm, T. A. D. Brown, C. Ruiz, K. A. Snover, D. F. Ottewell, L. Buchmann, C. Vockenhuber, D. A. Hutcheon, and J. A. Caggiano, Phys. Rev. Lett. **105**, 209901 (2010).
[146] A. L. Sallaska, C. Wrede, A. García, D. W. Storm, T. A. D. Brown, C. Ruiz, K. A. Snover, D. F. Ottewell, L. Buchmann, C. Vockenhuber, D. A. Hutcheon, J. A. Caggiano, and J. José, Phys. Rev. C **83**, 034611 (2011).
[147] K. Peräjärvi, T. Siiskonen, A. Honkanen, P. Dendooven, A. Jokinen, P.O. Lipas, M. Oinonen, H. Penttilä, J. Äystö, Phys. Lett. B **492**, 1 (2000).
[148] A. Saastamoinen, L. Trache, A. Banu, M. A. Bentley, T. Davinson, J. C. Hardy, V. E. Iacob, M. McCleskey, B. T. Roeder, E. Simmons, G. Tabacaru, R. E. Tribble, P. J. Woods, and J. Äystö, Phys. Rev. C **83**, 045808 (2011).
[149] M. Friedman, T. Budner, D. Pérez-Loureiro, E. Pollacco, C. Wrede, J. José, B. A. Brown, M. Cortesi, C. Fry, B. Glassman, J. Heideman, M. Janasik, M. Roosa, J. Stomps, J. Surbrook, P. Tiwari, Phys. Rev. C **101**, 052802(R) (2020).
[150] Chloé Fougères, Ph.D. Thesis, Normandie Université, France, 2022.
[151] Chloé Fougères, François de Oliveira Santos, Jordi José, Caterina Michelagnoli, Emmanuel Clément, Yung Hee Kim, Antoine Lemasson, Valdir Guimarães, Diego Barrientos, Daniel Bemmerer, Giovanna Benzoni, Andrew J. Boston, Roman Böttger, Florent Boulay, Angela Bracco, Igor Čeliković, Bo Cederwall, Michał Ciemala, Clément Delafosse, César Domingo-Pardo, Jérémie Dudouet, Jürgen Eberth, Zsolt Fülöp, Vicente González, Andrea Gottardo, Johan Goupil, Herbert Hess, Andrea Jungclaus, Ayşe Kaşkaş, Amel Korichi, Silvia M. Lenzi, Silvia Leoni, Hongjie Li, Joa Ljungvall, Araceli Lopez-Martens, Roberto Menegazzo, Daniele Mengoni, Benedicte Million, Jaromír Mrázek, Daniel R. Napoli, Alahari Navin, Johan Nyberg, Zsolt Podolyák, Alberto Pullia, Begoña Quintana, Damien Ralet, Nadine Redon, Peter Reiter, Kseniia Rezynkina, Frédéric Saillant, Marie-Delphine Salsac, Angel M. Sánchez-Benítez, Enrique Sanchis, Menekşe Şenyiğit, Marco Siciliano, Nadezda A. Smirnova, Dorottya Sohler, Mihai Stanoiu, Christophe Theisen, Jose J. Valiente-Dobón, Predrag Ujić, and Magdalena Zielińska, Nat. Commun. **14**, 4536 (2023).
[152] D. G. Jenkins, C. J. Lister, R. V. F. Janssens, T. L. Khoo, E. F. Moore, K. E. Rehm, B. Truett, A. H. Wuosmaa, M. Freer, B. R. Fulton, and J. José, Phys. Rev. Lett. **92**, 031101 (2004).
[153] D. G. Jenkins, M. Bouhelal, S. Courtin, M. Freer, B. R. Fulton, F. Haas, R. V. F. Janssens, T. L. Khoo, C. J. Lister, E. F. Moore, W. A. Richter, B. Truett, and A. H. Wuosmaa, Phys. Rev. C **87**, 064301 (2013).
[154] M. S. Kwag, K. Y. Chae, S. Ahn, D. W. Bardayan, K. A. Chipps, J. A. Cizewski, M. E. Howard, R. L. Kozub, K. Kwak, B. Manning, M. Matos, P. D. O'Malley, S. D. Pain, W. A. Peters, S. T. Pittman, A. Ratkiewicz, M. S. Smith, and S. Strauss, Eur. Phys. J. A **56**, 108 (2020).
[155] V. E. Iacob, Y. Zhai, T. Al-Abdullah, C. Fu, J. C. Hardy, N. Nica, H. I. Park, G. Tabacaru, L. Trache, and R. E. Tribble, Phys. Rev. C **74**, 045810 (2006).
[156] Y. Zhai, Ph.D. Thesis, Texas A&M University, Texas, USA, 2007.
[157] I. Goldberg, Master's Thesis, The Hebrew University of Jerusalem, Israel, 2024.
[158] M. Shamsuzzoha Basunia and A. Chakraborty, Nuclear Data Sheets **171**, 1 (2021).
[159] S. J. Jin, Y. B. Wang, J. Su, S. Q. Yan, Y. J. Li, B. Guo, Z. H. Li, S. Zeng, G. Lian, X. X. Bai, W. P. Liu, H. Yamaguchi, S. Kubono, J. Hu, D. Kahl, H. S. Jung, J. Y. Moon, C. S. Lee, T. Teranishi, H. W. Wang, H. Ishiyama, N. Iwasa, T. Komatsubara, and B. A. Brown, Phys. Rev. C **88**, 035801 (2013).
[160] J. Peng, E. C. Jury , P. Dönnes, and C. Ciurtin, Front. Pharmacol. **12**, 720694 (2021).
[161] M. Pfützner, M. Karny, L. V. Grigorenko, and K. Riisager, Rev. Mod. Phys. **84**, 567 (2012).
[162] B. Blank and M. J. G. Borge, Prog. Part. Nucl. Phys. **60**, 403 (2008).
[163] M. J. G. Borge, Phys. Scr. **T152**, 014013 (2013).
[164] J. C. Hardy and I. S. Towner, Phys. Rev. C **91**, 025501 (2015).

[165] R. K. Wallace and S. E. Woosley, Astrophys. J. Suppl. Ser. **45**, 389 (1981).
[166] T. Kajino, W. Aoki, A.B. Balantekin, R. Diehl, M.A. Famiano, G.J. Mathews, Prog. Part. Nucl. Phys. **107**, 109 (2019).
[167] M. Arnould and S. Goriely, Phys. Rep. **384**, 1 (2003).
[168] J.C. Batchelder, At. Data Nucl. Data Tables **132**, 101323 (2020).
[169] R. Barton, R. McPherson, R. E. Bell, W. R. Frisken, W. T. Link, and R. B. Moore, Can. J. Phys. **41**, 2007 (1963).
[170] R. McPherson and J. C. Hardy, Can. J. Phys. **43**, 1 (1965).
[171] J. C. Hardy and R. E. Bell, Can. J. Phys. **43**, 1671 (1965).
[172] P. L. Reeder, A. M. Poskanzer, R. A. Esterlund, and R. McPherson, Phys. Rev. **147**, 781 (1966).
[173] R G. Sextro, Ph.D. Thesis, University of California, Berkeley, USA, 1973.
[174] Z. Y. Zhou, E. C. Schloemer, M. D. Cable, M. Ahmed, J. E. Reiff, and J. Cerny, Phys. Rev. C **31**, 1941 (1985).
[175] A. García, E. G. Adelberger, H. E. Swanson, T. F. Lang, and D. M. Moltz, Phys. Rev. C **42**, 765 (1990).
[176] S. Hatori, H. Miyatake, S. Morinobu, K. Katori, M. Fujiwara, I. Katayama, N. Ikeda, T. Fukuda, T. Shinozuka, and K. Ogawa, Nucl. Phys. A **549**, 327 (1992).
[177] J. D. Robertson, D. M. Moltz, T. F. Lang, J. E. Reiff, J. Cerny, and B. H. Wildenthal, Phys. Rev. C **47**, 1455 (1993).
[178] J.-C. Thomas, L. Achouri, J. Äystö, R. Béraud, B. Blank, G. Canchel, S. Czajkowski, P. Dendooven, A. Ensallem, J. Giovinazzo, N. Guillet, J. Honkanen, A. Jokinen, A. Laird, M. Lewitowicz, C. Longour, F. de Oliveira Santos, K. Peräjärvi, and M. Stanoiu, Eur. Phys. J. A **21**, 419 (2004).
[179] A. Piechaczek, M.F. Mohar, R. Anne, V. Borrel, B.A. Brown, J.M. Corre, D. Guillemaud-Mueller, R. Hue, H. Keller, S. Kubono, V. Kunze, M. Lewitowicz, P. Magnus, A.C. Mueller, T. Nakamura, M. Pfützner, E. Roeckl, K. Rykaczewski, M.G. Saint-Laurent, W.-D. Schmidt-Ott, O. Sorlin, Nucl. Phys. A **584**, 509 (1995).
[180] M. V. Lund, A. Andreyev, M. J. G. Borge, J. Cederkäll, H. De Witte, L. M. Fraile, H. O. U. Fynbo, P. T. Greenlees, L. J. Harkness-Brennan, A. M. Howard, M. Huyse, B. Jonson, D. S. Judson, O. S. Kirsebom, J. Konki, J. Kurcewicz, I. Lazarus, R. Lica, S. Lindberg, M. Madurga, N. Marginean, R. Marginean, I. Marroquin, C. Mihai, M. Munch, E. Nacher, A. Negret, T. Nilsson, R. D. Page, S. Pascu, A. Perea, V. Pucknell, P. Rahkila, E. Rapisarda, K. Riisager, F. Rotaru, C. Sotty, M. Stanoiu, O. Tengblad, A. Turturica, P. Van Duppen, V. Vedia, R. Wadsworth, and N. Warr, Eur. Phys. J. A **52**, 304 (2016).
[181] L. J. Sun, X. X. Xu, D. Q. Fang, C. J. Lin, J. S. Wang, Z. H. Li, Y. T. Wang, J. Li, L. Yang, N. R. Ma, K. Wang, H. L. Zang, H. W. Wang, C. Li, C. Z. Shi, M. W. Nie, X. F. Li, H. Li, J. B. Ma, P. Ma, S. L. Jin, M. R. Huang, Z. Bai, J. G. Wang, F. Yang, H. M. Jia, H. Q. Zhang, Z. H. Liu, P. F. Bao, D. X. Wang, Y. Y. Yang, Y. J. Zhou, W. H. Ma, J. Chen, Y. G. Ma, Y. H. Zhang, X. H. Zhou, H. S. Xu, G. Q. Xiao, and W. L. Zhan, Phys. Rev. C **95**, 014314 (2017).
[182] D. E. Alburger, G. Wang, and E. K. Warburton, Phys. Rev. C **35**, 1479 (1987).
[183] J. Lee, X. X. Xu, K. Kaneko, Y. Sun, C. J. Lin, L. J. Sun, P. F. Liang, Z. H. Li, J. Li, H. Y. Wu, D. Q. Fang, J. S. Wang, Y. Y. Yang, C. X. Yuan, Y. H. Lam, Y. T. Wang, K. Wang, J. G. Wang, J. B. Ma, J. J. Liu, P. J. Li, Q. Q. Zhao, L. Yang, N. R. Ma, D. X. Wang, F. P. Zhong, S. H. Zhong, F. Yang, H. M. Jia, P. W. Wen, M. Pan, H. L. Zang, X. Wang, C. G. Wu, D. W. Luo, H. W. Wang, C. Li, C. Z. Shi, M. W. Nie, X. F. Li, H. Li, P. Ma, Q. Hu, G. Z. Shi, S. L. Jin, M. R. Huang, Z. Bai, Y. J. Zhou, W. H. Ma, F. F. Duan, S. Y. Jin, Q. R. Gao, X. H. Zhou, Z. G. Hu, M. Wang, M. L. Liu, R. F. Chen, and X. W. Ma, Phys. Rev. Lett. **125**, 192503 (2020).
[184] L. Weissman, A. F. Lisetskiy, O. Arndt, U. Bergmann, B. A. Brown, J. Cederkall, I. Dillmann, O. Hallmann, L. Fraile, S. Franchoo, L. Gaudefroy, U. Köster, K.-L. Kratz, B. Pfeiffer, and O. Sorlin, J. Phys. G: Nucl. Part. Phys. **31**, 143 (2005).
[185] Y. Ichikawa, T. K. Onishi, D. Suzuki, H. Iwasaki, T. Kubo, V. Naik, A. Chakrabarti, N. Aoi, B. A. Brown, N. Fukuda, S. Kubono, T. Motobayashi, T. Nakabayashi, T. Nakamura, T. Nakao, T. Okumura, H. J. Ong, H. Suzuki, M. K. Suzuki, T. Teranishi, K. N. Yamada, H. Yamaguchi, and H. Sakurai, Phys. Rev. C **80**, 044302 (2009).
[186] Y. Ichikawa, T. K. Onishi, D. Suzuki, H. Iwasaki, T. Kubo1, V. Naik, A. Chakrabarti, N. Aoi1, B. A. Brown, N. Fukuda, S. Kubono, T. Motobayashi1, T. Nakabayashi, T. Nakamura, T. Nakao, T. Okumura, H. J. Ong, H. Suzuki, M. K. Suzuki, T. Teranishi, K. N. Yamada, H. Yamaguchi, and H. Sakurai, J. Phys.: Conf. Ser. **312**, 092031 (2011).
[187] R. E. McDonald, J. A. Becker, A. D. W. Jones, and A. R. Poletti, Phys. Rev. **181**, 1631 (1969).
[188] D. Pérez-Loureiro, C. Wrede, M. B. Bennett, S. N. Liddick, A. Bowe, B. A. Brown, A. A. Chen, K. A. Chipps, N. Cooper, D. Irvine, E. McNeice, F. Montes, F. Naqvi, R. Ortez, S. D. Pain, J. Pereira, C. J. Prokop, J. Quaglia, S. J. Quinn, J. Sakstrup, M. Santia, S. B. Schwartz, S. Shanab, A. Simon, A. Spyrou, and E. Thiagalingam, Phys. Rev. C **93**, 064320 (2016).
[189] G. F. Grinyer, C. E. Svensson, C. Andreoiu, A. N. Andreyev, R. A. E. Austin, G. C. Ball, R. S. Chakrawarthy, P. Finlay, P. E. Garrett, G. Hackman, J. C. Hardy, B. Hyland, V. E. Iacob, K. A. Koopmans, W. D. Kulp, J. R. Leslie, J. A. Macdonald, A. C. Morton, W. E. Ormand, C. J. Osborne, C. J. Pearson, A. A. Phillips, F. Sarazin, M. A. Schumaker, H. C. Scraggs, J. Schwarzenberg, M. B. Smith, J. J. Valiente-Dobón, J. C. Waddington, J. L. Wood, and E. F. Zganjar, Phys. Rev. C **71**, 044309 (2005).
[190] Ł. Janiak, N. Sokołowska, A. A. Bezbakh, A. A. Ciemny, H. Czyrkowski, R. Dabrowski, W. Dominik, A. S. Fomichev, M. S. Golovkov, A. V. Gorshkov, Z. Janas, G. Kamiński, A. G. Knyazev, S. A. Krupko, M. Kuich, C. Mazzocchi, M. Mentel, M. Pfützner, P. Plucíński, M. Pomorski, R. S. Slepniev, and B. Zalewski, Phys. Rev. C **95**, 034315 (2017).
[191] L. J. Sun, X. X. Xu, C. J. Lin, J. Lee, S. Q. Hou, C. X. Yuan, Z. H. Li, J. José, J. J. He, J. S. Wang, D. X. Wang, H. Y. Wu, P. F. Liang, Y. Y. Yang, Y. H. Lam, P. Ma, F. F. Duan, Z. H. Gao, Q. Hu, Z. Bai, J. B. Ma, J. G. Wang, F. P. Zhong, C. G. Wu, D. W. Luo, Y. Jiang, Y. Liu, D. S. Hou, R. Li, N. R. Ma, W. H. Ma, G. Z. Shi, G. M. Yu, D. Patel, S. Y. Jin, Y. F. Wang, Y. C. Yu, Q. W. Zhou, P. Wang, L. Y. Hu, X. Wang, H. L. Zang, P. J. Li, Q. Q. Zhao, L. Yang, P. W. Wen, F. Yang, H. M. Jia, G. L. Zhang, M. Pan, X. Y. Wang, H. H. Sun, Z. G. Hu, R. F. Chen, M. L. Liu, W. Q. Yang, Y. M. Zhao, and H. Q. Zhang, Phys. Rev. C **99**, 064312 (2019).
[192] C. Détraz, D. Guillemaud, G. Huber, R. Klapisch, M. Langevin, F. Naulin, C. Thibault, L. C. Carraz, and F. Touchard, Phys. Rev. C **19**, 164 (1979).
[193] D. Guillemaud-Mueller, C. Detraz, M. Langevin, F. Naulin, M. de Saint-Simon, C. Thibault, F. Touchard, and M. Epherre, Nucl. Phys. A **426**, 37 (1984).
[194] A. D. W. Jones, J. A. Becker, R. E. McDonald, and A. R. Poletti, Phys. Rev. C **1**, 1000 (1970).
[195] D. E. Alburger and D. H. Wilkinson, Phys. Rev. C **3**, 1957 (1971).

[196] D. E. Alburger and E. K. Warburton, Nucl. Phys. A **385**, 474 (1982).
[197] M. Friedman, D. Pérez-Loureiro, T. Budner, E. Pollacco, C. Wrede, M. Cortesi, C. Fry, B. Glassman, M. Harris, J. Heideman, M. Janasik, B.T. Roeder, M. Roosa, A. Saastamoinen, J. Stomps, J. Surbrook, P. Tiwari, J. Yurkon, Nucl. Instrum. Methods Phys. Res. A **940**, 93 (2019).
[198] D.J. Morrissey, B.M. Sherrill, M. Steiner, A. Stolz, I. Wiedenhoever, Nucl. Instrum. Methods Phys. Res. A **204**, 90 (2003).
[199] W.F. Mueller, J.A. Church, T. Glasmacher, D. Gutknecht, G. Hackman, P.G. Hansen, Z. Hu, K.L. Miller, P. Quirin, Nucl. Instrum. Methods Phys. Res. A **466**, 492 (2001).
[200] C.J. Prokop, S.N. Liddick, B.L. Abromeit, A.T. Chemey, N.R. Larson, S. Suchyta, J.R. Tompkins, Nucl. Instrum. Methods Phys. Res. A **741**, 163 (2014).
[201] M. J. Martin, Nucl. Data Sheets **108**, 1583 (2007).
[202] R. B. Firestone, Nucl. Data Sheets **110**, 1691 (2009).
[203] M. Piiparinen, Z. Phys. **252**, 206 (1972).
[204] R. B. Firestone, Nucl. Data Sheets **108**, 2319 (2007).
[205] M. J. Martin, Nucl. Data Sheets **114**, 1497 (2013).
[206] H. O. U. Fynbo, Nucl. Instrum. Methods Phys. Res. B **207**, 275 (2003).
[207] H. Fynbo, M. Borge, J. Cederkäll, S. Courtin, P. Dessagne, B. Jonson, G. L. Scornet, T. Nilsson, G. Nyman, E. Poirier, K. Riisager, O. Tengblad, and K. Wilhelmsen, Nucl. Phys. A **736**, 39 (2004).
[208] F. Sarazin, J. S. Al-Khalili, G. C. Ball, G. Hackman, P. M. Walker, R. A. E. Austin, B. Eshpeter, P. Finlay, P. E. Garrett, G. F. Grinyer, K. A. Koopmans, W. D. Kulp, J. R. Leslie, D. Melconian, C. J. Osborne, M. A. Schumaker, H. C. Scraggs, J. Schwarzenberg, M. B. Smith, C. E. Svensson, J. C. Waddington, and J. L. Wood, Phys. Rev. C **70**, 031302(R) (2004).
[209] C. M. Mattoon, F. Sarazin, C. Andreoiu, A. N. Andreyev, R. A. E. Austin, G. C. Ball, R. S. Chakrawarthy, D. Cross, E. S. Cunningham, J. Daoud, P. E. Garrett, G. F. Grinyer, G. Hackman, D. Melconian, C. Morton, C. Pearson, J. J. Ressler, J. Schwarzenberg, M. B. Smith, and C. E. Svensson, Phys. Rev. C **80**, 034318 (2009).
[210] S. B. Schwartz, C. Wrede, M. B. Bennett, S. N. Liddick, D. Pérez-Loureiro, A. Bowe, A. A. Chen, K. A. Chipps, N. Cooper, D. Irvine, E. McNeice, F. Montes, F. Naqvi, R. Ortez, S. D. Pain, J. Pereira, C. Prokop, J. Quaglia, S. J. Quinn, J. Sakstrup, M. Santia, S. Shanab, A. Simon, A. Spyrou, and E. Thiagalingam, Phys. Rev. C **92**, 031302(R) (2015).
[211] R. B. Firestone, Nucl. Data Sheets **108**, 1 (2007).
[212] Steve Baker and Robert D. Cousins, Nucl. Instrum. Methods Phys. Res. **221**, 437 (1984).
[213] A. Chester, G. C. Ball, R. Caballero-Folch, D. S. Cross, S. Cruz, T. Domingo, T. E. Drake, A. B. Garnsworthy, G. Hackman, S. Hallam, J. Henderson, R. Henderson, W. Korten, R. Krücken, M. Moukaddam, B. Olaizola, P. Ruotsalainen, J. Smallcombe, K. Starosta, C. E. Svensson, J. Williams, and K. Wimmer Phys. Rev. C **96**, 011302(R) (2017).
[214] E. K. Warburton, C. J. Lister, D. E. Alburger, and J. W. Olness, Phys. Rev. C **23**, 1242 (1981).
[215] P. M. Endt, Nucl. Phys. A **521**, 1 (1990).
[216] P. M. Endt and C. Van Der Leun, Nucl. Phys. A **310**, 1 (1978).
[217] H. S. Wilson, R. W. Kavanagh, and F. M. Mann, Phys. Rev. C **22**, 1696 (1980).
[218] N. Anyas-Weiss and A. E. Litherland, Can. J. Phys. **47**, 2609 (1969).
[219] R. J. van Reenen, Z. B. D. Toit, and W. L. Mouton, Z. Phys. **227**, 326 (1969).
[220] G. J. McCallum, R. J. Sparks, G. E. Coote, and K. P. Pohl, Can. J. Phys. **49**, 467 (1971).
[221] P. Tikkanen, J. Keinonen, A. Kangasmäki, Zs. Fülöp, Á. Z. Kiss, and E. Somorjai, Phys. Rev. C **43**, 2162 (1991).
[222] D.C. Powell, C. Iliadis, A.E. Champagne, S.E. Hale, V.Y. Hansper, R.A. Surman, and K.D. Veal, Nucl. Phys. A **644**, 263 (1998).
[223] D. W. O. Rogers, N. Anyas-Weiss, S. P. Dolan, N. A. Jelley, and T. K. Alexander, Can. J. Phys. **55**, 206 (1977).
[224] C. P. Browne, J. D. Goss, and A. A. Rollefson, Phys. Rev. C **8**, 1805 (1973).
[225] R.M. Prior, S.E. Darden, K.R. Nyga, and H.Paetz Gen. Schieck, Nucl. Phys. A **533**, 411 (1991).
[226] Y. Fujita, I. Hamamoto, H. Fujita, Y. Shimbara, T. Adachi, G. P. A. Berg, K. Fujita, K. Hatanaka, J. Kamiya, K. Nakanishi, Y. Sakemi, Y. Shimizu, M. Uchida, T. Wakasa, and M. Yosoi, Phys. Rev. Lett. **92**, 062502 (2004).
[227] J.C. Hardy, L.C. Carraz, B. Jonson, P.G. Hansen, Phys. Lett. B **71**, 307 (1977).
[228] B. A. Brown and B. H. Wildenthal, Annu. Rev. Nucl. Part. Sci. **38**, 29 (1988).
[229] A. R. Barnett, Comput. Phys. Commun. **27**, 147 (1982).
[230] M. Wang, G. Audi, F. G. Kondev, W. J. Huang, S. Naimi, and X. Xu, Chin. Phys. C **41**, 030003 (2017).
[231] N. B. Gove and M. J. Martin, At. Data Nucl. Data Tables **10**, 205 (1971).
[232] J. C. Hardy and I. S. Towner, Phys. Rev. C **102**, 045501 (2020).
[233] D.C. Powell, C. Iliadis, A.E. Champagne, C.A. Grossmann, S.E. Hale, V.Y. Hansper, L.K. McLean, Nucl. Phys. A **660**, 349 (1999).
[234] P.G. Ikossi, T.B. Clegg, W.W. Jacobs, E.J. Ludwig, W.J. Thompson, Nucl. Phys. A **274**, 1 (1976).
[235] P. G. Ikossi, W. J. Thompson, T. B. Clegg, W. W. Jacobs, and E. J. Ludwig, Phys. Rev. Lett. **36**, 1357 (1976).
[236] J.F. Wilkerson, T.M. Mooney, R.E. Fauber, T.B. Clegg, H.J. Karwowski, E.J. Ludwig, W.J. Thompson, Nucl. Phys. A **549**, 223 (1992).
[237] G. C. Morrison, D. H. Youngblood, R. C. Bearse, and R. E. Segel, Phys. Rev. **174**, 1366 (1968).
[238] Vandana Tripathi, S. L. Tabor, A. Volya, S. N. Liddick, P. C. Bender, N. Larson, C. Prokop, S. Suchyta, P.-L. Tai, and J. M. VonMoss, Phys. Rev. Lett. **111**, 262501 (2013).
[239] S. E. A. Orrigo, B. Rubio, Y. Fujita, B. Blank, W. Gelletly, J. Agramunt, A. Algora, P. Ascher, B. Bilgier, L. Cáceres, R.B. Cakirli, H. Fujita, E. Ganioglu, M. Gerbaux, J. Giovinazzo, S. Grévy, O. Kamalou, H. C. Kozer, L. Kucuk, T. Kurtukian-Nieto, F. Molina, L. Popescu, A. M. Rogers, G. Susoy, C. Stodel, T. Suzuki, A. Tamii, J. C. Thomas, Phys. Rev. Lett. **112**, 222501 (2014).
[240] J. J. Liu, X. X. Xu, L. J. Sun, C. X. Yuan, K. Kaneko, Y. Sun, P. F. Liang, H. Y. Wu, G. Z. Shi, C. J. Lin, J. Lee, S. M. Wang, C. Qi, J. G. Li, H. H. Li, L. Xayavong, Z. H. Li, P. J. Li, Y. Y. Yang, H. Jian, Y. F. Gao, R. Fan, S. X. Zha, F. C. Dai, H. F. Zhu, J. H. Li, Z. F. Chang, S. L. Qin, Z. Z. Zhang, B. S. Cai, R. F. Chen, J. S. Wang, D. X. Wang, K. Wang, F. F. Duan, Y. H. Lam, P. Ma, Z. H. Gao, Q. Hu, Z. Bai, J. B. Ma, J. G. Wang, C. G. Wu, D. W. Luo, Y. Jiang, Y. Liu, D. S. Hou, R. Li, N. R. Ma, W. H. Ma, G. M. Yu, D. Patel, S. Y. Jin, Y. F.

Wang, Y. C. Yu, L. Y. Hu, X. Wang, H. L. Zang, K. L. Wang, B. Ding, Q. Q. Zhao, L. Yang, P. W. Wen, F. Yang, H. M. Jia, G. L. Zhang, M. Pan, X. Y. Wang, H. H. Sun, H. S. Xu, X. H. Zhou, Y. H. Zhang, Z. G. Hu, M. Wang, M. L. Liu, H. J. Ong, and W. Q. Yang (RIBLL Collaboration), Phys. Rev. Lett. **129**, 242502 (2022).
[241] W. E. Ormand and B. A. Brown, Phys. Lett. B **174**, 128 (1986).
[242] M. Arnould, S. Goriely, and K. Takahashi, Phys. Rep. **450**, 97 (2007).
[243] I. V. Panov, Yu. S. Lutostansky, F.-K. Thielemann, Nucl. Phys. A **947**, 1 (2016).
[244] R. Surman, M. Mumpower, and A. Aprahamian, JPS Conf. Proc. **6**, 010010 (2015).
[245] Peter Möller, Bernd Pfeiffer, and Karl-Ludwig Kratz, Phys. Rev. C **67**, 055802 (2003).
[246] S. Lyons, A. Spyrou, S. N. Liddick, F. Naqvi, B. P. Crider, A. C. Dombos, D. L. Bleuel, B. A. Brown, A. Couture, L. Crespo Campo, J. Engel, M. Guttormsen, A. C. Larsen, R. Lewis, P. Möller, S. Mosby, M. R. Mumpower, E. M. Ney, A. Palmisano, G. Perdikakis, C. J. Prokop, T. Renstrøm, S. Siem, M. K. Smith, and S. J. Quinn, Phys. Rev. C **100**, 025806 (2019).
[247] A. Spyrou, S. N. Liddick, F. Naqvi, B. P. Crider, A. C. Dombos, D. L. Bleuel, B. A. Brown, A. Couture, L. Crespo Campo, M. Guttormsen, A. C. Larsen, R. Lewis, P. Möller, S. Mosby, M. R. Mumpower, G. Perdikakis, C. J. Prokop, T. Renstrøm, S. Siem, S. J. Quinn, and S. Valenta, Phys. Rev. Lett. **117**, 142701 (2016).
[248] M.R. Mumpower, R. Surman, G.C. McLaughlin, and A. Aprahamian, Prog. Part. Nucl. Phys. **86**, 86 (2016).
[249] M. Birch, B. Singh, I. Dillmann, D. Abriola, T. D. Johnson, E. A. McCutchan, and A. A. Sonzogni, Nucl. Data Sheets **128**, 131 (2015).
[250] J. Liang, B. Singh, E.A. McCutchan, I. Dillmann, M. Birch, A.A. Sonzogni, X. Huang, M. Kang, J. Wang, G. Mukherjee, K. Banerjee, D. Abriola, A. Algora, A.A. Chen, T.D. Johnson, and K. Miernik, Nucl. Data Sheets **168**, 1 (2020).
[251] B. Singh, D. Abriola, and I. Dillmann, Summary Report of Consultants' Meeting on Beta-delayed neutron emission evaluation, INDC(NDS)-0599 (2011).
[252] A. B. Garnsworthy and P. E. Garrett, Hyperfine Interact. **225**, 121 (2014).
[253] P. Baumann, Ph. Dessagne, A. Huck, G. Klotz, A. Knipper, G. Marguier, C. Miehé, M. Ramdane, C. Richard-Serre, G. Walter, and B. H. Wildenthal, Phys. Rev. C **36**, 765 (1987).
[254] P. Baumann, Ph. Dessagne, A. Huck, G. Klotz, A. Knipper, Ch. Miehé, M. Ramdane, G. Walter, G. Marguier, H. Gabelmann, C. Richard-Serre, K. Schlösser, and A. Poves, Phys. Rev. C **39**, 626 (1989).
[255] M. Aliotta, R. Buompane, M. Couder, A. Couture, R. J. deBoer, A. Formicola, L. Gialanella, J. Glorius, G. Imbriani, M. Junker, J. Phys. G: Nucl. Part. Phys. **49**, 010501 (2022).
[256] R. E. Tribble, C. A. Bertulani, M. La Cognata, A. M. Mukhamedzhanov, and C. Spitaleri, Rep. Prog. Phys. **77**, 106901 (2014).
[257] C. R. Brune and B. Davids, Annu. Rev. Nucl. Part. Sci. **65**, 87 (2015).
[258] Faïrouz Hammache and Nicolas de Séréville, Front. Phys. **8**, 602920 (2021).
[259] C. Angulo, M. Arnould, M. Rayet, P. Descouvemont, D. Baye, C. Leclercq-Willain, A. Coc, S. Barhoumi, P. Aguer, C. Rolfs, R. Kunz, J. W. Hammer, A. Mayer, T. Paradellis, S. Kossionides, C. Chronidou, K. Spyrou, S. Degl'Innocenti, G. Fiorentini, B. Ricci, S. Zavatarelli, C. Providencia, H. Wolters, J. Soares, C. Grama, J. Rahighi, A. Shotter, and M. Lamehi Rachti, Nucl. Phys. A **656**, 3 (1999).
[260] C. E. Rolfs and W. S. Rodney, *Cauldrons in the Cosmos*, University of Chicago Press, Chicago, USA (1988).
[261] T. Rauscher and F. K. Thielemann, At. Data Nucl. Data Tables **75**, 1 (2000).
[262] T. Rauscher, *Essentials of Nucleosynthesis and Theoretical Nuclear Astrophysics*, IOP Publishing, Bristol, UK (2020).
[263] J. C. Hardy, J. A. Macdonald, H. Schmeing, H. R. Andrews, J. S. Geiger, R. L. Graham, T. Faestermann, E. T. H. Clifford, and K. P. Jackson, Phys. Rev. Lett. **37**, 133 (1976).
[264] A. Spyrou, D. Richman, A. Couture, C. E. Fields, S. N. Liddick, K. Childers, B. P. Crider, P. A. DeYoung, A. C. Dombos, P. Gastis, M. Guttormsen, K. Hermansen, A. C. Larsen, R. Lewis, S. Lyons, J. E. Midtbø, S. Mosby, D. Muecher, F. Naqvi, A. Palmisano-Kyle, G. Perdikakis, C. Prokop, H. Schatz, M. K. Smith, C. Sumithrarachchi, and A. Sweet, Nat. Commun. **15**, 9608 (2024).
[265] H. Schatz and K. E. Rehm, Nucl. Phys. A **777**, 601 (2006).
[266] A. Parikh, J. José, G. Sala, and C. Iliadis, Prog. Part. Nucl. Phys. **69**, 225 (2013).
[267] L. van Wormer, J. Görres, C. Iliadis, M. Wiescher, and F.-K. Thielemann, Astrophys. J. **432**, 326 (1994).
[268] Richard H. Cyburt, A. Matthew Amthor, Ryan Ferguson, Zach Meisel, Karl Smith, Scott Warren, Alexander Heger, R. D. Hoffman, Thomas Rauscher, Alexander Sakharuk, Hendrik Schatz, F. K. Thielemann, Michael Wiescher, Astrophys. J. Suppl. Ser. **189**, 240 (2010).
[269] T. Rauscher and F. K. Thielemann, At. Data Nucl. Data Tables **79**, 47 (2001).
[270] A. Parikh, J. José, F. Moreno, and C. Iliadis, Astrophys. J. Suppl. Ser. **178**, 110 (2008).
[271] R. H. Cyburt, A. M. Amthor, A. Heger, E. Johnson, L. Keek, Z. Meisel, H. Schatz, and K. Smith, Astrophys. J. **830**, 55 (2016).
[272] Zach Meisel, Grant Merz, and Sophia Medvid, Astrophys. J. **872**, 84 (2019).
[273] C. Fröhlich, G. Martínez-Pinedo, M. Liebendörfer, F.-K. Thielemann, E. Bravo, W. R. Hix, K. Langanke, and N. T. Zinner, Phys. Rev. Lett. **96**, 142502 (2006).
[274] A. Arcones, C. Fröhlich, and G. Martínez-Pinedo, Astrophys. J. **750**, 18 (2012).
[275] Kirby Hermansen, Sean M. Couch, Luke F. Roberts, Hendrik Schatz, MacKenzie L. Warren, Astrophys. J. **901**, 77 (2020).
[276] J. S. Randhawa, R. Kanungo, J. Refsgaard, P. Mohr, T. Ahn, M. Alcorta, C. Andreoiu, S. S. Bhattacharjee, B. Davids, G. Christian, A. A. Chen, R. Coleman, P. E. Garrett, G. F. Grinyer, E. Gyabeng Fuakye, G. Hackman, J. Hollett, R. Jain, K. Kapoor, R. Krücken, A. Laffoley, A. Lennarz, J. Liang, Z. Meisel, B. Nikhil, A. Psaltis, A. Radich, M. Rocchini, N. Saei, M. Saxena, M. Singh, C. Svensson, P. Subramaniam, A. Talebitaher, S. Upadhyayula, C. Waterfield, J. Williams, and M. Williams, Phys. Rev. C **104**, L042801 (2021).
[277] D. Soltesz, M. A. A. Mamun, A. V. Voinov, Z. Meisel, B. A. Brown, C. R. Brune, S. M. Grimes, H. Hadizadeh, M. Hornish, T. N. Massey, J. E. O'Donnell, and W. E. Ormand, Phys. Rev. C **103**, 015802 (2021).
[278] Chanhee Kim, Kyungyuk Chae, Soomi Cha, Kyujin Kwak, Gwangeon Seong, and Michael Smith, Astrophys. J. **929**, 96 (2022).
[279] Konrad Schmidt, NSCL Experiment 18039.
[280] Melina Avila, FRIB Experiment 21026.
[281] C. Lederer, M. Aliotta, T. Davinson, D. Doherty, A. Estrade, C. Griffin, T. Kemp, M. Kowalska, S.J. Lonsdale, V. Margerin, A. Murphy, C. Weiß, F. Wenander, P.J. Woods, and L. Zhang, CERN-INTC-2015-036.

[282] Gavin Lotay, FRIB Experiment 21014.
[283] Takumi Okamura, Graduation Thesis, Osaka University, Osaka, Japan, 2024.
[284] Tatsuya Furuno, private communication.
[285] Zach Meisel, NSCL Experiment 17009.
[286] Chris Wrede, FRIB Experiment 23035.
[287] T. Rauscher, Phys. Rev. C **81**, 045807 (2010).
[288] S. E. A. Orrigo, B. Rubio, W. Gelletly, P. Aguilera, A. Algora, A. I. Morales, J. Agramunt, D. S. Ahn, P. Ascher, B. Blank, C. Borcea, A. Boso, R. B. Cakirli, J. Chiba, G. de Angelis, G. de France, F. Diel, P. Doornenbal, Y. Fujita, N. Fukuda, E. Ganioğlu, M. Gerbaux, J. Giovinazzo, S. Go, T. Goigoux, S. Grévy, V. Guadilla, N. Inabe, G. G. Kiss, T. Kubo, S. Kubono, T. Kurtukian-Nieto, D. Lubos, C. Magron, F. Molina, A. Montaner-Pizá, D. Napoli, D. Nishimura, S. Nishimura, H. Oikawa, V. H. Phong, H. Sakurai, Y. Shimizu, C. Sidong, P.-A. Söderström, T. Sumikama, H. Suzuki, H. Takeda, Y. Takei, M. Tanaka, J. Wu, and S. Yagi, Phys. Rev. C **103**, 014324 (2021).
[289] S. F. Paul, J. Bergmann, J. D. Cardona, K. A. Dietrich, E. Dunling, Z. Hockenbery, C. Hornung, C. Izzo, A. Jacobs, A. Javaji, B. Kootte, Y. Lan, E. Leistenschneider, E. M. Lykiardopoulou, I. Mukul, T. Murböck, W. S. Porter, R. Silwal, M. B. Smith, J. Ringuette, T. Brunner, T. Dickel, I. Dillmann, G. Gwinner, M. MacCormick, M. P. Reiter, H. Schatz, N. A. Smirnova, J. Dilling, and A. A. Kwiatkowski, Phys. Rev. C **104**, 065803 (2021).
[290] Huo Junde, Huo Su, Yang Dong, Nucl. Data Sheets **112**, 1513 (2011).
[291] M. Shamsuzzoha Basunia, Nucl. Data Sheets **151**, 1 (2018).
[292] E. Browne and J. K. Tuli, Nucl. Data Sheets **114**, 1849 (2013).
[293] C. Mazzocchi, Z. Janas, J. Döring, M. Axiotis, L. Batist, R. Borcea, D. Cano-Ott, E. Caurier, G. de Angelis, E. Farnea, A. Faßbender, A. Gadea, H. Grawe, A. Jungclaus, M. Kapica, R. Kirchner, J. Kurcewicz, S.M. Lenzi, T. Martínez, I. Mukha, E. Nácher, D. R. Napoli, E. Roeckl, B. Rubio, R. Schwengner, J. L. Tain, and C. A. Ur, Eur. Phys. J. A **12**, 269 (2001).
[294] M. J. López Jiménez, B. Blank, M. Chartier, S. Czajkowski, P. Dessagne, G. de France, J. Giovinazzo, D. Karamanis, M. Lewitowicz, V. Maslov, C. Miehé, P. H. Regan, M. Stanoiu, and M. Wiescher, Phys. Rev. C **66**, 025803 (2002).
[295] L. Kucuk, S. E. A. Orrigo, A. Montaner-Pizá, B. Rubio, Y. Fujita, W. Gelletly, B. Blank, Y. Oktem, T. Adachi, A. Algora, P. Ascher, R. B. Cakirli, G. de France, H. Fujita, E. Ganioğlu, J. Giovinazzo, S. Grévy, F. M. Marqués, F. Molina, F. de Oliveira Santos, L. Perrot, R. Raabe, P. C. Srivastava, G. Susoy, A. Tamii, J. C Thomas, Eur. Phys. J. A **53**, 134 (2017).
[296] Thomas Goigoux, Ph.D. Thesis, Université de Bordeaux, Gradignan, France, 2017.
[297] J. Giovinazzo, T. Goigoux, B. Blank, P. Ascher, M. Gerbaux, S. Grévy, T. Kurtukian-Nieto, C. Magron, P. Doornenbal, N. Fukuda, N. Inabe, G.G. Kiss, T. Kubo, S. Kubono, S. Nishimura, H. Sakurai, Y. Shimizu, C. Sidong, P.-A. Söderström, T. Sumikama, H. Suzuki, H. Takeda, P. Vi, J. Wu, D.S. Ahn, J. Agramunt, A. Algora, V. Guadilla, A. Montaner-Piza, A.I. Morales, S.E.A. Orrigo, B. Rubio, Y. Fujita, M. Tanaka, W. Gelletly, P. Aguilera, F. Molina, F. Diel, D. Lubos, G. de Angelis, D. Napoli, C. Borcea, A. Boso, R.B. Cakirli, E. Ganioglu, J. Chiba, D. Nishimura, H. Oikawa, Y. Takei, S. Yagi, K. Wimmer, G. de France, S. Go, B.A. Brown, Acta Phys. Pol. B **51**, 577 (2020).
[298] J. Chen, ENSDF Analysis and Utility Programs, Gamma to Level Scheme Computation.
[299] R. Kamermans, H. W. Jongsma, J. van der Spek, and H. Verheul, Phys. Rev. C **10**, 620 (1974).
[300] Carl Svensson, Ph.D. Thesis, McMaster University, Ontario, Canada, 1998.
[301] L. J. Sun, X. X. Xu, S. Q. Hou, C. J. Lin, J. José, J. Lee, J. J. He, Z. H. Li, J. S. Wang, C. X. Yuan, F. Herwig, J. Keegans, T. Budner, D. X. Wang, H. Y. Wu, P. F. Liang, Y. Y. Yang, Y. H. Lam, P. Ma, F. F. Duan, Z. H. Gao, Q. Hu, Z. Bai, J. B. Ma, J. G. Wang, F. P. Zhong, C. G. Wu, D. W. Luo, Y. Jiang, Y. Liu, D. S. Hou, R. Li, N. R. Ma, W. H. Ma, G. Z. Shi, G. M. Yu, D. Patel, S. Y. Jin, Y. F. Wang, Y. C. Yu, Q. W. Zhou, P. Wang, L. Y. Hu, X. Wang, H. L. Zang, P. J. Li, Q. Q. Zhao, H. M. Jia, L. Yang, P. W. Wen, F. Yang, M. Pan, X. Y. Wang, Z. G. Hu, R. F. Chen, M. L. Liu, W. Q. Yang, Y. M. Zhao, Phys. Lett. B **802**, 135213 (2020).
[302] J. Chen, ENSDF Analysis and Utility Programs, Radiation Report.
[303] S. T. Perkins, D. E. Cullen, M.-H. Chen, J. H. Hubbell, J. Rathkopf, and J. H. Scofield, LLNL Evaluated Atomic Data Library (EADL), Tech. Rep. UCRL-50400 **30** (1991).
[304] W. Bambynek, B. Crasemann, R. W. Fink, H. U. Freund, H. Mark, C. D. Swift, R. E. Price, and P. Venugopala Rao, Rev. Mod. Phys. **44**, 716 (1972).
[305] J. H. Scofield, Chap. 6 Radiative Transitions in *Atomic Inner-Shell Processes*, B. Crasemann ed., Academic Press: New York, USA, 1975).
[306] Karol Kozioł, Phys. Rev. A **89**, 022515 (2014).
[307] J. L. Campbell and T. Papp, At. Data Nucl. Data Tables **77**, 1 (2001).
[308] I. Massa and G. Vannini, Riv. Nuovo Cim. **5**, 1 (1982).
[309] E. Browne, J.K. Tuli, Nucl. Data Sheets **111**, 2425 (2010).
[310] J. Giovinazzo, Ph. Dessagne, and Ch. Miehé, Nucl. Phys. A **674**, 394 (2000).
[311] J.C. Hardy, J.A. MacDonald, H. Schmeing, T. Faestermann, H.R. Andrews, J.S. Geiger, R.L. Graham, K.P. Jackson, Phys. Lett. B **63**, 27 (1976).
[312] K. Vierinen, Nucl. Phys. A **463**, 605 (1987).
[313] J.C. Hardy, T. Faestermann, H. Schmeing, J.A. Macdonald, H.R. Andrews, J.S. Geiger, R.L. Graham, and K.P. Jackson, Nucl. Phys. A **371**, 349 (1981).
[314] C.D. Nesaraja, Nucl. Data Sheets **115**, 1 (2014).
[315] J. A. Macdonald, J. C. Hardy, H. Schmeing, T. Faestermann, H. R. Andrews, J. S. Geiger, R. L. Graham, and K. P. Jackson, Nucl. Phys. A **288**, 1 (1977).
[316] Ph. Dessagne, Ch. Miehé, P. Baumann, A. Huck, G. Klotz, M. Ramdane, G. Walter, and J. M. Maison, Phys. Rev. C **37**, 2687 (1988).
[317] B. Singh and J. Chen, Nucl. Data Sheets **158**, 1 (2019).
[318] P. Hornshøj, K.Wilsky, P.G.Hansen, and B.Jonson, Nucl. Phys. A **187**, 637 (1972).
[319] Ch. Miehé, Ph. Dessagne, Ch. Pujol, G. Walter, B. Jonson, and M. Lindroos, Eur. Phys. J. A **5**, 143 (1999).
[320] P. Asboe-Hansen, E. Hagberg, P. G. Hansen, J. C. Hardy, P. Hornshøj, B. Jonson, S. Mattsson, P. Tidemand-Petersson, Phys. Lett. B **77**, 363 (1978).

[321] P. Asboe-Hansen, E. Hagberg, P. G. Hansen, J. C. Hardy, B. Jonson, and S. Mattsson, Nucl. Phys. A **361**, 23 (1981).
[322] B. Singh and N. Nica, Nucl. Data Sheets **113**, 1115 (2012).
[323] Jean Blachot, Nucl. Data Sheets **111**, 1471 (2010).
[324] Z. Janas, L. Batist, R. Borcea, J. Döring, M. Gierlik, M. Karny, R. Kirchner, M. La Commara, S. Mandal, C. Mazzocchi, F. Moroz, S. Orlov, A. Płochocki, E. Roeckl, and J. Żylicz, Eur. Phys. J. A **24**, 205 (2005).
[325] Jean Blachot, Nucl. Data Sheets **95**, 679 (2002).
[326] Z. Janas, L. Batist, J. Döring, M. Gierlik, R. Kirchner, J. Kurcewicz, H. Mahmud, C. Mazzocchi, A. Płochocki, E. Roeckl, K. Schmidt, P. J. Woods, and J. Żylicz, Eur. Phys. J. A **23**, 401 (2005).
[327] Balraj Singh and Jun Chen, Nucl. Data Sheets **178**, 41 (2021).
[328] X. Zhou, M. Wang, Y. H. Zhang, Yu. A. Litvinov, Z. Meisel, K. Blaum, X. H. Zhou, S. Q. Hou, K. A. Li, H. S. Xu, R. J. Chen, H. Y. Deng, C. Y. Fu, W. W. Ge, J. J. He, W. J. Huang, H. Y. Jiao, H. F. Li, J. G. Li, T. Liao, A. Litvinov, M. L. Liu, Y. F. Niu, P. Shuai, J. Y. Shi, Y. N. Song, M. Z. Sun, Q. Wang, Y. M. Xing, X. Xu, F. R. Xu, X. L. Yan, J. C. Yang, Y. Yu, Q. Yuan, Y. J. Yuan, Q. Zeng, M. Zhang, and S. Zhang, Nat. Phys. **19**, 1091 (2023).
[329] B. Rubio, P. Aguilera, F. Molina, J. Agramunt, A. Algora, V. Guadilla, A. Montaner-Pizá, A. I. Morales, S. E. A. Orrigo, W. Gelletly, B. Blank, P. Asher, M. Gerbaux, J. Giovinazzo, S. Grevy, T. Kurtukian, C. Magron, J. Chiba, D. Nishimura, H. Oikawa, Y. Takei, S. Yang, D. S. Ahn, P. Doornenbal, N. Fukuda, N. Inabe, G. Kiss, T. Kubo, S. Kubono, S. Nishimura, Y. Shimizu, C. Sidong, P.-A. Söderström, T. Sumikama, H. Suzuki, H. Takeda, P. Vi, J. Wu, Y. Fujita, M. Tanaka, F. Diel, D. Lubos, G. de Angelis, D. Napoli, C. Borcea, A. Boso, R. B. Cakirli, E. Ganioglu, G. de France, S. Go, J. Phys.: Conf. Ser. **1308**, 012018 (2019).
[330] S. Röhl, S. Hoppenau, and M. Dost, Phys. Rev. Lett. **43**, 1300 (1979).
[331] S. Röhl, S. Hoppenau, and M. Dost, Nucl. Phys. A **369**, 301 (1981).
[332] J. F. Chemin, S. Andriamonje, J. Roturier, and B. Saboya, Nucl. Phys. A **331**, 407 (1979).
[333] Per Amund Amundsen and Martin Dost, Phys. Rev. C **33**, 1079 (1986).
[334] U. Heinz, Rep. Prog. Phys. **50**, 145 (1987).
[335] A. Gilbert and A. G. W. Cameron, Can. J. Phys. **43**, 1446 (1965).
[336] W. Dilg, W. Schantl, H. Vonach, and M. Uhl, Nucl. Phys. A **217**, 269 (1973).
[337] J. C. Hardy, Phys. Lett. B **109**, 242 (1982).
[338] B. L. Berman and S. C. Fultz, Rev. Mod. Phys. **47**, 713 (1975).
[339] C. H. Johnson, Phys. Rev. C **16**, 2238 (1977).
[340] V. Avrigeanu and M. Avrigeanu, Phys. Rev. C **106**, 024615 (2022).
[341] J. Wei, H. Ao, B. Arend, S. Beher, G. Bollen, N. Bultman, F. Casagrande, W. Chang, Y. Choi, S. Cogan, C. Compton, M. Cortesi, J. Curtin, K. Davidson, X. Du, K. Elliott, B. Ewert, A. Facco, A. Fila, K. Fukushima, V. Ganni, A. Ganshyn, J. Gao, T. Glasmacher, J. Guo, Y. Hao, W. Hartung, N. Hasan, M. Hausmann, K. Holland, H. C. Hseuh, M. Ikegami, D. Jager, S. Jones, N. Joseph, T. Kanemura, S.-H. Kim, P. Knudsen, B. Kortum, E. Kwan, T. Larter, R. E. Laxdal, M. Larmann, K. Laturkar, J. LeTourneau, Z.-Y. Li, S. Lidia, G. Machicoane, C. Magsig, P. Manwiller, F. Marti, T. Maruta, A. McCartney, E. Metzgar, S. Miller, Y. Momozaki, D. Morris, M. Mugerian, I. Nesterenko, C. Nguyen, W. O'Brien, K. Openlander, P. N. Ostroumov, M. Patil, A. S. Plastun, J. Popielarski, L. Popielarski, M. Portillo, J. Priller, X. Rao, M. Reaume, H. Ren, K. Saito, M. Smith, M. Steiner, A. Stolz, O. B. Tarasov, B. Tousignant, R. Walker, X. Wang, J. Wenstrom, G. West, K. Witgen, M. Wright, T. Xu, Y. Xu, Y. Yamazaki, T. Zhang, Q. Zhao, S. Zhao, K. Dixon, M. Wiseman, M. Kelly, K. Hosoyama, and S. Prestemon, Mod. Phys. Lett. A **37**, 2230006 (2022).
[342] M. Portillo, B.M. Sherrill, Y. Choi, M. Cortesi, K. Fukushima, M. Hausmann, E. Kwan, S. Lidia, P.N. Ostroumov, R. Ringle, M.K. Smith, M. Steiner, O.B. Tarasov, A.C.C. Villari, and T. Zhang, Nucl. Instrum. Methods Phys. Res. B **540**, 151 (2023).
[343] C.S. Sumithrarachchi, D.J. Morrissey, S. Schwarz, K. Lund, G. Bollen, R. Ringle, G. Savard, and A.C.C. Villari, Nucl. Instrum. Methods Phys. Res. B **463**, 305 (2020).
[344] K.R. Lund, G. Bollen, D. Lawton, D.J. Morrissey, J. Ottarson, R. Ringle, S. Schwarz, C.S. Sumithrarachchi, A.C.C. Villari, and J. Yurkon, Nucl. Instrum. Methods Phys. Res. B **463**, 378 (2020).
[345] A.C.C. Villari, G. Bollen, A. Henriques, A. Lapierre, S. Nash, R. Ringle, S. Schwarz, C.S. Sumithrarachchi, Nucl. Instrum. Methods Phys. Res. B **541**, 350 (2023).
[346] FRIB beam rate calculator.
[347] MIRION Low Energy Germanium Detector.
[348] MIRION Extended Range Coaxial Germanium Detector.
[349] MIRION Cryo-Pulse 5 Plus Electrically Refrigerated Cryostat.
[350] D. Willems, R. Arts, B.V.-J. Douwen, MIRION Technical Paper (2015).
[351] MIRCON MSD12 Circular Silicon Detector.
[352] MIRCON MSD26 Circular Silicon Detector.
[353] MIRION Intelligent Preamplifier.
[354] J. Eberth, H. Hess, P. Reiter, S. Bertoldo, C. Carraro, G. Maggioni, D. R. Napoli, W. Raniero, and D. De Salvador, Eur. Phys. J. A **59**, 179 (2023).
[355] ORTEC 660 Dual 5-kV Bias Supply.
[356] Mesytec MPR-1 Charge Integrating Preamplifier.
[357] Mesytec MHV-4 High Voltage Supply.
[358] Mesytec MNV-4 NIM Power Supply.
[359] XIA Pixie-16 Digitizer.
[360] K. Starosta, C. Vaman, D. Miller, P. Voss, D. Bazin, T. Glasmacher, H. Crawford, P. Mantica, H. Tan, W. Hennig, M. Walby, A. Fallu-Labruyere, J. Harris, D. Breus, P. Grudberg, W.K. Warburton, Nucl. Instrum. Methods Phys. Res. A **610**, 700 (2009).
[361] XIA Pixie-16 Digitizer User Manual.
[362] H.Y. Wu, Z.H. Li, H. Tan, H. Hua, J. Li, W. Hennig, W.K. Warburton, D.W. Luo, X. Wang, X.Q. Li, S.Q. Zhang, C. Xu, Z.Q. Chen, C.G.

Wu, Y. Jin, J. Lin, D.X. Jiang, Y.L. Ye, Nucl. Instrum. Methods Phys. Res. A **975**, 164200 (2020).
[363] D. Weisshaar, D. Bazin, P.C. Bender, C.M. Campbell, F. Recchia, V. Bader, T. Baugher, J. Belarge, M.P. Carpenter, H.L. Crawford, M. Cromaz, B. Elman, P. Fallon, A. Forney, A. Gade, J. Harker, N. Kobayashi, C. Langer, T. Lauritsen, I.Y. Lee, A. Lemasson, B. Longfellow, E. Lunderberg, A.O. Macchiavelli, K. Miki, S. Momiyama, S. Noji, D.C. Radford, M. Scott, J. Sethi, S.R. Stroberg, C. Sullivan, R. Titus, A. Wiens, S. Williams, K. Wimmer, S. Zhu, Nucl. Instrum. Methods Phys. Res. A **847**, 187 (2017).
[364] BNC Model DB-2 NIM Random Pulse Generator.
[365] Y. Isozumi, Nucl. Instrum. Methods Phys. Res. A **280**, 151 (1989).
[366] M. S. Freedman, Annu. Rev. Nucl. Part. Sci. **24**, 209 (1974).
[367] B. Crasemann, *Atomic Inner-Shell Processes*, Academic Press, New York, USA (1975).
[368] Juhani Kantele, *Handbook of Nuclear Spectrometry*, Academic Press, London (1995).
[369] Matt Newville, easyXAFS, Matteo Levantino, Christian Schlepuetz, Damian Günzing, Max Rakitin, Sang-Woo Kim, and kalvdans, xraypy/XrayDB: (4.5.1). Zenodo (2023).
[370] M. Basunia, Nucl. Data Sheets **107**, 2323 (2006).
[371] M.-M. Bé, V. Chisté, C. Dulieu, X. Mougeot, E. Browne, V. Chechev, N. Kuzmenko, F. Kondev, A. Luca, M. Galán, A.L. Nichols, A. Arinc, and X. Huang, Mono. BIPM-5 - Table of Radionuclides, Vol.2 (2004).
[372] Devinder Mehta, M.L. Garg, Jasbir Singh, Nirmal Singh, T.S. Cheema, P.N. Trehan, Nucl. Instrum. Methods Phys. Res. A **245**, 447 (1986).
[373] M.-M. Bé, V. Chisté, C. Dulieu, X. Mougeot, E. Browne, V. Chechev, N. Kuzmenko, F. Kondev, A. Luca, M. Galán, A.L. Nichols, A. Arinc, and X. Huang, Mono. BIPM-5 - Table of Radionuclides, Vol.5 (2010).
[374] Glenn F. Knoll, *Radiation Detection and Measurement*, John Wiley & Sons (2010).
[375] M. J. Martin, Nucl. Data Sheets **114**, 1497 (2013).
[376] Gordon R. Gilmore, *Practical Gamma-ray Spectroscopy*, John Wiley & Sons (2008).
[377] T. Palazzo, A. J. Mitchell, G. J. Lane, A. E. Stuchbery, B. A. Brown, M. W. Reed, A. Akber, B. J. Coombes, J. T. H. Dowie, T. K. Eriksen, M. S. M. Gerathy, T. Kibédi, T. Tornyi, and M. O. de Vries, Phys. Rev. Lett. **130**, 122503 (2023).
[378] Erik Jensen, Ph.D. Thesis, Aarhus University, Aarhus, Denmark, 2024.
[379] Justus Eder, Master Thesis, Aarhus University, Aarhus, Denmark, 2024.
[380] R. Mahajan, T. Wheeler, E. Pollacco, C. Wrede, A. Adams, H. Alvarez-Pol, A. Andalib, A. Anthony, Y. Ayyad, D. Bazin, T. Budner, M. Cortesi, J. Dopfer, M. Friedman, B. Jain, A. Jaros, D. Pérez-Loureiro, B. Mehl, R. De Oliveira, S. Ravishankar, L. J. Sun, and J. Surbrook, Phys. Rev. C **110**, 035807 (2024).
[381] FRIB Decay Station White Paper.
[382] Y.A. Akovali, Nucl. Data Sheets **84**, 1 (1998).
[383] Mono. BIPM-5 - Table of Radionuclides, Vol.9 (to be published).
[384] Canberra Model 1407P Pulse Pair Generator.
[385] Marcell P. Takács, Karsten Kossert, Appl. Radiat. Isot. **176**, 109858 (2021).
[386] Chavdar Dutsov, Benoît Sabot, Philippe Cassette, Krasimir Mitev, Appl. Radiat. Isot. **176**, 109845 (2021).
[387] M. Honma, T. Otsuka, B. A. Brown, and T. Mizusaki, Phys. Rev. C **69**, 034335 (2004).
[388] T. Rauscher, Int. J. Mod. Phys. E **20**, 1071 (2011).
[389] T. Rauscher, code SMARAGD, version v0.10.2 (2014).
[390] A. Adams, C. Wrede, B. A. Brown, R. Longland, L. J. Sun, J. Dopfer, C. Marshall *et al*., in preparation.
[391] K. Hämäläinen, S. Manninen, P. Suortti, S. P. Collins, M. J. Cooper, and D. Laundy, J. Phys.: Condens. Matter **1**, 5955 (1989).
[392] Ning Lu, Yi Hua Lam, Alexander Heger, Zi Xin Liu, and Hidetoshi Yamaguchi, Phys. Rev. C **110**, 065804 (2024).
[393] M. Wang, Y. H. Zhang, X. Zhou, X. H. Zhou, H. S. Xu, M. L. Liu, J. G. Li, Y. F. Niu, W. J. Huang, Q. Yuan, S. Zhang, F. R. Xu, Yu. A. Litvinov, K. Blaum, Z. Meisel, R. F. Casten, R. B. Cakirli, R. J. Chen, H. Y. Deng, C. Y. Fu, W. W. Ge, H. F. Li, T. Liao, S. A. Litvinov, P. Shuai, J. Y. Shi, Y. N. Song, M. Z. Sun, Q. Wang, Y. M. Xing, X. Xu, X. L. Yan, J. C. Yang, Y. J. Yuan, Q. Zeng, and M. Zhang, Phys. Rev. Lett. **130**, 192501 (2023).
[394] M. Aliotta, R. Buompane, M. Couder, A. Couture, R. J. deBoer, A. Formicola, L. Gialanella, J. Glorius, G. Imbriani, M. Junker, J. Phys. G: Nucl. Part. Phys. **49**, 010501 (2022).
[395] R. E. Tribble, C. A. Bertulani, M. La Cognata, A. M. Mukhamedzhanov, and C. Spitaleri, Rep. Prog. Phys. **77**, 106901 (2014).
[396] C. R. Brune and B. Davids, Annu. Rev. Nucl. Part. Sci. **65**, 87 (2015).
[397] Faïrouz Hammache and Nicolas de Séréville, Front. Phys. **8**, 602920 (2021).
[398] C. Angulo, M. Arnould, M. Rayet, P. Descouvemont, D. Baye, C. Leclercq-Willain, A. Coc, S. Barhoumi, P. Aguer, C. Rolfs, R. Kunz, J. W. Hammer, A. Mayer, T. Paradellis, S. Kossionides, C. Chronidou, K. Spyrou, S. Degl'Innocenti, G. Fiorentini, B. Ricci, S. Zavatarelli, C. Providencia, H. Wolters, J. Soares, C. Grama, J. Rahighi, A. Shotter, and M. Lamehi Rachti, Nucl. Phys. A **656**, 3 (1999).
[399] C. E. Rolfs and W. S. Rodney, *Cauldrons in the Cosmos* (University of Chicago Press, Chicago, 1988).
[400] C. Iliadis, *Nuclear Physics of Stars* (Wiley-VCH, Weinheim, 2015).
[401] T. Rauscher and F. K. Thielemann, At. Data Nucl. Data Tables **75**, 1 (2000).
[402] T. Rauscher, *Essentials of Nucleosynthesis and Theoretical Nuclear Astrophysics* (IOP, Bristol, 2020).
[403] J. C. Hardy, J. A. Macdonald, H. Schmeing, H. R. Andrews, J. S. Geiger, R. L. Graham, T. Faestermann, E. T. H. Clifford, and K. P. Jackson, Phys. Rev. Lett. **37**, 133 (1976).
[404] J. José, *Stellar Explosions: Hydrodynamics and Nucleosynthesis* (CRC, Boca Raton, 2016).
[405] H. Schatz and K. E. Rehm, Nucl. Phys. A **777**, 601 (2006).
[406] A. Parikh, J. José, G. Sala, and C. Iliadis, Prog. Part. Nucl. Phys. **69**, 225 (2013).
[407] L. van Wormer, J. Görres, C. Iliadis, M. Wiescher, and F.-K. Thielemann, Astrophys. J. **432**, 326 (1994).
[408] Richard H. Cyburt, A. Matthew Amthor, Ryan Ferguson, Zach Meisel, Karl Smith, Scott Warren, Alexander Heger, R. D. Hoffman, Thomas Rauscher, Alexander Sakharuk, Hendrik Schatz, F. K. Thielemann, Michael Wiescher, Astrophys. J. Suppl. Ser. **189**, 240 (2010).
[409] T. Rauscher and F. K. Thielemann, At. Data Nucl. Data Tables **79**, 47 (2001).

[410] A. Parikh, J. José, F. Moreno, and C. Iliadis, Astrophys. J. Suppl. Ser. **178**, 110 (2008).
[411] R. H. Cyburt, A. M. Amthor, A. Heger, E. Johnson, L. Keek, Z. Meisel, H. Schatz, and K. Smith, Astrophys. J. **830**, 55 (2016).
[412] Zach Meisel, Grant Merz, and Sophia Medvid, Astrophys. J. **872**, 84 (2019).
[413] C. Fröhlich, G. Martínez-Pinedo, M. Liebendörfer, F.-K. Thielemann, E. Bravo, W. R. Hix, K. Langanke, and N. T. Zinner, Phys. Rev. Lett. **96**, 142502 (2006).
[414] A. Arcones, C. Fröhlich, and G. Martínez-Pinedo, Astrophys. J. **750**, 18 (2012).
[415] Kirby Hermansen, Sean M. Couch, Luke F. Roberts, Hendrik Schatz, MacKenzie L. Warren, Astrophys. J. **901**, 77 (2020).
[416] J. S. Randhawa, R. Kanungo, J. Refsgaard, P. Mohr, T. Ahn, M. Alcorta, C. Andreoiu, S. S. Bhattacharjee, B. Davids, G. Christian, A. A. Chen, R. Coleman, P. E. Garrett, G. F. Grinyer, E. Gyabeng Fuakye, G. Hackman, J. Hollett, R. Jain, K. Kapoor, R. Krücken, A. Laffoley, A. Lennarz, J. Liang, Z. Meisel, B. Nikhil, A. Psaltis, A. Radich, M. Rocchini, N. Saei, M. Saxena, M. Singh, C. Svensson, P. Subramaniam, A. Talebitaher, S. Upadhyayula, C. Waterfield, J. Williams, and M. Williams, Phys. Rev. C **104**, L042801 (2021).
[417] D. Soltesz, M. A. A. Mamun, A. V. Voinov, Z. Meisel, B. A. Brown, C. R. Brune, S. M. Grimes, H. Hadizadeh, M. Hornish, T. N. Massey, J. E. O'Donnell, and W. E. Ormand, Phys. Rev. C **103**, 015802 (2021).
[418] Chanhee Kim, Kyungyuk Chae, Soomi Cha, Kyujin Kwak, Gwangeon Seong, and Michael Smith, Astrophys. J. **929**, 96 (2022).
[419] Konrad Schmidt, NSCL Experiment 18039.
[420] Melina Avila, FRIB Experiment 21026.
[421] C. Lederer, M. Aliotta, T. Davinson, D. Doherty, A. Estrade, C. Griffin, T. Kemp, M. Kowalska, S.J. Lonsdale, V. Margerin, A. Murphy, C. Weiß, F. Wenander, P.J. Woods, and L. Zhang, CERN-INTC-2015-036.
[422] Gavin Lotay, FRIB Experiment 21014.
[423] Takumi Okamura, Graduation Thesis, Osaka University, Osaka, Japan, 2024.
[424] Tatsuya Furuno, private communication.
[425] Zach Meisel, NSCL Experiment 17009.
[426] Chris Wrede, FRIB Experiment 23035.
[427] T. Rauscher, Phys. Rev. C **81**, 045807 (2010).
[428] M. Wang, W. J. Huang, F. G. Kondev, G. Audi, S. Naimi, Chin. Phys. C **45**, 030003 (2021).
[429] S. E. A. Orrigo, B. Rubio, W. Gelletly, P. Aguilera, A. Algora, A. I. Morales, J. Agramunt, D. S. Ahn, P. Ascher, B. Blank, C. Borcea, A. Boso, R. B. Cakirli, J. Chiba, G. de Angelis, G. de France, F. Diel, P. Doornenbal, Y. Fujita, N. Fukuda, E. Ganioğlu, M. Gerbaux, J. Giovinazzo, S. Go, T. Goigoux, S. Grévy, V. Guadilla, N. Inabe, G. G. Kiss, T. Kubo, S. Kubono, T. Kurtukian-Nieto, D. Lubos, C. Magron, F. Molina, A. Montaner-Pizá, D. Napoli, D. Nishimura, S. Nishimura, H. Oikawa, V. H. Phong, H. Sakurai, Y. Shimizu, C. Sidong, P.-A. Söderström, T. Sumikama, H. Suzuki, H. Takeda, Y. Takei, M. Tanaka, J. Wu, and S. Yagi, Phys. Rev. C **103**, 014324 (2021).
[430] S. F. Paul, J. Bergmann, J. D. Cardona, K. A. Dietrich, E. Dunling, Z. Hockenbery, C. Hornung, C. Izzo, A. Jacobs, A. Javaji, B. Kootte, Y. Lan, E. Leistenschneider, E. M. Lykiardopoulou, I. Mukul, T. Murböck, W. S. Porter, R. Silwal, M. B. Smith, J. Ringuette, T. Brunner, T. Dickel, I. Dillmann, G. Gwinner, M. MacCormick, M. P. Reiter, H. Schatz, N. A. Smirnova, J. Dilling, and A. A. Kwiatkowski, Phys. Rev. C **104**, 065803 (2021).
[431] M. Wang, Y. H. Zhang, X. Zhou, X. H. Zhou, H. S. Xu, M. L. Liu, J. G. Li, Y. F. Niu, W. J. Huang, Q. Yuan, S. Zhang, F. R. Xu, Yu. A. Litvinov, K. Blaum, Z. Meisel, R. F. Casten, R. B. Cakirli, R. J. Chen, H. Y. Deng, C. Y. Fu, W. W. Ge, H. F. Li, T. Liao, S. A. Litvinov, P. Shuai, J. Y. Shi, Y. N. Song, M. Z. Sun, Q. Wang, Y. M. Xing, X. Xu, X. L. Yan, J. C. Yang, Y. J. Yuan, Q. Zeng, and M. Zhang, Phys. Rev. Lett. **130**, 192501 (2023).
[432] C. Mazzocchi, Z. Janas, J. Döring, M. Axiotis, L. Batist, R. Borcea, D. Cano-Ott, E. Caurier, G. de Angelis, E. Farnea, A. Faßbender, A. Gadea, H. Grawe, A. Jungclaus, M. Kapica, R. Kirchner, J. Kurcewicz, S.M. Lenzi, T. Martínez, I. Mukha, E. Nácher, D. R. Napoli, E. Roeckl, B. Rubio, R. Schwengner, J. L. Tain, and C. A. Ur, Eur. Phys. J. A **12**, 269 (2001).
[433] Thomas Goigoux, Ph.D. Thesis, Université de Bordeaux, Gradignan, France, 2017.
[434] Huo Junde, Huo Su, Yang Dong, Nucl. Data Sheets **112**, 1513 (2011).
[435] M. Shamsuzzoha Basunia, Nucl. Data Sheets **151**, 1 (2018).
[436] E. Browne and J. K. Tuli, Nucl. Data Sheets **114**, 1849 (2013).
[437] M. J. López Jiménez, B. Blank, M. Chartier, S. Czajkowski, P. Dessagne, G. de France, J. Giovinazzo, D. Karamanis, M. Lewitowicz, V. Maslov, C. Miehé, P. H. Regan, M. Stanoiu, and M. Wiescher, Phys. Rev. C **66**, 025803 (2002).
[438] L. Kucuk, S. E. A. Orrigo, A. Montaner-Pizá, B. Rubio, Y. Fujita, W. Gelletly, B. Blank, Y. Oktem, T. Adachi, A. Algora, P. Ascher, R. B. Cakirli, G. de France, H. Fujita, E. Ganioğlu, J. Giovinazzo, S. Grévy, F. M. Marqués, F. Molina, F. de Oliveira Santos, L. Perrot, R. Raabe, P. C. Srivastava, G. Susoy, A. Tamii, J. C Thomas, Eur. Phys. J. A **53**, 134 (2017).
[439] J. Giovinazzo, T. Goigoux, B. Blank, P. Ascher, M. Gerbaux, S. Grévy, T. Kurtukian-Nieto, C. Magron, P. Doornenbal, N. Fukuda, N. Inabe, G.G. Kiss, T. Kubo, S. Kubono, S. Nishimura, H. Sakurai, Y. Shimizu, C. Sidong, P.-A. Söderström, T. Sumikama, H. Suzuki, H. Takeda, P. Vi, J. Wu, D.S. Ahn, J. Agramunt, A. Algora, V. Guadilla, A. Montaner-Piza, A.I. Morales, S.E.A. Orrigo, B. Rubio, Y. Fujita, M. Tanaka, W. Gelletly, P. Aguilera, F. Molina, F. Diel, D. Lubos, G. de Angelis, D. Napoli, C. Borcea, A. Boso, R.B. Cakirli, E. Ganioglu, J. Chiba, D. Nishimura, H. Oikawa, Y. Takei, S. Yagi, K. Wimmer, G. de France, S. Go, B.A. Brown, Acta Phys. Pol. B **51**, 577 (2020).
[440] J. Chen, ENSDF Analysis and Utility Programs, Gamma to Level Scheme Computation.
[441] R. Kamermans, H. W. Jongsma, J. van der Spek, and H. Verheul, Phys. Rev. C **10**, 620 (1974).
[442] Carl Svensson, Ph.D. Thesis, McMaster University, Ontario, Canada, 1998.
[443] T. Budner, M. Friedman, C. Wrede, B. A. Brown, J. José, D. Pérez-Loureiro, L. J. Sun, J. Surbrook, Y. Ayyad, D. Bardayan, K. Chae, A. Chen, K. Chipps, M. Cortesi, B. Glassman, M. R. Hall, M. Janasik, J. Liang, P. O'Malley, E. Pollacco, A. Psaltis, J. Stomps, and T. Wheeler, Phys. Rev. Lett. **128**, 182701 (2022).
[444] L. J. Sun, X. X. Xu, S. Q. Hou, C. J. Lin, J. José, J. Lee, J. J. He, Z. H. Li, J. S. Wang, C. X. Yuan, F. Herwig, J. Keegans, T. Budner, D. X. Wang, H. Y. Wu, P. F. Liang, Y. Y. Yang, Y. H. Lam, P. Ma, F. F. Duan, Z. H. Gao, Q. Hu, Z. Bai, J. B. Ma, J. G. Wang, F. P. Zhong, C. G. Wu, D. W. Luo, Y. Jiang, Y. Liu, D. S. Hou, R. Li, N. R. Ma, W. H. Ma, G. Z. Shi, G. M. Yu, D. Patel, S. Y. Jin, Y. F. Wang, Y. C. Yu, Q. W. Zhou, P. Wang, L. Y. Hu, X. Wang, H. L. Zang, P. J. Li, Q. Q. Zhao, H. M. Jia, L. Yang, P. W. Wen, F. Yang, M. Pan, X. Y. Wang, Z. G.

Hu, R. F. Chen, M. L. Liu, W. Q. Yang, Y. M. Zhao, Phys. Lett. B **802**, 135213 (2020).
[445] J. Chen, ENSDF Analysis and Utility Programs, Radiation Report.
[446] S. T. Perkins, D. E. Cullen, M.-H. Chen, J. H. Hubbell, J. Rathkopf, and J. H. Scofield, LLNL Evaluated Atomic Data Library (EADL), Tech. Rep. UCRL-50400 **30** (1991).
[447] W. Bambynek, B. Crasemann, R. W. Fink, H. U. Freund, H. Mark, C. D. Swift, R. E. Price, and P. Venugopala Rao, Rev. Mod. Phys. **44**, 716 (1972).
[448] J. H. Scofield, Radiative Transitions, in *Atomic Inner-Shell Processes*, edited by B. Crasemann (Academic, New York, 1975), Chap. 6.
[449] Karol Kozioł, Phys. Rev. A **89**, 022515 (2014).
[450] J. L. Campbell and T. Papp, At. Data Nucl. Data Tables **77**, 1 (2001).
[451] P. J. Nolan and J. F. Sharpey-Schafer, Rep. Prog. Phys. **42**, 1 (1979).
[452] I. Massa and G. Vannini, Riv. Nuovo Cim. **5**, 1 (1982).
[453] E. Browne, J.K. Tuli, Nucl. Data Sheets **111**, 2425 (2010).
[454] J. Giovinazzo, Ph. Dessagne, and Ch. Miehé, Nucl. Phys. A **674**, 394 (2000).
[455] J.C. Hardy, J.A. MacDonald, H. Schmeing, T. Faestermann, H.R. Andrews, J.S. Geiger, R.L. Graham, K.P. Jackson, Phys. Lett. B **63**, 27 (1976).
[456] K. Vierinen, Nucl. Phys. A **463**, 605 (1987).
[457] J.C. Hardy, T. Faestermann, H. Schmeing, J.A. Macdonald, H.R. Andrews, J.S. Geiger, R.L. Graham, and K.P. Jackson, Nucl. Phys. A **371**, 349 (1981).
[458] C.D. Nesaraja, Nucl. Data Sheets **115**, 1 (2014).
[459] J. A. Macdonald, J. C. Hardy, H. Schmeing, T. Faestermann, H. R. Andrews, J. S. Geiger, R. L. Graham, and K. P. Jackson, Nucl. Phys. A **288**, 1 (1977).
[460] Ph. Dessagne, Ch. Miehé, P. Baumann, A. Huck, G. Klotz, M. Ramdane, G. Walter, and J. M. Maison, Phys. Rev. C **37**, 2687 (1988).
[461] B. Singh and J. Chen, Nucl. Data Sheets **158**, 1 (2019).
[462] P. Hornshøj, K.Wilsky, P.G.Hansen, and B.Jonson, Nucl. Phys. A **187**, 637 (1972).
[463] Ch. Miehé, Ph. Dessagne, Ch. Pujol, G. Walter, B. Jonson, and M. Lindroos, Eur. Phys. J. A **5**, 143 (1999).
[464] P. Asboe-Hansen, E. Hagberg, P. G. Hansen, J. C. Hardy, P. Hornshøj, B. Jonson, S. Mattsson, P. Tidemand-Petersson, Phys. Lett. B **77**, 363 (1978).
[465] P. Asboe-Hansen, E. Hagberg, P. G. Hansen, J. C. Hardy, B. Jonson, and S. Mattsson, Nucl. Phys. A **361**, 23 (1981).
[466] B. Singh and N. Nica, Nucl. Data Sheets **113**, 1115 (2012).
[467] Jean Blachot, Nucl. Data Sheets **111**, 1471 (2010).
[468] Z. Janas, L. Batist, R. Borcea, J. Döring, M. Gierlik, M. Karny, R. Kirchner, M. La Commara, S. Mandal, C. Mazzocchi, F. Moroz, S. Orlov, A. Płochocki, E. Roeckl, and J. Żylicz, Eur. Phys. J. A **24**, 205 (2005).
[469] Jean Blachot, Nucl. Data Sheets **95**, 679 (2002).
[470] Z. Janas, L. Batist, J. Döring, M. Gierlik, R. Kirchner, J. Kurcewicz, H. Mahmud, C. Mazzocchi, A. Płochocki, E. Roeckl, K. Schmidt, P. J. Woods, and J. Żylicz, Eur. Phys. J. A **23**, 401 (2005).
[471] Balraj Singh and Jun Chen, Nucl. Data Sheets **178**, 41 (2021).
[472] X. Zhou, M. Wang, Y. H. Zhang, Yu. A. Litvinov, Z. Meisel, K. Blaum, X. H. Zhou, S. Q. Hou, K. A. Li, H. S. Xu, R. J. Chen, H. Y. Deng, C. Y. Fu, W. W. Ge, J. J. He, W. J. Huang, H. Y. Jiao, H. F. Li, J. G. Li, T. Liao, A. Litvinov, M. L. Liu, Y. F. Niu, P. Shuai, J. Y. Shi, Y. N. Song, M. Z. Sun, Q. Wang, Y. M. Xing, X. Xu, F. R. Xu, X. L. Yan, J. C. Yang, Y. Yu, Q. Yuan, Y. J. Yuan, Q. Zeng, M. Zhang, and S. Zhang, Nat. Phys. **19**, 1091 (2023).
[473] B. Rubio, P. Aguilera, F. Molina, J. Agramunt, A. Algora, V. Guadilla, A. Montaner-Pizá, A. I. Morales, S. E. A. Orrigo, W. Gelletly, B. Blank, P. Asher, M. Gerbaux, J. Giovinazzo, S. Grevy, T. Kurtukian, C. Magron, J. Chiba, D. Nishimura, H. Oikawa, Y. Takei, S. Yang, D. S. Ahn, P. Doornenbal, N. Fukuda, N. Inabe, G. Kiss, T. Kubo, S. Kubono, S. Nishimura, Y. Shimizu, C. Sidong, P.-A. Söderström, T. Sumikama, H. Suzuki, H. Takeda, P. Vi, J. Wu, Y. Fujita, M. Tanaka, F. Diel, D. Lubos, G. de Angelis, D. Napoli, C. Borcea, A. Boso, R. B. Cakirli, E. Ganioglu, G. de France, S. Go, J. Phys.: Conf. Ser. **1308**, 012018 (2019).
[474] S. Röhl, S. Hoppenau, and M. Dost, Phys. Rev. Lett. **43**, 1300 (1979).
[475] S. Röhl, S. Hoppenau, and M. Dost, Nucl. Phys. A **369**, 301 (1981).
[476] J. F. Chemin, S. Andriamonje, J. Roturier, and B. Saboya, Nucl. Phys. A **331**, 407 (1979).
[477] Per Amund Amundsen and Martin Dost, Phys. Rev. C **33**, 1079 (1986).
[478] U. Heinz, Rep. Prog. Phys. **50**, 145 (1987).
[479] A. Gilbert and A. G. W. Cameron, Can. J. Phys. **43**, 1446 (1965).
[480] W. Dilg, W. Schantl, H. Vonach, and M. Uhl, Nucl. Phys. A **217**, 269 (1973).
[481] J. C. Hardy, Phys. Lett. B **109**, 242 (1982).
[482] B. L. Berman and S. C. Fultz, Rev. Mod. Phys. **47**, 713 (1975).
[483] C. H. Johnson, Phys. Rev. C **16**, 2238 (1977).
[484] V. Avrigeanu and M. Avrigeanu, Phys. Rev. C **106**, 024615 (2022).
[485] J. Wei, H. Ao, B. Arend, S. Beher, G. Bollen, N. Bultman, F. Casagrande, W. Chang, Y. Choi, S. Cogan, C. Compton, M. Cortesi, J. Curtin, K. Davidson, X. Du, K. Elliott, B. Ewert, A. Facco, A. Fila, K. Fukushima, V. Ganni, A. Ganshyn, J. Gao, T. Glasmacher, J. Guo, Y. Hao, W. Hartung, N. Hasan, M. Hausmann, K. Holland, H. C. Hseuh, M. Ikegami, D. Jager, S. Jones, N. Joseph, T. Kanemura, S.-H. Kim, P. Knudsen, B. Kortum, E. Kwan, T. Larter, R. E. Laxdal, M. Larmann, K. Laturkar, J. LeTourneau, Z.-Y. Li, S. Lidia, G. Machicoane, C. Magsig, P. Manwiller, F. Marti, T. Maruta, A. McCartney, E. Metzgar, S. Miller, Y. Momozaki, D. Morris, M. Mugerian, I. Nesterenko, C. Nguyen, W. O'Brien, K. Openlander, P. N. Ostroumov, M. Patil, A. S. Plastun, J. Popielarski, L. Popielarski, M. Portillo, J. Priller, X. Rao, M. Reaume, H. Ren, K. Saito, M. Smith, M. Steiner, A. Stolz, O. B. Tarasov, B. Tousignant, R. Walker, X. Wang, J. Wenstrom, G. West, K. Witgen, M. Wright, T. Xu, Y. Xu, Y. Yamazaki, T. Zhang, Q. Zhao, S. Zhao, K. Dixon, M. Wiseman, M. Kelly, K. Hosoyama, and S. Prestemon, Mod. Phys. Lett. A **37**, 2230006 (2022).

[486] M. Portillo, B.M. Sherrill, Y. Choi, M. Cortesi, K. Fukushima, M. Hausmann, E. Kwan, S. Lidia, P.N. Ostroumov, R. Ringle, M.K. Smith, M. Steiner, O.B. Tarasov, A.C.C. Villari, and T. Zhang, Nucl. Instrum. Methods Phys. Res. B **540**, 151 (2023).
[487] C.S. Sumithrarachchi, D.J. Morrissey, S. Schwarz, K. Lund, G. Bollen, R. Ringle, G. Savard, and A.C.C. Villari, Nucl. Instrum. Methods Phys. Res. B **463**, 305 (2020).
[488] K.R. Lund, G. Bollen, D. Lawton, D.J. Morrissey, J. Ottarson, R. Ringle, S. Schwarz, C.S. Sumithrarachchi, A.C.C. Villari, and J. Yurkon, Nucl. Instrum. Methods Phys. Res. B **463**, 378 (2020).
[489] A.C.C. Villari, G. Bollen, A. Henriques, A. Lapierre, S. Nash, R. Ringle, S. Schwarz, C.S. Sumithrarachchi, Nucl. Instrum. Methods Phys. Res. B **541**, 350 (2023).
[490] FRIB beam rate calculator.
[491] J. F. Ziegler, M. D.Ziegler, and J. P. Biersack, Nucl. Instrum. Methods Phys. Res. B **268**, 1818 (2010).
[492] MIRION Low Energy Germanium Detector.
[493] MIRION Extended Range Coaxial Germanium Detector.
[494] MIRION Cryo-Pulse 5 Plus Electrically Refrigerated Cryostat.
[495] D. Willems, R. Arts, B.V.-J. Douwen, MIRION Technical Paper (2015).
[496] MIRCON MSD12 Circular Silicon Detector.
[497] MIRCON MSD26 Circular Silicon Detector.
[498] MIRION Intelligent Preamplifier.
[499] J. Eberth, H. Hess, P. Reiter, S. Bertoldo, C. Carraro, G. Maggioni, D. R. Napoli, W. Raniero, and D. De Salvador, Eur. Phys. J. A **59**, 179 (2023).
[500] ORTEC 660 Dual 5-kV Bias Supply.
[501] Mesytec MPR-1 Charge Integrating Preamplifier.
[502] Mesytec MHV-4 High Voltage Supply.
[503] Mesytec MNV-4 NIM Power Supply.
[504] XIA Pixie-16 Digitizer.
[505] K. Starosta, C. Vaman, D. Miller, P. Voss, D. Bazin, T. Glasmacher, H. Crawford, P. Mantica, H. Tan, W. Hennig, M. Walby, A. Fallu-Labruyere, J. Harris, D. Breus, P. Grudberg, W.K. Warburton, Nucl. Instrum. Methods Phys. Res. A **610**, 700 (2009).
[506] C.J. Prokop, S.N. Liddick, B.L. Abromeit, A.T. Chemey, N.R. Larson, S. Suchyta, J.R. Tompkins, Nucl. Instrum. Methods Phys. Res. A **741**, 163 (2014).
[507] XIA Pixie-16 Digitizer User Manual.
[508] H.Y. Wu, Z.H. Li, H. Tan, H. Hua, J. Li, W. Hennig, W.K. Warburton, D.W. Luo, X. Wang, X.Q. Li, S.Q. Zhang, C. Xu, Z.Q. Chen, C.G. Wu, Y. Jin, J. Lin, D.X. Jiang, Y.L. Ye, Nucl. Instrum. Methods Phys. Res. A **975**, 164200 (2020).
[509] D. Weisshaar, D. Bazin, P.C. Bender, C.M. Campbell, F. Recchia, V. Bader, T. Baugher, J. Belarge, M.P. Carpenter, H.L. Crawford, M. Cromaz, B. Elman, P. Fallon, A. Forney, A. Gade, J. Harker, N. Kobayashi, C. Langer, T. Lauritsen, I.Y. Lee, A. Lemasson, B. Longfellow, E. Lunderberg, A.O. Macchiavelli, K. Miki, S. Momiyama, S. Noji, D.C. Radford, M. Scott, J. Sethi, S.R. Stroberg, C. Sullivan, R. Titus, A. Wiens, S. Williams, K. Wimmer, S. Zhu, Nucl. Instrum. Methods Phys. Res. A **847**, 187 (2017).
[510] BNC Model DB-2 NIM Random Pulse Generator.
[511] Nuclear Wallet Cards, 2023.
[512] Y. Isozumi, Nucl. Instrum. Methods Phys. Res. A **280**, 151 (1989).
[513] M. S. Freedman, Annu. Rev. Nucl. Part. Sci. **24**, 209 (1974).
[514] B. Crasemann, *Atomic Inner-Shell Processes* (Academic, New York, 1975).
[515] Juhani Kantele, *Handbook of Nuclear Spectrometry* (Academic, London, 1995).
[516] L. J. Sun, M. Friedman, T. Budner, D. Pérez-Loureiro, E. Pollacco, C. Wrede, B. A. Brown, M. Cortesi, C. Fry, B. E. Glassman, J. Heideman, M. Janasik, A. Kruskie, A. Magilligan, M. Roosa, J. Stomps, J. Surbrook, and P. Tiwari, Phys. Rev. C **103**, 014322 (2021).
[517] Matt Newville, easyXAFS, Matteo Levantino, Christian Schlepuetz, Damian Günzing, Max Rakitin, Sang-Woo Kim, and kalvdans, xraypy/XrayDB: (4.5.1). Zenodo (2023).
[518] M. Basunia, Nucl. Data Sheets **107**, 2323 (2006).
[519] M.-M. Bé, V. Chisté, C. Dulieu, E. Browne, V. Chechev, N. Kuzmenko, R. Helmer, A. Nichols, E. Schönfeld, and R. Dersch, Mono. BIPM-5 - Table of Radionuclides, Vol.2 (2004).
[520] Devinder Mehta, M.L. Garg, Jasbir Singh, Nirmal Singh, T.S. Cheema, P.N. Trehan, Nucl. Instrum. Methods Phys. Res. A **245**, 447 (1986).
[521] M.-M. Bé, V. Chisté, C. Dulieu, X. Mougeot, E. Browne, V. Chechev, N. Kuzmenko, F. Kondev, A. Luca, M. Galán, A.L. Nichols, A. Arinc, and X. Huang, Mono. BIPM-5 - Table of Radionuclides, Vol.5 (2010).
[522] S. Agostinelli, J. Allison, K. Amako, J. Apostolakis, H. Araujo, P. Arce, M. Asai, D. Axen, S. Banerjee, G. Barrand, F. Behner, L. Bellagamba, J. Boudreau, L. Broglia, A. Brunengo, H. Burkhardt, S. Chauvie, J. Chuma, R. Chytracek, G. Cooperman, G. Cosmo, P. Degtyarenko, A. Dell'Acqua, G. Depaola, D. Dietrich, R. Enami, A. Feliciello, C. Ferguson, H. Fesefeldt, G. Folger, F. Foppiano, A. Forti, S. Garelli, S. Giani, R. Giannitrapani, D. Gibin, J. J. Gómez Cadenas, I. González, G. Gracia Abril, G. Greeniaus, W. Greiner, V. Grichine, A. Grossheim, S. Guatelli, P. Gumplinger, R. Hamatsu, K. Hashimoto, H. Hasui, A. Heikkinen, A. Howard, V. Ivanchenko, A. Johnson, F. W. Jones, J. Kallenbach, N. Kanaya, M. Kawabata, Y. Kawabata, M. Kawaguti, S. Kelner, P. Kent, A. Kimura, T. Kodama, R. Kokoulin, M. Kossov, H. Kurashige, E. Lamanna, T. Lampén, V. Lara, V. Lefebure, F. Lei, M. Liendl, W. Lockman, F. Longo, S. Magni, M. Maire, E. Medernach, K. Minamimoto, P. Mora de Freitas, Y. Morita, K. Murakami, M. Nagamatu, R. Nartallo, P. Nieminen, T. Nishimura, K. Ohtsubo, M. Okamura, S. O'Neale, Y. Oohata, K. Paech, J. Perl, A. Pfeiffer, M. G. Pia, F. Ranjard, A. Rybin, S. Sadilov, E. Di Salvo, G. Santin, T. Sasaki, N. Savvas, Y. Sawada, S. Scherer, S. Sei, V. Sirotenko, D. Smith, N. Starkov, H. Stoecker, J. Sulkimo, M. Takahata, S. Tanaka, E. Tcherniaev, E. Safai Tehrani, M. Tropeano, P. Truscott, H. Uno, L. Urban, P. Urban, M. Verderi, A. Walkden, W. Wander, H. Weber, J. P. Wellisch, T. Wenaus, D. C. Williams, D. Wright, T. Yamada, H. Yoshida, and D. Zschiesche, Nucl. Instrum. Methods Phys. Res. A **506**, 250 (2003).
[523] J. Allison, K. Amako, J. Apostolakis, P. Arce, M. Asai, T. Aso, E. Bagli, A. Bagulya, S. Banerjee, G. Barrand, B.R. Beck, A.G. Bogdanov,

D. Brandt, J.M.C. Brown, H. Burkhardt, Ph. Canal, D. Cano-Ott, S. Chauvie, K. Cho, G.A.P. Cirrone, G. Cooperman, M.A. Cortés-Giraldo, G. Cosmo, G. Cuttone, G. Depaola, L. Desorgher, X. Dong, A. Dotti, V.D. Elvira, G. Folger, Z. Francis, A. Galoyan, L. Garnier, M. Gayer, K.L. Genser, V.M. Grichine, S. Guatelli, P. Guèye, P. Gumplinger, A.S. Howard, I. Hřivnáčová, S. Hwang, S. Incerti, A. Ivanchenko, V.N. Ivanchenko, F.W. Jones, S.Y. Jun, P. Kaitaniemi, N. Karakatsanis, M. Karamitros, M. Kelsey, A. Kimura, T. Koi, H. Kurashige, A. Lechner, S.B. Lee, F. Longo, M. Maire, D. Mancusi, A. Mantero, E. Mendoza, B. Morgan, K. Murakami, T. Nikitina, L. Pandola, P. Paprocki, J. Perl, I. Petrović, M.G. Pia, W. Pokorski, J.M. Quesada, M. Raine, M.A. Reis, A. Ribon, A. Ristić Fira, F. Romano, G. Russo, G. Santin, T. Sasaki, D. Sawkey, J.I. Shin, I.I. Strakovsky, A. Taborda, S. Tanaka, B. Tomé, T. Toshito, H.N. Tran, P.R. Truscott, L. Urban, V. Uzhinsky, J.M. Verbeke, M. Verderi, B.L. Wendt, H. Wenzel, D.H. Wright, D.M. Wright, T. Yamashita, J. Yarba, H. Yoshida, Nucl. Instrum. Methods Phys. Res. A **835**, 186 (2016).

[524] G. F. Knoll, *Radiation Detection and Measurement* (John Wiley & Sons, New York, 2010).

[525] M. J. Martin, Nucl. Data Sheets **114**, 1497 (2013).

[526] B. E. Glassman, D. Pérez-Loureiro, C. Wrede, J. Allen, D. W. Bardayan, M. B. Bennett, K. A. Chipps, M. Febbraro, M. Friedman, C. Fry, M. R. Hall, O. Hall, S. N. Liddick, P. O'Malley, W. -J. Ong, S. D. Pain, S. B. Schwartz, P. Shidling, H. Sims, L. J. Sun, P. Thompson, and H. Zhang, Phys. Rev. C **99**, 065801 (2019).

[527] G. R. Gilmore, *Practical Gamma-ray Spectroscopy* (John Wiley & Sons, New York, 2008).

[528] T. Palazzo, A. J. Mitchell, G. J. Lane, A. E. Stuchbery, B. A. Brown, M. W. Reed, A. Akber, B. J. Coombes, J. T. H. Dowie, T. K. Eriksen, M. S. M. Gerathy, T. Kibédi, T. Tornyi, and M. O. de Vries, Phys. Rev. Lett. **130**, 122503 (2023).

[529] Y.A. Akovali, Nucl. Data Sheets **84**, 1 (1998).

[530] Xavier Mougeot, Christophe Dulieu, Xiaolong Huang, Mark A. Kellett, Sylvain Leblond, and Baosong Wang, Metrologia **62**, 029002 (2025).

[531] Canberra Model 1407P Pulse Pair Generator.

[532] Marcell P. Takács, Karsten Kossert, Appl. Radiat. Isot. **176**, 109858 (2021).

[533] Chavdar Dutsov, Benoît Sabot, Philippe Cassette, Krasimir Mitev, Appl. Radiat. Isot. **176**, 109845 (2021).

[534] O.C.B. Santos, J.R.B. Oliveira, E. Macchione, R. Lichtenthäler, K.C.C. Pires, and A. Lépine-Szily, Nucl. Phys. A **1040**, 122745 (2023).

[535] Erik Jensen, Ph.D. Thesis, Aarhus University, Aarhus, Denmark, 2024.

[536] Justus Eder, Master Thesis, Aarhus University, Aarhus, Denmark, 2024.

[537] R. Mahajan, T. Wheeler, E. Pollacco, C. Wrede, A. Adams, H. Alvarez-Pol, A. Andalib, A. Anthony, Y. Ayyad, D. Bazin, T. Budner, M. Cortesi, J. Dopfer, M. Friedman, B. Jain, A. Jaros, D. Pérez-Loureiro, B. Mehl, R. De Oliveira, S. Ravishankar, L. J. Sun, and J. Surbrook, Phys. Rev. C **110**, 035807 (2024).

[538] FRIB Decay Station White Paper.

[539] M. Honma, T. Otsuka, B. A. Brown, and T. Mizusaki, Phys. Rev. C **69**, 034335 (2004).

[540] B. A. Brown and W. D. M. Rae, Nucl. Data Sheets **120**, 115 (2014).

[541] T. Rauscher, Int. J. Mod. Phys. E **20**, 1071 (2011).

[542] T. Rauscher, code SMARAGD, version v0.10.2 (2014).

[543] A. Adams, C. Wrede, B. A. Brown, R. Longland, L. J. Sun, J. Dopfer, C. Marshall *et al*., in preparation.

[544] R. Longland, C. Iliadis, A. E. Champagne, J. R. Newton, C. Ugalde, A. Coc, and R. Fitzgerald, Nucl. Phys. A **841**, 1 (2010).

[545] C. Iliadis, R. Longland, A. E. Champagne, A. Coc, and R. Fitzgerald, Nucl. Phys. A **841**, 31 (2010).

[546] C. Iliadis, R. Longland, A. E. Champagne, and A. Coc, Nucl. Phys. A **841**, 251 (2010).

[547] P. Mohr, R. Longland, and C. Iliadis, Phys. Rev. C **90**, 065806 (2014).

[548] C. Iliadis, R. Longland, A. Coc, F. X. Timmes, and A. E. Champagne, J. Phys. G: Nucl. Part. Phys. **42**, 034007 (2015).

[549] K. Hämäläinen, S. Manninen, P. Suortti, S. P. Collins, M. J. Cooper, and D. Laundy, J. Phys.: Condens. Matter **1**, 5955 (1989).

[550] Ning Lu, Yi Hua Lam, Alexander Heger, Zi Xin Liu, and Hidetoshi Yamaguchi, Phys. Rev. C **110**, 065804 (2024).